ANALYSIS ON FIBER LASER MICRO-MACHINING OF ENGINEERING MATERIALS

Thesis submitted by

ABHISHEK SEN

DOCTOR OF PHILOSOPHY (ENGINEERING)

DEPARTMENT OF PRODUCTION ENGINEERING
FACULTY COUNCIL OF ENGINEERING & TECHNOLOGY
JADAVPUR UNIVERSITY
KOLKATA-700 032
INDIA

2019

JADAVPUR UNIVERSITY
KOLKATA-700032

Index No: 171/13/E

TITLE OF THE Ph.D. (Engg.) THESIS:

Analysis on Fiber Laser Micro-Machining of Engineering Materials

NAME, DESIGNATION & INSTITUTION OF THE SUPERVISOR:

Prof (Dr.) BISWANATH DOLOI
Professor, Department of Production Engineering,
Jadavpur University,
Kolkata –700032, India.

LIST OF PUBLICATIONS

International Journal:
Published-

1. "Fibre Laser Microchanneling of Polymethyl Methacrylate (PMMA)," Lasers in Engineering (Old City Publishing), (2016), Vol. 35, Issue 1-4, Pp. 123-138.
2. "An Experimental Investigation into Fibre Laser Micro-Drilling of Quartz," International Journal of Mechatronics and Manufacturing Systems (IJMMS), Inderscience, (2018), Vol. 11, No. 2/3, Pp. 182-202.

International Journal:

Accepted/Communicated-

1. "Analysis of Fiber Laser Micro-Grooving on 316L Stainless Steel," Lecture Notes in Management and Industrial Engineering, Springer, (2019). – Accepted.
2. "Analysis of Fiber Laser Micro-Drilling on Quartz," Lecture Notes in Mechanical Engineering, Springer, (2019). – Under Review.

National Journal: Nil

Book Chapter:

1. "Fiber Laser Micro-machining of Ti-6Al-4V." Lasers Based Manufacturing. Topics in Mining, Metallurgy and Materials Engineering, Springer, New Delhi, (2015), Pp. 255-281. ISBN: 978-81-322-2352-8. DOI: 10.1007/978-81-322-2352-8_15.
2. "Fiber Laser Micro-Machining of Engineering Materials." Non-Traditional Micromachining Processes. Materials Forming, Machining and Tribology. Springer, Cham, (2017), Pp. 227-252, ISBN: 978-3-319-52009-4, DOI: 10.1007/978-3-319-52009-4_6.

LIST OF NATIONAL/INTERNATIONAL CONFERENCES:

International Conference:

1. "Experimental Investigation and Process Parameter Optimization of Laser Micro-Channelling on PMMA," 8th International Conference on Precision, Meso, Micro and Nano Engineering (COPEN-2013), Vol. 1, Pp.746-751, NIT, Calicut.

2. "Experimental Studies of Fibre Laser Micro-Machining of Ti-6Al-4V," 5th International and 26th National Conference on All India Manufacturing Technology, Design and Research (AIMTDR-2014). Pp. 229-1-229-7, IIT, Guwahati.
3. "Fibre Laser Micro-Machining of Polymethyl Methacrylate," 3rd International Conference on Laser and Plasma Applications in Material Science (LAPAMS-2015), IIT, Kharagpur.
4. "Parametric Influences on IR Fiber Laser Micro-Machining on PMMA," 9th International Conference on Precision, Meso, Micro and Nano Engineering (COPEN-2015). IIT, Bombay.
5. "Modelling and Analysis of Fiber Laser Micro-Channeling on Polymethyl Methacrylate (PMMA)," Second International Conference on Advanced Materials for Power Engineering (ICAMPE-2016). Mahatma Gandhi University, Kottayam.
6. "Fiber Laser Micro-Grooving of 316L Stainless Steel Utilizing Variable Temperature Heating Apparatus," 6th International and 27th National Conference on All India Manufacturing Technology, Design and Research (AIMTDR-2016). Pp. 285-289, ISBN: 978-93-86256-27-0. College of Engineering, Pune.
7. "Parametric Analysis on Fiber Laser Surface Texturing of Hastelloy C-276," 10th International Conference on Precision, Meso, Micro and Nano Engineering (COPEN-2017), Pp. 198-201, ISBN: 978-93-80689-28-9. IIT, Madras.
8. "Analysis of Fiber Laser Micro-Grooving on 316L Stainless Steel," 7th International and 28th National Conference on All India Manufacturing Technology, Design and Research (AIMTDR-2018). Anna University, Chennai.
9. "Analysis of Fiber Laser Micro-Drilling on Quartz," International Conference on Advances in Material and Manufacturing Engineering (ICAMME- 2019). KIIT University, Bhubaneswar.

National Conference: Nil

Patents: Nil

JADAVPUR UNIVERSITY

FACULTY OF ENGINEERING AND TECHNOLOGY

DEPARTMENT OF PRODUCTION ENGINEERING

CERTIFICATE FROM THE SUPERVISORS

This is to certify that the thesis entitled ***"ANALYSIS ON FIBER LASER MICRO-MACHINING OF ENGINEERING MATERIALS"*** *submitted by Shri. Abhishek Sen, who got his name registered on 2nd May 2013 for the award of Ph.D. (Engg.) degree of Jadavpur University is absolutely based upon his own work under the supervision of Prof. Biswanath Doloi and that neither his thesis nor any part of the thesis has been submitted for any degree/diploma or any other academic award anywhere before.*

(Signature of the Supervisor
and date with official seal)

PREFACE

The laser, the acronym for light amplification by stimulated emission of radiation, is a coherent and monochromatic source of electromagnetic radiation with a wavelength ranging from the ultraviolet to the infrared range. The initial foundation of the laser theory was laid by Einstein, and later, Kopfermann and Ladenburg confirmed Einstein's prediction. In the mid-1970s, more reliable and powerful lasers were developed for industrial applications such as cutting, welding, drilling, and melting. During the 1980s and early 1990s, lasers were successfully applied for heating, cladding, alloying, glazing, and thin film deposition.

Advances in the laser technology combined with a better understanding of laser-matter interaction make laser micro-machining a viable, attractive, cost-effective, and enabling technology to support various engineering applications. At present, laser micro-machining has become one of the versatile fabrication process owing to its superior features like contact and wear less machining, better flexibility and a possibility for a high degree of automation, etc. As a result, laser micro-machining is being widely used for fabricating micro-components on various metals, ceramics, and polymer for medical industries, automobile sectors, etc.

Laser micro-machining attributes a wide range of pulse duration from microsecond to femtosecond, a variety of wavelengths and different pulse repetition rates from single to megahertz allowing the process to fabricate complex machined micro parts with high aspect ratio. Various micro-manufacturing domains like micro-cutting, micro-drilling are classified as laser micro-machining processes to remove the material by rapid heating, melting, and evaporation. Besides, the detrimental micro-machining effects, i.e., burr formation, melting, heat affected zone (HAZ), etc. can also be minimized with the aid of short pulsed lasers.

Fiber lasers have evolved as the most versatile and rapid growing laser systems during the last decade and successfully emerged in the various fields of manufacturing, medical, meteorological and military applications that were previously dominated by conventional solid-state lasers along with gas lasers.

From the survey of past literature, it is evident that few investigations have been reported about the fiber laser micro-machining processes such as micro-channeling, micro-drilling, micro-grooving, surface texturing on PMMA, Ti-6Al-4V, Hastelloy C-276, Quartz, and 316L till now. The focus of this research work is to study the fiber laser micro-machining processes in detail and explore the possibilities of machining different micro-features on those aforesaid materials. For generating different types of micro-features, different combinations of process parameters for each of the workpieces are considered for the analyses. A preheating setup is

also developed to analyze the effect of different process parameters at the different elevated temperatures.

The present research work has been planned and designed to investigate and optimize the fiber laser micro-machining quality characteristics during machining on various alloys, polymer, and quartz. Within the limitation of the available resources, the objectives of the present research work have been combined as follows:

(i) To perform basic experiments for process parameter selection for generating micro-channels on PMMA by the fiber laser system. To analyze and optimize the influences of process parameters on the responses for fabricating micro-channels on PMMA with the aid of fiber laser.

(ii) To carry out the preliminary experiments for process parameter selection for generating micro-grooves on Ti-6Al-4V. To analyze the influences of process parameters on the responses for generating micro-grooves on Ti-6Al-4V with the aid of the fiber laser.

(iii) To design and develop a preheating setup for fiber laser micro-machining process to study the effect of preheating.

(iv) To perform experiments for process parameters selection for generating micro-grooves on 316L. To analyze the influences of process parameters on the responses for generating micro-grooves on 316L with the aid of the fiber laser and further comparing the results of micro-grooves on 316L at elevated temperatures, with the same combination of process parameters.

(v) To analyze the influences of process parameters on the responses for the generation of micro-holes on quartz with the aid of fiber laser. To carry out multi-objective optimization for all the responses for determining the optimal process parametric combination and also to compare with the actual value of responses for determining the percentage of error for achieving good quality micro-drilled hole on quartz by the pulsed mode fiber laser system.

(vi) To analyze the primary influences of process parameters on the responses for generating textured surfaces on Hastelloy C-276 with the aid of fiber laser. To carry out multi-objective optimization for all the responses for determining the optimal process parametric combination and also compare with the actual value of responses for determining the percentage of error for achieving suitable quality surfaces on Hastelloy C-276 by the pulsed mode fiber laser. To compare the results of textured surfaces on

Hastelloy C-276 at elevated temperatures, with the same combination of process parameters by the pulsed mode fiber laser.

The thesis is prepared in a well-organized manner into eight chapters. A summary of each chapter is provided as below:

Chapter 1 outlines an overview of different fiber laser micro-machining processes, material removal mechanism, present needs, and applications. The selection of different engineering materials, along with their applications, is also discussed in this chapter. Literature reviews of previous works are incorporated and studied for finding out the existing knowledge gap to outline the research objectives. Details of fiber laser machining set up along with the preheating set up have been discussed in chapter 2. Chapter 3 presents process parameter selection and experimentation for fiber laser micro-channeling on PMMA. Influences of process parameters on the responses of fiber laser micro-channeling on PMMA have been discussed. Multi-objective optimization is also carried out in order to find out the optimized combinations of process parameters for achieving desired geometrical dimensions of PMMA micro-channels. In chapter 4, an in-depth study of the fiber laser micro-grooving of Ti-6Al-4V, the occurring physical processes, machining strategy, and the influence of various process parameters have also been discussed. Chapter 5 includes a comparative analysis of fiber laser process parameters in atmospheric condition as well as in the condition of flowing assist air pressure on the considered responses of micro-groove cut on 316L by fiber laser micro-machining process. Also, the present chapter deals with a comparative analysis of fiber laser micro-grooving operation of 316L at room temperature along with different elevated temperatures ranging from 200°C to 250°C, with the aid of a developed heating setup. Chapter 6 emphasizes the experimental investigation into quartz for generating micro-holes with the aid of the fiber laser system. In this chapter, the influences of process parameters on the responses during fiber laser micro-drilling on quartz have been analyzed. A multi-objective optimized result for achieving micro-hole dimensions has also been discussed. In chapter 7, the effect of process parameters on the different responses has also been carried out at different temperatures for fiber laser surface texturing of Hastelloy C-276. Besides, an effort has been made to analyze the different surface roughness parameters during the fiber laser surface texturing of Hastelloy C-276. In chapter 8, the general conclusions based upon various experimental results and discussions have been summarized. The future scope of the present research work also has been concluded in chapter 8.

ACKNOWLEDGEMENT

The author wishes to express his deep sense of gratitude to the PhD (Engg.) thesis supervisor Prof. Biswanath Doloi, Professor, Production Engineering Department, Jadavpur University, Kolkata for his constant guidance, valuable advice, helpful suggestions, supports, encouragement and continuous association at every aspect from the budding stage to the final stage of this research work. Without his helpful and timely advice, this thesis would not have been progressed as smoothly as it did towards its completion. The author is undeniably grateful to him for his valuable time, which he has spent on the present research work.

The author wishes to express his deep sense of gratitude to Dr. Bijoy Bhattacharyya, Professor, Production Engineering Department, Jadavpur University, Kolkata for his constant guidance, valuable advice, helpful suggestions, supports, encouragement and continuous association at every aspect. The author is obliged to him for his valuable advice which he has given on the present research work.

The author gratefully acknowledges the co-operation and encouragement received from Dr. Shankar Chakraborty, Professor, Dr. Debamalya Banerjee, Professor, Dr. Biplab Ranjan Sarkar, Associate Professor and Head of the Department, Dr. Arunanshu Shekhar Kuar, Professor, Dr. Soumya Sarkar, Professor, and all the faculty members and staff members of Production Engineering Department, Jadavpur University during this research work.

The author gratefully acknowledges the Centre of Advanced Study (CAS)–Phase IV Programme of the University Grants Commission (UGC), New Delhi and Technical Quality Improvement Programme of Phase II (TEQIP-II) for the financial support, and Department of Production Engineering, Jadavpur University for providing the laboratory facilities. Thanks are also extended to FET office and Research section for their cordial assistance and administrative support. The author is also grateful to Shajanand Laser Technology Limited for extending their machining facilities in Gandhinagar, Gujrat to carry out some of the research works.

A very special thanks to Mr. Nilanjan Roy and Dr. Somnath Das for their constant guidance, unconditional love, and support during the time needed. They are the main supporting strength throughout this journey. A special thanks to Mr. Kingshuk Mandal, Mr. Debal Pramanik, Mr. Subhrajit Debnath, Mr. Subham Biswas, Mr. Santosh Kumar, Mr. Omar Faruk Biswas, Dr. Golam Kibria, and Mr. Kaushik Mishra for their constant co-operation, valuable

assistance and support during this research work and without their help the thesis could not be completed.

Last but not least, the author would express his gratitude to Smt. Anuradha Sen (Grand Mother), Mrs. Ruma Sen (Mother), Mr. Swapanendu Sen (Father) for their love, motivation, encouragement, support, and sacrifice during the tenure of research work. The author is also thankful to his wife, Mrs. Salini Das for her support and care. The author is also thankful to Mr. Anirban Sen (Elder Brother), Dr. Amlan Sen (Elder Brother), Smt. Shukla Sen (Aunty), Late Bhudev Chandra Ghosh (Grand Parent), Mr. Anjan Banerjee (Uncle), Late Smt. Manju Thakur (Aunty), Dr. Sanjoy Kumar Ghosh (Friend), Smt. Esita Das Mahapatra (Friend), Mr. Sounak Bhattacharyya (Friend), Mr. Sanat Kumar Dey (Teacher), Mr. Nirvik Banerjee (Colleague), and Mr. Debashish Dey for their continuous support, love, and motivation.

(Abhishek Sen)

VITA

The author, Mr. Abhishek Sen, son of Mr. Swapanendu Sen and Mrs. Ruma Sen, was born on 22nd September 1986 in Serampore, Hooghly, West Bengal. He studied in Serampore Union Institution and passed the Secondary Examination of WBBSE and Higher Secondary Examination of WBCHSE in 2003 and 2005 respectively with 1st class.

The author graduated in Production Engineering in 2009 from Haldia Institute of Technology, Haldia, West Bengal under the West Bengal University of Technology with First class. The author completed his M.E. in Metallurgical Engineering in 2011 from Metallurgical and Material Engineering Department, Jadavpur University, Kolkata. Then he joined Bengal Institute of Technology and Management, Shantiniketan as an Assistant Professor in Mechanical Engineering Department in July 2011. After that, he joined as a Junior Research Fellow under "Technical Quality Improvement Programme" under Phase II in August 2012 in the Department of Production Engineering of Jadavpur University. He has done his research work in the area of fiber laser micro-machining of engineering materials during the entire duration. In August 2014, he became Senior Research Fellow of "Technical Quality Improvement Programme under Phase II. The author is currently working as an Assistant Professor and Teacher in charge of Mechanical Engineering Department from Calcutta Institute of Technology, Uluberia, Howrah. The author has published two research papers in international journals, three book chapters as well as presented more than fourteen research papers in reputed international conferences related to advanced machining processes.

Dedicated to Didibhai, Maa and Baba

My foundation of strength and source of inspiration,
For their trust in education, never-ending
support, love and encouragement

TABLE OF CONTENTS

TITLE SHEET **I**

LIST OF PUBLICATIONS OUT OF THE RESEARCH WORK **V**

CERTIFICATE FROM THE SUPERVISORS **VII**

PREFACE **IX**

ACKNOWLEDGEMENT **XIII**

VITA **XV**

DEDICATION **XVII**

CHAPTER 1. INTRODUCTION 1
1.1 Need and Advantages of Laser Micro-Machining 3
1.2 Fiber Laser in Micro-Machining 6
1.2.1 Brief History of Fiber Laser 6
1.2.2 Present Status of Fiber Laser 7
1.2.3 Classification of Fiber Laser 8
1.2.4 Comparison between Fiber Laser and Other Lasers for Micro- Machining 10
1.3 Basic Principle of Fiber Laser Generation Process 11
1.4 Principle of Fiber Laser Micro-Machining Process 13
1.5 Advantages of Fiber Laser Micro-Machining 15
1.6 Applications of Fiber Laser for Micro-Machining 16
1.7 Literature Review of Fiber Laser Micro-Machining Processes 17
1.7.1 Fiber Laser Micro-Cutting Process 18
1.7.1.1 Fiber Laser Stent Cutting Process 21
1.7.1.2 Fiber Laser Micro-Grooving Process 24
1.7.2 Fiber Laser Micro-Drilling Process 25
1.7.3 Fiber Laser Milling Process 29
1.7.4 Fiber Laser Micro-Turning Process 30
1.7.5 Fiber Laser Marking Process 31
1.8 Selection of Workpiece Materials 31
1.8.1 Polymethyl Methacrylate (PMMA) 32
1.8.1.1 Applications of PMMA 33
1.8.2 Quartz 33
1.8.2.1 Applications of Quartz 33
1.8.3 Titanium Alloy-Ti-6Al-4V 34
1.8.3.1 Applications of Ti-6Al-4V 34
1.8.4 Nickel Super Alloy-Hastelloy C-276 35

1.8.4.1 Applications of Hastelloy C-276 35
1.8.5 Stainless Steel-316L 36
1.8.5.1 Applications of 316L 36
1.9 Objectives and Scope of the Present Research Work 37

CHAPTER 2. DETAILS OF DIODE PUMPED FIBER LASER MICRO-MACHINING SYSTEM
2.1 Introduction 39
2.2 Fiber Laser Generation Unit 41
2.2.1 Optical Fiber 42
2.2.2 Silicate Glass 42
2.2.3 Rare Earth Doped Elements 43
2.2.4 Fiber Bragg Gratings (FBGs) 43
2.2.5 Laser Diodes 44
2.2.6 Fiber Couplers 44
2.2.7 Fiber Laser Isolators 44
2.2.8 Fiber Coupled Acousto-Optic Modulator 44
2.3 Fiber Laser Delivery System 46
2.3.1 Collimator 46
2.3.2 Beam Bender 47
2.3.3 Beam Delivery Unit and Focusing Lens 48
2.4 Assist Air Supply Unit 49
2.5 CNC Controller for X–Y–Z Movement 49
2.6 Development of Preheating Setup 50
2.6.1 Details of Preheating Setup 50

CHAPTER 3. EXPERIMENTAL INVESTIGATION INTO FIBER LASER MICRO-CHANNELING ON PMMA
3.1 Introduction 55
3.1.1 Properties and Applications of PMMA 55
3.1.2 Mechanism of Material Removal during Fiber Laser Micro-Machining of PMMA 56
3.2 Experimentation 59
3.2.1 Selection of the Process Parameters 60
3.2.2 Measurements of Responses 61
3.3 Preliminary Study of Fiber Laser Micro-Channeling on PMMA 62
3.3.1 Results and Discussions 63
3.3.1.1 Influence of Scan Speed and Laser Power on the Cut Width, Depth, HAZ Width and Aspect Ratio of Micro-Channels on PMMA 64
3.3.1.2 Influence of Pulse Frequency on the Cut Width, Depth, HAZ Width and Aspect Ratio of Micro-Channels on PMMA 71
3.3.1.3 Influence of Number of Passes on the Cut Width, Depth, HAZ Width and Aspect Ratio of Micro-Channels on PMMA 73

3.4 Research Findings from Preliminary Study 76
3.5 Modeling and Analysis of Fiber Laser Micro-Channeling on PMMA 76
3.5.1 Response Surface Methodology 77
3.5.2 Mathematical Modeling for Cut Width (Y_1), Depth (Y_2) and HAZ Width (Y_3) of Micro-Channels on PMMA 78
3.5.2.1 ANOVA Test Results and Discussion 79
3.5.3 Results and Analysis Based on Response Surface Plots and Contour Plots 81
3.5.3.1 Parametric Analysis on Cut Width of Micro-Channels on PMMA 82
3.5.3.2 Parametric Analysis on Depth of Micro-Channels on PMMA 84
3.5.3.3 Parametric Analysis on HAZ Width of Micro-Channels on PMMA 87
3.5.4 Parametric Optimization of Fiber Laser Micro-Channeling on PMMA 91
3.5.4.1 Single Objective Optimization of the Responses 91
3.5.4.2 Multi-Objective Optimization of the Responses 92
3.6 Outcomes of the Present Research Work 95

CHAPTER 4. EXPERIMENTAL INVESTIGATIONS INTO FIBER LASER MICRO-GROOVING OF Ti-6Al-4V
4.1 Introduction 97
4.2 Selection of Process Parameters and Responses 97
4.3 Properties of Ti-6Al-4V 98
4.4 Material Removal Mechanism of Fiber Laser Micro-Grooving of Ti-6Al-4V 98
4.5 Experimental Planning 101
4.6 Measurements 102
4.7 Results and Discussion 104
4.7.1 Influence of Scan Speed on Cut Width, Depth, and Surface Roughness on Ti-6Al-4V Micro-Grooves 105
4.7.2 Influence of Pulse Frequency on Cut Width, Depth, and Surface Roughness on Ti-6Al-4V Micro-Grooves 106
4.7.3 Influence of Number of Pass on Cut width, Depth, and Surface Roughness on Ti-6Al-4V Micro-Grooves 108
4.7.4 Influence of Laser Power on Cut Width, Depth, and Surface Roughness on Ti-6Al-4V Micro-Grooves 109
4.8 Outcomes of the Present Research Work 113

CHAPTER 5. EXPERIMENTAL INVESTIGATIONS INTO FIBER LASER MICRO-GROOVING OF 316L STAINLESS STEEL
5.1.Introduction 115
5.2 Selection of Process Parameters and Responses 115
5.3 Properties of 316L 117
5.4 Experimental Planning 118
5.5 Measurements 119
5.6 Comparative Study on the Performance of Laser Micro-Grooving on 316L with and without Assist Air 120

5.6.1 Effect of Laser Power on Cut Width and Surface Roughness, R_a 121
5.6.2 Effect of Pulse Frequency on Cut Width and Surface Roughness, R_a 123
5.6.3 Effect of Scan Speed on Cut Width and Surface Roughness, R_a 126
5.7 Comparative Study on the Performance of the Laser Micro-Grooving on 316L with and without Elevated Temperature 128
5.7.1 Effect of Scan Speed and Change in Focal Point Position at Elevated Temperatures on Cut Width of 316L Micro-Grooves 130
5.7.2 Effect of Scan Speed and Change in Focal Point Position at Elevated Temperatures on HAZ Width of 316L Micro-Grooves 132
5.8 Outcomes of the Present Research Work 135

CHAPTER 6. EXPERIMENTAL INVESTIGATION INTO FIBER LASER MICRO-DRILLING ON QUARTZ
6.1 Introduction 137
6.2 Selection of the Process Parameters and Responses 137
6.3 Properties of Quartz 139
6.4 Material Removal Mechanism of Quartz by Fiber Laser Percussion Drilling 140
6.5 Preliminary Study of Fiber Laser Micro-Drilling on Quartz 141
6.5.1 Results and Discussion 142
6.5.1.1 Effects of Laser Power on Taper Angle, Entrance Hole Circularity and HAZ Thickness of Micro-Holes on Quartz 142
6.5.1.2 Effects of Pulse Frequency on Taper Angle, Entrance Hole Circularity and HAZ Thickness of Micro-Holes on Quartz 146
6.5.1.3 Effects of Duty Cycle on Taper Angle, Entrance Hole Circularity and HAZ Thickness of Micro-Holes on Quartz 149
6.5.1.4 Effects of Air Pressure on Taper Angle, Entrance Hole Circularity and HAZ Thickness of Micro-Holes on Quartz 151
6.6 Research Findings from Preliminary Study 153
6.7 Modeling and Analysis of Fiber Laser Micro-Drilling of Quartz 154
6.7.1 Development of Empirical Modeling based on RSM 155
6.7.2 ANOVA Test Results of the Developed Models 156
6.7.3 Analysis of Fiber Laser Process Parameters based on Response Surface and Contour Plots 159
6.7.3.1 Parametric Influences on Entry Hole Diameter of Micro-Holes on Quartz 160
6.7.3.2 Parametric Influences on Exit Hole Diameter of Micro-Holes on Quartz 162
6.7.3.3 Parametric Influences on HAZ Thickness of Micro-Holes on Quartz 165
6.7.3.4 Parametric Influences on Entrance Hole Circularity of Micro-Holes on Quartz 167
6.8 Parametric Optimization of Fiber Laser Micro-Drilling of Quartz 170
6.8.1 Single Objective Optimization of the Responses 170
6.8.2 Multi-Objective Optimization of the Responses 172

6.8.3 Confirmation Experiments 173
6.9 Outcomes of the Present Research Work 174

CHAPTER 7. EXPERIMENTAL INVESTIGATION INTO FIBER LASER SURFACE TEXTURING ON HASTELLOY C-276
7.1 Introduction 177
7.2 Selection of the Process Parameters and Responses 178
7.3 Properties of Hastelloy C-276 178
7.4 Experimental Strategy for Fiber Laser Surface Texturing on Hastelloy C-276 179
7.5 Preliminary Study of Fiber Laser Surface Texturing on Hastelloy C-276 181
7.5.1 Results and Discussion 181
7.5.1.1 Effect of Scan Speed on R_a, R_{sk}, R_{ku}, and R_z of Textured Surfaces on Hastelloy C-276 182
7.5.1.2 Effect of Laser Power on R_a, R_{sk}, R_{ku}, and R_z of Textured Surfaces on Hastelloy C-276 185
7.5.1.3 Effect of Pulse Frequency on R_a, R_{sk}, R_{ku}, and R_z of Textured Surfaces on Hastelloy C-276 188
7.6 Research Findings from Preliminary Study 190
7.7 Modelling and Analysis of Fiber Laser Surface Texturing of Hastelloy C-276 190
7.7.1 Influence of Process Parameters on the Surface Criteria 193
7.7.1.1 Parametric Effects on the Surface Characteristic, R_a 194
7.7.1.2 Parametric Effects on the Surface Characteristic, R_{sk} 196
7.7.1.3 Parametric Effects on the Surface Characteristic, R_{ku} 199
7.7.2 Multi-Objective Optimization 203
7.7.3 Confirmation Experiments 205
7.8 Outcomes of the Present Research Work 205

CHAPTER 8. GENERAL CONCLUSIONS
8.1 General Conclusions 207
8.2 Future Scope of the Present Work 213

BIBLIOGRAPHY 215

1. INTRODUCTION

The present era belongs to the maximum demand for minimization of the products with the requirement of stringent quality control. The tolerance limit for minimized products has become more stringent than previously. The demand for micro-products in the area of automotive, biomedical, and aerospace engineering is ever increasing. The boom of newly developed materials has also contributed to the growth of micro-products in the vast area of manufacturing. Researchers have always tried to contribute to the growth of the manufacturing industries by inventing newly developed set up to fabricate intricate shapes and sizes on difficult to machine materials. Popular conventional methods employed to generate intricate shapes and sizes are always found to be complicated. In addition to this, the cost ineffectiveness, higher machining time have laid a foundation for looking at alternative improved machining technologies which can solve out the unresolved problems associated with traditional machining approaches. Therefore, non-traditional machining approaches towards fabricating smaller shapes and sizes become an immediate success story for both the researchers and industrial people.

In 1953, the introduction of numerical control (NC) technology also brought about other advanced technologies such as computer numerical control (CNC) and direct numerical control (DNC) in the manufacturing industries. These technologies have provided better accuracy and uniformity of the products over the decades. Rapid boom in the electronics and computer industries bought about various developments in machine tools and machining processes. In modern technologies, materials with harder, stronger, and tougher as well as challenging to cut are more preferred. Therefore, a significant amount of research is directed to develop such machining processes where the mechanical properties of the material will enforce limitation in the removal of material. In this regard, the non-traditional machining techniques have become possible alternative methods for the machining of difficult to machine materials such as high-strength thermal-resistant alloys, various kinds of carbides, fiber-reinforced composite materials, stellites, and ceramics. The non-traditional methods play an essential role in the aircraft, automobile, tool, die, and mold making industries. The non-traditional machining methods are classified according to the number of machining actions causing the removal of material from the workpiece. These methods can be classified as mechanical, thermal, chemical, and electrochemical depending on the source of energy [1].

Among the various mechanical machining processes, ultrasonic machining (USM) and water jet machining (WJM) are the typical examples of mechanical non-traditional machining processes. Thermal machining removes material from the workpiece by melting or vaporizing the workpiece material. Plasma is the required heat source the removal of material for electro-discharge machining (EDM) and plasma beam machining (PBM). On the contrary, photons, electrons, and ions are the required heat sources for laser beam machining (LBM), electron beam machining (EBM), and ion beam machining (IBM) respectively [2]. For each of the processes above, the machining mediums are different and also have many advantages as well as disadvantages.

Laser beam machining (LBM) offers the right solution for the machining of difficult to machine materials. The laser, the acronym for light amplification by stimulated emission of radiation, is a coherent and monochromatic source of electromagnetic radiation with a wavelength ranging from the ultraviolet to the infrared range. The initial foundation of the laser theory was laid by Einstein [3], and later, Kopfermann and Ladenburg [4] confirmed Einstein's prediction. However, lasers were first demonstrated in the 1950s in the microwave region of the electromagnetic spectrum. This subset of lasers was called a MASER (Microwave Amplified by Stimulated Emission of Radiation) [3]. During the year of 1964, although most of the lasers have already been conceptualized and conceived, however, the acceptability of laser towards the industrial environments was still lagging far behind. By the mid-1970s, more reliable and powerful lasers were developed for industrial applications such as cutting, welding, drilling, and melting. During the 1980s and early 1990s, lasers were successfully applied for heating, cladding, alloying, glazing, and thin film deposition [3]. There are three fundamental, essential elements of a laser: the lasing medium which is dependent on the type of laser and wavelength, the pumping process, and optical feedback elements [5]. The laser medium can be solid, liquid, or gaseous. Different laser types are commonly named according to the state or the physical properties of the active medium.

Consequently, there are solid state, liquid, and gas lasers [6]. Gas-based lasers can be further subdivided into neutral atom lasers, ion lasers, molecular lasers, and excimer lasers. Among the existing conventional laser systems, carbon dioxide (CO_2) laser, excimer (KrF, ArF, XeCl) laser, neodymium-doped yttrium aluminum garnet (Nd-YAG) laser systems are the most popular conventional laser systems utilized in the industrial and medical applications [3]. However,

among the recent advancements in the laser systems, fiber lasers have observed a rapid and consistent growth from the stent cutting to the thick and thin material cutting, drilling [7], etc. Different type of conventional laser systems along with their medium and wavelength is shown in table 1.1.

Table 1.1 Laser systems with their medium and wavelength [3]

Type	**Medium**	**Wavelength**
Gas lasers	Excimer	193–351 nm
Gas lasers	CO_2	10 µm
Solid State Lasers	Nd- YAG (fundamental)	1.064 µm
	Nd- YAG (second harmonic)	532 µm
	Nd- YAG (third harmonic)	355 µm
	Nd- YAG (fourth harmonic)	266 µm
Fiber Lasers	Doped fibers	1064-2000 µm
Disk Lasers	Doped thin disks	1030-1064 µm

1.1 Need and Advantages of Laser Micro-Machining

Miniaturization is an essential trend in many modern technologies. The requirement for material processing with micron or submicron resolution at high speed and low unit cost of high-tech micro-products for biotechnological, microelectronics, telecommunication, MEMS, and medical applications are ever increasing. Given this increasing trend toward miniaturization, micro-machining becomes an essential activity in the fabrication of micro-parts. In the early 1990s, Masuzawa [8] was the first person to draw attention towards the need for the characterization of micro-machining along with the need for direct determination of the shape of its products. Micro-machining can be considered as a unit removal of material in the range of microns. Scientific Technical Committee of the Physical and Chemical Machining Processes of CIRP, has adopted the dimension range of 1 to 500 µm for micro-machining work [9]. Various technologies such as mechanical micro-machining, i.e., micro-drilling and micro-milling, micro-ultrasonic machining, laser micro-machining, electron beam machining, ion beam micro-machining, micro-ion beam machining, are utilized based on the specific requirements of the part to be produced for micro-fabrication.

The various micro-machining processes and their drawbacks as follows:

(i) **Micro-Abrasive Machining (AM):** Tapered sidewalls, limited aspect ratio.

(ii) **Micro-Ultrasonic Machining (USM):** High tool wear, low machining rate.

(iii) **Micro-Electro-Discharge Machining (EDM):** Only can be used for conductive materials, comparatively expensive process.

(iv) **Ion Beam Machining (IBM):** Ideal process for only ceramics, semiconductors, diamonds, etc.

(v) **Electron Beam Machining (EBM):** Limited availability, presence of recast layer, high capital investment cost.

(vi) **Micro-Electrochemical Machining (ECM):** Large overcut, a requirement of micro-tool development.

Advances in the laser technology combined with a better understanding of laser-matter interaction make laser micro-machining a viable, attractive, cost-effective, and enabling technology. At present, laser micro-machining has become one of the versatile fabrication process owing to its superior features like contact and wear less machining, better flexibility and a possibility for a high degree of automation, etc. As a result, laser beam micro-machining is being widely used for fabricating micro-components on various metals, ceramics, and polymer to be applied in medical industries, automobile sectors, etc. Laser micro-machining attributes a wide range of pulse duration from femtosecond to microsecond, a variety of wavelengths and different pulse repetition rates from single to megahertz allowing the process to fabricate complex machined micro parts with high aspect ratio.

The interaction between the laser and the workpiece is a complex phenomenon. The process can be classified under the photo-thermal and photo-chemical process. Figure 1.1 shows the various aspects of laser micro-machining process along with interplay relationship between the two processes mentioned above. The details of each phenomenon as indicated in the figure are discussed in chapter 3, 4, 5, 6, and 7 subsequently. The dotted arrow signifies an indirect relationship, whereas the line arrow signifies the direct relationship between the cause and effect.

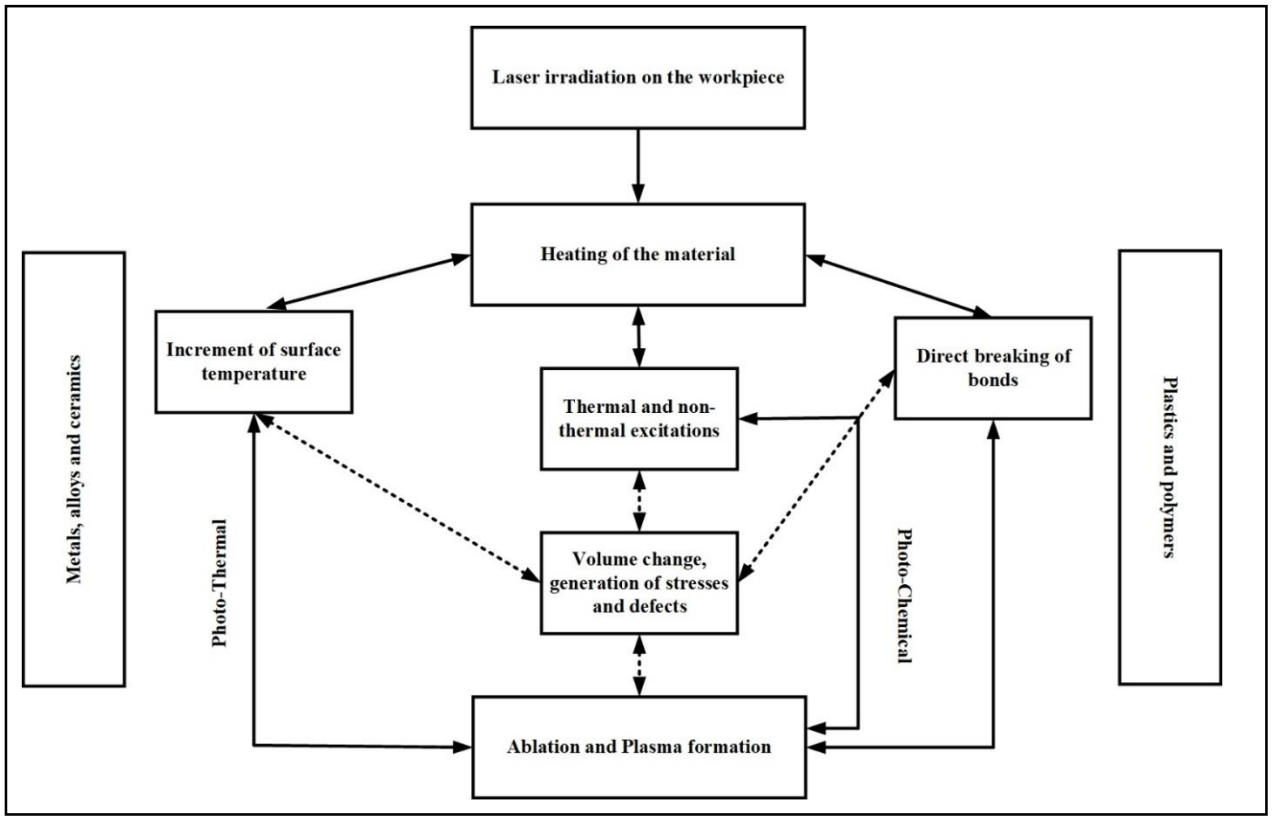

Figure 1.1 Schematic diagram of laser micro-machining process

The advantages of lasers over other non-traditional micro-machining processes as follows:

(i) Coverage of a wide range of engineering materials-from metals, alloys, plastics, ceramics to super alloys;

(ii) Potentiality for different micro-machining applications;

(iii) Low processing time;

(iv) Less wastage of material;

(v) High automation as well as easy integration;

(vi) A wide range of power variation ranging from very low output power (mW) to extreme high output (kW).

The pulsed mode of the fiber laser system, with an output power less than 200 W, is most suitable for micro-machining of a wide range of engineering materials owing to its superior features such as simplicity, ruggedness, cost effectiveness, low maintenance, higher efficiency, higher reliability, and smaller spot size [7]. Fiber laser micro-machining approaches towards various difficult to machine materials for generating precise micro-features such as micro-channels, micro-grooves, micro-holes, etc., mainly in the domain of bio-medical, automotive and

aerospace engineering, have aided to become the most versatile and rapid growing laser systems in the last decade.

1.2 Fiber Laser in Micro-Machining

Fiber lasers have evolved as the most versatile and rapid growing laser systems during the last decade and successfully emerged in the various fields of manufacturing, medical, meteorological and military applications that were previously dominated by conventional solid-state lasers along with gas lasers. Global sales of fiber lasers for metal cutting not only have reached 1.1 billion dollars but also increasing at a rate of 3-4% per year. In addition to this, fiber laser has been steadily replacing CO_2 and Nd-YAG lasers in various manufacturing domains due to its higher efficiency, higher beam quality, less maintenance, and the ability to process highly reflective material.

1.2.1 Brief History of Fiber Laser

Fiber lasers with an average laser power of 10–50 W, hold a good market share in the domain of fine and precise micro-cutting that involves the combination of both continuous mode and pulsed mode with the aid of fusion cutting to sublimation cutting. The initiation of combining optical fiber with laser system was started when the advantages of introducing a rare earth doped single-mode optical fiber in a laser cavity to provide a robust single spatial mode at the laser output were recognized in 1961 by Snitzer [10]. After the initial development, Snitzer and Koester [10] demonstrated flash lamps pumped neodymium doped multimode optical fiber lasers. Further, in the mid-1980s, practical work on single-mode optical fiber lasers commenced, after the initial advancement of rare earth doping methods that used modern optical fiber fabrication processes based on vapor-phase deposition technique. However, the advancement of the single high-power mode optical fiber lasers was turned out to be irrelevant in the case of commercial, industrial applications due to the generation of the low average power of most of the single-mode fiber lasers. Finally, the booming of the telecommunications during 2001 caused the thrust needed for the development of high-power optical fiber lasers. An extensive amount of dedicated research works and development of multimode diodes brought about significantly more powerful and reliable multimode diodes at a radically lower cost for the generation of the fiber laser. Moreover, the contribution of the military-funded programs was another driving force for achieving higher power fiber lasers and the development of related technologies.

1.2.2 Present Status of Fiber Laser

The fundamental wavelength of fiber lasers is between 1 and 2 μm depending on the dopant and host material. Presently, high-power fiber lasers are being operated at shortwave and midwave infrared wavelengths. In a fiber laser, the active gain medium is an optical fiber doped with rare earth elements such as erbium (Er^{3+}), ytterbium (Yb^{3+}), or neodymium (Nd^{3+}). High powered fiber lasers operate at near-infrared (NIR) wavelengths. Yb^{3+} ions are the most popular rare earth ions due to its energy level structure combined with a small quantum defect. Fiber laser power output up to 4 kW range is the most desirable for various material processing applications, e.g., metal cutting, and welding. However, for micro-machining applications, fiber lasers with an output of less than 200W are preferable than that of high power lasers. Fiber lasers can also be Q-switched to obtain high peak power pulses at pulse repetition rates of tens or hundreds of kilohertz. In addition to this, the fundamental wavelength of the fiber laser can be utilized for the machining of a wide range of metals and ceramics. As a result, fiber lasers have started to dominate in applications related to high power lasers sources with high brightness and several areas dealing with pulsed oscillators and spectral manipulation. Fiber lasers, as a guided-wave laser system, are advantageous as than conventional laser systems as the modes are determined firmly by the laser cavity. In the present era, ultrafast fiber lasers, based on passively mode-locked fiber oscillators, have also found their place in both the industrial and scientific realms. The amplification during the several stages of ultrafast fiber laser generation and beam delivery system; has allowed them to reach the desired output pulse energies. In addition to this, the large surface area to volume ratio of the fiber geometry can effectively dissipate the heat generated. Thus, fiber lasers are compact because of the absence of chiller unit and higher runtime compared to other conventional laser systems.

Efforts over the last few decades have been put into developing alternative fiber laser host glasses for propagation in the shortwave to midwave infrared spectrum. Importantly, the phonon energy of the alternative glasses must be lower than the energy of the rare earth-transition for having sufficient luminescence efficiency. The glasses that have been used for shortwave and midwave infrared fiber lasers are fluoride oxide, tellurite, germanate, and chalcogenide glasses. ZBLAN is the most developed fluoride glass for short to midwave infrared fiber lasers [11]. To date, the fluoride glasses are by far the most successful host material for the longer emission wavelengths compared to a silicate glass host. A large variety of fiber components rely on the

entire fiber systems instead of being dependent only on the beam delivery system. Chirped pulse amplification (CPA) technique for ultrafast fiber laser systems, is an ongoing design concept for the prevention of nonlinear processes in the fiber amplifiers for better utilization in various micro-machining applications [7]. To date, the highest single mode power available from a fiber laser is 10 kW, whereas the highest multimode power reached is 50 kW, both from IPG Photonics.

Figure 1.2 represents a schematic diagram of a pulsed fiber laser system. Fiber laser generation is achieved in the ytterbium fiber laser head through the power source, following which the beam propagates to the collimator. Further, the beam travels through a bending mirror and finally to an F-Θ lens. The camera assembly unit process through CCDTV whether the workpiece is on a focal point or not. The detail components of the fiber laser system are discussed in chapter 2.

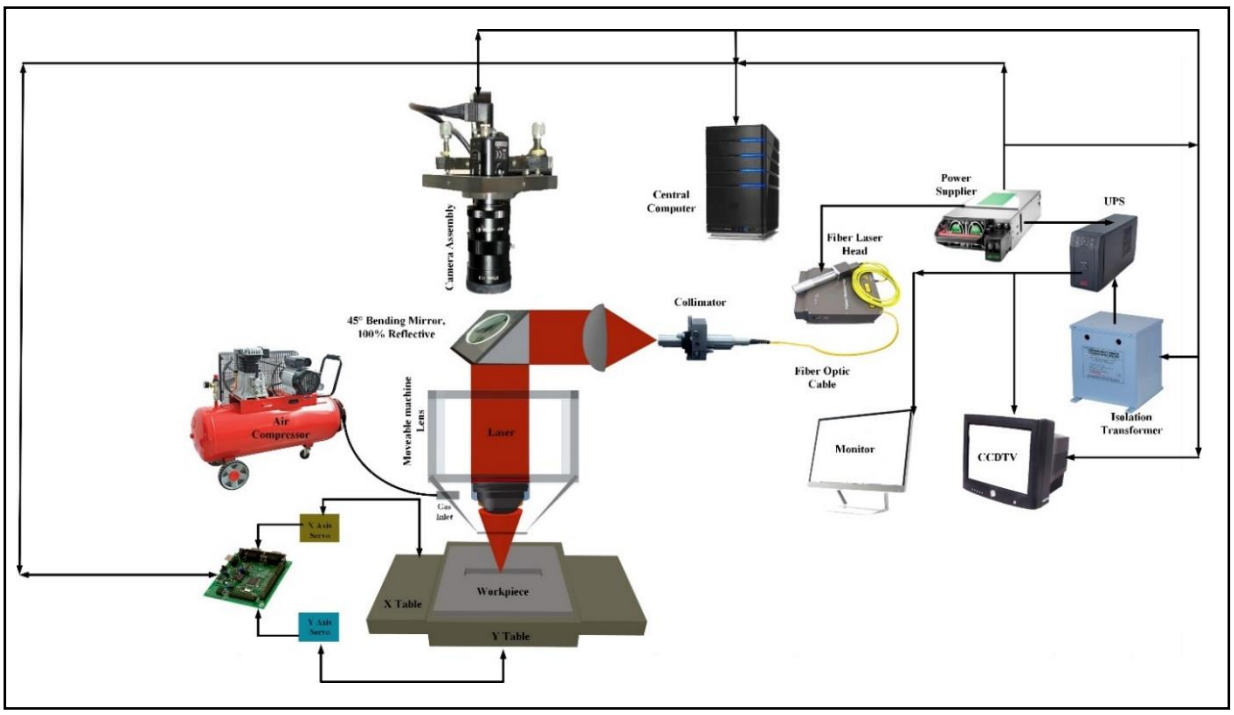

Figure 1.2 Schematic diagram of a pulsed fiber laser system

1.2.3 Classification of Fiber Laser

The fiber laser can be broadly classified as (a) continuous fiber laser and (b) pulse fiber laser. Further, the fiber laser is classified into a single frequency fiber laser, Q-switched fiber laser, and mode-locked fiber lasers. A continuous fiber laser consists of a high reflector (HR) and an output coupler (OC) along with fiber Bragg gratings [7]. Continuous wave fiber lasers can be either

single or multimode, i.e., regarding transverse modes. A single mode, continuous fiber laser can generate a high-quality beam for the working of materials, whereas multimode industrial lasers are capable of generating higher power.

For pulsed mode operation of the fiber laser, a single frequency fiber laser is pumped by a single-mode pump diode to obtain an output power, ranging from a few tens up to hundreds of milliwatts. Q switching is possible with fiber lasers where lengths range from low nanosecond up to the microsecond range pulse. In Q switched fiber lasers, longer pulses are obtained due to the extended length of the fibers. However, if the pulse duration becomes longer than round-trip cavity time, pulse breakup may occur [7].

On the flip side, optimal utilization of the fundamental cavity mode structure in an optical fiber oscillator is utilized by the mode-locked fiber laser, in order to produce a short pulse, as depicted in figure 1.3. The back mirror is 100 % reflective, whereas the front mirror reflects only 20% of the photons, which are utilized to generate the laser light. An acousto-optical modulator (AOM) as shown in figure 1.3, is used to as a pulse selector. In recent years, end to end all fusion fiber master oscillator power amplifier (MOPA) designs are also utilized in fiber-coupled semiconductor lasers, as shown in figure 1.4. In MOPA, the pulsed operation is obtained utilizing an external electronically controlled modulator. Pulsed fiber-based MOPA is utilized in bulk solid-state laser as the master oscillator. In figure 1.4, a single transverse mode ytterbium-doped fiber laser is shown with a large core diameter. The preamplifier is used to boost the signal pulse energy, which allows the photonic crystal fiber (PCF) to achieve high pulse energies.

However, for the thick material cutting, a continuous mode of the fiber laser is more suitable, whereas a pulse fiber laser is commonly employed to produce the high peak intensity laser beam for achieving a high aspect ratio micro-channels, micro-holes, etc. Depending on the regime of the pulse width of the fiber laser, fiber laser can also be termed as a nanosecond, picosecond, or femtosecond pulsed fiber laser systems [7].

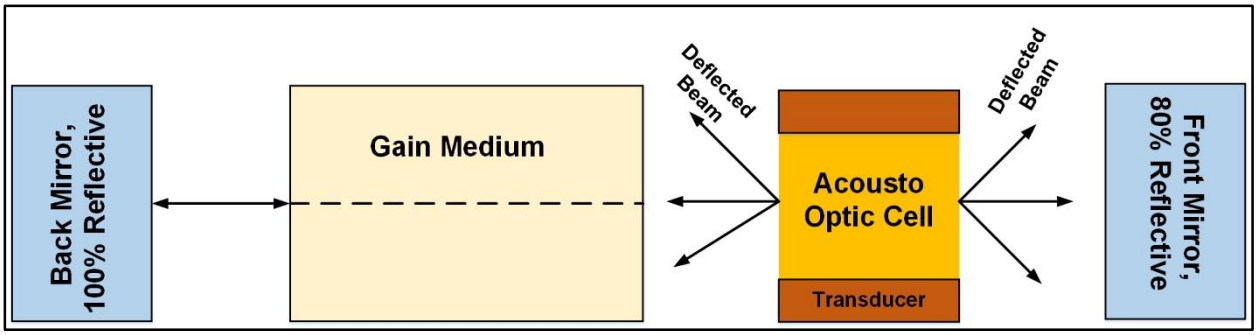

Figure 1.3 Schematic representation of a mode-locked fiber laser with acousto optic modulator [7]

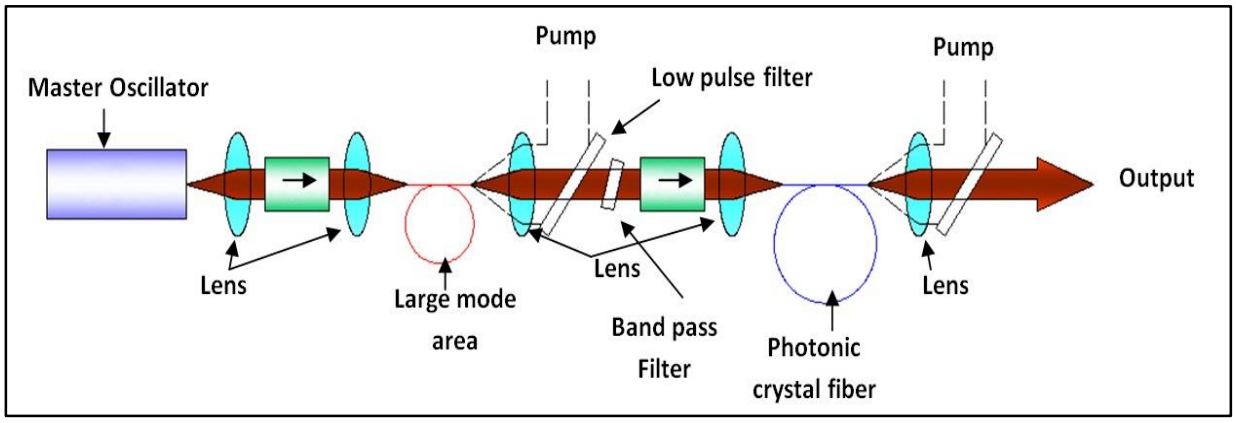

Figure 1.4 Schematic diagram of a master oscillator power amplifier (MOPA) design of fiber laser

1.2.4 Comparison between Fiber Laser and Other Lasers for Micro-Machining

Shorter wavelength in combination with the high focus ability, better system flexibility, high component yield and uptime along with improved reliability, high repeatability, high aspect ratios with utmost precision, extensive material coverage, cost-effective and fully automated processes seem to be advantageous for fiber lasers for micro-machining of thin sheet metal cutting. On the contrary, CO_2 lasers are probably still capable of machining thicker materials more efficiently. Although, Olsen et al. [12] found that the efficiency of fiber laser cutting operation for thick materials is higher than of CO_2 laser. Their experimental results also revealed that burr-free cuts could be achieved in 1 and 2 mm thick AISI 304 stainless steel, over a wide range of cutting rates using fiber laser micro-machining system. Further research studies in the domain of fiber laser micro-machining process also brought about the observations that fiber lasers can produce better results as compared to CO_2 and Nd-YAG lasers [10] during machining

of different materials. In addition to this, 4 kW fiber laser has taken the place of 4 kW CO_2 lasers in terms of fabrication of the number of products and parts. As a result, the cost of maintenance and electrical costs have been reduced drastically. A 2 kW fiber laser can cut thick plate up to 1inch or even higher with speeds similar to a 4 kW CO_2 laser, producing the same edge quality. Furthermore, a 4 kW CO_2 laser consumes around 50-60 kW of power, whereas a 2 or 3 kW fiber laser, producing the same quality part in the same amount of time, consumes only 10-15 kW of power [10].

Fiber lasers have also replaced Nd-YAG lasers in various micro-machining applications such as micro-cutting of stents, cutting of thin sheet of ferrous and non-metals regarding in terms of higher cutting speed, better cut edge quality, less heat affected zone (HAZ), lower surface roughness and less formation of micro-cracks [13, 14]. Fiber laser cutting of thick polycrystalline silicon (silicon wafer) is another significant area where it produces better results compared to Nd-YAG laser. The number of research works employing fiber laser micro-machining of difficult to machine materials is increasing rapidly in recent years.

1.3 Basic Principle of Fiber Laser Generation Process

The basic principle of the fiber laser can be realized with the production of laser light that requires material (a rare earth element) in the active medium to be raised from its ground state to an excited state creating a population inversion in that medium. Usually, atoms in the active medium reside in their ground states, and some external form of energy must be added to raise these atoms to an excited state [10]. In a fiber laser, there are several options for launching pump light at very high power levels [7]. The simplest is to launch directly into the pump cladding at one or both fiber ends. In many cases, fiber coupled pump diodes are utilized to pump light inside the fibers. A population in the active medium is achieved with the aid of multiple diode lasers, i.e., pumping. The exact number of diode lasers depends on the application of the fiber laser and the output power required. In pulsed mode (PM) optical fiber, the plane of propagation light polarization remains unchanged as the property of PM fiber is conditional. The condition requires the light polarization plane to be aligned at a certain angle to the fiber stress gradient direction during coupling into the fiber.

The light propagation into the fiber itself is dependent on five characteristics; (a) fiber type, (b) fiber size, (c) numerical aperture, (d) refractive index and (e) doping of the fiber [7]. Fibers are

combined with one core and one cladding along with the protective coating. The propagation of the lasing mode is in the core, whereas, the propagation of the pumped beam is by the outer layer cladding. The guided modes of a waveguide can be derived from the Helmholtz Eigenvalue equation, which is derived from Maxwell's equations. The equations ensure all the relevant field continuities at all boundaries. A guided mode, as a robust fundamental spatial distribution, propagates at β (propagation constant) and maintains a constant wavefront. It is shown in equation 1.1 as follows:

$$E(r,\theta,z)=E_0(r,\theta)e^{-i\beta z} \quad ...[Eq^n\ 1.1]$$

Where, E_0 is termed as transverse mode distribution, r and Θ are the polar coordinates in the considered region, v is normalized frequency and z as the propagation distance. When the normalized frequency is known, then the waveguide's mode properties can be entirely determined. The primary function of the outer layer cladding is to confine the pump light, which allows the pumping of the core with a high power beam. With all the individual diode laser outputs combined into a single beam, the beam is next injected into the inner cladding of the fiber laser at an angle that ensures total internal reflection occurs at the interface between the inner and outer cladding of the fiber laser. Two conditions must be met for this to occur. One condition is that the index of refraction of the medium in which the light beam is incident must be higher than the index of refraction of the medium the beam is moving towards [7]. This condition is met as the pump beam travels from the inner cladding towards the outer cladding. The second condition is that the angle of incidence of the pump beam (Θ_a) on the inner/outer cladding interface must be greater than the critical angle (Θ_c) as shown in figure 1.5.

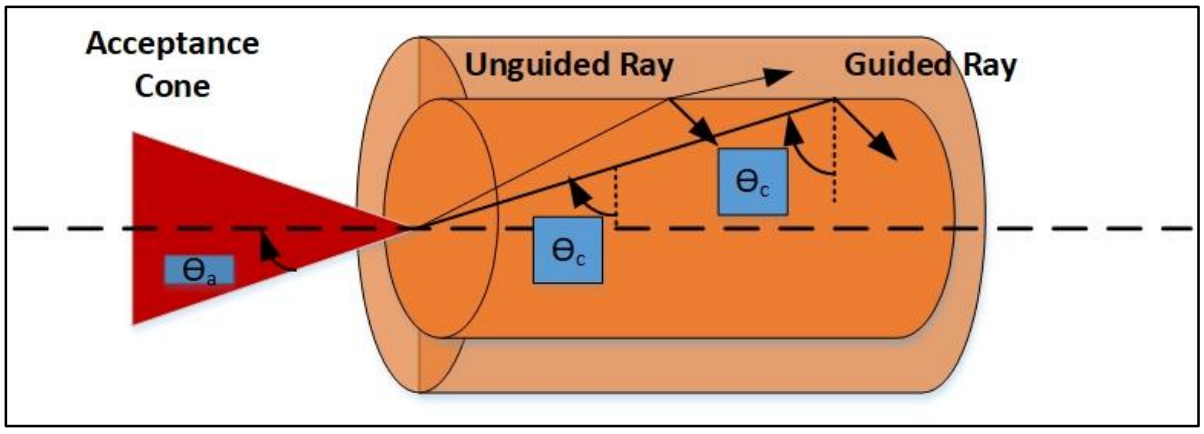

Figure 1.5 Acceptance angle of fiber with quantities related to the numerical aperture

After total internal reflection, some amount of light passes through from inner core into the outer core. Therefore, the rare earth doping atoms reach to excited states absorbing the energy available in the pump light. After the incidence of total internal reflection at the inner or outer cladding interface, the pump light reaches to the core of the fiber laser. Further, the majority (>90%) will be transmitted in the core to interact with the rare earth doping atoms to generate a population inversion. A portion of these energized atoms rapidly drops to bring down energies through fluorescence making within the core photons. The photons will then have the energies equivalent to the energy difference between the excited and lower energy states in the rare earth atoms. These photons at that point travel through the core and prompt other earth photons to drop to their most minimal energy levels with the aid of stimulated emission. As this procedure further proceeds, the core ends up saturated with photons which are not only coherent but also have a similar wavelength and collimated. Thus, the laser light is generated. As the light progresses to the end of the core, it interfaces with mirrors or fiber Bragg gratings (FBG). Two phenomena occur here, i.e., the light is fully reflected into the core, and some amount of light partially reflects into the core. The first phenomenon causes more stimulated emission, while in the latter phenomenon results in the transmission of light.

1.4 Principle of Fiber Laser Micro-Machining Process

The working range of the fiber laser is either in the near-infrared (NIR) or infrared region (IR) [7]. Fiber laser micro-machining process is based on the interaction of the laser light with the top surface of the working material to remove a small amount of material from the surface. It is a well-known fact that the photon energy is inversely proportional to the laser working wavelength, i.e., shorter the wavelength-higher the photon energy [7]. The thermal process changes into a chemical process when the working wavelength of the fiber laser of 1064 nm is shortened either to the first order harmonic wavelength of 532 nm or second order harmonic wavelength of 264 nm. As a result, the breaking of bonds of the workpiece material occurs instead of melting and vaporization. As a result of this, the fiber laser micro-machining process can be classified into two distinct features, i.e., the photo-thermal process and photo-chemical process. Photo-thermal processes are identified mostly in metals, ceramics, alloys, etc. Photo-thermal processes are characterized by a rapid thermal cycle, heating, melting, and partial evaporation of the heated volume of the material [7]. Fiber laser micro-machining process for

various engineering materials ranges from nanosecond regime to the femtosecond regime. In figure 1.6, a schematic diagram of a fiber laser photo-thermal process is shown. As shown in figure 1.6, the process is initiated by the absorption of the laser light and ablation subsequently. Further, a thin layer is removed by a single pulse.

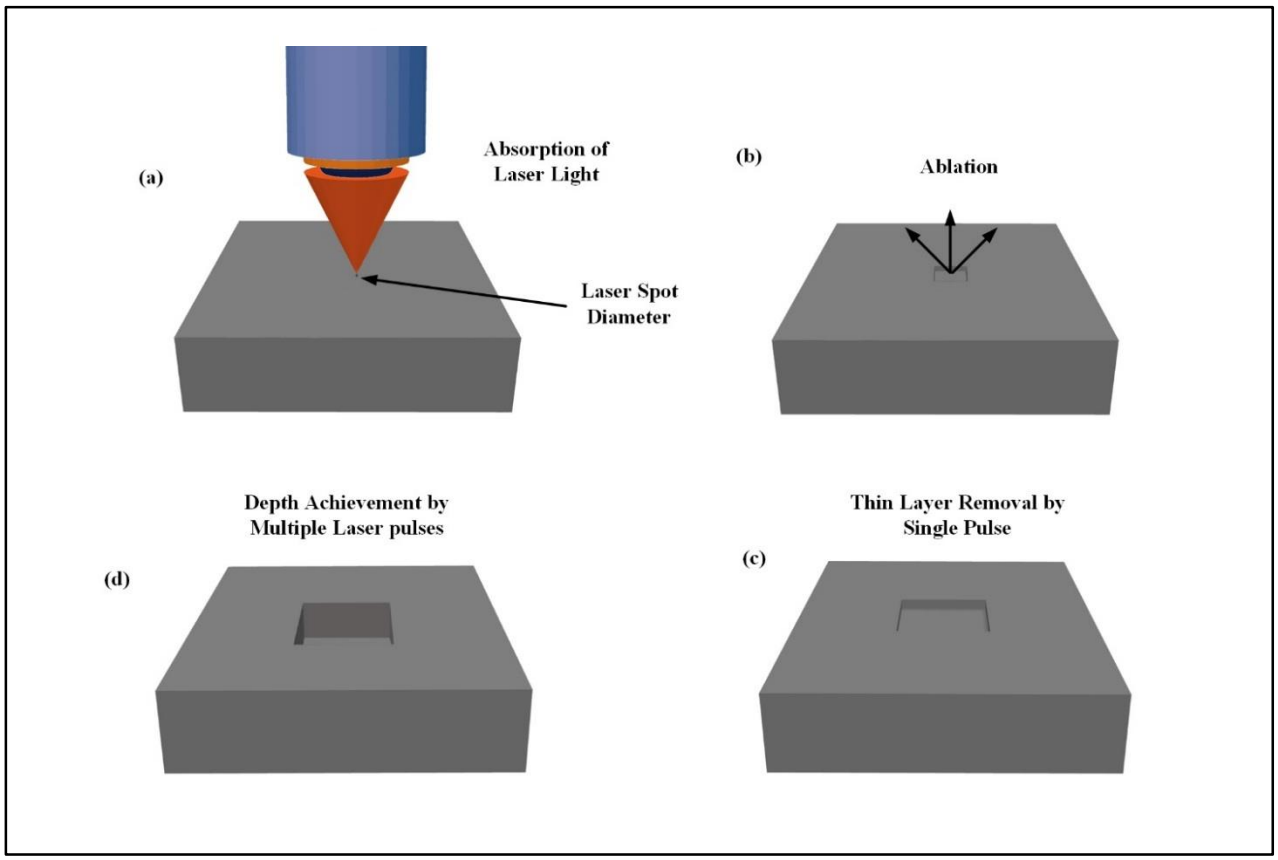

Figure 1.6 Schematic diagram of the photo-thermal process

Depending on the laser-material interaction time, the micro-machining quality is varied. Based on the laser-material interaction time regime, three processes can be distinguished. In all the three processes, first, absorption of the photon by an electron occurs, and then the rest of the set of other physical steps is varied depending on the time regime [7]. In nanosecond ablation of the metals, the absorbed laser energy first, heats the workpiece to its melting point and further to the vaporization temperature. During the interaction time, the loss of energy is associated with the heat conduction into the solid material. Nanosecond pulse ablation is associated with the detrimental heat affected zone (HAZ), which can be partially overcome by picosecond ablation. In picosecond ablation, the pulse length is in the same order during the time of transferring the

energy from the electrons to the lattice. However, the picosecond ablation also suffers from a considerable amount of evaporation and the formation of the melted zone inside the material [7]. This related problem can be eliminated by femtosecond ablation as no time is available for the heat transfer to the lattice during this series of processes in femtosecond ablation. As a result, minimum or no heat affected zone, as well as precise micro-machining characteristics, are observed in femtosecond ablation.

1.5 Advantages of Fiber Laser Micro-Machining

The importance of fiber laser system for the micro-machining domain is inevitable. Fiber lasers are ideally suited for the generation of micro-features required for the biomedical applications, electronics industries, automotive and aerospace industries. The importance of fiber laser for the fabrication of micro-features on a wide range of engineering materials lies in its characteristic features. The astounding features of fiber laser such as compactness, elimination of complex cooling systems, excellent constant beam properties, long focal lengths, and rapid warm-up make it ideal for the applications in the manufacturing industries as mentioned above [7].

(a) Superior Beam Quality

Commercially available fiber lasers produce high-quality beams ranging up to a few kW. Therefore, a larger area of parameter space is achieved because of the high beam quality and hence, the optical parameters for a process are easily optimized.

(b) High Wall Plug Efficiency and Reduction of Operating Cost

High wall plug efficiency around 25–30% can be achieved for the fiber lasers due to the high efficiency of the pump source and the extraction from the gain medium. Therefore, this not only involves lower operating cost but also requires reduced electrical supply along with reduced cooling requirements, which are up to 300 W, compact laser head design. Further, fewer mechanical components are required in the construction of the laser as compared to the other solid-state lasers. As a result, a fiber laser is the most cost competitive laser systems compared to other high power lasers, i.e., CO_2 laser, Nd-YAG laser, etc.

(c) High Reliability and Low Maintenance

At present, the fiber laser products have demonstrated over 40,000 hours of operation time. In addition to this, the diode-pumped fiber laser system has low routine maintenance. This feature is primarily because of its all-fiber construction, which means that no beam delivery optics or alignment of the resonator is required. Minimum or almost no cooling system is required for the running of the fiber laser system as compared to the Nd-YAG laser system.

(d) Compact Size

Fiber lasers are compact compared to the rod or gas lasers of comparable power because the fiber can be bent and coiled to save space.

(e) Ease of Beam Delivery

Fiber lasers possess simple operating features which enable the light that generates inside the fiber, delivers to the work material within the fiber.

1.6 Applications of Fiber Laser for Micro-Machining

As discussed in previous sections, fiber laser has a widespread application ranging from material processing to the medical industry.

The applications of fiber lasers are as follows:

(i) The most promising possibility of a fiber laser in the field of bio-medical lies in the profile cutting for the cardiovascular stent, which is a lattice-shaped metal tube which is utilized for the implantation into arteries [7].

(ii) Fiber laser ablated micro-holes in various super alloys such as Ti-6Al-4V, nickel super alloys are utilized for various automotive and aerospace applications.

(iii) Fiber laser marking process is one of the critical areas that have emerged through the marking of electronic goods to daily household products. Several manufacturers have adopted hard coated plastic cases to provide scratch resistance.

(iv) Fiber laser engraving is another emerging area of a fiber laser in the field of micro-machining.

(v) Other key applications of fiber lasers are hallmarking, texturing, and personalized marking on a wide range of precious materials [7].

1.7 Literature Review of Fiber Laser Micro-Machining Processes

Commercial acceptance and application of fiber laser micro-machining have increased in recent years due to the astounding quality and high focusing ability of the fiber laser beam, which are necessary for generating precise micro-features. The growth of more efficient, compact, high beam quality fiber laser is due to the increased demand for excellent machining. In the present era, several optimizing research works have been carried out to improve the micro-machining quality. Compared to the conventional lasers, fiber laser functions at near-infrared (IR) spectral region and provide a range of advantages along with the promise to create avenues for new micro-machining applications. Fiber laser micro-machining of metals, alloys are governed mainly by the photo-thermal process, whereas the photo-chemical process is attributed for plastics and polymers. Various process input parameters such as laser power, laser beam focal position, composition, and thickness of the workpiece material, scan speed/cutting speed, pulse width, pulse repetition frequency, number of passes, type of assisting gasses along with assisting gas pressure, etc. are the primary governing variables considered for the fiber laser micro-machining of a wide range of engineering materials. The quality characteristics of interest in fiber laser micro-machining are material removal rate (MRR), machined geometry such as kerf/cut width, hole diameter, taper, surface quality in the form of surface roughness, surface morphology, metallurgical characteristics such as recast layer, heat affected zone, dross formation and mechanical properties such as hardness, strength, etc. However, fiber laser micro-machining of metals and alloys are commonly associated with the formation of striation, dross, recast layer, HAZ, micro-cracks, along with the micro-machining zone [7].

Jaworski et al. [15] showcased fiber delivered laser pulses could be utilized in precision micro-machining and marking of metals and glass. They reported a low loss of negative curvature fiber (NCF) for the flexible delivery of high energy nanosecond and picosecond pulses in the green spectral region for various micro-machining applications. The fabricated fiber could transmit 6 ps laser pulses with a maximum energy of 30 μJ and average laser power of 12 W at 515 nm wavelength. The NCF also provided a stable single mode output, with very low bend sensitivity. Degradation of the temporal and spectral properties of the guided beam was also minimized. Furthermore, the delivered light was found to be suitable for precision micro-machining systems.

The combination of a high-quality NCF delivered beam, and sufficient pulse energy allowed very high-quality features to be generated in aluminum, titanium, and fused silica.

Fiber laser micro-machining process can be classified under micro-cutting, micro-drilling, engraving, surface texturing, marking, etc. as shown in figure 1.7. Micro-cutting can be further divided into stent cutting, micro-channeling, and micro-grooving. The literature reviews of various fiber laser micro-machining processes are discussed subsequently.

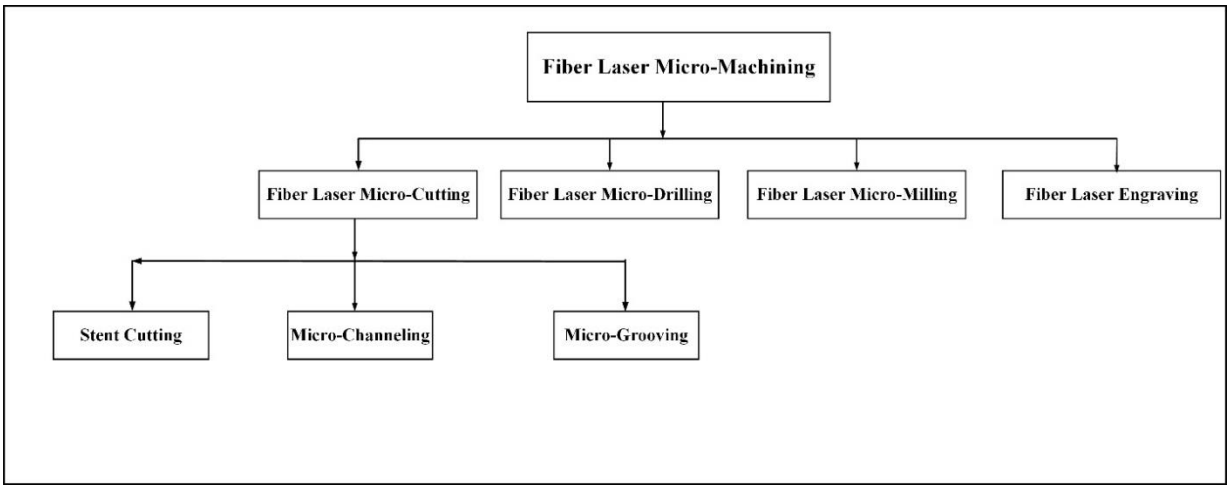

Figure 1.7 Schematic diagram of various fiber laser micro-machining processes

1.7.1 Fiber Laser Micro-Cutting Process

Okamoto et al. [16] tried to overcome dross free fiber laser micro-cutting of a copper plate of 100 µm of thickness in the presence of nitrogen assists gas with the different set of nozzles. It can be summarized from the experimental results that the maximum cutting speed varied for the different set of nozzles. Straight cut profiles were also achieved with minimum HAZ [7, 16]. García-López et al. [17] focused on assessing the influence of process parameters on average surface roughness (R_a) and back wall dross during fiber laser micro-cutting of small stainless steel tubes. The study revealed that the highest level of spot overlaps (60% to 93%) reduced average surface roughness to a considerable amount. Also, both compressed air and argon gas contributed to lowering the back wall dross formation. The control treatment showed that 6% of the back wall dross, while minimum values of 1.5% to 2% were obtained with the aid of compressed air and argon gas. They concluded that when an external gas passed through the tiny tubes to drag the molten particles produced by laser micro-cutting, lowering of back wall dross formation occurred.

Investigations on laser cutting of various micro-patterns on carbon fiber reinforced polymer (CFRP) with a continuous wave fiber near-IR laser (k = 1090 nm) to achieve précised cutting of CFRP, devoid of debris and thermal damages around the grooves were made by Niino et al. [18]. A fast beam galvanometer scanning with the multiple-scan-pass method was performed during fiber laser irradiation on CFRP. The kerf width dimension of 600 µm with free of debris and other thermal damages around the periphery of the micro-machining zone of CFRP sample, were observed at 15 multiple scan pass and scanning speed of 0.8 m/s. Jäschke et al. [19] further studied CFRP micro-cutting utilizing a 6 kW fiber laser. The authors utilized thermoplastic, i.e., carbon fiber reinforced polyphenylene sulfide (CF/PPS) and thermosetting, carbon fiber reinforced epoxy (CF/epoxy) matrix for the experimentation. The results showed that HAZ decreased with the increment of cutting velocity and laser power. In addition to this, the maximum measured HAZ for CF/PPS workpiece was found to be higher than those of CF/epoxy at cutting velocity of 20 m/min. Herzog et al. [20] carried out laser cutting operation on 6 mm thick CFRP workpiece at a high delay of 2 seconds between each passes in order to reduce the heat accumulation from the cutting zone. It was concluded that the multiple pass technique combined with ultra-high power pulses could reduce HAZ significantly from the cutting zone.

Thin film solar cell micro-machining with the aid of high power ultrashort fiber laser was carried out by Lecourt et al. [21], where the pulse repetition rate was varied from 100 to 1 MHz. Another set of comparative study [22] showcased the advantages of using bursts of picosecond pulse for micro-machining of materials compared to the nanosecond source, utilizing the same pulse energy along with pulse width and pulse shape. It was concluded that when bursts of picosecond pulses were used, the material removal along with the surface quality was more than 25% compared to the nanosecond pulses.

Femtosecond pulsed micro-machining on an amorphous carbon film and polyvinyl chloride film were carried out by Mizunami et al. [23] with 1.56 µm erbium-doped fiber laser oscillator-amplifier system along with direct amplification and pulse extraction. Peak power, as high as 25 kW, was obtained during the pulse extraction and amplification. Further, with the process of pulse extraction and amplification, a 6 µm trace of ablation was observed. On the flip side, when polyvinyl chloride film was utilized for micro-machining with the aid of a fiber laser, direct amplification was found to be more suitable. The cut width dimension of 4 µm was observed

from the experiment. Further, for an increased repetition rate of 100 kHz, the optical damage was reduced owing to the lower peak power of the fiber laser.

Laser micro-machining of multiple layers on ceramic/metal (thermal barrier coated super alloy) was conducted by Qi et al. [24]. In this experiment, an industrial-grade economic nanosecond pulsed fiber laser was utilized to study the relationship between the process parameters and machining geometric features of stainless steel (SS) 304, copper, Inconel 718 and thermal barrier coating (TBC) coating samples. It was found that the depth of the trench was dependent on the laser peak fluence in a logarithmic relationship. When the beam waist was 50 µm for SS304 and 30 µm for copper, the volume removal rate was high. It was also observed that a similar trend was followed by the finite element method (FEM) predicted volume removal rate along with the beam waist variation. Finally, fiber laser micro-machined surface roughness (R_a) using laser scanning for TBC coating and Inconel 718 was measured as 5.96 µm and 7.32 µm respectively.

Wu et al. [25] carried out experiments on fiber laser micro-cutting of square micro-structure on a diamond surface to study ablation depth, material removal rate along with the machined surface topography. The influence of the fiber laser machining parameters, i.e., laser power, scanning speed, defocusing condition, and the scanning pitch, on the aforesaid response criteria was studied. It was observed that the absorption of the laser plasma plume resulted in the reduction of the growth rate of both the ablation depth and material removal rate. Besides, high overlap ratio combined with high laser power resulted in smooth microstructure topography.

Genna et al. [26] carried out a micro-cutting of NIMONIC 263 sheet with the aid of a 100 W Yb-YAG fiber laser. The considered process parameters were pulse duration, the nozzle diameter and the position of the focusing lens, while average laser power and air pressure were kept as constants. The critical cutting speed for micro-cutting of NIMONIC 263 was calculated with the variation of pulse duration along with cutting speed, the nozzle diameter, and the focus position at an average laser power of 80W. Under these adopted conditions, it was observed that the critical cutting speed was dependent on both pulse duration and nozzle diameter. The critical cutting speed was varied in the range 4000 to 5500 mm/min. The bottom kerf was affected only by the nozzle diameter, while the upper kerf was governed by both nozzle diameter and change in focus position. It was also observed that all the aforesaid control factors governed the taper angle. The optimum taper angle was obtained when the focusing position was 0.2 mm below the

surface. Besides, it was concluded that the molten material removal from the kerf was more efficient when the nozzle diameter was reduced.

1.7.1.1 Fiber Laser Stent Cutting Process

The most promising possibility of a fiber laser in the field of bio-medical is in profile cutting of cardiovascular stent. A stent is a lattice-shaped metal tube which is utilized for the implantation into arteries [27]. Cardiovascular stents can be made of various materials such as nickel-titanium (NiTi) alloy, stainless steel. Liu et al. [28] analyzed the effect of fiber laser process parameters on responses such as surface roughness, kerf width, HAZ and formation of dross for the fabrication of cardiovascular stent of NiTi alloy tube (outer diameter of 1.8 mm and a wall thickness of 240 μm). The experiments were performed with continuous water flowing through the inside walls of the tube in the presence of argon as an inert gas (constant pressure of 0.45 bar). It was observed that striation on the surface topography was not formed at the wet cutting conditions. The optimum choice to achieve low surface roughness and kerf width, and small recast layer, was the mixed topography striation ratio for the micro-cuts. The power density influenced kerf width geometry. An increment in the power density caused an increase in pulse energy. As a result, an increment of the kerf width dimensions was observed. Further, at a medium power density combined with the low cutting speed, the smallest entry width of 25.53 μm was achieved. On the other hand, at high power density followed by fast cutting speed, entry kerf width of 38.59 μm was obtained. With the increase in the power density, it was also observed that both surface roughness and kerf width were increased. The cutting speed was the most critical parameter for obtaining excellent surface finish compared to the other process parameters. Spot overlapping factor determined the uniformity and smoothness of the micro-machined profiles, i.e., higher the spot overlapping factor, higher the uniformity and smoothness of the profiles. When the cutting speed was high, the spot overlapping factor was low. The phenomenon reversed back with the increment in the cutting speed.

Meng et al. [14] utilized a 50 W fiber laser system for the micro-cutting of 316L stainless steel tube (thickness 110 mm, diameter 2 mm) cardiovascular stents in order to observe the effects of various micro-cutting parameters on the kerf width profiles. The process parameters were laser output power, pulse length, repeat frequency, cutting speed, and assisting gas pressure. The pulse

frequency was set at 1500 Hz, followed by pulse length of 0.15 ms and assisting oxygen gas pressure of 0.3 MPa.

It was concluded that the kerf width dimensions were increased with the increment of laser output powers owing to high power density. The phenomenon reversed back when the cutting speed increased, because of the low power density. The kerf width was also increased when both the pulse length and pulse frequency were increased. It was also observed that the kerf width was less than 20 μm along with low roughness and HAZ at laser output power of 7 W, a pulse length of 0.15 ms, pulse frequency of 1500 Hz, cutting speed of 8 mm/s and assisting oxygen pressure of 0.3 MPa.

Muhammed et al. [29] showed the effect of both wet and dry 316L stainless steel with the aid of a fiber laser system. It was concluded from the experiment that in the case of wet stainless steel cutting, the results were comparatively better regarding narrower kerf width along with low surface roughness, less dross, no back wall damages, and smaller HAZ. In order to control the micro-cutting quality, low average power with the combination of low pulse width was selected. It was observed that the low pulse width increased the laser beam penetration rate, which led to the high aspect ratio micro-cut profiles.

Erika et al. [30] assessed the influence of process parameters on average surface roughness (R_a) and formation of back wall dross of fiber laser micro-cutting of miniature tubes, made of AISI 316L stainless steel with two different dimensions of wall thickness and hardness conditions. Type A material was annealed with 110 μm wall thickness, whereas type B was hard drawn with 160 μm wall thickness. The author carried a quantitative evaluation of the back-wall dross adherence phenomenon. High level of pulse overlapping factor and pulse energy below of 32 mJ resulted in R_a value of 1 μm in at the edge of the laser cut tube and less than 3.5% dross deposition at the back wall of the miniature tube. Pulse frequency, pulse width, peak power, cutting speed, and gas pressure combined with the central point curvature, significantly affected the response criteria. It was concluded that hard drawn tubes showed better results compared to the miniature tubes under the annealed condition in terms of back wall dross formation.

Kliene et al. [31] also demonstrated the fiber laser micro-cutting of stainless steel stent implants using a single-mode fiber laser. Kerf width and surface quality on the side wall was selected as the responses. It was observed that due to its good beam quality, the fiber laser produced a

narrow kerf width. High pulse to pulse overlap also produced good cut quality, but beyond 85% overlap with no significant improvement in surface roughness was observed.

Kliene and Watkins [32] compared the results of micro-cutting using pulsed fiber laser and pulsed Nd-YAG lasers. It was observed that the micro-cuts produced by fiber laser had similar features to those produced by Nd-YAG laser. At lower peak power, the surface quality was degraded from bottom to top edge of the cut. Low peak power produced low striations, and hence, surface roughness was improved.

Liu et al. [33] studied the influences of assist gas during fiber laser micro-profiling of thin CoCr tubes. It was found out that oxygen and argon had different impacts on the CoCr fiber laser cutting process. Oxygen reduced molten melt burning, although many oxide particles were observed on the surface of the oxygen cuts. The acid pickling process carried out by the researchers, eliminated dross formation. As a result, uniform cutting kerfs, and non-dross formation were observed. Interestingly, it was observed that the acid pickling process resulted in similar cut quality to the raw material and did not effect on the micro-cutting surface topography as well as the formation of dross in the presence of argon gas. Oxygen as assist medium showed better results compared to argon gas during the fiber laser cutting of CoCr stents. Besides, pulse repetition rate and pulse width had more impact on micro-cutting quality compared to laser power. Cutting speed had a more complex impact on micro-cutting quality due to the combined effects of the cooling, ejecting, and combustion supporting effects. Finally, it was concluded that pulse frequency up to a suitable range could lead to the desired striation topology.

Sealy et al. [34] carried out millisecond pulsed fiber laser cutting of MgCa to investigate the cut quality. Laser peak power and cutting speed were considered the process parameters. Kerf geometry, surface topography, surface roughness, and microstructure were measured as the response criteria. Lower laser power led to smaller taper angles and less thermal damage. Lower laser power also caused columnar striations on the surface and reduced surface roughness value. It was concluded that thinner recast layer could be achieved in the combination of low power and cutting speed.

Demir et al. [35] investigated the surface quality after laser micro-cutting AZ31 tubes with a Q-switched nanosecond pulsed fiber laser. The investigators compared micro-cutting quality with argon gas and oxygen gas. A significant amount of dross formation was observed on the top surface when argon gas utilized. It was observed that that chemical etching after argon assisted

micro-cutting, significantly improved the geometrical integrity and the surface roughness was decreased by more than 11%. Micro-cut profiles in oxygen medium showed less dross on the surface and non-uniform kerf dimensions. An introduction of the liquid flow on the workpiece was also carried out to address optical, chemical, and mechanical effects on the micro-cut profiles. An analytical approach showed that the absorptivity of the liquid caused a significant loss of energy. The results showed that submersion in 0.5 mm alcohol height produced dross free micro-cuts, which was due to the reduction of adverse optical and mechanical effects. The optimal condition obtained in alcohol was further compared to the micro-cut quality obtained with a femtosecond laser with the coaxial gas supply. The results also demonstrated the feasibility of the submersion approach for dross-free micro-cutting.

1.7.1.2 Fiber Laser Micro-Grooving Process

The jet flow of gas influences to remove an excessive amount of molten material from the micro-grooved zone during fiber laser micro-grooving process. The characteristics of three-dimensional heat transfer, moving boundary, a multi-phase and spatially distributed heat source are associated with the fiber laser micro-grooving process [36]. Research work carried out by Biffi et al. [37] revealed that a nanosecond pulse fiber laser could be utilized to fabricate linear grooves of on polycrystalline FSMA$Ni_{45}Mn_{33}Ga_{22}$. The authors observed that the scanning velocity was a more critical parameter on the micro-grooves width dimensions rather than the number of the laser pulses. On the contrary, micro-groove depth dimensions tend to vary with the change in the laser pulses. However, the formation of micro-cracks in the middle of the micro-grooves was a problem associated with the material described above.

Singh and Melkote [38] demonstrated the improved dimensional accuracy of the micro-machined feature in laser-assisted mechanical micro-machining (LAMM) for micro-grooving of H-13 (H stands for Chromium hot work tool steels by the AISI classification system) die steel (42 HRC). In this study, CW fiber laser power of 35 W was utilized for the micro-grooving process. A 70 to 120 µm spot size laser beam was focused in front of a small grooving tool to soften the workpiece, hence lowering the forces required to cut the material and further the deflections of the tool. The process also enhanced the material removal rates in micro-cutting and minimized catastrophic tool failure. However, the authors failed to address the detrimental HAZ from the micro-machined zone. Singh et al. [39] further presented the characterization and

prediction of the HAZ caused by laser heating in the laser-assisted mechanical micro-machining (LAMM) process with the aid of 35 W solid-state ytterbium-doped fiber laser. The authors analyzed the HAZ caused by pure laser heating of H-13 mold/die steel (42 HRC) using metallographic methods and micro-hardness measurements. A 3D transient finite element model for a moving Gaussian laser heat source was also developed to analyze the temperatures generated in the workpiece and validated through actual temperature measurements. The computed temperature distribution was also correlated with the HAZ via micro-hardness tests. A critical temperature range for the formation of the HAZ was also identified. It was concluded that the size of the HAZ was dependent on both scan speed and laser power. The maximum width and depth of the HAZ dimensions were decreased by 32% and 62%, respectively, when the scan speed was increased from 10 mm/min to 100 mm/min at laser power of 10 W. A critical temperature ranges of 840–890˚C for the depth of HAZ on H-13 steel (42 HRC) at different scan speeds, was also identified by the authors. The researchers also observed that if the temperature in the material removal region was below the critical range, then no residual HAZ in the material could be observed after micro cutting.

1.7.2 Fiber Laser Micro-Drilling Process

Pulsed mode of the fiber laser system is quite suitable for micro-drilling of ductile and brittle materials. Many research works are being carried out in this area, and the results are being discussed as follows. From the past research works, it is evident that spattering along with other metallurgical defects, i.e., cracks and morphological irregularities are always associated with the laser micro-drilling process owing to the rapid solidification of the molten materials [40]. In this regard, Biffi et al. [40] carried out percussion micro-drilling of commercially pure titanium sheets having 0.5 mm of thickness with the aid of a nanosecond pulsed fiber laser system. The authors obtained entrance and the exit holes with the combination of pulse frequency of 20 kHz, pulse energy of 0.5 mJ; and pulse frequency of 50 kHz, pulse energy of 1.2 mJ respectively. A lesser amount of drops and spatter at the exit holes were observed compared to the entry hole. However, when ultrafast fiber laser percussion micro-drilling on high purity copper, stainless steel (Fe/Cr18Ni10) and high-carbon steel (C 1095) sheets with 0.25-mm thickness each [41] were performed, the results were satisfactory compared to Q-switched nanosecond laser.

Ghosal et al. [42] identified that wait time and modulation frequency were the most critical parameters of the material removal rate (MRR) during the micro-drilling of Al/Al_2O_3-MMC by a ytterbium-doped fiber laser system. The authors concluded that the material removal rate increased with an increase of N_2 gas pressure and maximum material removal rate was observed within the range of 400 to 475 W of laser power. The minimum taper angle of the micro-hole was observed with the combination of nitrogen pressure of 18–20 bar, along with 600–680 Hz of modulation frequency. The optimal parametric combination for maximized MRR and minimized taper was identified as laser power of 473.12 W, modulation frequency of 604.54 Hz, wait time of 0.18 s, assist gas pressure of 19.82 bar and duty cycle of 93.47%.

Huang et al. [43] produced high aspect ratio micro-holes on glass, as well as, on metal and tissues using a femtosecond pulsed fiber laser system. The fabricated micro-holes were free from any debris formation and thermal damages. The researchers observed that in the absence of micro-cracks around the periphery of the micro-holes, high aspect ratio, i.e., 8:1 micro-holes were generated in both glass and metals with the aid of the femtosecond pulsed fiber laser system. It was concluded that the fiber laser could also be successfully applied to the generation of micro-holes on the ceramic substrates.

Adelmann et al. [44] carried out rapid single mode fiber laser micro-drilling of alumina and aluminum nitride to analyze the effect of various process parameters such as laser focus position, laser power, gas pressure, and laser modulation scheme on the hole diameters. The experimental observations revealed that single mode fiber laser was capable of generating 50 µm diameter of micro-holes with a minimum taper angle of 1.57° and a high circularity of 1.07. However, some amount of spatters on the top side of the micro-holes were observed, which could be further eliminated by the utilization of pre-pigmenting and ultrasonic cleaning.

Harp et al. [45] investigated whether a fiber laser could be utilized in a continuous mode to perform pulsed ablation. It was observed that 100 pulses were needed to create the same depth as by CW mode compared to pulsed mode. The experimental results showed that at 18 µs of pulse duration, a blind hole of 43.6 µm diameter and 23.5 µm depth could be generated. As the pulse duration increased from 20 µs to 40 µs, the diameters of the micro-holes were increased with the simultaneous decrease in the depth dimension. It was also found that the highest aspect ratio was obtained for a pulse duration of 18 µs, even though the pulse duration of 20 µs produced the highest depth.

Ancona et al. [46] studied the effect of pulse repetition rate and average laser power for drilling breakthrough time. Materials with different thermal properties, i.e., copper and stainless steel sheet of 0.5 mm thickness, were selected to obtain melt free holes without any particle shielding. Ultrafast ytterbium-doped fiber laser with an average laser power of 100 W and pulse repetition rate of 1 MHz were utilized for experimentation. It was found that metals having low thermal conductivity and heat diffusivity, the accumulation of heat played a critical role in the determination of drilling time. Besides, the accumulation of heat deteriorated the quality of holes due to the formation of large amounts of molten material. It was concluded that particle shielding and heat accumulation had negligible effect for materials having high thermal conductivity, and therefore high aspect ratio hole was obtained at the maximum power of the fiber laser. However, in laser trepanning drilling, high-quality holes were obtained at lower laser average power compared to laser percussion drilling.

Tu et al. [47] carried out microsecond laser micro-hole drilling on stainless steel using continuous mode fiber laser of 300 W. The CW fiber laser produced modulated pulses ranging from 1 μs to 8 μs which generated an initial spike with a peak power of 1500 W for 1 μs. Further, an increment of the laser pulse, the stead-state power of 300 W was generated. The CW fiber laser was focused to a small spot size of 10 μm to achieve very high power density up to 1.9 GW/cm^2. With one single laser pulse at approximately 1 μs, a blind hole of 167 μm in depth and 23 μm in opening diameter was created on the stainless steel workpiece. The experimental characterization of the micro-hole drilling process included laser control, laser beam characterization, hole formation, photodiode measurements of the vapor intensity, high-speed photography of vapor/plasma formation, and spectroscopic measurements of plasma. The results showed that due to very high irradiance of the fiber laser beam, the absorbed energy was sufficient to melt and vaporize the material. However, this energy was sufficient to dissociate vapor into intense plasma at temperatures over 16,000 K. It was concluded that the hole drilling mechanism by this short microsecond laser ablation was due to the combination of adiabatic evaporation and ejection of fine droplets.

Stefan et al. [48] studied the fiber laser drilling process on 0.8 mm thick titanium sheet for the utilization in the aerospace industry. Fiber laser with a power of 200 W at a pulse repetition rate of 200 kHz was utilized for the research work. The fiber laser combined with a galvanic scanner and a plane field optic led to precise and fast drilling over an area of 100 mm x 100 mm. With

the aid of a precise stage, several of these drilling fields were placed side by side to machine the complete panel area. The authors successfully reduced micro-hole diameter to 30 μm with a drilling rate of more than 400 holes per second.

Further, blind micro-hole array templates were generated with the aid of a 20 W fiber laser on a Ti-6Al-4V workpiece by Meng et al. [49]. The influence of laser parameters on the morphology of the blind holes was investigated, and the optimized laser parameters were calculated to generate the blind micro-hole array templates on Ti-6Al-4V. Three different morphologies were generated by adjusting the laser parameters. A type II micro-hole was characterized by a column-shaped entrance and a hemispherical dome bottom with a suitable morphology. The optimized laser parameters were obtained at an average laser power of 16 W, laser irradiation time of 1 ms and pulse repetition rate of 25 kHz at focus condition. Nano-sized hydroxyapatite (HA) powders were further uniformly deposited into the blind micro-hole templates by electrophoretic deposition to analyze the dynamic behavior of the laser drilling process. It was observed that variations of laser focusing distance produced three kinds of blind micro-hole morphologies. The type II micro-hole at the defocusing distance of from 0 mm to −0.2 mm was adopted for sequent electrophoretic deposition. The authors found that average laser power had a significant influence on the top diameter and the depth of the micro-holes. The diameters and the depth values of the micro-drilled holes were increased from 25 μm to 64 μm and 78 μm to 105 μm respectively for average laser power of 8 W to 16 W. It was also observed that laser irradiation time had less influence on the top diameters of the blind holes. However, the combinations of process parameters mentioned above, led to the increment of the depth of the blind hole from about 33 μm to 105 μm when the laser irradiation time was increased from 0.3 ms to 1 ms. It was observed that cone-shaped (type III) micro-holes were generated by at the initial stage of laser drilling ranging from 0.3 ms to 0.8 ms. On the contrary, type II micro-holes were generated during a longer irradiation time of 0.9 ms to 1 ms. Optimized laser parameters, i.e., a combination of defocusing distance of 0 mm, average laser power of 16 W, laser irradiation time of 1 ms and pulse repetition rate of 25 kHz led to the generation of type II micro-hole array templates with different blind micro-hole densities.

Pak et al. [50] investigated fiber laser percussion drilling on Inconel 718. Laser power, laser pulse frequency, and assist gas pressure were selected as the process parameters. Oxygen was used as an assist gas for the research work. 300 to 700 μm of diameters of micro-holes were

generated on the Inconel 718 by the fiber laser. It was observed that the combination of high laser power, pulse frequency, and lower assist gas pressure produced large hole entrance diameter. At high laser power, exit hole diameters were also increased. Besides, low pulse frequency increased the hole entrance circularity. It was also observed that laser power and assist gas pressure variations had little effect on both entrance and exit hole circularity. An increment of pulse frequency also led to the decrement of hole exit circularity. Hole taper was influenced by the combination of pulse frequency, laser power, and lower assist gas pressure.

1.7.3 Fiber Laser Milling Process

Saklakoglu et al. [51] investigated and evaluated the machinability of AISI H13 by 30W fiber laser milling process. The surface roughness and milling depth for all the experiments were found out to be significantly dependent on scan speed and laser power. The scan speed of 200 mm/s and laser power of 100% produced the highest value of milling depth, i.e., 195 μm. It was found out that the values of surface roughness were decreased with a decrease in laser power and pulse frequency with the combination of high scan speed. The milling depth was also increased with the decrease of scan speed and filled spacing. However, a lower value of scan speed and filled spacing decreased surface roughness value. The optimum experimental condition for minimum surface roughness was observed at the combination of scan speed of 800 mm/s, the laser power of 60%, pulse frequency of 20 kHz, and filled spacing of 0.03 mm. However, the maximum milling depth was achieved at scan speed of 200, laser power of 100%, pulse frequency of 40 kHz, and filled spacing of 0.02 mm.

Deladurantaye et al. [52] utilized a fiber laser system operating at 1064 nm to compare of micro-milling observations with stainless steel and aluminum. The experimental results showed that both the aforesaid materials could be utilized for micro-milling operation with different pulse shapes at pulse duration of 3 ns and 80 ns, respectively for steel and aluminum. Preusch et al. [53] carried out micro-milling on alumina and aluminum nitride using a nanosecond pulsed fiber laser. It was concluded that maximum MRR of 94 and 135 mm^3/h for alumina and aluminum nitride respectively could be achieved using laser fluence of 64 J/cm^2 and high pulse overlap.

Zhou et al. [54] carried out fiber laser micro-milling on a copper sheet to generate micro-channel. The authors investigated the effects of different process parameters such as scanning speed, laser output power, and the number of scans on the surface morphology and geometrical

dimension of the micro-channels. It was observed that with the change in scanning speed and laser output power, the surface morphology of micro-channel was significantly affected. Moreover, the depth of micro-channel was increased when the laser output power and number of scans were increased. To reduce the error of the machine width, they concluded that the error compensation setting could be utilized during fiber laser micro-milling process for the fabrications of different micro-channels.

Engraving process, with the aid of fiber lasers, is an emerging field of interest. An engraving operation was carried out on C45 carbon steel by Genna et al. [55]. A Q-Switched 20 W Yb-YAG fiber laser with the fundamental wavelength of 1070 nm was utilized in order to study the influence of process parameters on surface roughness along with MRR. The engraved depth was found out to be highly dependent on the scan speed, pulse frequency along with the scan number. It was also observed that the line spacing, pulse frequency along with the scan speed governed the surface roughness of the engraved profiles. However, after around 10 scans, the surface roughness remained unaltered with the combination of aforesaid parameters. It was summarized that the selection of appropriate and accurate process conditions could lead to higher values of MRR and better surface roughness. Finally, at the combination of scan speed of 20 mm/s, pulse frequency of 30 to 40 kHz and line spacing of 0.04 mm, better MRR and R_a were observed.

Further, experimental works were carried out by Tagliaferri et al. [56] on Ti-6A1-4V alloy sheet having a thickness of 4 mm, using a Q-Switched 30 W Yb-YAG fiber laser. The experimental work identified the effect of the process parameters over the depth of the machined volume along with the quality of the roughness of the machined surface. After the first phase of the experiment, the effect of the process parameters over the machined volume along with the roughness of the engraved surface was identified. The results of the experiment revealed that the machined volume was linearly dependent on the total amount of releasing energy, for each of the pulse frequency.

1.7.4 Fiber Laser Micro-Turning Process

Laser micro-turning process is utilized to generate micro-patterns on the cylindrical workpieces, ranging from metal to ceramics. However, only a few research works are highlighted on the fiber laser micro-turning operation process on the engineering materials. Till date, Nd-YAG laser systems are the most preferred systems by the researchers in the micro-turning process instead of

fiber laser micro-machining system. Biswas et al. [57] carried out spiral micro-grooving on pure aluminium with the aid of a 50 W ytterbium-doped fiber laser system. Average laser power, pulse frequency, and axis feed rate were considered as the fiber laser process parameters to study the influence of spiral micro-grooves geometries regarding groove width and groove depth. Around 115.2 µm of maximum micro-groove width was achieved at a parametric combination of the average laser power of 42.5 W along with pulse frequency of 55 kHz, and the pitch value of 0.4 mm. The micro-groove depth, as high as 51.95 µm, at a parametric combination of the average laser power of 45 W was also be achieved along with pulse frequency of 70 kHz and the pitch value of 0.2 mm.

1.7.5 Fiber Laser Marking Process

Fiber laser marking is a critical area that has emerged in recent times. The utilization of fiber laser for marking applications produces clean and high-end finishing of a wide variety of materials. Astarita et al. [58] carried out a fiber laser marking of titanium cold sprayed coatings on aluminum substrates. The authors observed that during fiber laser marking process, the irregular groove was observed when high laser energy was utilized. The authors concluded that regular mark with a low dimension groove was observed due to a low heat input during the process. The homogeneity of the cold spray coating played a crucial role in obtaining better quality marking. The discontinuous nature of coating affected the nature of the marking process. The penetration depth of more than 0.4 mm was observed on the titanium sheet (without coating), the penetration depth of 0.2 mm was obtained with cold sprayed coating.

1.8 Selection of Workpiece Materials

In the present day scenario, a wide range of engineering materials is available with their various applications in bio-medical, aerospace and automotive industries. In designing a structure or device, it is challenging to select a material from the vast array of materials that are the best fit for a specific application. Most of the engineering components are made of metals and alloys than of any other class of solid. Traditionally, materials can be classified into three major groups– metals, ceramics, and polymers. Metallic materials are made up of pure metals such as titanium, iron, copper, and a wide range of alloys. Polymers consist of carbon and another host of materials, such as polyvinyl chloride, polyethylene, polymethyl methacrylate, and nylon. Increasingly, polymers are replacing metals because they offer a combination of properties that

are more attractive to the designer [59]. Silicon carbide, glass, synthetic gemstones, ruby, alumina, and zirconia are the most common examples of ceramics. Ceramics materials represent a broad range of inorganic materials, typically oxides, borides, carbides, and nitrides. Many ceramics are crystalline or have significant amounts of crystalline phases in their microstructure [60]. Non-crystalline ceramics are generally termed as glasses. In addition to these crucial divisions, composites and biomaterials are other groups of materials that have a wide range of application in various engineering fields. Composites are essential materials which combine compounds from more than one of the groups listed above and have superior engineering properties from the separate compounds. Biomaterials are naturally occurring materials, and they are invariably composites, made of more than one material type.

The engineering materials can also be classified further under two categories, structural and functional. The functional engineering materials can be further characterized by biomaterials, polymer and soft materials, glass and amorphous materials, super alloys, etc. The research materials are selected from the aforesaid classification of the functional engineering materials. Details are listed of workpiece materials are listed hereunder.

1.8.1 Polymethyl Methacrylate (PMMA)

In the present era, the usage of polymer material in microfluidic devices has increased significantly, owing to the need of performing large-scale applications. The general micro-fabrication strategies employed over the glass as well as silicon suffers a considerable amount due to cost ineffectiveness of both the fabrication process as well as the processing of those materials. At present, with the advancement of a host of polymer materials with their superior properties and cost-effectiveness, the entire micro-fluidic marketplace has shifted towards the micro-fabrication of polymer materials instead of glass as well as silicon. Among the various polymer materials, thermoplastic polymers have gained popularity in the domain of microfluidic devices due to robust elasticity and melting by thermal energy over other polymers and plastics [61]. However, among the extensive range of thermoplastics family, polymethyl methacrylate (PMMA) is classified among the group of thermoplastics, which comprises a chemical combination of a vast number of monomer molecules [61]. PMMA is characterized as a rigid thermoplastic characterized by superior mechanical, chemical, and electrical properties.

1.8.1.1 Applications of PMMA

The various applications of PMMA lie in orthopedics, biological applications, micro-electro-mechanical system (MEMS), etc. The various applications of PMMA are as follows:

(i) PMMA has been widely used in the area of biomedical applications, especially for drug delivery and cranioplasty [62].

(ii) PMMA can be grafted to natural polymers to obtain high molecular weight copolymers of high intrinsic viscosity for utilizing as viscosifier [63]. PMMA is also utilized in a composite for the construction of pneumatic actuators for micro-pumps.

(iii) PMMA composite is an excellent choice of material for the fabrication of chemical sensors.

(iv) PMMA is also utilized in the production of a quasi-solid state dye-sensitized solar cell (DSSC) using a high conductivity polymer gel electrolyte.

1.8.2 Quartz

Quartz can be attributed as a polymorph of silica (SiO_2), i.e., a continuously connected network of $(SiO_4)^{4-}$ tetrahedra where silicon is placed at the center, and each of the oxygen (O_2) atoms is being linked to the silicon atoms. The critical properties of quartz can be summarized as high corrosion resistance, high electrical insulation property, high temperature, and thermal shock resistance. On the other hand, the optical transmissivity of the quartz is almost 80% of 1,500 nm wavelength [63]. In addition to this, phase transformation starts to occur with fewer distortions due to the instability of quartz at a moderately higher temperature of 550°C. With the more heating of quartz, optical activity of quartz is lost [64, 65]. In the present day scenario, quartz is utilized in the fabrication of microelectronic chips, micro-fluidics along with the biochips and biological channels owing to its strong covalent bonding, stability, and smaller in size.

1.8.2.1 Applications of Quartz

Various applications of quartz in different areas as follows:

(i) Quartz crystals are widely used in electronics circuits and resonators. Besides, quartz is also utilized in radio frequency applications.

(ii) The integration of advanced microelectronics technology with signal processing and biological sensing interfaces has emerged as a rapidly growing area of quartz.

(iii) Quartz is widely used in micro-gravimetric devices, generally known as quartz crystal microbalance (QCM), in a variety of different applications, i.e., monitoring and characterization of film deposition, detection of specific antigens, biomolecule binding kinetics, cell adhesion, and DNA detection.

1.8.3 Titanium Alloy-Ti-6Al-4V

Titanium has been recognized as an element over 200 years. Two alloys of titanium are widely used in various manufacturing and bio-medical fields, i.e., Ti-6Al-4V and Ti-5Al-2.5Sn. Ti-6Al-4V alloy accounts for more than half of the current titanium market. The rapid growth of the titanium industry is a testimony to the metal's high specific strength and corrosion resistance. Titanium alloys are widely used for highly loaded aerospace components that operate at low to moderately elevated temperatures, including both airframe and jet engine components for having a density about 55% of the steel [66]. Titanium exists in two crystallographic forms. At room temperature, unalloyed (commercially pure) titanium has a hexagonal close-packed (hcp) crystal structure referred to as alpha (α) phase. At 883 °C, this structure transforms into a body-centered cubic (BCC) structure known as beta (β) phase. Alpha and beta alloys have compositions that support a mixture of α and β phases and may contain between 10 and 50% β phase at room temperature [67]. The most common form of α + β alloy is Ti-6Al-4V. Although this particular alloy is relatively difficult to form even in the annealed condition, α + β alloys generally have good formability [68].

1.8.3.1 Applications of Ti-6Al-4V

The main applications of Ti-6Al-4V lie in aerospace, automotive and bio-medical industries. The various applications of Ti-6Al-4V are as follows:

(i) Ti-6Al-4V is widely used in airframes such as fittings, bolts, landing gear beam, wing boxes, fuselage frames, flap tracks, slat tracks, brake assemblies, fuselage panels, engine support mountings, undercarriage components, inlet guide vanes, wing pivot lugs, keels, firewalls, fairs, hydraulic tubing, etc.

(ii) In engines, compressor disks and blades, fan disks and blades, casings, afterburner cowlings, flange rings, spacers, bolts, hydraulic tubing, hot-air ducts, helicopter rotor hubs are all being comprised of Ti-6Al-4V.

(iii) Ti-6Al-4V is widely used in various biomedical engineering such as hip and knee joint prostheses, bone plates, screws and nails for fractures, pacemaker housings, heart valves, instruments, dentures, hearing aids, high-speed centrifugal separators for blood, wheelchairs, insulin pumps.

(iv) Chemical processing areas of storage tanks, agitators, pumps, columns, frames, screens, mixers, valves, pressurized reactors, filters, piping and tubing, heat exchangers are the products of Ti-6Al-4V.

1.8.4 Nickel Super Alloy-Hastelloy C-276

Nickel is a versatile element and alloys with most of the metals. Complete solid solubility exists between nickel and copper. Broad solubility ranges between iron, chromium, and nickel make possible to form various alloy combinations. The face-centered cubic structure of the nickel matrix (γ) is strengthened by solid-solution hardening, carbide precipitation, and precipitation hardening. The commercial forms of nickel and nickel-based alloys are fully austenitic and are selected mainly for their resistance to high temperature and aqueous corrosion environment [69]. Among the various nickel-based super alloys, Hastelloy series has gained a wide range of applications in the various automotive and nuclear domains due to their outstanding performance in a wide range of corrosive mediums. Developmental works during the 1920s of nickel-molybdenum alloys have led to the discovery of the Hastelloy series of alloys, which are known for their high corrosion resistance.

Hastelloy C-276 is a nickel-molybdenum-chromium-tungsten alloy having excellent corrosion resistance in a wide range of severe environments. The high molybdenum content makes the exceptional alloy resistant to pitting. The low carbon content minimizes carbide precipitation during welding to maintain corrosion resistant welded structures. The attributes of Hastelloy C-276 include high resistance to regular attack, excellent localized corrosion resistance, excellent stress corrosion cracking resistance, and ease of welding and fabrication.

1.8.4.1 Applications of Hastelloy C-276

The various applications of Hastelloy C-276 in the area of manufacturing, as well as in pharmaceutical, are as follows:

(i) Hastelloy C-276 is widely used in the chemical processing industries.

(ii) Hastelloy C-276 has widespread applications in the areas of energy, health, and environmental, pharmaceutical and flue gas desulfurization industries.

(iii) Hastelloy C-276 alloy also has a high potential for large area applications at temperatures below 1200 °C, such as heating components for solar power-related applications, optically absorptive coatings inside large optical chambers, etc.

1.8.5 Stainless Steel-316L

316L stainless steel is a particular type of stainless steel which is comprised of molybdenum-bearing austenitic stainless steels. The addition of molybdenum improves general corrosion and chloride pitting resistance than that of conventional chromium-nickel austenitic stainless steels such as Type 304. It also offers higher creep, stress-to-rupture, and tensile strength at elevated temperature. The low carbon composition and the addition of nitrogen enable 316L to meet the mechanical properties of 316. 316L resists atmospheric corrosion, as well as, moderately oxidizing and reducing environments. This alloy has excellent resistance to intergranular corrosion along with high strength and toughness at cryogenic temperatures. 316L is widely used for biomedical applications due to its mechanical properties, biocompatibility, and corrosion resistance.

1.8.5.1 Applications of 316L

Various applications of 316L are as follows:

(i) The most promising application of 316L is in the fabrication of the stent.

(ii) 316L is a favourable metal for the use as an acetabular cup, one half of an artificial hip joint, applications.

(iii) High-temperature applications in reactor vessels and piping systems are the most common applications of 316L.

(iv) The excellent corrosive resistance of 316L allows it for the various marine applications.

(v) 316L has also found a great application in the structural domain.

1.9 Objectives and Scope of the Present Research Work

Fiber laser micro-machining has emerged as an alternative to the conventional solid-state laser system and gas laser systems during the last few years. From the literature survey of fiber laser along with the aforesaid engineering materials, it can be found that the research work with fiber laser on those materials is limited. Predominant research works were carried out by primarily focusing only on the biomedical aspects. Experimental investigation along with the influence of process parameters need to be carried out for generating micro-features of different engineering materials such as titanium alloys, stainless steels, Hastelloy, polymer, quartz, etc. with the aid of fiber laser system. Utilization of fiber laser for titanium alloys and Hastelloy are also very few. Besides, this, the infrared wavelength of the fiber laser is yet to be utilized to fabricate micro-features on PMMA and quartz.

The present research work has been planned and designed to investigate and optimize the fiber laser micro-machining quality characteristics during machining on various alloys, polymer, and quartz. Within the limitation of the available resources, the objectives of the present research work have been combined as follows:

(i) To analyze the influences of fiber laser micro-machining process parameters on the characteristics of generated micro-channels on PMMA and also to carry out optimization analysis for determining the optimal process parametric combination of fiber laser micro-machining for achieving the optimum value of responses.

(ii) To carry out experimental investigations into fiber laser micro-grooving on Ti-6Al-4V and also to analyze influences of the process parameter on the responses during the generation of micro-grooves.

(iii) To design and develop a preheating setup for fiber laser micro-machining process to study the effect of preheating.

(iv) To analyze the influence of the process parameters on the responses during generation micro-grooves on 316L and also to design and develop a heating set up for preheating the workpiece materials during fiber laser micro-grooving and also to compare the results of fiber laser micro-grooving on 316L at preheating temperatures, with the same combination of process parameters and without preheating of workpiece.

(v) To analyze the influences of the process parameters on the responses during the generation of micro-holes on quartz with the aid of fiber laser based on the developed empirical relations between process parameters and responses and also to carry out optimization analysis for determining the optimal process parametric combination.

(vi) To carry out experimental investigations for process parameter selection for generating textured surfaces on Hastelloy C-276 and also to analyze the influences of process parameters on the responses for fabricating textured surfaces on Hastelloy C-276 with the aid of fiber laser. Finally, to carry out optimization for all the responses for determining the optimal process parametric combination for achieving quality surfaces on Hastelloy C-276 by a pulsed mode fiber laser system.

The present research work includes a detailed study on fiber laser micro-machining of various engineering materials to achieve quality micro-machining characteristics. Moreover, the present research work will open up new directions of research in the area of fiber laser micro-machining of various engineering materials and explore the possibilities of future scope of research on other surface characteristics features.

2. DETAILS OF DIODE PUMPED FIBER LASER MICRO-MACHINING SYSTEM

2.1 Introduction

Fiber lasers are the most versatile and rapid growing laser systems used for micro-machining applications. At present, fiber lasers are competing with the most of high-power, bulk solid-state lasers and gas lasers, primarily in the areas of automotive and emerging bio-medical fields.

Fiber lasers have a wide range of application in the micro-machining field, as discussed in chapter 1. The most promising utilization of fiber laser is in the fabrication of stents for bio-medical applications. Besides, fiber lasers have widespread applications in vast areas of automotive, aerospace, high power applications, etc.

From the literature survey as discussed in chapter 1, it is found that no research work is carried with simultaneous heating of the workpiece utilizing fiber laser micro-machining processes for the removal of internal stress as well as achieving slower cooling rate and reduced shrinkage stresses. In the present research study, a preheating set up is thus developed to perform simultaneous heating while performing fiber laser micro-machining operations on different materials.

Multi diodes pumped CNC based Ytterbium (Yb^{3+}) doped 50W fiber laser having a wavelength of 1064 nm with a TEM_{00} mode of operation, made by M/S Sahajanand Laser Technology Limited (Model: AKSHAR Fiber Pro-309) is utilized for different laser micro-machining operations. The detailed view of the fiber laser system is shown in figure 2.1. The fiber laser system consists of (a) laser generation unit; (b) fiber laser delivery system; and (c) assist air supply unit. The laser generation unit further consists of (i) optical fiber; (ii) silicate glass; (c) rare earth doped elements; (iv) fiber Bragg gratings; (v) laser diodes; (vi) fiber couplers; (vii) isolators; and (viii) fiber coupled acousto-optic modulator (AOM). Under fiber laser delivery system, (i) collimator; (ii) beam bender; and (iii) beam delivery unit are the subsystems. Besides, assist air supply unit, as well as a CNC controller unit for X-Y-Z axis, are also integral parts of the fiber laser system. The working table transverses in the X-Y direction for the present system. The maximum attainable speed is limited to 40 mm/sec. The specifications of the CNC pulsed fiber laser beam machining system are given in table 2.1. The detail of each system, along with their subsystems, is discussed in hereunder.

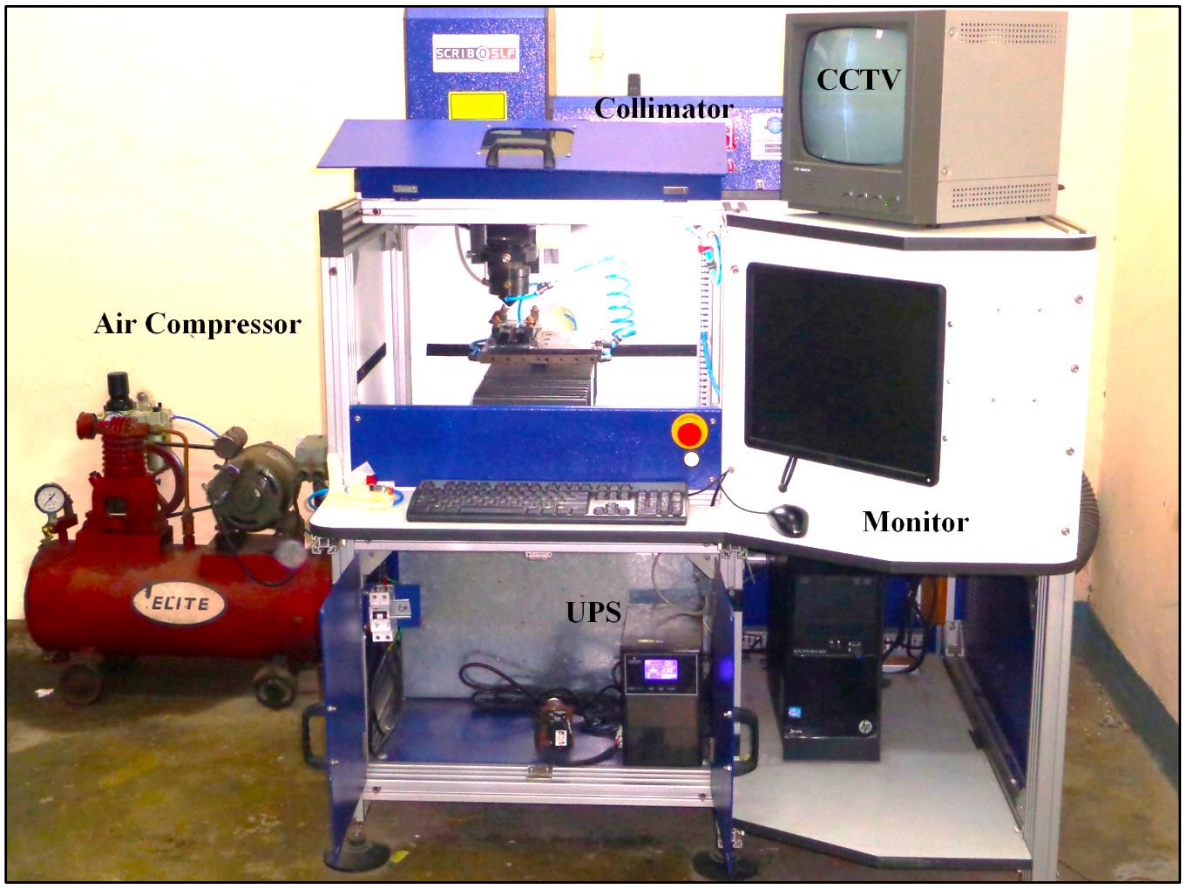

Figure 2.1 Photographic view of CNC pulsed fiber laser machining system

Table 2.1 Details of fiber laser beam machining system

Description	
Laser	Multi diodes Pumped Fiber Laser
Spectral Characteristics	
Wavelength	1060± 10nm
Optical Characteristics	
Polarization Type	Linear/Random
Maximum Pulse Energy	>1mJ
Max. Peak Power	> 7.5 kW
Nominal Average Power	≥ 50 W
Power Tunability	10-100%
Pulse Repetition Rate	50-120 kHz
Pulse Duration	According to PRR/<120ns
Power Stability	>95%
Inbuilt Guide Laser	0.5-4.0 mW
Wall-plug Efficiency	>30%
Spot Diameter	21µm

Beam Characteristics	
Beam Quality (M^2)	<1.5
Beam Roundness	>90%
Controller & CNC system	
Axis Travel (X & Y)	≥150mm
Drive	Servo Control Drives
Vision system	CCTV Camera
Cooling	Integrated
Electrical	
Power Supply	230V/50 Hz-115V/60 Hz
Software	I mark, Gyro, Q-saw

2.2 Fiber Laser Generation Unit

The fiber laser generation unit consists of a total of eight elements, i.e., (i) optical fiber; (ii) silicate glass; (c) rare earth doped elements; (iv) fiber Bragg gratings; (v) laser diodes; (vi) fiber couplers; (vii) isolators; and (viii) fiber coupled acousto-optic modulator. A photographic view of a fiber laser generation unit is shown in figure 2.2. The details description is given hereunder.

Figure 2.2 Photographic view of fiber laser generation unit

2.2.1 Optical Fiber

The primary constituent of a fiber laser is an optical fiber. An optical fiber made of silicate glass is shown in figure 2.3. The core of the fiber, as well as the cladding, is made of with silicate glass. The detail of silicate glass is discussed in the next sub-topic. Doping in the core of the fiber is essential to raise the core's refractive index. Germanium is added for doping of the fiber core. On the contrary, if fluorine and boron are used as dopants, the refractive index of silicate glass decreases. As the present fiber laser system operates in 1064 nm wavelength, the intrinsic loss within the fiber (dB/km) is high. The fiber laser is elongated to a few meters long to reduce the loss. In the present system, the length of the optical fiber is 3 meters. For protecting the glass surface, a layer of acrylic coating with a higher refractive index is used. The coating used in fiber further prohibits the propagation of unwanted light in the cladding glass.

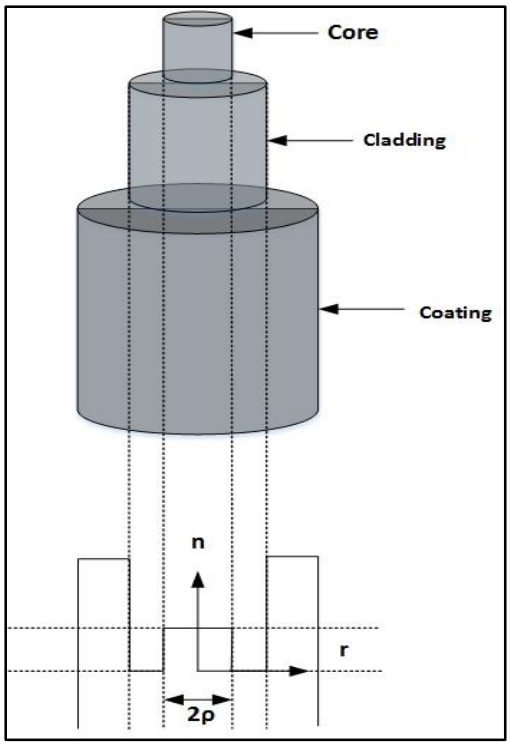

Figure 2.3 Optical fiber with refractive index distribution

2.2.2 Silicate Glass

Silicate glass is the most widely used as optical fiber in several low powers to high power fiber laser applications. Unlike crystals, glass molecules are disordered but are rigidly bound. The structure of the glass is bonded with several matrix molecules such as $(SiO_4)^{4-}$ or $(PO_4)^{3-}$ for

silicate or phosphate glasses, respectively [70]. In addition to this, a wide range of optical transparency, allows the silicate glass to achieve the lowest loss of optical communication. Silicate glass is mechanically robust, demonstrating remarkable tolerance to bending. Silicate glass also demonstrates a high degree of chemical resistance.

2.2.3 Rare Earth Doped Elements

Fiber amplifiers are doped with laser-active rare earth ions in the fiber core to absorb the light. These doped earth elements amplify the light via stimulated emission. Some of the examples of rare earth ions are ytterbium (Yb^{3+}), erbium (Er^{3+}), thorium (Tm^{3+}), and neodymium (Nd^{3+}). Incorporation of rare earth ions inside the fiber core requires disruption of the regular glass network. Some of the critical factors leading to the characterization of rare earth doped fibers are: (a) passive optical fiber; (b) active mode area; (c) numerical aperture; (d) cut off length; (e) bend losses; (f) rare earth doping concentration; (g) wavelength-dependent effective absorption and emission cross sections and (h) the speed of the energy transfer.

In the present system, fiber laser boosts of ytterbium-doped rare earth ions in the multimode regime of the fiber. Yb^{3+} ions have recently become the dopant of choice for high-power fiber lasers. As a laser-active ion in solids, such as crystals and glasses, Yb^{3+} offers several advantages compared with commonly used Nd^{3+} ions [70]. These advantages include:

(i) A longer upper-state lifetime.

(ii) Yb^{3+}doped laser-active glasses have broad and robust absorption bands near 915 and 976 nm.

(iii) A small quantum defect which results in lower thermal load per unit of pump power.

(iv) An absence of the excited state absorption and up-conversion losses.

(v) Room-temperature excited state lifetime is approximately 1 ms.

2.2.4 Fiber Bragg Gratings (FBGs)

Fiber Bragg gratings (FBGs) are critical elements in enabling the development and commercial success of fiber lasers. Most fiber Bragg gratings are mainly used in single-mode fibers, and the physical modeling of FBGs are often relatively simple. The working principle of FBGs same as dielectric mirrors. At each periodic refraction of FBGs, a small amount of light is reflected. FBGs are found to be highly stable at room temperature. For utilizing FBGs in fiber lasers, the

wavelength and bandwidth required are in the region of 0.1–1 nm and center wavelength control ± 0.5 nm, respectively.

2.2.5 Laser Diodes

Laser diodes are utilized in fiber lasers for pumping of the photons. In the present system, to generate 50W of average laser power, five numbers of diodes are utilized for optical pumping. Optical pump sources based on single-emitters are typically coupled into a 105/125 fiber, i.e., 105μm of diameter core along with a 125 μm diameter of silica glass cladding. Depending on the number of diodes, the average laser power of the laser is varied, i.e., the higher number of diodes, higher the average power. Typical commercially available multi-emitter pumps consist of 3, 5, 7, or more laser diodes combined into a single 105/125 delivery fiber and delivering 60–140 W depending on power per emitter.

2.2.6 Fiber Couplers

Fiber couplers are the essential elements of a fiber laser. The delivery fibers are limited due to the industry standard fibers have either 105μm or 200μm of core diameters in most of the cases. Fiber couplers combine one or more input fibers and also several output fibers depending on power distribution within the fiber laser.

2.2.7 Fiber Laser Isolators

Inter-stage optical isolation is required during multiple stages of amplification with the aid of a fiber amplifier. Fiber-coupled isolators are the cost-effective components which prevent back reflections by only allowing light to travel in one direction. Fiber to free space isolators, for output from a master oscillator power amplifier (MOPA) system, is commercially available at 50 W [71]. Currently, the limit for commercially available high-power isolators occurs around 50 W in the case of fiber to fiber Isolators. Thus, they are commonly utilized in the nanosecond pulsed fiber amplifier.

2.2.8 Fiber Coupled Acousto-Optic Modulator

Pulsed fiber lasers with nanosecond pulse durations and mill joule pulse energy have many applications in materials processing. Q-switching is generally used to generate optical pulses in an oscillator, which are then amplified in MOPA arrangement to boost their power further. The

Q-switch function is typically implemented by an acoustic-optic modulator (AOM), which can turn off a beam by deflecting it in a different direction. The beam is deflected by a traveling acoustic wave, which is controlled electrically by radio frequency (RF) signal typically at the few tens to few hundreds of MHz. AOM takes to turn a beam on or off is typically 5 to 100 ns, roughly limited by the transit time of the acoustic wave across the beam. When faster control is necessary electro-optic modulators (EOMs) are typically used. Typically, a commercially available fiber coupled AOM Q-switch is limited to 1 W of average power handling and peak power handling of 30 kW. The principle of AOM is shown in figure 2.4. A schematic representation of the ytterbium-doped fiber laser head is shown in figure 2.5.

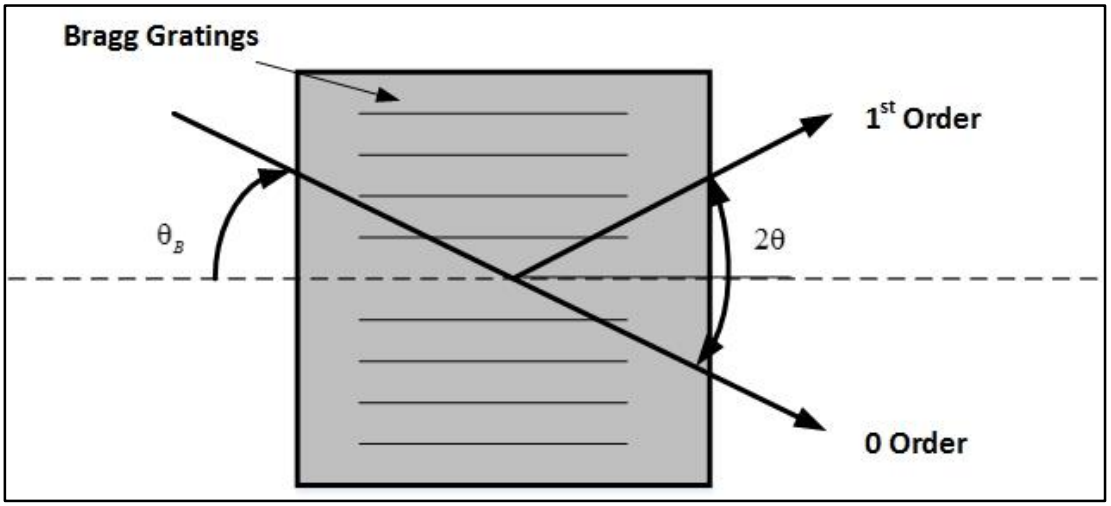

Figure 2.4 Principle of AOM

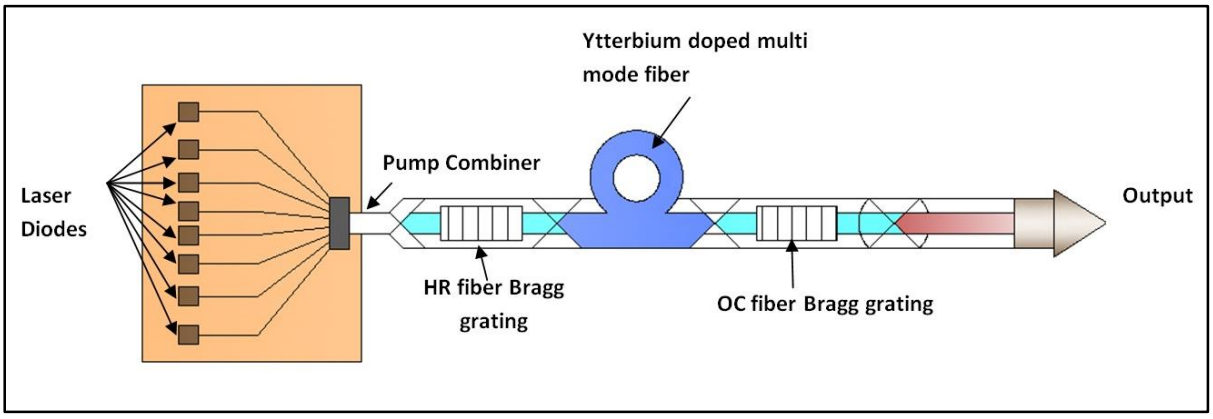

Figure 2.5 Schematic representation of ytterbium-doped fiber laser head [10]

2.3 Fiber Laser Delivery System

The fiber laser delivery system consists of a collimator, beam bender, beam delivery unit, and focusing lens. The details of each aforesaid unit are discussed in the following subsections.

2.3.1 Collimator

A collimator is used to transform the light output from an optical fiber into a free-space collimated beam where the fiber end is firmly fixed at a distance from the lens which is approximately equal to the focal length. Fiber optic collimators are available in different collimated beam sizes, which results in different values of the focal length, i.e., larger collimated beams need to be both longer and larger in diameter.

For multimode fiber laser systems, the collimated beam size depends on the launch conditions as well as bending of the fiber. The schematic diagram of a collimator and the photographic view of the collimators are shown in figure 2.6 and 2.7, respectively. In the present set up, the beam diameter at the collimator end is 9 mm.

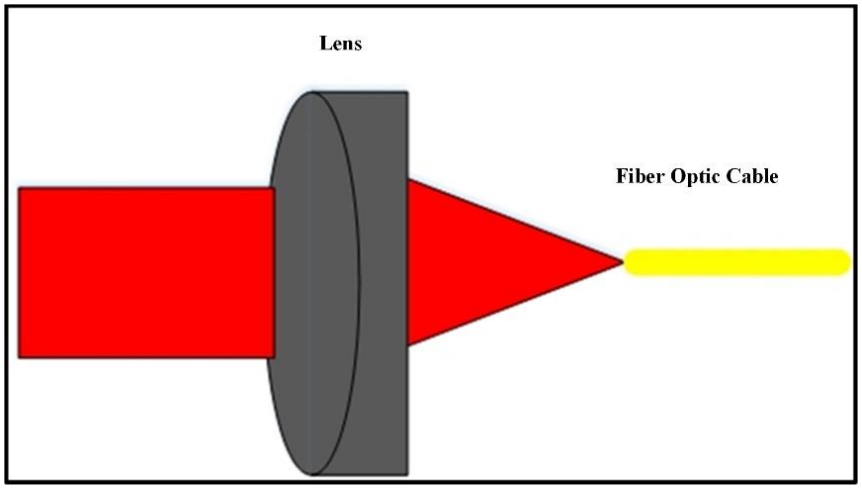

Figure 2.6 Schematic diagram of the collimator

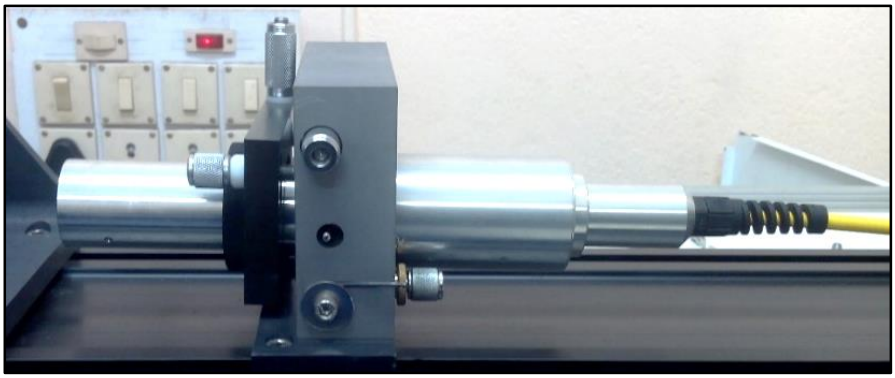

Figure 2.7 Photographic view of the collimator

2.3.2 Beam Bender

After the collimator, a beam bender with 100% reflectivity is placed at an angle of 45º with the horizontal plane so that the laser can be perpendicular to the focus lens. At the top of the beam bender, a charge coupled device camera (CCD) is placed which is further connected to a CCTV. In figure 2.8, the photographic view of a beam bender is shown.

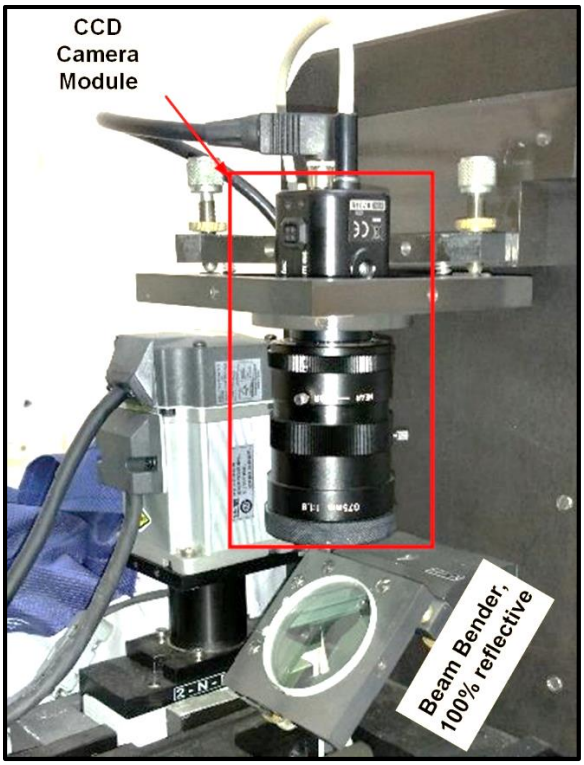

Figure 2.8 Photographic view of beam bender

2.3.3 Beam Delivery Unit and Focusing Lens

The laser finally propagates through an F-θ lens of 71 mm diameter of the focusing lens, which is protected by a nozzle for preventing against dust and other contaminations. The F-θ lens is commonly used in laser marking, engraving, and cutting systems. The spot diameter of the fiber laser beam is 21 µm. The laser beam falling on the surface of the focusing lens has to be précised and appropriately aligned. If the center of the lens does not coincide with the beam center, then the beam that will pass through the lens will not be linear, resulting in low energy of the laser beam and less micro-machining efficiency. CCTV and CCD camera are the two units used for focusing as shown in figure 2.1. At the top of the laser head, the CCD camera is placed in order to capture the image during the operation of the laser micro-machining. Further, the beam should also be focused on the surface to receive optimum micro-machining operations. The function of the CCTV is to adjust the position of the focused beam on the workpiece. This device is connected to the CCD camera to obtain a précised laser beam focusing condition. The laser beam is appropriately focused for the proper utilization of the energy of the laser beam on the workpiece surface. Thus, the focal point position of the laser beam should be adjusted properly. A CNC controlled arrangement is provided in the experimental setup, in order to effectively adjust the focal point of controlling the lens movement position along the Z axis. Figure 2.9 represents the photographic view of the F-θ lens.

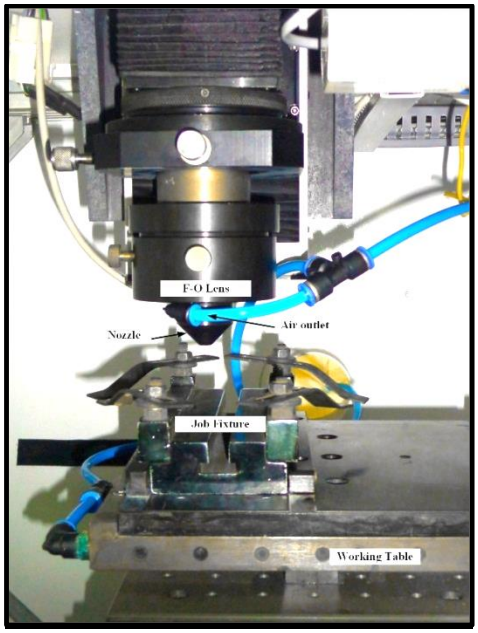

Figure 2.9 Photographic view of beam delivery unit and working table

2.4 Assist Air Supply Unit

Inert gases such as nitrogen, argon, helium, etc., along with compressed air, can be supplied through a co-axial nozzle attached to the beam delivery system depending upon the selection of micro-machining process and materials. The jet flow of assisting gas assists in removing the molten material from the ablated surface to partially overcome re-solidification of the molten material from the micro-machining zone. If any compressed air flow is required, then the supply line must pass through a moisture separator and should be connected further to a pressure regulating valve. It results in the jet flow of dry, pressurized air to the laser micro-machining zone. The laboratory setup has a vacuum job fixture which can hold a workpiece up to 1 mm of thickness when the compressed gas pressure is 6 kgf/cm^2. A moisture separation unit is also attached to the air compressor for the removal of the moisture from the gas. Figure 2.10 shows the photographic view of an air compressor with a moisture separator.

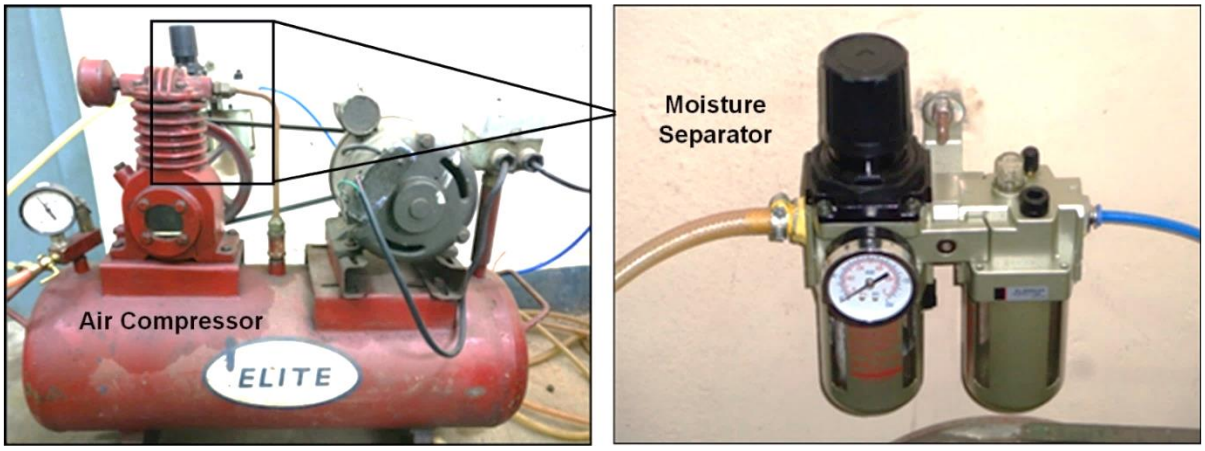

Figure 2.10 Photographic view of an air compressor with moisture separator.

2.5 CNC Controller for X–Y–Z Movement

A CNC controller unit not only controls the movement of the worktable along the X-Y axis but also controls the movement of the laser nozzle along the Z axis. Servo motors are attached to each of the axes and also connect to the servo interfacing unit. This servo controller is connected to the computer system (interface software-I mark plus) by which the axis movements of the X–Y worktable are controlled. If any movement of the X, Y or Z axis is required, then the computer system sends a command to the servo interfacing unit which is followed by receiving a command for the respective servo motor movement in the specific directions. The axis of the fiber laser system can be governed by either CNC based motor system or galvanometer type motor system,

depending upon the applications of the fiber laser systems. For marking and scribing applications, a galvanometer type system is most preferable. In contrast to the system described above, a CNC based system is well recognized for cutting, drilling, and various micro-machining applications

The software interfaced with CNC laser system has provisions to coordinate the operation of the laser beam supply, motion control of workstation, etc. In the present system, I mark, gyro and Q-Saw software are utilized for various micro-machining operations, i.e., micro-cutting, micro-drilling, marking, surface texturing, etc. I mark software is mainly utilized for CNC programming, whereas the other two software described above is for setting the depth of cut and cutting angle.

2.6 Development of Preheating Setup

Preheating of a workpiece is required before and also during laser beam micro-machining operation for the removal of internal stress, minimization of thermal strain along with the detrimental effect of heat affected zone (HAZ) without affecting the mechanical strength of the material.

In the present research work, a preheating setup has been developed in order to preheat the workpiece material along with continuous heating of the material during laser micro-machining process. As the workpiece is preheated to elevated temperature, a considerable amount of reduction of heat affected zone (HAZ) and re-solidification layer occur. The importance of preheating setup is yet to be tried out for micro-machining application. The objective of developing preheating setup is to carry out fiber laser micro-machining at elevated temperature. Further, elimination of the moisture and contaminants present in the workpiece along with the reduction of the thermal gradients of the machining zone to non-machining zone. Besides, the preheating setup is developed to achieve uniform micro-cutting surface at elevated temperature, and reduction of the shrinkage stress, cracks from the micro-machining zone. Finally, to carry out a comparative study of fiber laser micro-machining with and without preheating setup.

2.6.1 Details of Preheating Setup

The preheating setup consists of an electric heater and digital temperature controller for controlling the temperature of the electric heater, as shown in figure 2.11. Digital temperature controller unit provides controlled power to the electric heater, which further provides

temperature feedback to the digital temperature controller unit. The digital temperature control unit is governed by signal processing unit, controller, and sensor. The bed of the preheating setup is made of aluminum, which allows a maximum heating up to 550°C. Under the heating coil, an insulator is also placed. The heating rate for the developed preheating set up is 10°C/min, and the variation of actual temperature from the desired temperature is around +4°C. After the end of fiber laser micro-machining operation at the elevated temperatures, the work-piece is allowed to cool from the elevated temperature to room temperature in an atmospheric condition. The photographic view of the digital controller is shown in figure 2.12. Figure 2.13 showcases the photographic view of the electrical heater module.

The workpiece is mounted on the preheating setup, which is fixed on the X-Y table of the fiber laser machining setup for the movement along with two mutually perpendicular directions as shown in figure 2.14. The specifications of the preheating system are given in table 2.2.

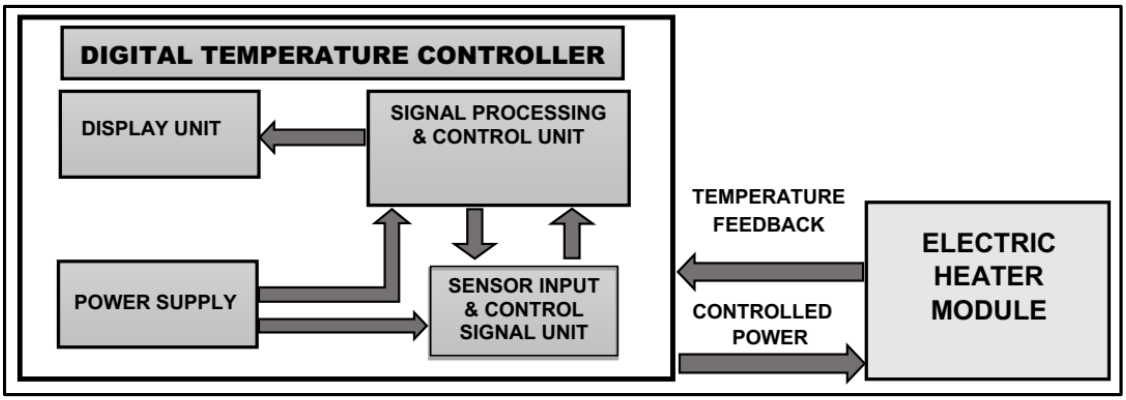

Figure 2.11 Schematic diagram of the preheating setup

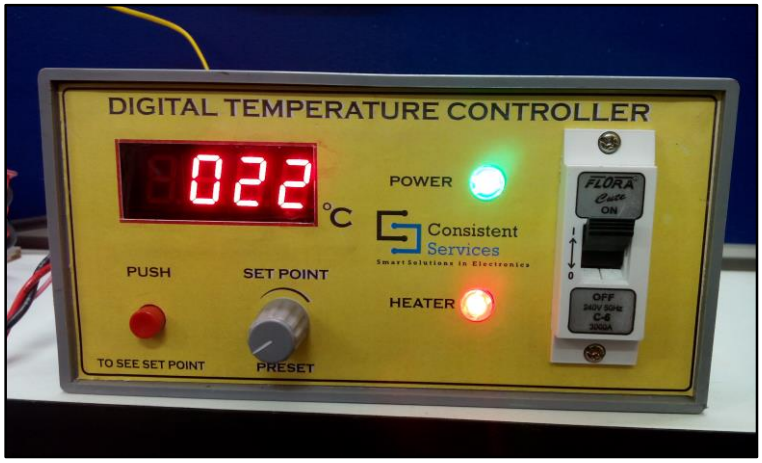

Figure 2.12 Photographic view of digital temperature controller

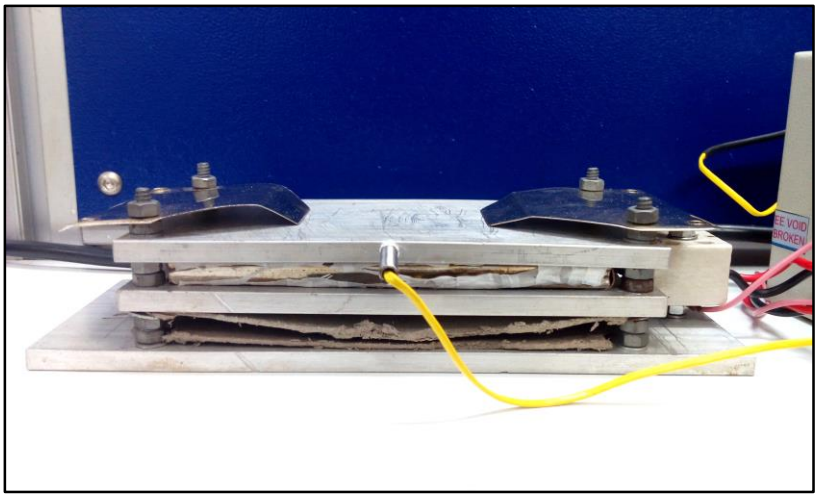

Figure 2.13 Photographic view of electrical heater

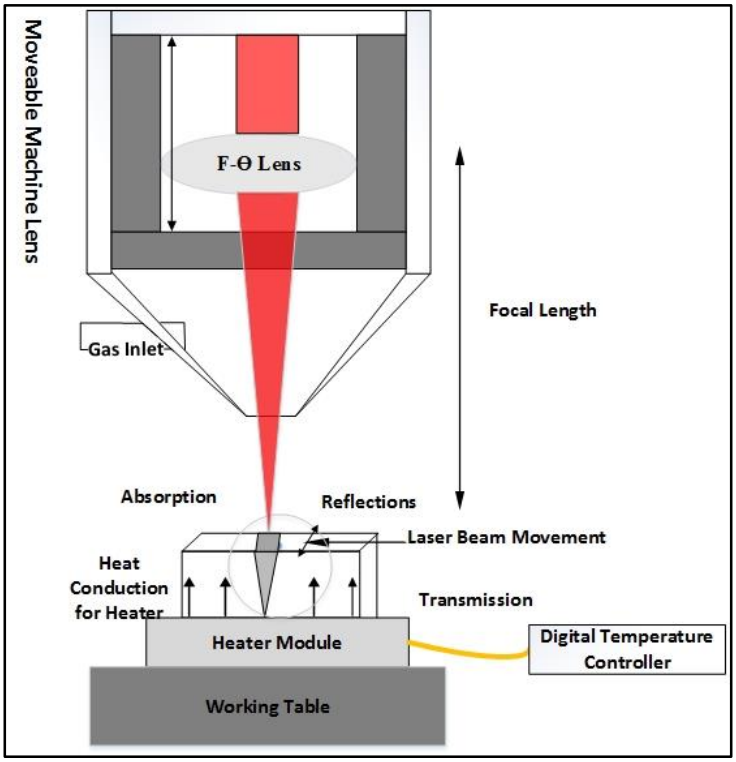

Figure 2.14 Schematic diagram of fiber laser beam irradiation on a workpiece with preheating setup

Table 2.2 Specifications of the preheating system

Descriptions	
Input	0 – 230v A.C 5A.
Output	0 – 230v A.C
Dimension of Base	8X3X0.2362 (inch) Base only & rest part 6X3X1.7632 (inch).
Maximum Temperature	550°C
Power	1kW

The experimentation has been planned to utilize the fiber laser machining set up with and without preheating setup for conducting successful research analysis to select process parameters and their ranges to derive useful research findings during fiber laser micro-machining on different engineering materials such as PMMA, Ti-6Al-4V, 316L, quartz and Hastelloy C-276.

3. EXPERIMENTAL INVESTIGATION INTO FIBER LASER MICRO-CHANNELING ON PMMA

3.1 Introduction

Polymethyl methacrylate (PMMA) in one of the widely used amorphous thermoplastics material, utilized for various biomedical applications. PMMA [CH_2–C (CH_3) $COOCH_3$], can also be used as a substitute for optically transparent glass. Processing of PMMA by the laser beam is widely needed, especially for different micro-machining applications. The literature survey of laser beam micro-channeling on PMMA signifies that very few research works have been carried out in the area of fiber laser micro-channeling of PMMA.

Considering the objectives of the present research work, the experimental observations and studies have been planned for conducting fruitful research analysis for deriving useful research findings of fiber laser micro-machining on PMMA. The preliminary planning has been made for the selection of process parameters and their ranges during the generation of micro-channels on PMMA.

All the experiments are carried out with the aid of a diode-pumped CNC based fiber laser system. The process parameters on fiber laser micro-channeling are laser power, pulse frequency, duty cycle, scan speed, and number of passes. The responses considered for the experimentation are cut width, depth, and HAZ width. Extensive trial works have been carried out to find out the ranges of the process parameters. The mathematic models have also been established to correlate the responses of laser micro-channeling on PMMA with the considered process parameters. Based on the developed mathematic models, the effects of process parameters on the responses have been analyzed with the aid of response surface methodology (RSM). The optimization analysis of the responses has been carried out to determine the optimal combination of process parameters during fiber laser micro-channeling on PMMA material.

3.1.1 Properties and Applications of PMMA

PMMA over the years has attracted considerable attention in orthopaedics and biological applications for the analysis of DNA. A PMMA workpiece of dimensions 50X50X1.5 mm is utilized for the fabrication of micro-channels utilizing multi-diodes pumped fiber laser. The detail of the specifications of PMMA workpiece is given in table 3.1.

Table 3.1 Properties of PMMA [61]

Properties	Values
Density	1.17-1.20 g/cm³
Refractive Index	1.4914 at 587.6 nm of wavelength
Max Water Absorption Ratio	0.3-0.4 % by weight.
Melting Point	160°C (320° F).
Specific Heat	1466 J/Kg K
Thermal Conductivity	0.167-0.25 W/m-k
Elongation	2-10 %
Thermal Expansion	72-162 ×10^{-6} /K
Energy Content	97-105 MJ/Kg

3.1.2 Mechanism of Material Removal during Fiber Laser Micro-Machining of PMMA

When the fiber laser irradiates on the PMMA top surface, some amount of radiation energy is absorbed by PMMA while some amount is reflected. When the pulse energy threshold value is overcome, PMMA vaporizes immediately. In the case of a single-pass micro-channeling of PMMA, it is assumed that the laser beam moves with a constant scan speed on a flat PMMA sheet. The optical intensity (I_1) of the Gaussian laser beam at any location (x, y) for the centre of the beam is determined as:

$$I_1 = I_{01} e^{\frac{-2(x^2+Y^2)}{w^2}} \quad \ldots[Eq^n 3.1]$$

Where, $I_{01} = 2P_1/\pi\, w^2$ is termed as the intensity at the beam center, P_1 is the laser power and w is the beam waist diameter. As the number of passes will go on increasing, the penetration rate along the micro-channel depth is increasing, as shown in figure 3.1.

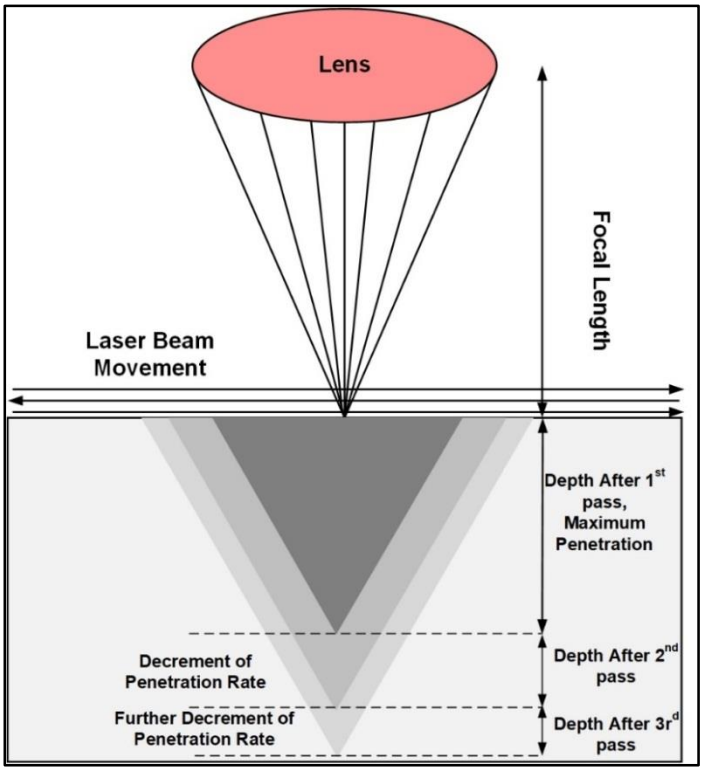

Figure 3.1 Schematic diagram of fiber laser micro-channeling process

Further, the material removal process can also be assumed as a sublimation of from the solid PMMA state to vapor without melting. In the photo-thermal ablation of PMMA, the temperature of the irradiated spot increases at a faster rate, when the pulse energy is increased. However, due to the low glass transition temperature (104°C), the molecular structure of PMMA remains in a definite shape, while mechanical properties would remain brittle. Exceeding the glass temperature, PMMA starts to melt instantaneously. Within the liquid phase, the decomposition of the molecular structure commences by reaching the temperature of decomposition (226-256°C). In this range of temperature, PMMA ($C_5O_2H_8$) decomposes into carbon dioxide (CO_2), monomer MMA (methyl methacrylate) units, carbon monoxide (CO) as well as water (H_2O) [72]. The alteration of different states of PMMA does not only depend on the material property, e.g., heat capacity or heat conduction, but also depends on the laser power and scan speed.

Further, as the absorptivity of PMMA is low in the infrared (IR) region owing to the chemical bond structure, thermal dissipation is higher in comparison to transferring energy into the material removal. Owing to the low thermal conductivity of PMMA, the heat gets accumulated inside the adjacent layer, which further generates bulges and heat affected zone (HAZ). Non-

uniformity of the micro-channels, as well as the formations of micro-cracks, are observed at a low laser power of 4 W and a high laser power of 20 W respectively as shown in figure 3.2 (a) and (b). Figure 3.3 represents the material removal mechanism during fiber laser micro-channeling of PMMA.

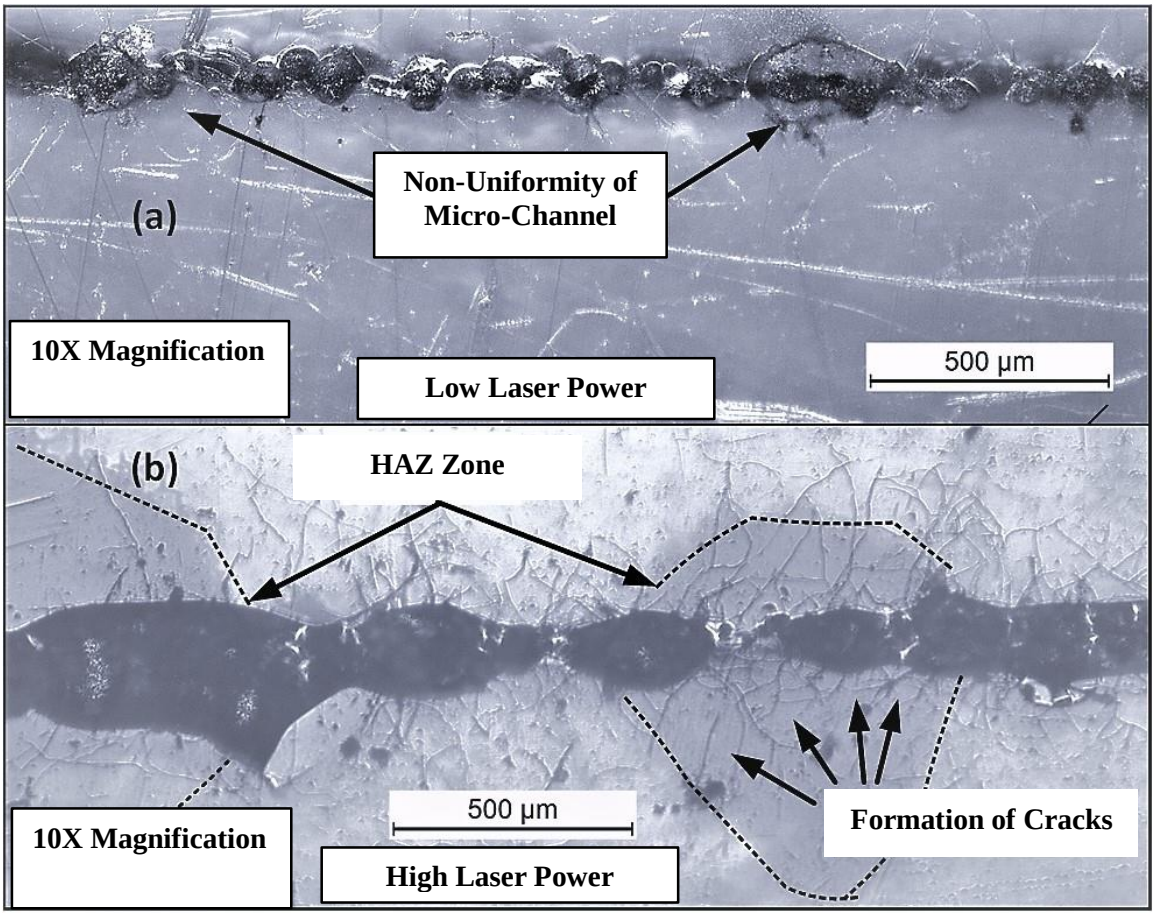

Figure 3.2 Microscopic view of fiber laser generated micro-channels

(a) At laser power of 4 W; (b) At laser power of 20 W; when other parameters are kept at duty cycle of 90%, pulse frequency of 50 kHz, scan speed of 300 mm/sec and single pass [61]

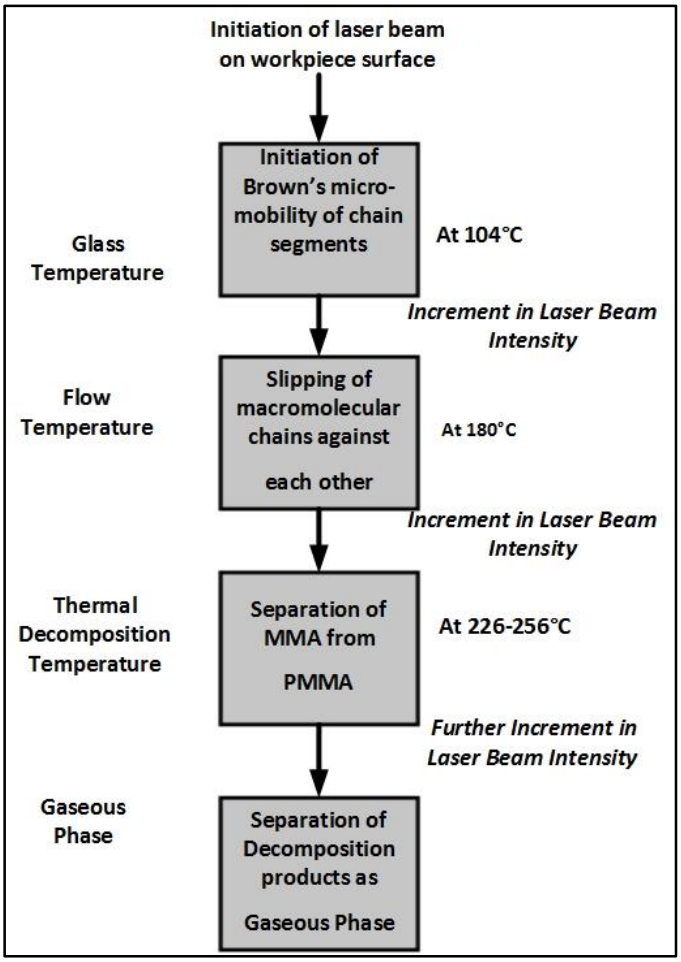

Figure 3.3 Material removal mechanism during fiber laser micro-channeling of PMMA

3.2 Experimentation

Depending on the micro-machining process, the responses are varied. For fiber laser micro-channeling operations, the considered responses are cut width, depth, HAZ width, and aspect ratio of the fabricated micro-channels or micro-grooves. Figure 3.4 represents a schematic diagram of a laser beam micro-machining process parameters and the responses.

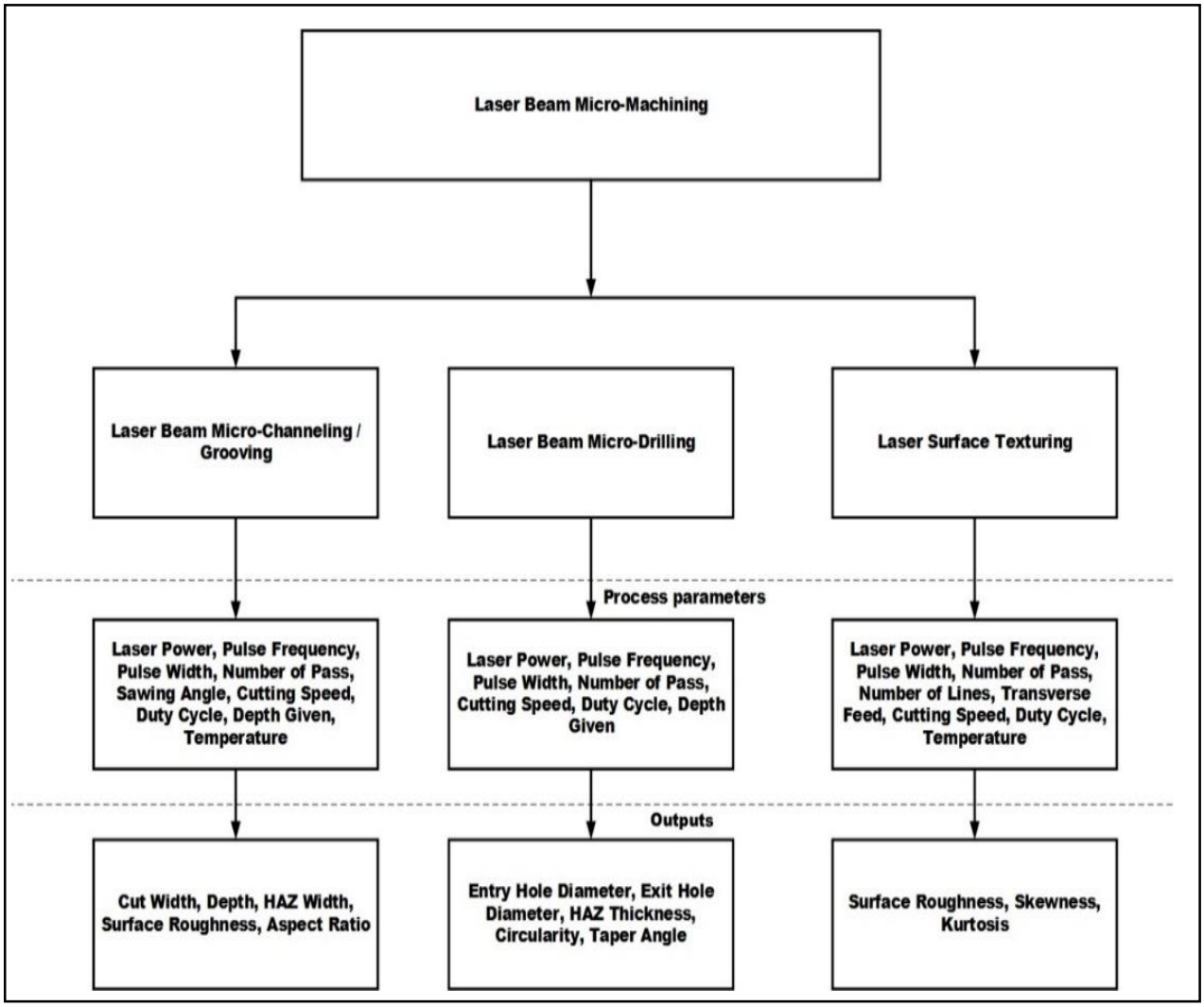

Figure 3.4 Process parameters and responses for laser micro-machining processes

3.2.1 Selection of the Process Parameters

To analyze the geometry of fiber laser generated micro-channels on PMMA, various process parameters such as laser power, duty cycle, pulse frequency, number of passes, and scan speed are considered. The detail of each process parameters are as follows:

(i) **Laser Power:** Laser power indicates the instantaneous power that is irradiated on a given workpiece for melting and evaporation of the molten material. It is usually the average power of the system.

(ii) **Duty Cycle:** The time duration of the laser pulse is combined with both the rise and fall. The pulse length is generally described as the width of the curve at half height. Duty cycle is considered as the percentage of the cycle time.

(iii) **Pulse Frequency:** Pulse frequency is the number of pulses per second (s^{-1} or Hz) and is the inverse of temporal pulse spacing. The following equation (equation 3.2) gives the relationship between laser power, peak power, duty cycle, and pulse frequency:

$$\text{Peak Power} = \frac{\text{Laser Power}}{\text{Pulse Frequency} \times \text{Duty Cycle}} \quad \ldots[\text{Eq}^{\text{n}}3.2]$$

(iv) **Number of Passes:** The number of passes is a unit less parameter which defines how many times the laser beam will move to and fro in a specific length for a specific geometrical feature.

(v) **Scan Speed:** Scan speed is defined by the speed at which working table transverses at X and Y directions. The unit is given at mm/sec. Scan Speed is controlled by a CNC controller system for each of the axis.

3.2.2 Measurements of Responses

The selected responses are cut width, depth, HAZ width, and aspect ratio of the micro-channels. The details of each response are given below:

(i) **Cut Width:** Cut width is preferred choice of response during fabrication of micro-groove or micro-channel in a given material. Cut width dimensions are measured by Leica optical microscope at 10X, 20X, and 50X optical lenses. The cut width dimensions are measured at four different places of the micro-channeling zones, following which; four values are averaged in order to obtain the cut width dimensions.

(ii) **Depth:** The depth of the channel is another response of laser micro-channeling process. Using Gaussian mode of the fiber laser beam, a channel is formed at the edge during micro-channeling. A schematic representation of micro-channel at the edge of PMMA is shown in figure 3.1. As shown in figure 3.1, the point of interaction between laser and workpiece to the length of laser beam penetration after the number of passes of 3, is considered as the depth dimension. The line arrow in figure 3.1 indicates the length of the depth dimension. The depth dimensions are measured with a 50X optical lens of the Leica optical microscope.

(iii) **HAZ Width:** The width of the heat affected zone at both side of the micro-channel during fiber laser micro-channeling process is depicted in figure 3.5.

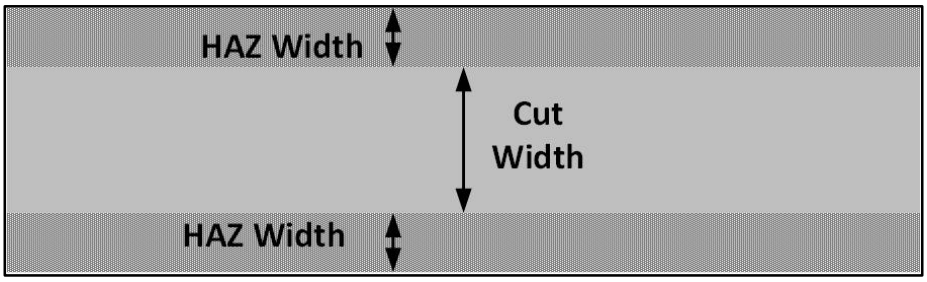

Figure 3.5 Schematic representation of the HAZ width

(iv) **Aspect Ratio:** It is a ratio of depth to the cut width of the micro-channel on PMMA.

The entire set of data is plotted graphically with the aid of statistical software (Origin) for the analysis.

3.3 Preliminary Study of Fiber Laser Micro-Channeling on PMMA

The primary focus of the experimental study is aimed to generate high aspect ratio micro-channels along with less HAZ. From the Trial experiments and previous research works, the process parameters are selected. All the experiments are conducted in an open atmosphere. All the experiments are carried out in the pulsed mode of operation which leads to high peak power. In the pulsed mode of operation, high peak power is capable enough for producing a sufficient amount of energy. This energy can lead to direct vaporization of PMMA skipping over the melting phase. During this phenomenon, the micro-channel profiles can suffer from several distinct characteristics, i.e., non-uniformity, high roughness, and HAZ.

Another important factor which governs laser micro-channeling quality is spot overlapping of the laser pulses. The micro-channels are found to be continuous and smooth profile when the spot overlapping factor is high. This phenomenon reverts when the spot overlapping is significantly low. The spot overlapping factor can be governed by the combination of pulse frequency, scan speed, and the number of passes. In the present research, only straight cut micro-channels can be obtained, following the beam moves along the straight line, as shown in figure 3.6.

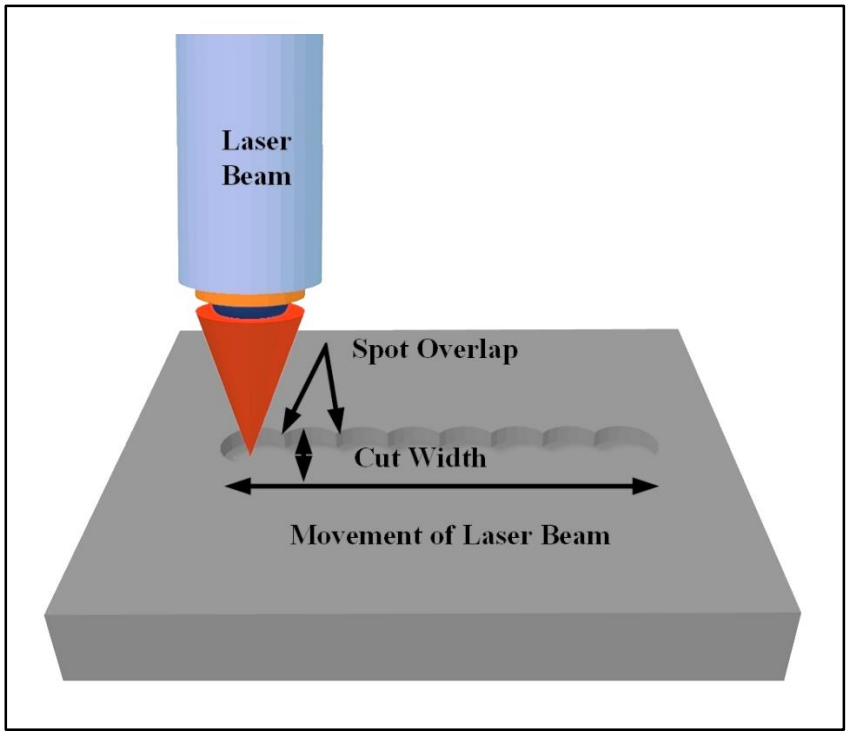

Figure 3.6 Schematic diagram of fiber laser micro-channeling process

All the experiments are carried out in atmospheric conditions, keeping the duty cycle of 90%. Most of the experiments are carried out at considerably high scan speed to reduce the detrimental effect of HAZ. A total of 25 micro-channeling operations are performed in which the entire experimentation was divided into six groups, designed for four process parameters. For each series, a single process parameter is altered, while the other parameters are kept constants to identify its effect on fiber laser micro-channel geometries.

3.3.1 Results and Discussions

As mentioned in the previous discussion, the results of the total of 25 experiments have obtained from the six sets of experiments which include the different level of micro-channeling process parameters. The results of the total of 25 experiments are listed in table 3.2.

Table 3.2 Values of process parameters and observed responses for micro-channel fabrication on PMMA

Process Parameters					Response Criteria			
Exp. No:	Scan Speed (mm/sec)	Laser Power (W)	Pulse Frequency (kHz)	Number of Pass	Cut Width (µm)	HAZ Width (µm)	Depth (µm)	Aspect Ratio
1	50	15	50	1	227.81	52.11	58.03	0.25
2	100	15	50	1	173.29	38.89	35.43	0.20
3	200	15	50	1	104.98	32.89	35.13	0.33
4	300	15	50	1	117.21	53.56	27.90	0.24
5	50	12.5	50	1	177.08	40.99	43.91	0.25
6	100	12.5	50	1	136.00	88.25	43.60	0.32
7	200	12.5	50	1	107.51	27.83	42.22	0.39
8	300	12.5	50	1	65.28	52.78	37.87	0.58
9	50	10	50	1	187.17	28.33	162.71	0.87
10	100	10	50	1	128.63	29.92	32.40	0.25
11	200	10	50	1	112.75	24.76	41.77	0.37
12	300	10	50	1	122.39	58.29	20.60	0.17
13	50	7.5	50	1	97.14	9.71	31.63	0.33
14	100	7.5	50	1	112.72	42.73	37.10	0.33
15	200	7.5	50	1	163.19	57.04	20.58	0.13
16	300	7.5	50	1	125.02	53.32	30.08	0.24
17	10	5	60	1	112.68	28.18	25.63	0.23
18	10	5	70	1	103.66	30.74	29.27	0.28
19	10	5	80	1	106.91	33.99	33.87	0.32
20	10	5	90	1	103.64	35.61	32.93	0.32
21	20	10	70	1	104.74	42.36	62.20	0.59
22	20	10	70	2	123.32	66.13	70.50	0.57
23	20	10	70	3	148.66	264.10	118.75	0.80
24	20	10	70	4	285.61	571.21	667.32	2.34
25	20	10	70	5	187.48	500.79	385.53	2.06

3.3.1.1 Influence of Scan Speed and Laser Power on the Cut Width, Depth, HAZ Width and Aspect Ratio of Micro-Channels on PMMA

Laser micro-channeling characteristics are primarily governed by the combination of the scan speed and pulse frequency. In the present experimental setup, four sets of experiments are carried out by varying scan speed from 50 mm/sec to 300 mm/sec, while keeping pulse frequency and the number of passes at their lowest value, i.e., 50 kHz and 1 respectively. The laser power is also varied from 5 W to 15 W in combination with the varying scan speed, to find out the effect of both laser power and scan speed on the response criteria. The primary objective of this experimental plan is to reduce the HAZ width of the micro-channeling surface. As all the experimenters are carried out under the atmospheric conditions, due to which, some of the molten material cannot be expelled from the micro-channel surfaces. In the final set of experiments, the range of the scan speed is varied from 10 mm/sec to 50 mm/sec with the combination of laser power of 5 W.

It is a well-established fact that high scan speed is associated with reducing HAZ, but on the flipside, it is also known to induce poor micro-channel quality. The pulse width of 90% of the cycle time is kept as a constant for the entire set of experiments. In figure 3.7, the effect of scan speed on micro-channel cut width at different ranges of laser power is shown. Cut width tends to decrease with the increment of scan speed for the laser power of 7.5 W and 12.5 W, as observed in figure 3.7. The decrement of cut width values occurs due to the low laser-material interaction time at high scan speed. For the other ranges of laser power, i.e., 10 W and 15 W, cut width tends to decrease continuously up to 250 mm/sec.

Further increment in cutting speed leads to an increment in cut width values. The spattering of molten material at the edges of the micro-channel during higher scan speed combined with a laser power of 10 W and 15 W causes an increment in the cut width dimension. Non-uniformity of micro-channels, as shown in figure 3.8, is also a prime contributor in the increment of cut width dimension at higher ranges of scan speed.

At low scan speed of 50 mm/sec for different settings of average power ranges from 10 W to 15 W, high level of spot overlapping and continuous power density per unit length are observed. The phenomena described above lead to a significant reduction of spattering, and re-solidification of the molten material as well as an increment in laser-material interaction time. As a result, cut width of the micro-channels tends to increase at the lower ranges of scan speed for the laser power of 10 W, 12 W and 15 W. Re-solidification of the molten material is the prime contributor that affects the micro-channel dimensions in the form of taper-shaped micro-channels. When re-solidification is low at low scan speed, better micro-channeling quality in term of waviness, as well as an increment in the cut width dimensions, are observed.

Another critical factor that has to be taken note of is that, during the micro-channeling operations at a considerably high laser power of 10 W, 12.5 W and 15 W with the combination of low pulse frequency, work-material is burnt considerably which further enhanced the fact of photo-thermal ablation of PMMA. When the range of scan speed is varied from 10 mm/sec to 50 mm/sec, laser-material interaction time, as well as the material removal rate, is increased compared to the other four sets as mentioned earlier of experimental settings. Thus, at a low average power of 7.5 W, the cut width of the micro-channels is increasing up to 200 mm/sec and follows by a gradual decrement in the cut dimensions. In the entire low settings of scan speed, i.e., 50 mm/sec, the waviness of the micro-channel profiles is less as shown in figure 3.9.

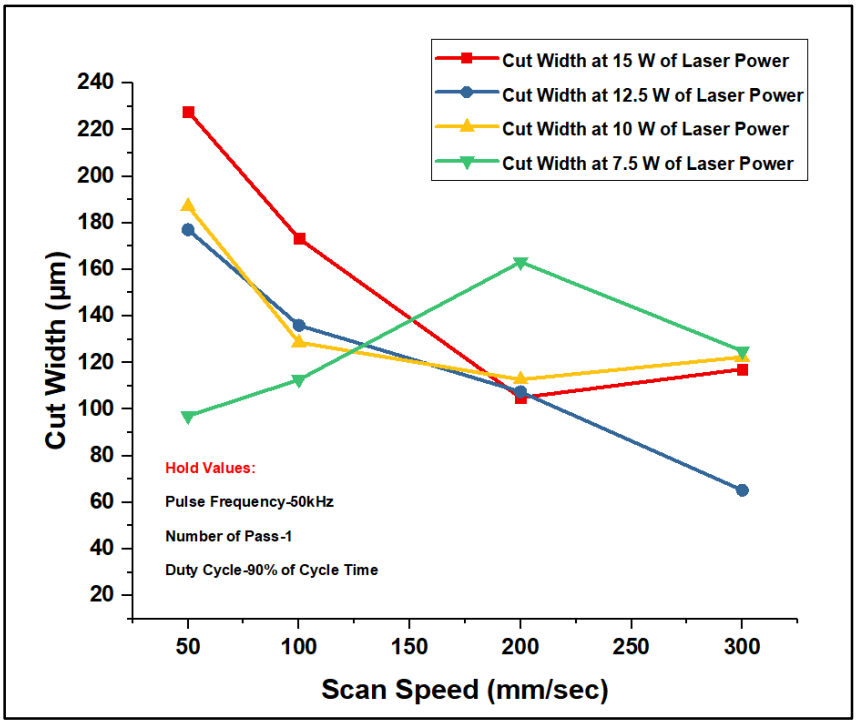

Figure 3.7 Effect of scan speed at varying laser power on the cut width of micro-channel

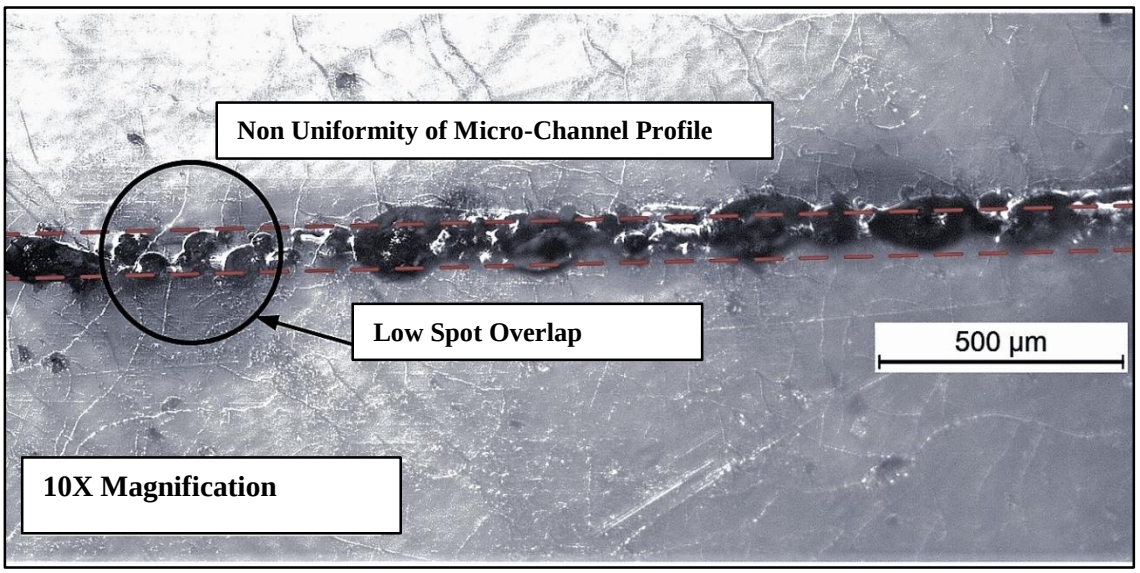

Figure 3.8 Microscopic image of PMMA micro-channel associated with non-uniformity at scan speed of 50 mm/sec of, laser power of 7.5 W, pulse frequency of 50 kHz and single pass [61]

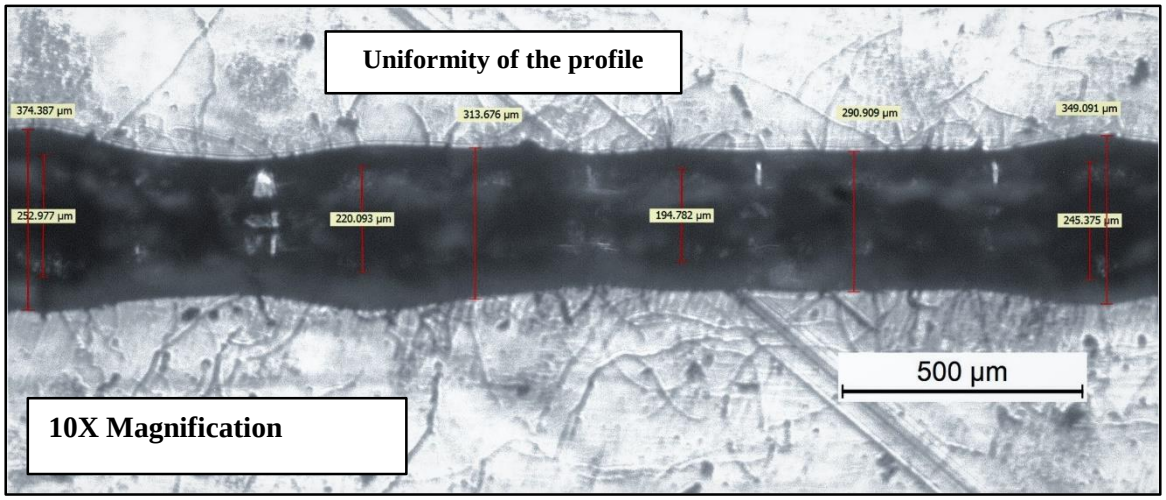

Figure 3.9 Microscopic image of PMMA micro-channel during scan speed of 50 mm/sec, laser power of 15 W, pulse frequency of 50 kHz and single pass [61]

Figure 3.10 represents the variation of depth dimensions for different ranges of scan speed at different laser power. The depth of the micro-channels tends to decrease, while the scan speed goes on increasing. From figure 3.10, it is observed that the variation of depth of micro-channel on PMMA with scan speed is very less. Larger depth dimension is achieved at the combination of 50 mm/sec and 10 W for scan speed and laser power respectively. At laser power of 10W, due to less burning and spattering at 50 mm/sec of scan speed, the higher penetration rate is achieved. At laser power of 12.5 W and 15 W, the laser penetration rate decreases due to the effect of burring and spattering. As a result of this phenomenon, larger depth dimensions are not observed at higher laser power combined with low scan speed. Besides, in some of the experiments, the depth of the micro-channels is found to be significantly low because all the micro-channeling operations are carried out by a single pass with the combination of low peak power. Low peak power is generated due to pulse cut width of 90% of the cycle time. When the scan speed increases, it causes low spot overlapping, low power density, and less laser-material interaction time. As a result of which the spattering effect is evident in the micro-channeling quality, as shown in figure 3.11.

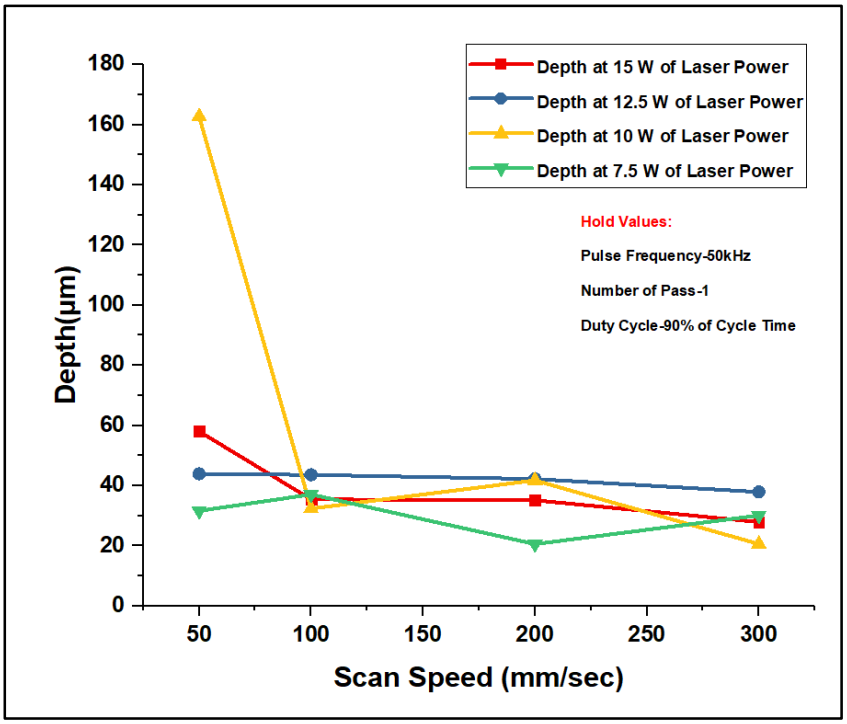

Figure 3.10 Effect of scan speed at varying laser power on the depth of micro-channel

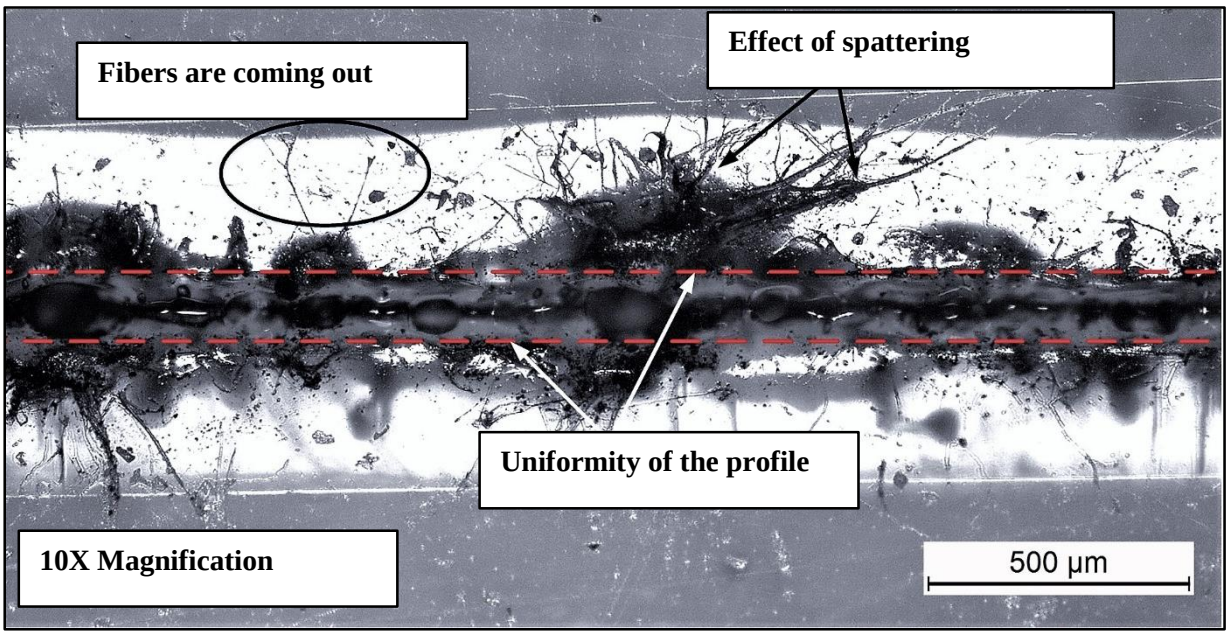

Figure 3.11 Microscopic view of PMMA micro-channel due to spattering effect

Figure 3.12 showcases the variation of HAZ width dimensions for scan speed at different ranges of laser power. The lower dimension of HAZ width is achieved at the scan speed of 50 mm/sec

with the combination of laser power of 7.5 W. The higher dimension of HAZ width dimension is observed at the high laser power of 15 W combined with scan speed of 100 mm/sec. The large HAZ width dimension is due to higher thermal energy in combination with an excessive amount of spattering around the periphery of the micro-channel zone. However, a steep fall of the HAZ width dimension is observed in the range of scan speed of 100 mm/sec to 200 mm/sec.

Further increment of scan speed results into lesser laser beam penetration rate and lower laser material interaction time and causes in the decrement of HAZ width dimension. The low range of laser power fails to generate a high amount of laser pulse energy incident on the surface of PMMA. As a result, HAZ width dimensions are considerably lower at the low setting of laser power. As the spattering phenomenon is lowered along with increment in laser spot overlap factor during low ranges of scan speed, HAZ width reduces significantly. Those phenomena mentioned reverse with the increment in laser power and cutting speed. Therefore, HAZ width dimensions tend to reduce with the increase of scan speed, but tend to increase after a certain point of time is observed, due to the excessive spattering of the molten material from the micro-channeling surfaces. The spattering effect also attributed to the waviness and non-uniformity of the micro-channel profiles.

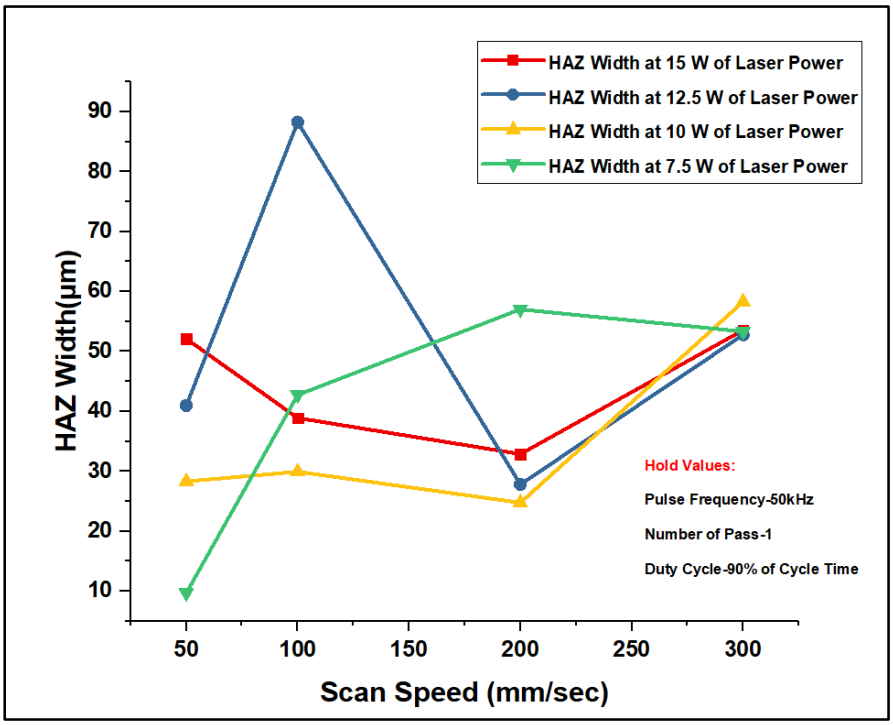

Figure 3.12 Effect of scan speed at varying laser power on the HAZ width of micro-channel

The variation of the aspect ratio of the fabricated PMMA micro-channel concerning laser power and scan speed is shown in figure 3.13. The higher aspect ratio of the micro-channels is observed with the combination of the laser power of 10 W and scan speed of 50 mm/sec. The high aspect ratio is due to the lower amount of spattering phenomenon and low thermal energy at laser power of 10 W as compared to higher laser power. At laser power of 12.5 W, the laser peak power is sufficiently high to achieve higher increment in depth dimension compared to the increment of cut width dimension. Thus, higher increment in depth dimension combined with low increment in cut width dimension results in a high aspect ratio of micro-channel on PMMA. For laser power of 15 W and 12.5 W, micro-channel aspect ratios are gradually increasing due to the higher penetration rate for high thermal energy. However, due to high thermal energy and high scan speed, cut width dimensions suffer both from HAZ and spattering phenomenon. The reverse phenomenon is observed for laser power of 7.5 W and 10 W due to low thermal energy and less laser-material interaction time. Figure 3.14 represents the micro-channel image at 50X magnification, fabricated at a scan speed of 200 mm/sec, laser power of 15 W, a pulse frequency of 50 kHz, and a single pass.

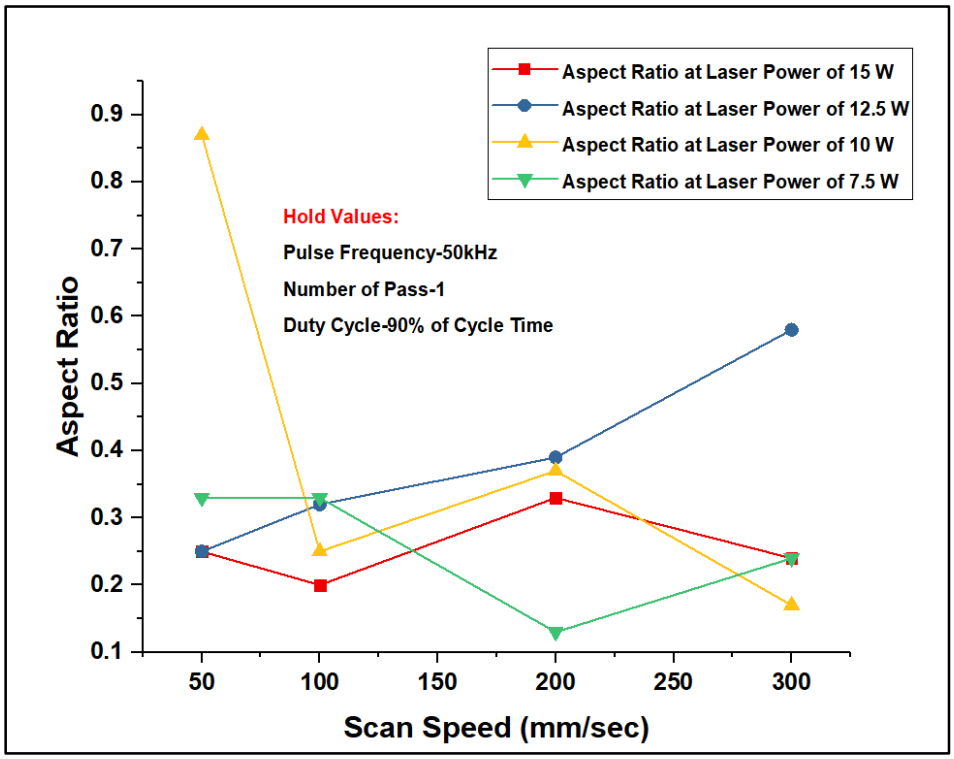

Figure 3.13 Effect of scan speed at varying laser power on the aspect ratio of the micro-channels

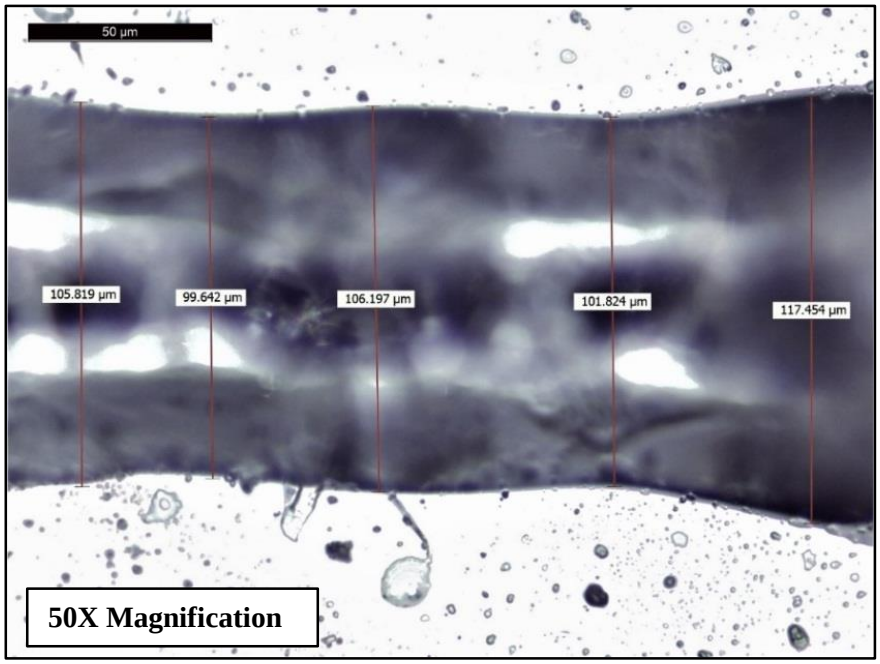

Figure 3.14 Microscopic image of PMMA micro-channel at 50X magnification

3.3.1.2 Influence of Pulse Frequency on the Cut Width, Depth, HAZ Width and Aspect Ratio of Micro-Channels on PMMA

Figure 3.15 represents the effect of pulse frequency on cut width, depth, and HAZ width dimensions of the fabricated micro-channels on PMMA. In the present set of experiments, the lower laser power is considered, i.e., 5 W, as compared to the previous set of experiments due to the effect of spattering and the high thermal energy associated with higher laser power. This is done to observe the find out the effect of lower pulse energy and lower peak power on the response criteria. Besides, change in pulse energy does not contribute change in pulse energy, except decrement of laser peak power with higher pulse energy. The other constant parameters are scan speed of 10 mm/sec and number of pass of 1. From figure 3.15, it is observed that cut width tends to decrease with the increment in pulse frequency. The changes in both depth and HAZ width dimensions for pulse frequency are considerably low due to low laser beam peak power (Equation 3.1). Besides, both the depth and HAZ width dimensions are found to be comparatively low for changes in pulse frequency as compared to the changes in laser power and scan speed.

This set of design is considered because, at low scan speed, the high spot overlapping is instrumental in attaining continuous micro-channel profiles. As the laser power is not high, the laser peak power is reduced significantly.

Moreover, when the pulse frequency increases, it also reduces the peak power to the micro-channeling zones, keeping pulse energy as constant. The number of repetitive pulses is also increased simultaneously with high settings of pulse frequency. It is important to note that, when multiple laser pulses are directed into PMMA sheets, the incubation effect might occur. This phenomenon occurs not only due to the poor absorptivity of PMMA in IR wavelength but also due to the first pulse of laser light. This first pulse of laser light can alter PMMA chemically, leading to change in response to the second pulse. In this set of experiments, some of the experimental results showcase that some of the micro-channeling operations are not able to reach beyond the threshold energy, which resulted in a reduction of the depth dimensions. Besides, low peak power, i.e., the pulse width is at 90% of the cycle time, has contributed to low depth dimensions of PMMA micro-channels.

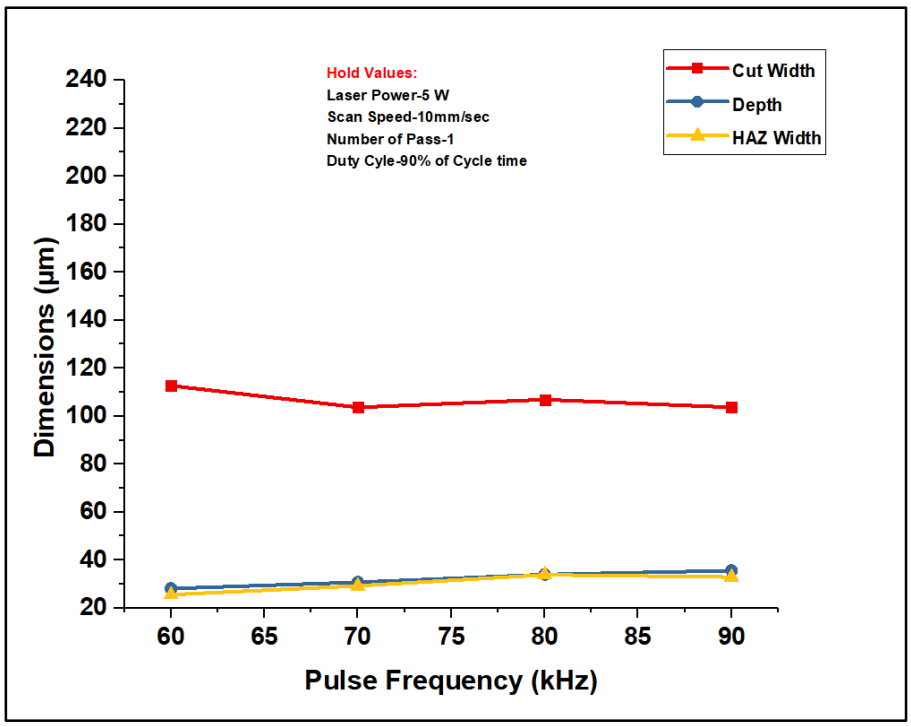

Figure 3.15 Effect of pulse frequency on the cut width, depth, and HAZ width

Figure 3.16 showcases the variation of the micro-channel aspect ratio due to the change in pulse frequency. Cut width dimensions tend to increase more than that of the depth dimension at low ranges of pulse frequency. However, at higher pulse frequency, the depth dimensions tend to increase more than the cut width dimensions due to the higher number of laser pulses. As a result, the aspect ratio of the micro-channel is higher during increment in pulse energy.

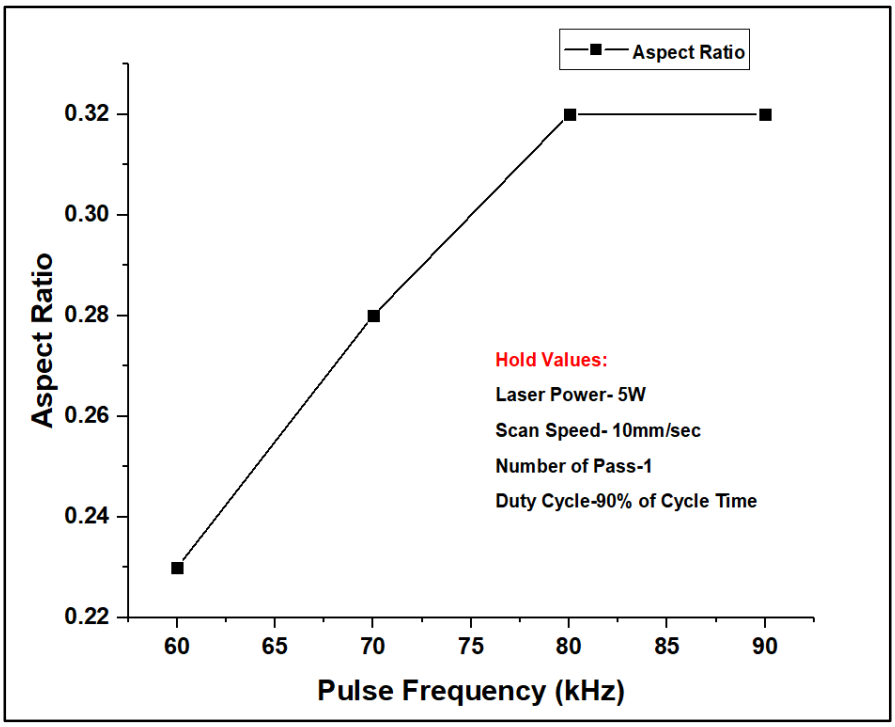

Figure 3.16 Effect of pulse frequency on the aspect ratio of PMMA micro-channels

3.3.1.3 Influence of Number of Passes on the Cut Width, Depth, HAZ Width and Aspect Ratio of Micro-Channels on PMMA

In photo-thermal process, the thermal conductivity in PMMA micro-channeling zone determines the micro-channeling quality. In this final set of experiments, the scan speed of 20 mm/sec and laser power of 10 W are kept as constant process parameters. Pulse frequency is set at a moderate value, i.e., 70 kHz. The primary objective in this set of experimental design is to observe the effect of HAZ width along with the cut width and depth of the micro-channels with the increase in the number of passes from 1 to 5. Figure 3.17 shows the effect of the number of passes on the response criteria of PMMA micro-channels, i.e., cut width, depth, and HAZ width.

From figure 3.17, it is observed that with the increment of the number of passes, a significant rise in the dimensions of cut width and depth of the micro-channels along with HAZ width. The depth of the micro-channels and HAZ width are significantly higher in this set of experiments. In this present set of experiments, significant burning and re-solidification are also observed, which causes the phenomena mentioned above. An increment in the number of passes leads to an increase in laser-material interaction time as well as the striking of the laser beam on the work-piece surface in a repetitive manner during the pulse on time. In addition to that, the length of focus is altered every time as the number of passes is increasing. In addition to that, the scan speed is not comparatively higher as compared to the first set of experiments. As a result, the laser-material interaction time has increased along with the material removal rate considerably.

Along with the increment number of passes, an excess amount of molten material is removed from the micro-channeling surfaces. The molten material is re-solidified on the side-wall of the micro-channels that cannot be expelled due to the absence of inert gas systems in the present machining setup. Interestingly, the waviness of the micro-channel profiles is significantly blemished, although, a thick layer of HAZ surrounded the micro-channeling edges in the form of a black cloud, as shown in figure 3.18. Figure 3.18 indicates the microscopic image of PMMA micro-channel at 10X magnification, generated during scan speed of 20 mm/sec, the laser power of 10 W, the pulse frequency of 70 kHz and the number of pass of 4.

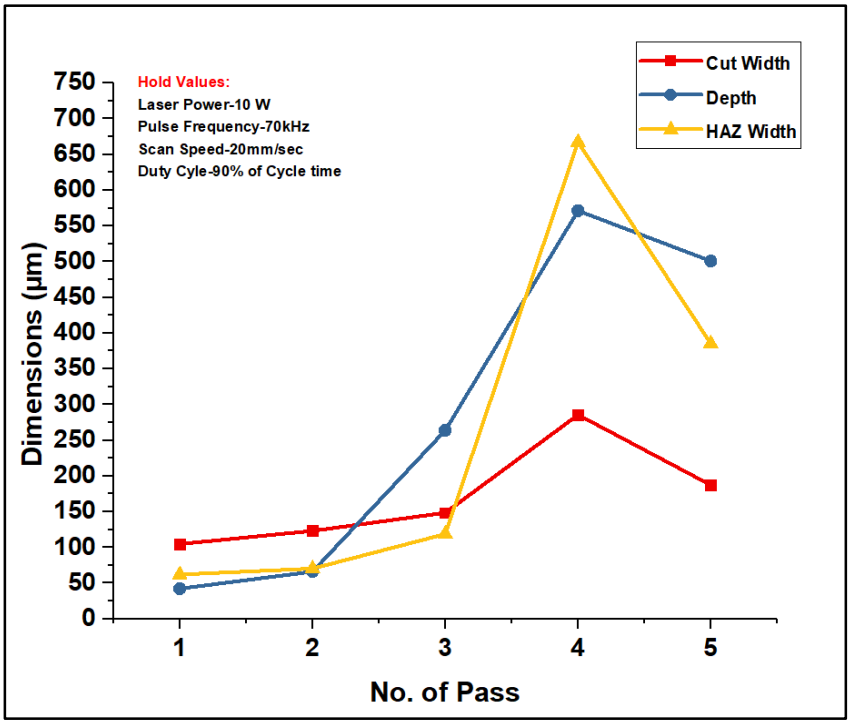

Figure 3.17 Effect of number of pass on the cut width, depth, and HAZ width

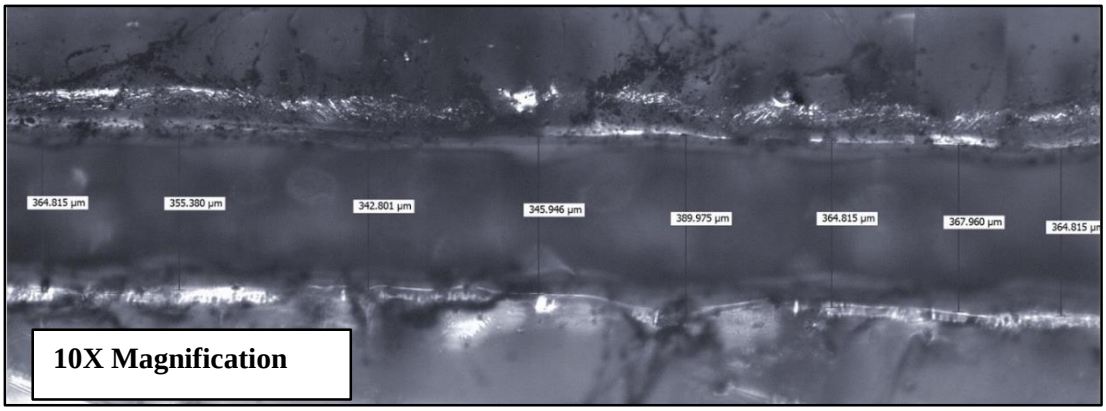

Figure 3.18 Microscopic image of PMMA micro-channel at 20X magnification

Figure 3.19 represents the effect of the number of passes on the aspect ratio of the fabricated micro-channels on PMMA. A steep increment of the micro-channel aspect ratio is observed from figure 3.19, for the variation of the number of passes 1 to 4. As the increment of depth dimensions are comparatively higher compared to cut width dimensions, high aspect ratios of PMMA micro-channels are observed. Further increment in the number of passes, the material removal rate, increases significantly. As a result, higher increment of the depth dimensions is observed compared to the cut width dimensions, for which the micro-channel aspect ratios are increased. However, at the number of passes of 5, re-solidification phenomenon around the micro-channel cause a decrement in the aspect ratio of PMMA micro-channel.

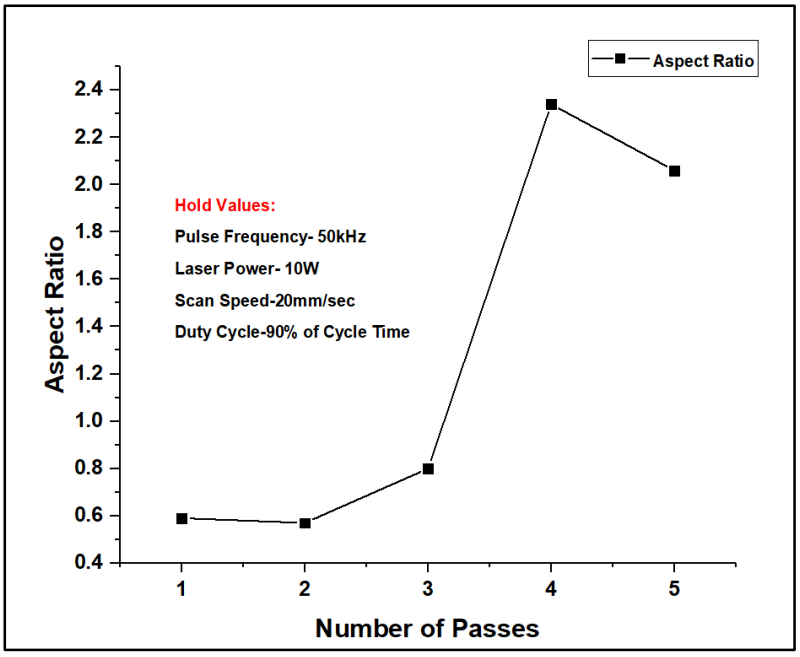

Figure 3.19 Effect of number of pass on the aspect ratio of the micro-channels

3.4 Research Findings from Preliminary Study

The preliminary experimental study mainly deals with the influence of four process parameters such as scan speed from 10 mm/sec to 300 mm/sec, pulse frequency from 50 kHz to 90 kHz, laser power of 5 W to 15 W and number of passes of 1 to 5. The research findings are as follows:

(i) In-depth study of the performance characteristics of multi diodes pumped fiber laser reveals that it is one of the most suitable machine tools to process difficult to machine materials in micro-domain. The preliminary experimental study on PMMA to fabricate micro-channels with the aid of the fiber laser deals with the influence of four process parameters such as scan speed from 10 mm/sec to 300 mm/sec, pulse frequency from 50 kHz to 90 kHz, laser power of 5 W to 15W and number of passes of 1 to 5.

(ii) With the increment of scan speed during different settings of average laser power, the cut width of the micro-channels on PMMA tends to reduce due to the effect of spattering and less material interaction time. The depth dimensions are significantly low and tend to decrease at higher scan speed for any value of laser power within the considered range.

(iii) HAZ width and depth of the micro-channels do not vary considerably, although, the cut width of the micro-channels reduces to a considerable extent with the increment of pulse frequency. The effect of the number of passes leads to more uniformity of the micro-channel profiles and significant increment in the depth dimensions of the micro-channels. A higher number of passes have also increased the aspect ratios of the PMMA micro-channels.

3.5 Modeling and Analysis of Fiber Laser Micro-Channeling on PMMA

Preliminary experimentation forms the basic structure for selecting process parameters and their ranges. Four process parameters, i.e., scan speed (X_1), pulse frequency (X_2), laser power (X_3) and a number of passes (X_4) are controllable process parameters of fiber laser micro-channeling on PMMA. The responses, i.e., cut width (Y_1), depth (Y_2) and HAZ width (Y_3) of the micro-channel profiles are considered for analysis.

3.5.1 Response Surface Methodology

Response surface methodology (RSM) is a combination of mathematical and statistical techniques so that experimental design can be planned for experimentation, modeling, and optimization of responses. The actual response function is written in equation 3.3 as:

$$Y_u = f\left(X_1, X_2, X_3, X_4\right) + \zeta \quad \ldots[\text{Eq}^{\text{n}}3.3]$$

Here, ζ is the noise factor. Further, a second-order polynomial response surface empirical model is represented in equation 3.4 as follows:

$$Y_u = \beta_0 + \sum_{i=1}^{n} \beta_i X_{iu} + \sum_{i=1}^{n} \beta_{ii} X^2_{iu} + \sum_{i=1}^{n-1} \sum_{j=2}^{n} \beta_{ij} X_{iu} X_{ij} + e_u \quad \ldots[\text{Eq}^{\text{n}}3.4]$$

Where, the terms β_o, β_i, β_{ij} represent regression coefficients and X_{iu}, X_{ij} represent the interaction terms which determine the interactive effects of the process parameters. The number of micro-channeling parameters, i.e., the variables selected for the research investigation is represented by *n*. Y_u represents the corresponding response criteria and e_u is an error term.

A set of 31 experiments has been conducted for the present research study by central composite design (CCD) with an alpha (α) value of 2.000, as depicted in table 3.3. Statistical software is used to design the experimental plan and also for the analysis of the experimental data. Four factors with five levels are considered for the experimental purpose, and the ranges of each factor are decided with the aid of pilot experiments.

Lack of fit test is performed as data contain repeated observations to assess the adequacy of the fitted response surface model. The sum of squares due to error (SSE) is divided into two parts as shown in the equation 3.5: one is the sum of squares due to lack of fit (SSLOF), the other is the sum of squares due to pure error (SSPE).

$$SS_E = SS_{PE} + SS_{LOF} \quad \ldots[\text{Eq}^{\text{n}}3.5]$$

The *F*-ratio for lack of fit is computed by comparing SS_{PE} and SS_{LOF}. If the ratio is significant, then the fitted model is inadequate.

Table 3.3 Values of process parameters and observed responses for micro-channel fabrication on PMMA

Process Parameters					Responses		
Exp. No.	**Scan Speed (X_1) mm/sec**	**Pulse Frequency (X_2) (kHz)**	**Laser Power (X_3) (W)**	**Number of Pass (X_4)**	**Cut Width (Y_1) (µm)**	**Depth (Y_2) (µm)**	**HAZ Width (Y_3) (µm)**
1	15	60	7.5	2	144.80	68.75	169.10
2	25	60	7.5	2	141.88	70.50	163.33
3	15	80	7.5	2	143.21	120.7	176.03
4	25	80	7.5	2	132.19	62.25	139.2
5	15	60	12.5	2	236.90	176.61	328.82
6	25	60	12.5	2	223.86	201.5	310.27
7	15	80	12.5	2	163.10	283.8	283.20
8	25	80	12.5	2	191.93	178.7	292.04
9	15	60	7.5	4	133.12	119.10	458.72
10	25	60	7.5	4	168.13	89.7	297.20
11	15	80	7.5	4	140.22	222.7	369.37
12	25	80	7.5	4	191.71	63.65	229.30
13	15	60	12.5	4	319.07	430.1	556.60
14	25	60	12.5	4	388.59	421.8	560.92
15	15	80	12.5	4	260.32	483.2	504.37
16	25	80	12.5	4	313.08	350.15	498.70
17	10	70	10	3	140.46	193.75	413.45
18	30	70	10	3	190.34	93.10	310.13
19	20	50	10	3	190.09	135.7	491.41
20	20	90	10	3	172.42	159.6	401.60
21	20	70	5	3	119.41	51.10	106.84
22	20	70	15	3	352.06	464.5	410.97
23	20	70	10	1	186.61	124.4	118.35
24	20	70	10	5	305.40	385.8	521.85
25	20	70	10	3	170.51	142.8	264.85
26	20	70	10	3	173.30	126.3	220.35
27	20	70	10	3	147.73	117.73	235.69
28	20	70	10	3	163.52	111.60	254.32
29	20	70	10	3	178.72	138.91	260.56
30	20	70	10	3	153.93	146.25	274.35
31	20	70	10	3	164.81	118.75	285.78

3.5.2 Mathematical Modeling for Cut Width (Y_1), Depth (Y_2) and HAZ Width (Y_3) of Micro-Channels on PMMA

Considering four variables and utilizing the results of the experiment from the 31 experiments, empirical models are based on RSM for correlating cut width (Y_1), depth (Y_2) and HAZ width (Y_3) with fiber laser micro-channeling process parameters are represented by the following regression equations 3.6, 3.7 and 3.8 respectively.

$$Y_1 = 655 - 11.32\,X_1 - 1.17\,X_2 - 24.1\,X_3 - 244.6\,X_4 - 0.0014\,X_1 \times X_1 + 0.0393\,X_2 \times X_2 + 2.808\,X_3 \times X_3 + 20.12\,X_4 \times X_4 + 0.0419\,X_1 \times X_2 + 0.0328\,X_1 \times X_3 + 2.587\,X_1 \times X_4 - 0.648\,X_2 \times X_3 + 0.084\,X_2 \times X_4 + 9.85\,X_3 \times X_4$$

…[Eq^{n}3.6]

$$Y_2 = 180 + 31.46 X_1 + 6.36 X_2 - 108.1 X_3 - 222.5 X_4 + 0.198 X_1 \times X_1 + 0.0601 X_2 \times X_2 + 5.368 X_3 \times X_3 + 32.87 X_4 \times X_4 - 0.5557 X_1 \times X_2 + 0.118 X_1 \times X_3 - 2.411 X_1 \times X_4 - 0.139 X_2 \times X_3 - 0.432 X_2 \times X_4 + 16.79 X_3 \times X_4$$

…[Eq^{n}3.7]

$$Y_3 = 2632 - 51.2 X_1 - 62.13 X_2 - 10.1 X_3 + 115.0 X_4 + 0.964 X_1 \times X_1 + 0.4528 X_2 \times X_2 - 0.259 X_3 \times X_3 + 13.68 X_4 \times X_4 + 0.010 X_1 \times X_2 + 1.666 X_1 \times X_3 - 3.13 X_1 \times X_4 - 0.010 X_2 \times X_3 - 1.192 X_2 \times X_4 + 4.98 X_3 \times X_4$$

…[Eq^{n}3.8]

3.5.2.1 ANOVA Test Results and Discussion

Minitab statistical software is utilized to analyze the responses and also to determine the empirical models. To determine each of the responses and their interactions with each other are statistically significant or not, p-values are calculated. A significance level of 0.05 (for p-value) is considered for each of the responses and model analysis to evaluate their significance to each output response. Further, the model adequacy is verified with the help of the lack of fit test. Finally, to determine how the data is fitted into the model, the goodness-of-fit statistics, i.e., R^2, R^2 (adjusted) and R^2 (predicted), have been evaluated to analyze each of the responses.

Table 3.4 represents the ANOVA results for the cut width, whereas table 3.5 shows the ANOVA table for depth. Table 3.6 showcases the ANOVA results of the HAZ width. The p-values, corresponding to lack of fit for responses, i.e., cut width, depth, and HAZ width are 0.417, 0.237 and 0.366 respectively. Thus, the results of each model of the responses described above are adequate, according to lack of fit results. In addition to this, the goodness of fit results, i.e., R^2, R^2 (adjusted) and R^2 (predicted) are close to 1 for all the models. It sums up that models for cut width, depth and HAZ width are adequate and further can be utilized for prediction of the optimized responses.

Table 3.4 ANOVA table for the response surface quadratic model of cut width

Source	DOF	Adjusted SS	Adjusted MS	F-Value	p-Value
Model	9	144537	16059.7	115.58	0.000
Linear	4	109551	27387.8	197.10	0.000
Pulse Frequency	1	2729	2729.2	19.64	0.001
Scan Speed	1	4014	4014.2	28.89	0.000
Laser Power	1	77850	77849.5	560.27	0.000
Number of Pass	1	24958	24958.3	179.62	0.003
Square	2	18394	9197.0	66.19	0.000
Laser Power*Laser Power	1	8611	8610.9	61.97	0.000
Number of Pass*Number of Pass	1	11378	11378.0	81.88	0.002
2-Way Interaction	3	16592	5530.7	39.80	0.000
Pulse Frequency*Laser Power	1	4205	4205.2	30.26	0.001
Scan Speed*Number of Pass	1	2676	2676.3	19.26	0.002
Laser Power*Number of Pass	1	9711	9710.6	69.89	0.000
Error	21	2918	139.0		
Lack-of-Fit	15	2208	147.2	1.25	0.417
Pure Error	6	710	118.3		
Total	30	147455			
Model Summary			**R^2**	**R^2 (Adjusted)**	**R^2 (Predicted)**
			98.02%	97.17%	95.81%

Table 3.5 ANOVA table for the response surface quadratic model of depth

Source	DOF	Adjusted SS	Adjusted MS	F-Value	p-Value
Model	9	485978	53998	181.34	0.000
Linear	4	387583	96896	325.40	0.000
Pulse Frequency	1	2299	2299	7.72	0.011
Scan Speed	1	18593	18593	62.44	0.000
Laser Power	1	267823	267823	899.41	0.002
Number of Pass	1	98868	98868	332.02	0.000
Square	2	55516	27558	93.22	0.000
Laser Power*Laser Power	1	30826	30826	103.52	0.003
Number of Pass*Number of Pass	1	29559	29559	99.26	0.000
2-Way Interaction	3	42879	14293	48	0.000
Pulse Frequency*Scan Speed	1	12354	12354	41.49	0.001
Scan Speed*Number of Pass	1	2326	2326	7.81	0.011
Laser Power*Number of Pass	1	28199	28199	94.70	0.000
Error	21	6253	298		
Lack-of-Fit	15	5125	342	1.82	0.237
Pure Error	6	1128	188		
Total	30	492231			
Model Summary			**R^2**	**R^2 (Adjusted)**	**R^2 (Predicted)**
			98.73%	98.19%	96.94%

Table 3.6 ANOVA table for the response surface quadratic model of HAZ width

Source	DOF	Adjusted SS	Adjusted MS	F-Value	p-Value
Model	14	514754	36768	59.86	0.000
Linear	4	425986	106497	173.38	0.000
Scan Speed	1	13155	13155	21.42	0.000
Pulse Frequency	1	11809	11809	19.23	0.000
Laser Power	1	156967	156967	255.55	0.000
Number of Pass	1	244055	244055	397.33	0.000
Square	4	73146	18287	29.77	0.000
Scan Speed *Scan Speed	1	16608	16608	27.04	0.000
Pulse Frequency*Pulse Frequency	1	58625	58625	95.44	0.000
Laser Power*Laser Power	1	75	75	0.12	0.731
Number of Pass*Number of Pass	1	5349	5349	8.71	0.009
2-Way Interaction	6	15622	2604	4.24	0.010
Scan Speed *Pulse Frequency	1	4	4	0.01	0.938
Scan Speed*Laser Power	1	6936	6936	11.29	0.004
Scan Speed *Number of Pass	1	3926	3926	6.39	0.022
Pulse Frequency*Laser Power	1	1	1	0.00	0.970
Pulse Frequency *Number of Pass	1	2272	2272	3.70	0.072
Laser Power *Number of Pass	1	2483	2483	4.04	0.062
Error	16	9828	614		
Lack-of-Fit	10	6821	682	1.36	0.366
Pure Error	6	3007	501		
Total	30	524582			
Model Summary			**R^2**	**R^2(adjusted)**	**R^2(predicted)**
			98.13%	96.49%	91.73%

3.5.3 Results and Analysis Based on Response Surface Plots and Contour Plots

In this research study, micro-channel width dimension of higher and lower values has been achieved as 388.59 µm and 119.41 µm respectively, whereas, for the depth dimensions, the values are 483.2 µm and 51.1 µm respectively. On the contrary, 560.92 µm and 106.84 µm are the higher and lower obtainable HAZ width of the current research study within the range of four process parameters. It is also observed from the results of the experiment that there are no single micro-channel width ranges below 100 µm owing to the multi-pass phenomenon. The lowest depth is achieved at the lowest laser power of 5 W. However; the result is achieved during the lowest laser power value combined with a moderate number of passes, i.e., 3. The high value of laser power, combined with the high number of passes, has produced a higher depth of micro-channel. In addition to this, high thermal input has also produced melting along with the vaporization. Although, at the combination described above, large dimensions of the micro-channel width are not observed owing to the effect of burning and re-solidification phenomena. Due to the introduction of burning in the micro-channeling zone, some amount of fume from the

micro-channeling zone is also observed. At this point, repeatability of the micro-channel geometry suffers at a significant amount. With the laser power reduction as well as the number of passes and with the combination of high pulse frequency, the burning phenomenon is stopped and provides better controlling over the geometry of the micro-channel. The effects of process parameters on the response criteria are analyzed via response surface plots. The effects of the process parameters on the response criteria are discussed by combining two process parameters at a time, while the remaining process parameters are kept constants at their mean values.

3.5.3.1 Parametric Analysis on Cut Width of Micro-Channel on PMMA

The variation of cut width dimension with scan speed and the number of passes is shown with the aid of a surface plot as shown in figure 3.20. The constant parameters are laser power of 10 W and pulse frequency of 70 kHz. From figure 3.20, it can be observed that in the combination of the higher range of scan speed and lower number of passes, cut width dimension is low. When the number of passes is increasing, the cut width increases rapidly. Increase in scan speed leads to the spattering of the molten material significantly, which eventually leads to discontinuity in the micro-channel profiles. The phenomenon described above also holds for low pulse energy or low laser beam peak power. An increment in scan speed further reduces the laser material interaction time along with the laser spot overlapping factor. As a result of this, cut width decreases with the increase of scan speed for less number of passes of the laser beam. When repeated to and fro motion of the laser beam is observed in the same region of the micro-channels, i.e., the number of pass increases, cut width dimensions tend to increase significantly.

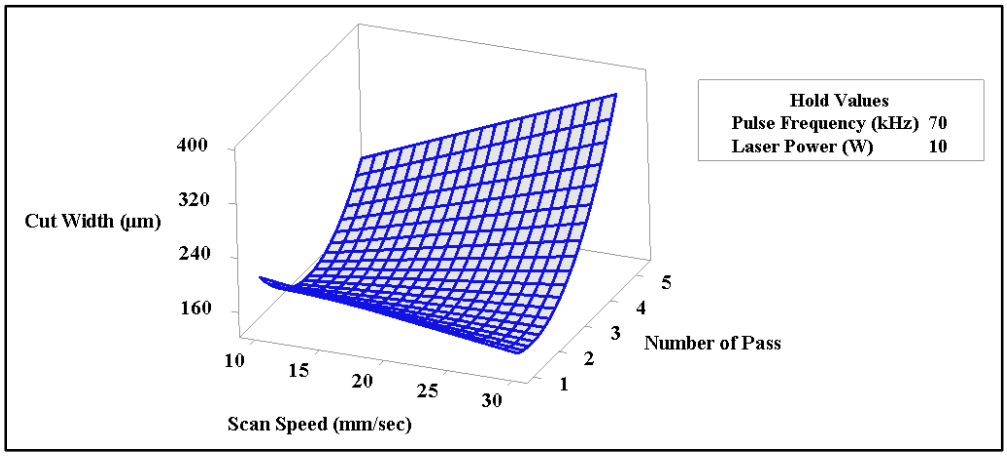

Figure 3.20 Surface plot for influences of scan speed and number of passes on the cut width

Figure 3.21 exhibits the contour plot for investigating the influences of scan speed and the number of passes on cut width. Each contour curve represents an infinite number of combinations of two process variables. The elliptical shape of the contour indicates a functional interaction between the two variables, and the circular shape indicates no interaction between the variables. There is a significant interaction between every two variables, and the surface confined in the smallest ellipse in the contour diagrams indicates the maximum predicted yield. It shows that the experimental values are accurate. Figure 3.21 also shows the low cut width dimensions are achieved during low ranges of the number of passes in combination with both high and low scan speed. Scan speed and number of passes are both significant parameters for achieving desired cut width dimensions.

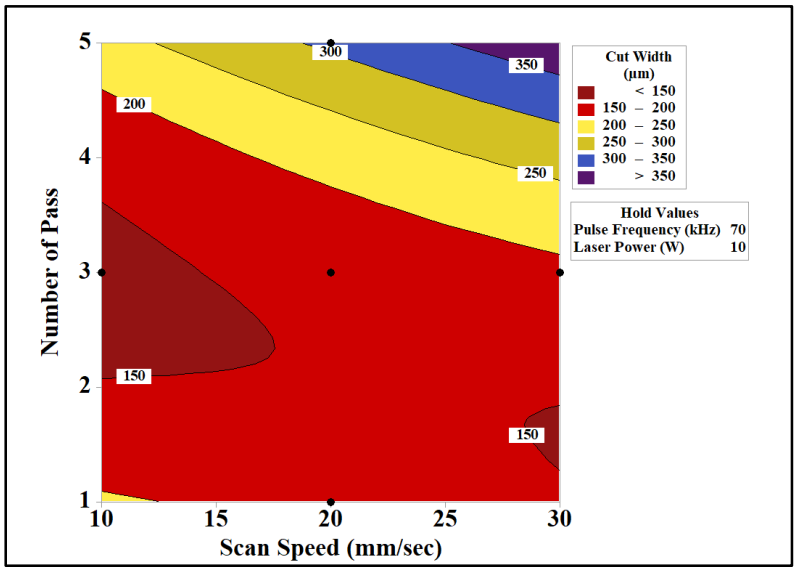

Figure 3.21 Contour plot for influences of scan speed and number of pass on the cut width

In figure 3.22, the surface plot shows the variation of cut width with laser power and pulse frequency. The constant parameters are scan speed of 20 mm/sec and the number of passes of 3. Figure 3.22 exhibits with the increment of laser power, a gradual increment in cut width dimensions are observed due to irradiation of high pulse energy on PMMA surface during high laser power. Increase in pulse frequency also causes an increment in the cut width dimensions of PMMA micro-channels for the moderate value of laser power (range of laser power of 10 to 15W). High pulse energy combined with high laser spot overlapping cause in the increment of the cut width dimension of PMMA micro-channels.

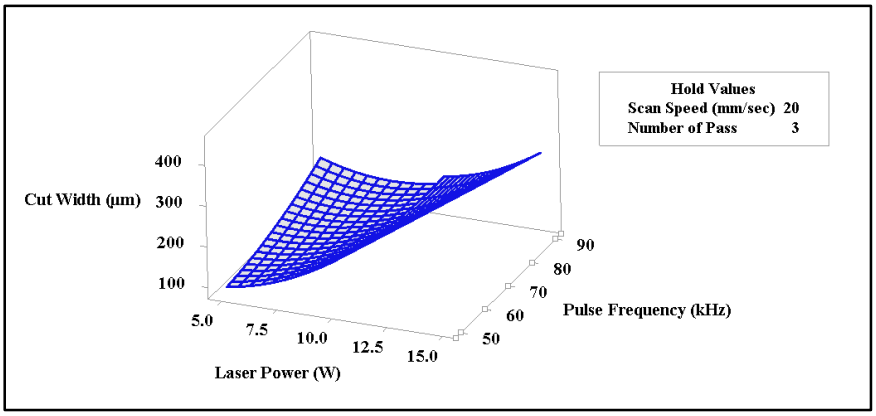

Figure 3.22 Surface plot for influences of laser power and pulse frequency on the cut width

Figure 3.23 showcases the contour plot for investigating the influences of laser power and pulse frequency on cut width dimensions during fiber laser micro-channeling of PMMA. The surface confined in the smallest region in the contour diagram indicates the minimum cut width dimensions for this set of experiments. From figure 3.23, it is observed that pulse frequency has less effect on cut width dimensions compared to laser power. For achieving the minimum cut width dimensions, the combination of low pulse frequency and low laser power is preferred.

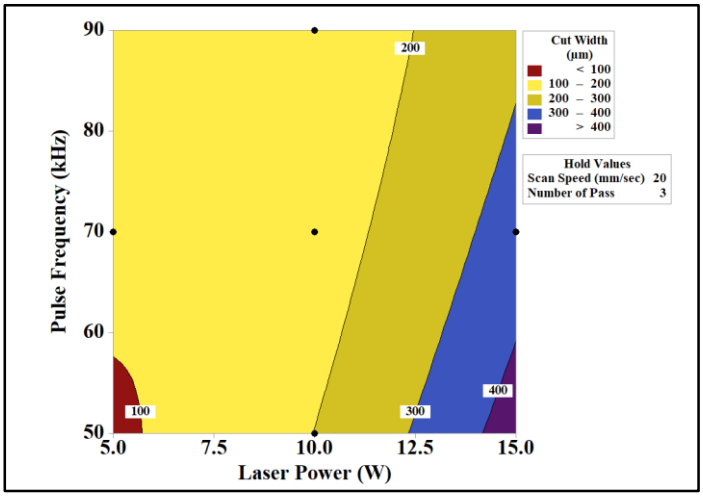

Figure 3.23 Contour plot for influences of laser power and pulse frequency on the cut width

3.5.3.2 Parametric Analysis on Depth of Micro-Channel on PMMA

The surface plot on depth variation with laser power and the number of passes is shown in figure 3.24. The constant parameters are a scan speed of 20 mm/sec and pulse frequency of 70 kHz. Figure 3.24 reveals that at low laser power setting with a single pass, the depth dimension of

micro-channel is low. The phenomenon reverses back when the number of pass goes on increasing. The controlling of depth dimensions in polymer materials during photo-thermal ablations is difficult. The high value of laser power will cause burning and significant re-solidification in the micro-channeling zone. This depth of micro-channel increases significantly with the combination of high laser power and a high number of passes.

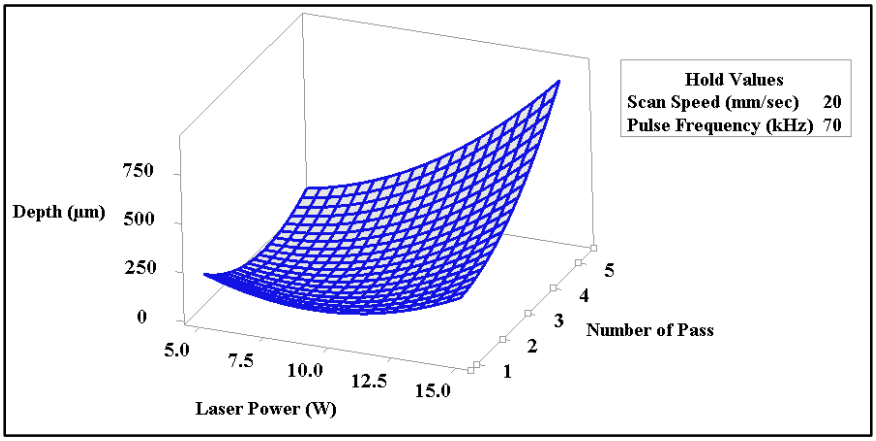

Figure 3.24 Surface plot for influences of laser power and number of pass on the depth

Figure 3.25 indicates the contour plot for the interaction of laser power and number of passes on depth dimensions. The number of passes has less importance on depth dimensions as compared to laser power. The laser power of 12.5 W along with any range of the number of passes attribute to 200 µm depth. The maximum depth is achieved at the highest value of the number of passes and laser power.

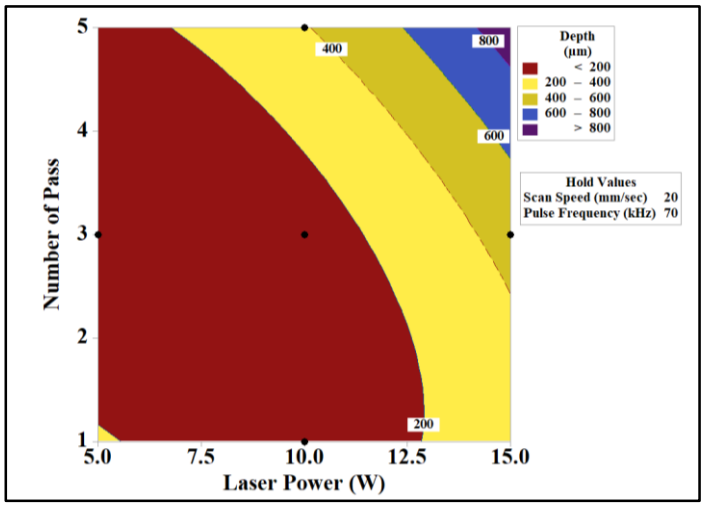

Figure 3.25 Contour plot for influences of laser power and number of pass on the depth

Figure 3.26 deals with the surface plot of depth dimensions for scan speed and pulse frequency. The constant parameters are laser power of 10 W along with the number of passes of 3. The depth dimensions tend to increase with the combination of low scan speed and high pulse frequency. Lower scan speed attributes in a high spot overlapping and better controlling of micro-channel dimensions due to high laser-material interaction time. Increase in pulse frequency also causes an increment in the laser pulses as well as laser-material interaction time. Most of the energy absorbed is confined within the irradiated area because the thermal diffusion length of polymers during laser interaction is lower than that of the photon-absorption depth, due to which, depth dimensions tend to increase. Repeated laser beam movement in the same region leads to an increase in depth as well as the width of micro-channel cut on PMMA.

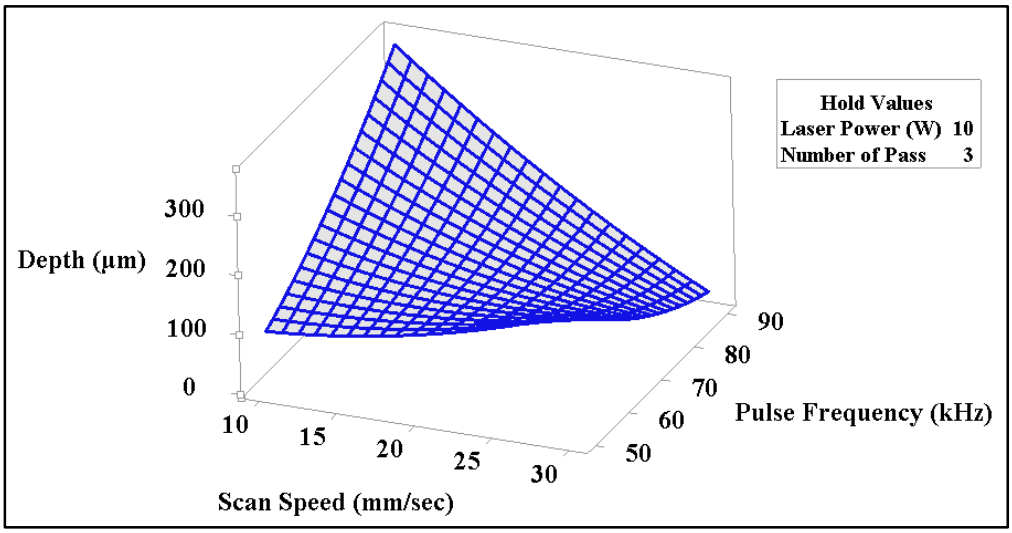

Figure 3.26 Surface plot for influences of scan speed and pulse frequency on the depth

Figure 3.27 showcases the contour plot for the variation of depth dimensions under the effect of scan speed and pulse frequency. There is a significant interaction between two process variables, i.e., scan speed and pulse frequency, and the surface confined in the smallest ellipse in the contour diagram indicates the maximum predicted depth dimensions. Figure 3.27 also indicates that both scan speed and pulse frequency are significant process parameters for achieving desired depth dimensions.

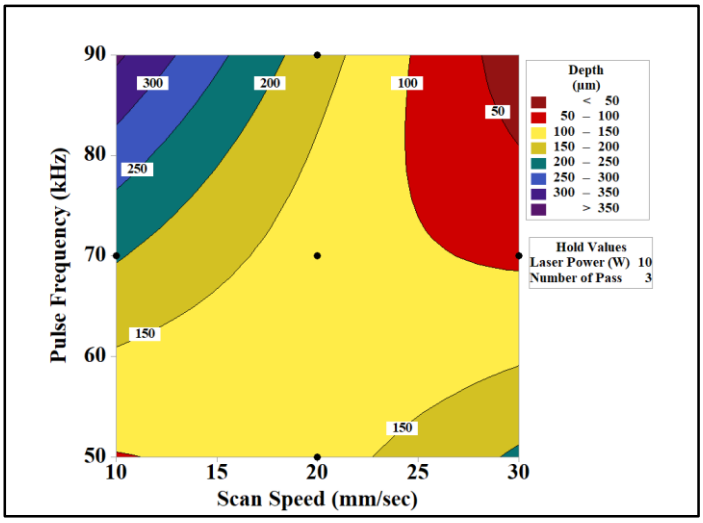

Figure 3.27 Contour plot for influences of scan speed and pulse frequency on the depth

3.5.3.3 Parametric Analysis on HAZ Width of Micro-Channel on PMMA

The variation of HAZ width dimensions for scan speed and the number of passes is shown in the surface plot 3.28. The constant process parameters are pulse frequency of 70 kHz, and laser power of 10 W. Increment in scan speed values reduces HAZ from the micro-channel surroundings. As a result, the HAZ width dimension is decreased with the high scan speed.

On the contrary, the reverse phenomenon is observed with the increment in the number of passes. A steep rise in the HAZ width dimensions is observed at the high number of passes. High scan speed attributes with low laser-material interaction time. As a result, laser beam energy which is converted into heat does get a sufficient amount of time to accumulate in the micro-channel surrounding. Repeated movement of the laser beam causes higher laser material interaction time as compared to a single repetition of the laser beam in the micro-channeling zone. Thus, accumulation of heat attributes in high values of HAZ width dimensions.

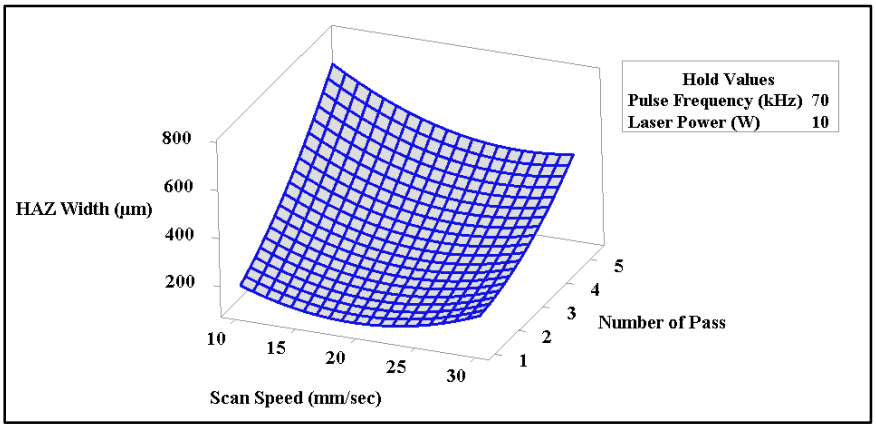

Figure 3.28 Surface plot for influences of scan speed and number of pass on the HAZ width

Figure 3.29 indicates the contour plot between scan speed and the number of the pass for analyzing their effect on HAZ width dimensions. A significant interaction between the number of passes and scan speed is observed for HAZ width dimensions. However, the effect of scan speed on HAZ width dimensions is less compared to the number of passes. It is evident from figure 3.29 that the low number of pass is required for any range of scan speed for achieving the lowest HAZ width dimensions.

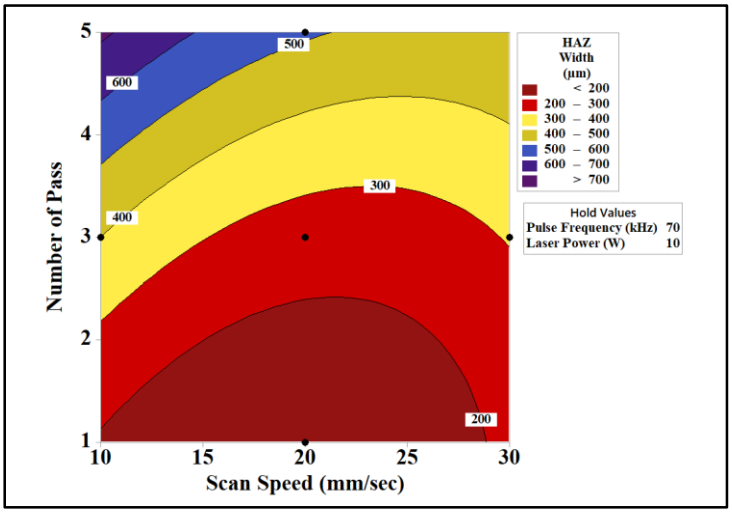

Figure 3.29 Contour plot for influences of scan speed and number of pass on the HAZ width

Figure 3.30 deals with the effect of laser power and scan speed on the HAZ width dimensions. The constant parameters are pulse frequency of 70 kHz and the number of passes of 3. Higher scan speed attributes less interaction time with the laser to the workpiece surface. Further, the high scan speed is associated with reducing HAZ, but on the flip side, it is also associated with the induction of poor micro-channeling quality. As a result of which the HAZ width dimensions tend to decrease drastically at higher scan speed. An increase in laser power generates excess energy, which is carried away by the ablation products. An increment in laser power also leads to an increment of energy into the surface of PMMA, which sometimes leads to the burning of PMMA sheet during the micro-channeling process. High intensity of the fiber laser beam with a small incident time leads to instant melting and further vaporization of PMMA from the top surface. The re-solidification phenomenon can be observed on the side wall of the micro-channels as well as the inner surface of the micro-channels. Due to which, the HAZ width of the

micro-channels is increased in a significant manner. This phenomenon mentioned above can be partly overcome by blowing in high pressure assist gas in the micro-machined zones. As all the experiments are performed in an open atmosphere, the re-solidified material and spattering phenomenon at the micro-channel edges cannot be eliminated.

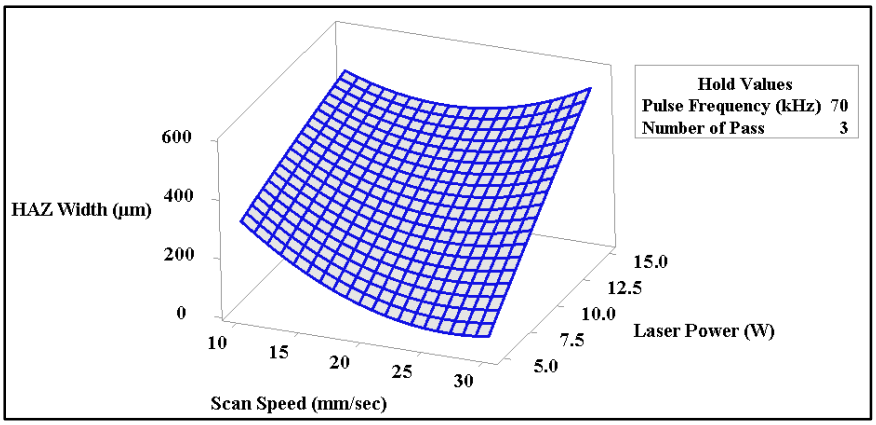

Figure 3.30 Surface plot for influences of scan speed and laser power on the HAZ width

Figure 3.31 showcases the contour plot of scan speed and laser power for investigating the effect of both process parameters on the HAZ width dimensions. It is evident from figure 3.31 that both the process parameters have contributed significantly in the HAZ width dimensions. The smallest ellipse in the contour diagram indicates the lowest predicted value of HAZ width. High scan speed along with low laser power attributes to low HAZ width.

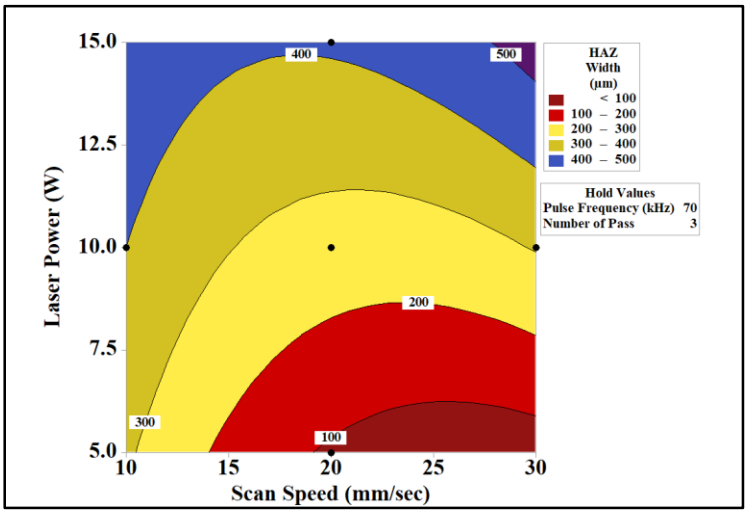

Figure 3.31 Contour plot for influences of scan speed and laser power on the HAZ width

In figure 3.32 (a), (b), (c), (d) fiber laser generated micro-channels on PMMA are shown at 50 X magnification. Figure 3.32 (a) represents the micro-channel generated at a scan speed of 15 mm/sec, laser power of 7.5 W, a pulse frequency of 80 kHz and a number of pass of 4, whereas figure 3.32 (b) indicates the microscopic image of PMMA micro-channel generated during scan speed of 20 mm/sec, the laser power of 10 W, the pulse frequency of 90 kHz and the number of pass of 3. Figure 3.32 (c) represents the micro-channel profile generated at the combination of scan speed of 25 mm/sec, laser power of 7.5 W, a pulse frequency of 80 kHz and a number of pass of 2, whereas the figure 3.32 (d) indicates the micro-channel profile generated during scan speed of 20 mm/sec, laser power of 5 W, a pulse frequency of 70 kHz and a number of pass of 3.

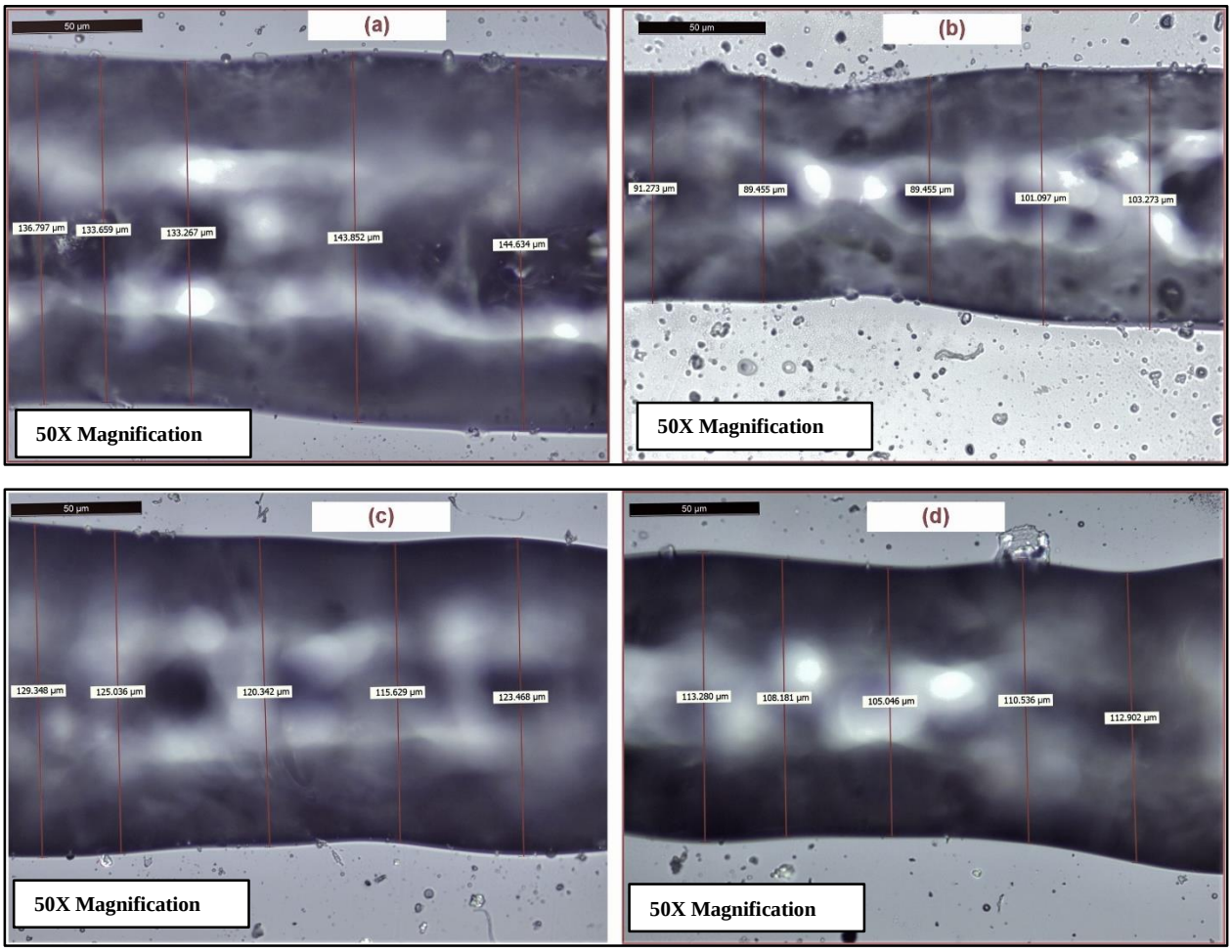

Figure 3.32 Microscopic images of various fiber laser generated micro-channels

3.5.4 Parametric Optimization of Fiber Laser Micro-Channeling on PMMA

For achieving optimal parametric combination during fiber laser micro-channeling of PMMA, single-objective as well as multi-objective optimization has been performed using MINITAB software.

3.5.4.1 Single Objective Optimization of the Responses

The results of single-objective optimization for cut width, depth, and HAZ width during the generation of micro-channels on PMMA by fiber laser micro-channeling, have been shown in figure 3.33, 3.34 and 3.35 respectively.

For achieving a minimum cut width of 67.4225 µm, the optimal parametric combination of single- objective optimization has been obtained as scan speed of 10 mm/sec pulse frequency of 50 kHz, laser power of 5 W and number of passes of 4.

For achieving maximum depth of 499.7832 µm, the optimal parametric combination of single-objective optimization has been obtained as scan speed of 12.64 mm/sec, pulse frequency of 82 kHz, scan speed of 9.5 W and number of passes of 5.

For achieving a minimum HAZ width of 8.7864 µm, the optimal parametric combination of single- objective optimization has been obtained as scan speed of 23.5354 mm/sec, pulse frequency of 69.798 kHz, laser power of 5.15 W and number of passes of 2.

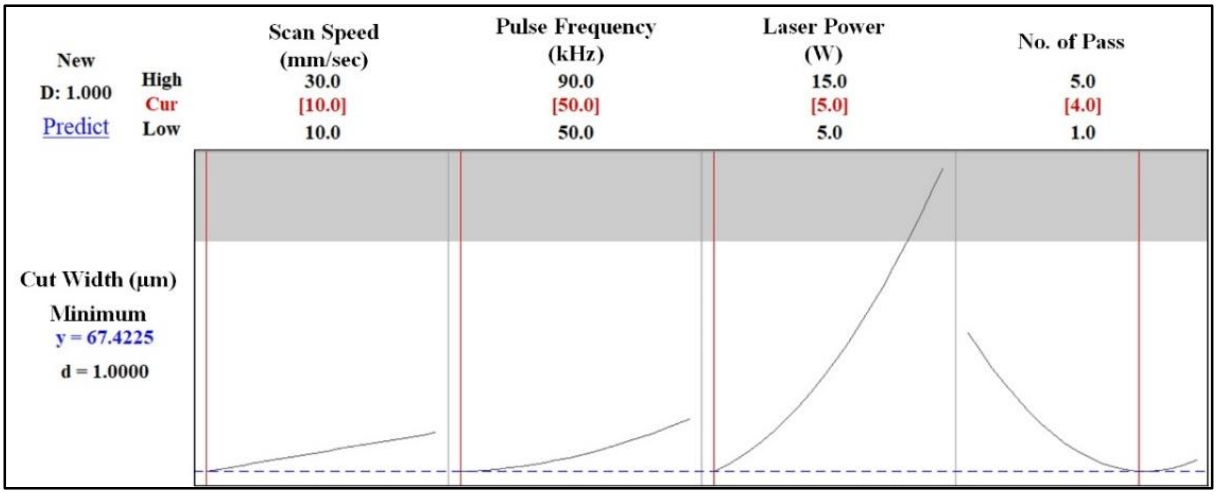

Figure 3.33 Single-objective optimization results for cut width

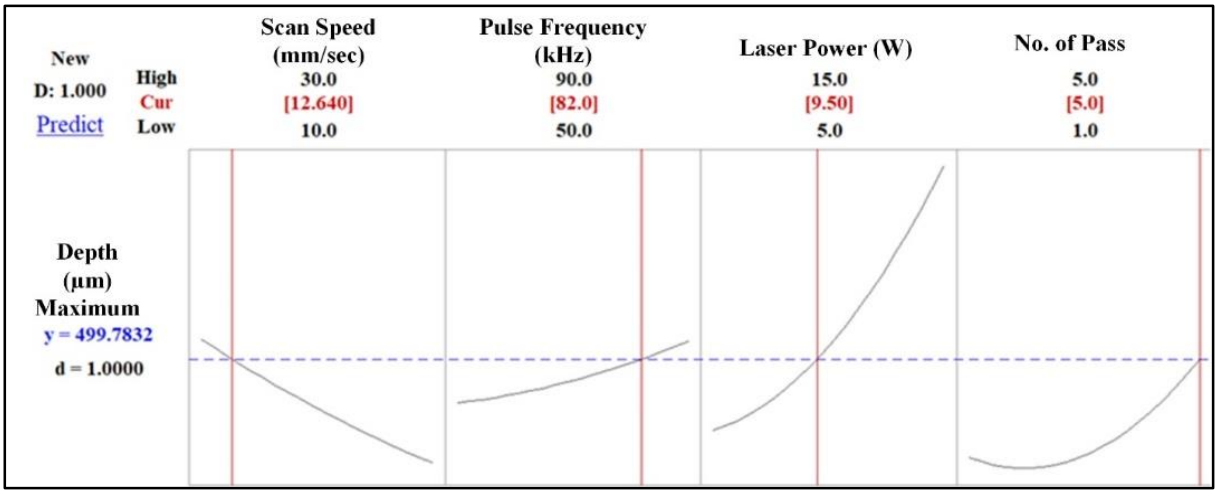

Figure 3.34 Single-objective optimization results for depth

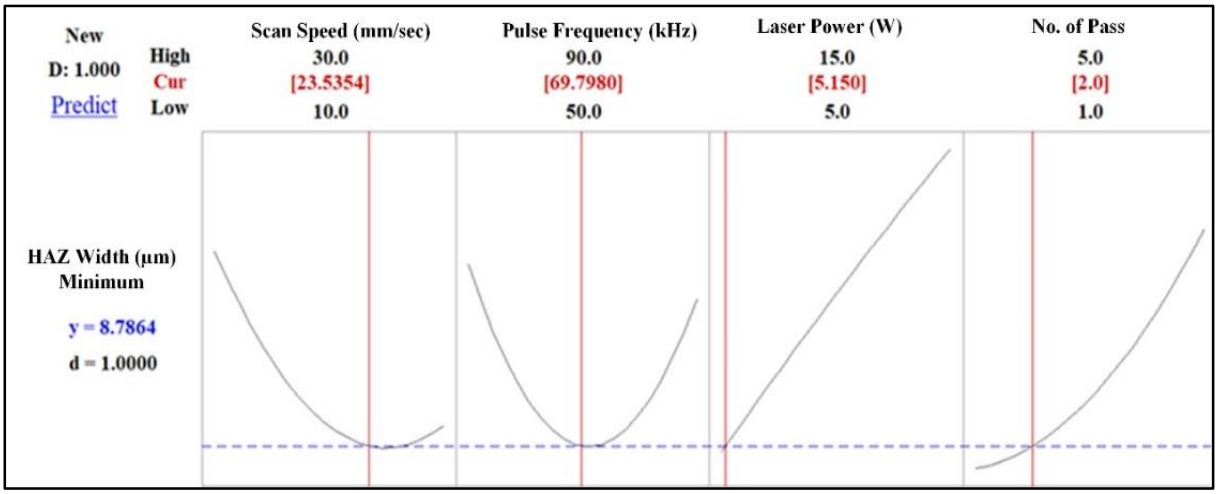

Figure 3.35 Single-objective optimization results for HAZ width

3.5.4.2 Multi-Objective Optimization of the Responses

Multi-objective optimization analysis has been carried out to minimize the responses, i.e., cut width, and HAZ width and also to maximize depth of the fiber laser fabricated micro-channels based on the developed mathematical equations of 3.6, 3.7 and 3.8 for PMMA. Figure 3.36 shows the optimized values of process parameters along with the responses. The current optimal parameter settings for achieving the lowest cut width and HAZ width along with maximized depth are scan speed of 30 mm/sec, a pulse frequency of 57.220 kHz, laser power of 5 W, number of pass of 2. The optimal values of cut width, depth, and HAZ width are respectively,

115.89 µm, 138.57 µm, and 110.62 µm. Experiments have been carried out to fabricate the micro-channels at the above optimal parameter set for achieving the desired dimensions of cut width, depth, and HAZ width. Observed dimensions of the machined micro-channels on PMMA are 110.18 µm, 132.37 µm, and 105.11 µm for cut width, depth and HAZ width respectively. Figure 3.37 represents the microscopic image of PMMA micro-channel (50X magnification) at the optimized settings showing the optimized depth and cut width profile.

A total of five experiments has been carried out with the optimal set of input process parameters to compare the optimal experimental values with the experimental values. Table 3.7 shows experimental results with the multi-objective parametric optimal setting as obtained from the RSM model. Predictions for all the three responses are in good agreement (below 5%) with the actual experimental results.

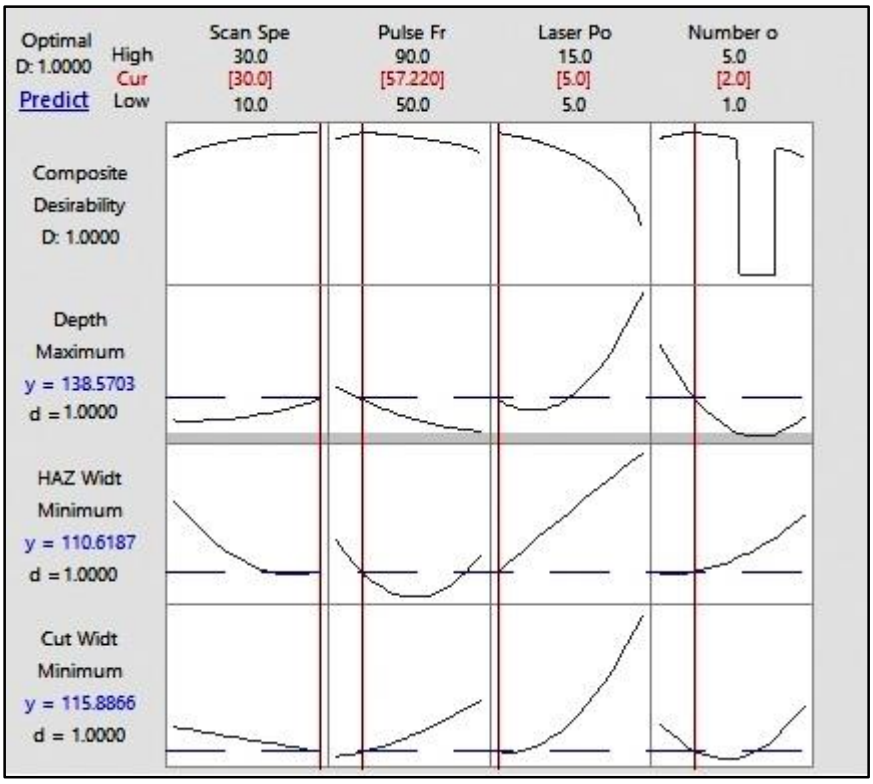

Figure 3.36 Multi-objective optimization results for cut width, depth, and HAZ width

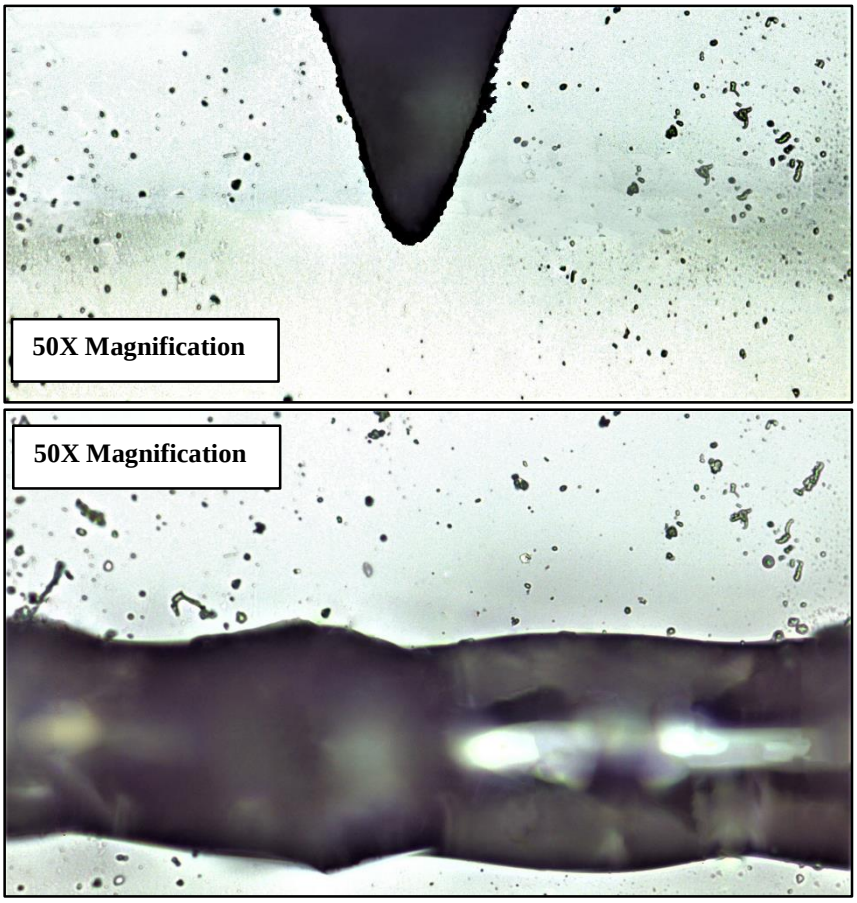

Figure 3.37 Microscopic image of PMMA micro-channel at the optimum condition (a) Optimized profile of depth; (b) optimized profile of cut width

Table 3.7 Comparison between multi-objective optimization results with actual results

Exp. No:	Cut Width (µm)			Depth (µm)			HAZ Width(µm)		
	Optimized Value	Actual Value at Optimum Condition	Percentage of Errors	Optimized Value	Actual value at Optimum Condition	Percentage of Errors	Optimized Value	Actual Value at Optimum Condition	Percentage of Errors
1	115.89	110.18	4.93	138.57	132.37	4.47	110.62	105.11	4.98
2	115.89	121.21	4.59	138.57	143.32	3.43	110.62	115.13	4.08
3	115.89	110.155	4.95	138.57	145.45	4.96	110.62	116.01	4.87
4	115.89	110.65	4.52	138.57	133.01	4.01	110.62	116.12	4.97
5	115.89	119.86	3.43	138.57	133.2	3.88	110.62	105.98	4.19
Mean Percentage of Errors (%)=4.48				**Mean Percentage of Errors (%)=4.15**			**Mean Percentage of Errors (%)=4.62**		

3.6 Outcomes of the Present Research Work

The present research work aims to determine the optimal combination of process parameters during fiber laser micro-channeling on transparent PMMA workpiece. The theoretical and experimental analysis reveals that photo-thermal ablation governs the process for which burning effect comes into a determining factor during fiber laser ablated micro-channel fabrication on PMMA. The developed mathematical models are validated by analyzing ANOVA of the considered responses, i.e., cut width, depth, and HAZ width during fiber laser micro-channeling on PMMA.

Further, a multi-objective optimization is carried out to achieve the optimal results of cut width, depth, and HAZ width, which are 115.89 µm, 138.57 µm, and 110.62 µm respectively. The optimal parameter settings are scan speed of 30 mm/sec, pulse frequency of 57.22 kHz, laser power of 5 W, number of pass of 2. The percentage of error obtained from the predicted and actual experimental results at optimal condition is found below 5%, which signifies good acceptability of prediction analysis of fiber laser machining of micro-channels on PMMA.

This research work can also be further utilized to find out the range of the fiber laser process parameters which is the key to obtain a uniform, smooth, high aspect ratio micro-channel on PMMA. Based on the findings, the study can be used as a technical guideline for fiber laser micro-channeling of PMMA. Complicated shapes of micro-channels on PMMA can also be achieved with the utmost precision with the aid of fiber laser micro-machining operation.

4. EXPERIMENTAL INVESTIGATIONS INTO FIBER LASER MICRO-GROOVING OF Ti-6Al-4V

4.1 Introduction

Ti-6Al-4V is the most used material among the other titanium alloys, and its total production is almost half of all titanium alloys. The present research work attributes the bio-medical features of this titanium alloy, considering both the geometrical, i.e., cut width, depth, and average surface roughness during the selection of the process parameters. Titanium alloy of grade 5 is often used in the different bio-medical field of applications such as artificial hip joints, knee joint replacements, dental implants, etc. It is essential that Ti-6Al-4V can bond firmly to a bone, for optimal function and durability. Therefore, enhanced bioactivity and improved implant-host interactions are essential to reduce biologically related implant failure. Therefore, the selection of precise machining parametric conditions holds the key for obtaining the desired profiles of the micro-grooves with minimum surface roughness value. The laser beam machined micro-grooves on Ti-6Al-4V is useful to integrate with the surrounding tissue within the human body.

The conventional machining methods intended for cutting these alloys not only suffer due to poor thermal conductivity, low elastic modulus and high chemical affinity at elevated temperatures but also have to undergo higher cost associated with the machining of Ti-6Al-4V, caused by lower cutting speeds and shorter tool life. Numerous research works have been carried out on laser beam micro-machining on Ti-6Al-4V. The present work includes the experimental investigations into fiber laser micro-grooving on Ti-6Al-4V to study the parametric influences on geometrical features of micro-groove and surface roughness on the generated machine surface.

4.2 Selection of Process Parameters and Responses

The considered process parameters for the present research work are laser power, pulse frequency, duty cycle, number of passes and scan speed. The detail of each process parameter is discussed previously in chapter 3. The output responses considered for the research works are cut/groove width, depth and surface roughness. The detail of cut groove width and depth is also discussed previously under chapter 3. The effect of each process parameter on the responses is discussed hereunder.

4.3 Properties of Ti-6Al-4V

The present work deals with the fiber laser micro-grooving of Ti-6Al-4V of 50X50X 1.1 mm of dimension. The chemical compositions of Ti-6Al-4V is given in table 4.1. The values of properties of titanium alloy of grade 5 are given in table 4.2.

Table 4.1 Chemical compositions of Ti-6Al-4V [10]

Al	Fe	C	N	O	V	Ti
5.55-6.5%	<0.25%	<0.08%	<0.05%	<0.2%	3.35-4.5%	Balance

Table 4.2 Properties of Ti-6Al-4V [73]

Properties	Values
Density	4.43 g/cc
Tensile Strength (UTS)	895–930 MPa
Yield Strength	825–869 MPa
Young's Modulus	110–114 GPa
Elongation	6-10 %
Fatigue Strength	240 MPa
Poisson's Ratio	0.342
Thermal Conductivity	6.7 W/m-K
Melting Point	1604 - 1660 °C

4.4 Material Removal Mechanism of Fiber Laser Micro-Grooving of Ti-6Al-4V

Most of the titanium alloys used in the industry contain α- and β- stabilizers, which include Ti-6Al-4V, Ti-6Al-6V-2Sn, and Ti-6Al-2Sn-4Zr-6Mo. They are heat treatable, and most are weldable, especially with the lower β- stabilizer [10]. Conventional machining process fails to meet stringent quality control at the time of machining of titanium alloys owing to the excessive amount of heat, work hardening, low thermal conductivity, abrasiveness, and high strength level. The heat generated during the laser beam machining process is used to remove material in a minimum volume without mechanical engagement with the work-piece material.

The underlying mechanism involved behind the laser beam micro-grooving process can be identified as the laser beam micro-cutting process involving several crucial factors. During laser beam micro-machining of titanium alloy of grade 5, temperature zones can be divided into solidus temperature of 1877 K, the liquidus temperature of 1923K, and the evaporation

temperature of 3533K. Four different approaches which govern the laser beam machining process are evaporative laser cutting, fusion cutting, reactive fusion cutting, and a controlled fracture technique [10]. The selection of the optimum laser cutting technique depends on the thermo-physical properties of the material, the thickness of the workpiece, and the type of laser employed. For thick section cutting of titanium alloys, the most preferred process is reactive fusion cutting. In reactive fusion cutting, molten material is removed, and the further melting of the work-piece compensates the lost material at the solid-liquid interface below the cutting front. It is worth to take a note that all the research experiments are carried out in atmospheric conditions, i.e., without the presence of assist air.

The fiber laser beam is focused on the surface of Ti-6Al-4V, and some portion of the heat energy converted from optical energy is absorbed. Theoretically, only 40 to 80% of that energy may be absorbed in most cases of the fiber laser. Remaining part of the energy is reflected, and some portions of the energy may be scattered through the work-piece. Absorption occurs through a very thin surface layer, and the absorbed energy diffuses to the bulk of the material. As the pulse width in the present system to be in a nanosecond pulse regime, the heat flow can be assumed to be one dimensional. The absorbed laser beam penetrates on the work-piece surface in the range of microns and sub-microns. As the temperature increases, the surface will reach the melting point at a certain point of time. The melting time reduces drastically when power density increases rapidly. Another essential aspect that should be taken into consideration is that all the experiments are accomplished in pulsed mode, and thus the peak power is high at a considerable amount, which can cause high vaporization rate. The high vaporization rate can create a shock wave, and high vapor pressure at the liquid surface considerably increases the boiling temperature. Finally, the molten material is removed as vapor by the expulsion of melt, as the resultant of the high pressure in combination with superheated liquid after the end of the laser pulse. As all the research experiments are carried out in atmospheric conditions, heat affected zone (HAZ) and re-solidification of the material may occur in the form of the rim. A fiber laser micro-grooving process, as well as the representation of a laser beam process for micro-groove generation, are shown in figure 4.1 and figure 4.2, respectively.

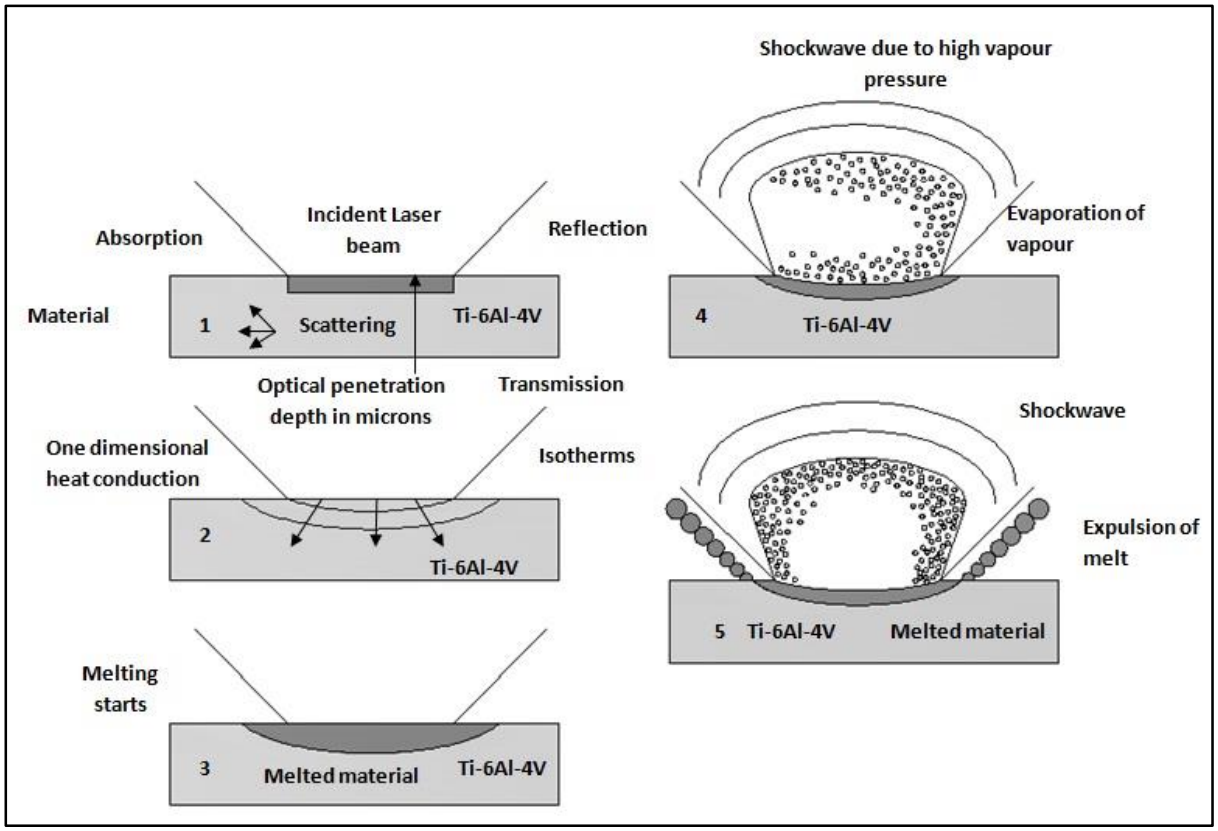

Figure 4.1 Representation of fiber laser beam micro-grooving of Ti-6Al-4V [10]

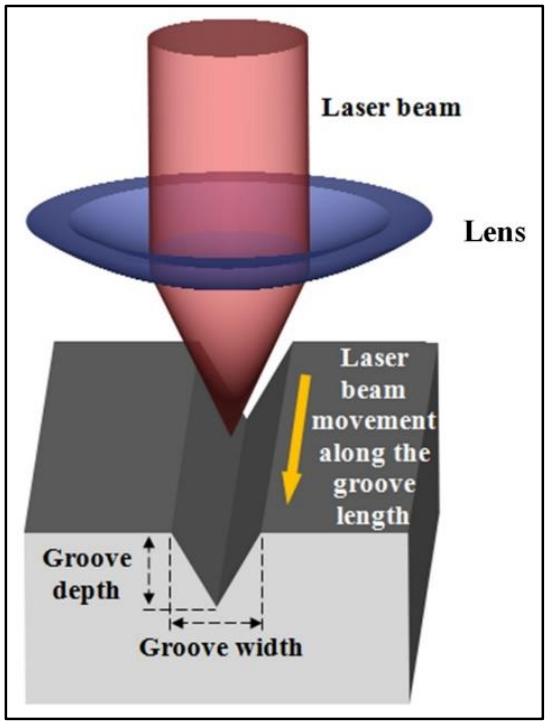

Figure 4.2 Schematic diagram of laser beam movement inside a micro-groove [10]

4.5 Experimental Planning

In the present experimental work, multi-diodes pumped Galvanometer based Ytterbium (Yb^{3+}) doped fiber laser machining system of 50 W, made by M/S Sahajanand Laser Technology Limited is utilized for the experimentation. The photographic view of the fiber laser machining system is shown in figure 4.3. The diode pointer and F-θ lens are used in the present research work are shown in figure 4.4. The main difference between CNC operated fiber laser system and a galvanometer operated fiber laser system is within the laser head. Laser head of the fiber laser consists of both electric and galvanometer units and as a result, the maximum attainable scan speed for the described system is 4000 mm/sec.

Four process parameters, i.e., scan speed, pulse frequency, laser power, and the number of passes are considered for the analysis. The influences of fiber laser micro-grooving process parameters on the responses such as cut width, depth, and average surface roughness have been determined graphically. A total of 20 experiments is carried out in the high range of scan speed in which scan speed varies from 100 mm/sec to 1000 mm/sec. For another set of experiments, the scan speed is varied from 5 mm/sec to 90 mm/sec. A comparative analysis of the micro-groove geometrical features for the lower and higher ranges of scan speed has carried out. The pulse frequency and laser power are varied from 50 to 100 kHz and 10 W to 30 W, respectively. The number of passes is varied from 1 to 12 to find out its effect on the fiber laser generated micro-groove geometry and surface finish.

A total of 42 experiments are carried out by varying one factor at a time (OFAT) to find out the influences of the process parameters on the response criteria. Pilot experiments are also carried out previously so that all the desirability is achieved. Another essential objective is to produce micro-grooves with utmost precision and better surface finish in atmospheric condition.

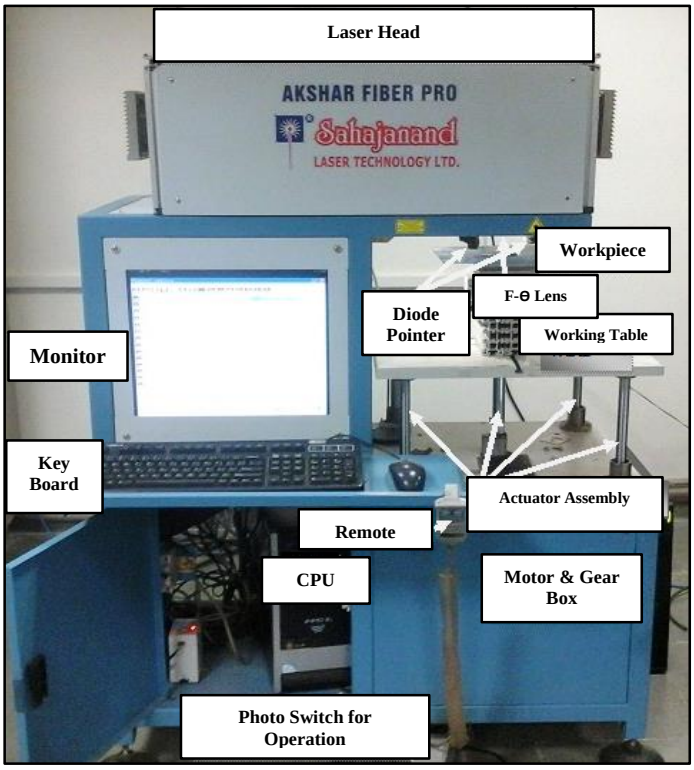

Figure 4.3 Photographic view of Galvanometer fiber laser machining experimental setup [10]

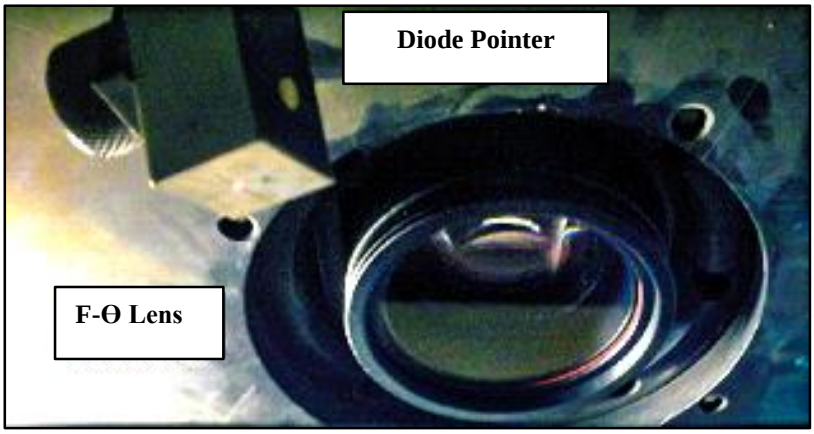

Figure 4.4 Photographic view of diode pointer and lens [10]

4.6 Measurements

Before micro-grooving on Ti-6Al-4V, the workpiece is subjected to X-ray diffraction (XRD) to identify the composition of Ti-6Al-4V. Figure 4.5 represents the XRD analysis of the titanium alloy of grade 5. The Bragg's peaks detected in the XRD scan belongs to hexagonal closed-

packed (hcp) α-Ti and body-centered cubic (bcc) β-Ti. Figure 4.5 identifies all of the peaks which are assigned to Ti-6Al-4V.

After the micro-machining, the samples are cleaned with the ultrasonic cleaner for 15 minutes to remove dust particles. The dimension of the depth is measured using a Leica optical microscope of 50X optical lens, while the cut /groove width dimension is measured using the 10X optical lens. The measurements of the cut widths are carried out at four different places of the micro-grooves. The average of four measured values is selected as the cut width dimension. The measurements of the depth are carried out from the surface edges of the sample material.

The surface roughness (R_a) of the micro-grooves is computed by an atomic force microscope (Nanosurf Easy Scan 2). The surface topology measurements are carried out by a small probe placed at the tip of a cantilever beam. The forward scanning is carried out from the left to right of the selected surface of the workpiece. All the measurements of the surface roughness using AFM are conducted by line fit which calculates the first order least squares fit, i.e., mean value and slope for each line of data points and subtracts the fitted values from the raw measurement data for each data point of that line. The 3D view of the surface topology and measured surface roughness values of each groove in terms of R_a are utilized to analyze and validate the micro-grooving process. Origin 17 is utilized for parametric plots with the aforesaid process parameters on the measured values of cut width, depth, and R_a to identify their effects.

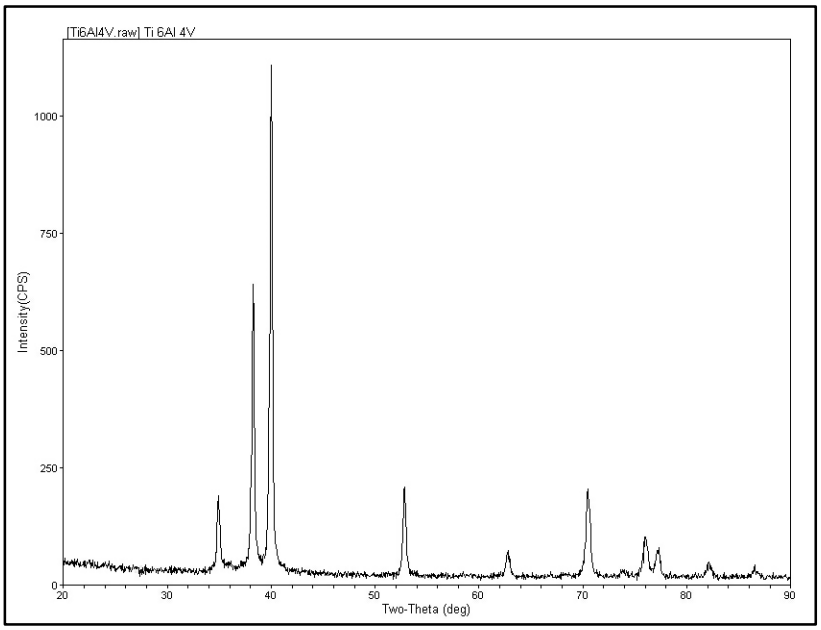

Figure 4.5 XRD analysis of Ti-6Al-4V

4.7 Results and Discussion

The results of the total of 42 experiments include a different level of micro-grooving parameters. The results of the total of 42 experiments are listed in table 4.3. Influence of each process parameters on the micro-groove geometry and surface roughness have been discussed hereunder.

Table 4.3 Values of process parameters and observed responses for micro-groove fabrication on Ti-6AL4V

Exp. No.	Number of passes	Scan speed (mm/sec)	Pulse Frequency (kHz)	Laser Power (W)	Cut Width (µm)	Depth (µm)	R_a (µm)
1	8	100	80	30	224.72	515.67	0.044
2	8	200	80	30	197.64	367.37	0.103
3	8	300	80	30	174.58	349.09	0.109
4	8	400	80	30	171.55	198.03	0.130
5	8	500	80	30	169.54	175.96	0.145
6	8	600	80	30	155.51	164.61	0.180
7	8	700	80	30	149.86	144.96	0.209
8	8	800	80	30	145.85	136.23	0.210
9	8	900	80	30	144.45	113.70	0.419
10	8	1000	80	30	124.65	112.28	0.450
11	8	5	80	30	271.39	758.92	0.069
12	8	10	80	30	236.89	750.83	0.100
13	8	20	80	30	233.85	613.83	0.115
14	8	30	80	30	232.77	483.87	0.179
15	8	40	80	30	220.69	481.51	0.212
16	8	50	80	30	213.67	454.67	0.205
17	8	60	80	30	207.66	418.32	0.236
18	8	70	80	30	205.69	415.25	0.245
19	8	80	80	30	188.61	401.59	0.505
20	8	90	80	30	186.27	387.89	0.511
21	8	40	50	30	275.59	646.96	0.087
22	8	40	60	30	251.12	603.63	0.108
23	8	40	70	30	245.87	521.56	0.119
24	8	40	90	30	210.46	434.65	0.263
25	8	40	100	30	199.01	401.12	0.298
26	1	40	50	30	136.65	346.96	0.262
27	2	40	50	30	175.63	361.65	0.237
28	3	40	50	30	213.78	403.65	0.228
29	4	40	50	30	238.47	498.36	0.169
30	5	40	50	30	246.85	523.03	0.140
31	6	40	50	30	247.78	586.98	0.137
32	7	40	50	30	262.21	620.35	0.103
33	9	40	50	30	324.25	747.45	0.067
34	10	40	50	30	340.46	755.31	0.045
35	5	40	50	10	320.02	473.04	0.198
36	5	40	50	12.5	373.09	475.50	0.272
37	5	40	50	15	379.65	479.65	0.286
38	5	40	50	17.5	384.78	504.32	0.329
39	5	40	50	20	398.56	509.07	0.379
40	5	40	50	22.5	356.36	512.45	0.235
41	5	40	50	25	322.06	514.32	0.179
42	5	40	50	27.5	275.63	522.32	0.153

4.7.1 Influence of Scan Speed on Cut Width, Depth, and Surface Roughness on Ti-6Al-4V Micro-Grooves

Micro-cutting quality is primarily governed by the combined effects of pulse frequency and scan speed due to the percentage of spot overlap. In pulsed mode of laser micro-machining operation, the extent of spot overlapping determines the surface roughness of the micro-groove geometries. During pulsed fiber laser micro-grooving operation of titanium alloys, minimization of surface roughness, cut width as well as an increase in dimensions of the depth of the micro-groove criterion is the highest priority for utilizing the micro-grooves in various fields of engineering applications. Another important concerning factor is the formation of a heat affected zone (HAZ) that can have a detrimental effect on the surface of the fabricated micro-groove. Many of the experiments are carried out with higher scan speed in the moderate setting of pulse frequency with the combination of other process parameters that are kept as constants.

Figure 4.6 shows the influence of higher range of scan speed (100 mm/sec to 1000 mm/sec) on cut width, depth, and surface roughness on fiber laser machined micro-groove surfaces, while figure 4.7 deals with the effect of lower range of scan speed (05 mm/sec to 100 mm/sec) speed on the responses. The remaining process parameters are kept constants at the number of passes of 8, pulse frequency of 80 kHz, and laser power of 30 W. Increase in scan speed causes percent of spot overlap to decrease and less amount of heat to conduct to the work-piece. As a result, the reduction in thickness of HAZ layers occurs. When spot overlapping increases, the surface roughness value decreases simultaneously. It is also observed that the lower value of scan speed produces a high level of spot overlapping.

On the other hand, when the scan speed is increased at a moderate setting of pulse frequency, it produces low spot overlapping and less material interaction time. Due to constant power density and more spot overlapping produced by the lower scan speeds, dimensions of both cut width and depth are more as compared to the phenomenon observed at higher scan speed. It is worth mentioning that at the lower range of scan speed, the variation in cut width dimensions is less.

On the contrary, at the lower range of scan speed, larger depth dimensions are achieved due to high material interaction time and continuous spot overlapping. In addition to that, reduction of laser penetration rate at each pass along with a spattering of molten materials is observed at the micro-groove surfaces because of the high number of passes. Therefore, both cut width and

depth dimensions tend to reduce with the lower scan speed. As a result, the surface of the machined micro-grooves becomes rough at higher scan speed and vice versa.

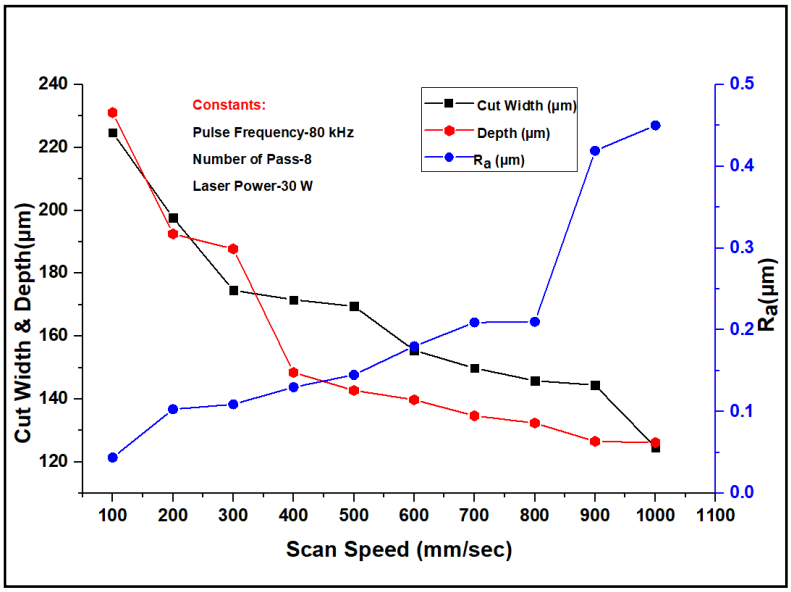

Figure 4.6 Effect of high scan speed on cut width, depth, and R_a

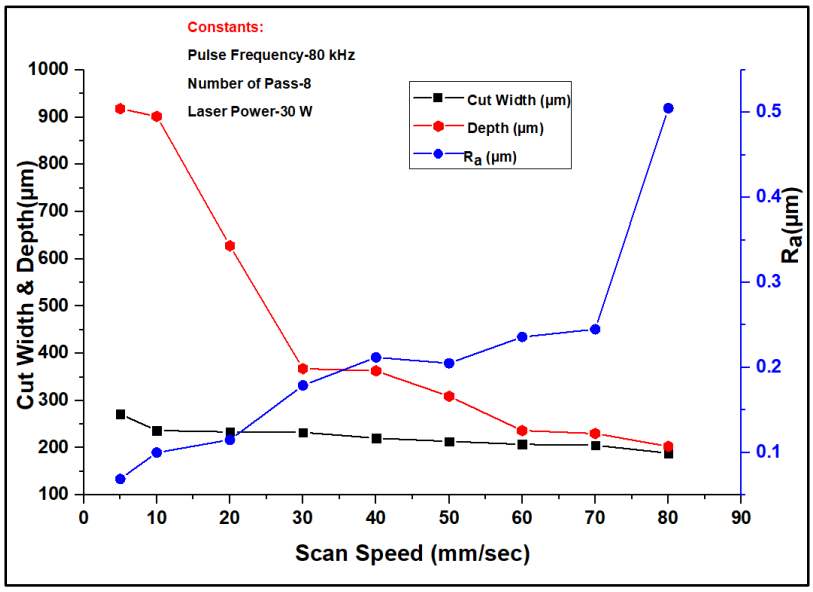

Figure 4.7 Effect of low scan speed on cut width, depth, and R_a

4.7.2 Influence of Pulse Frequency on Cut Width, Depth, and Surface Roughness on Ti-6Al-4V Micro-Grooves

Pulsed mode of operation of the fiber laser system provides high instantaneous power for a period of pulse duration and follows with a period of power off. During pulsed mode fiber laser

micro-grooving operation, melt ejection occurs in each laser pulse on time while melt front cools during pulse off-time. It is essential for the micro-grooving operation to reduce the quantity of the dross formation, which can be achieved by producing low heat input. Low heat input can also reduce the quantity of melt formed but also imparts sufficient cooling between two successive laser pulses.

Figure 4.8 shows the influence of pulse frequency on cut width, depth, and surface roughness of fiber laser machined micro-groove surfaces while other process parameters are kept constants at number of pass of 8, scan speed of 40 mm/sec and laser power of 30 W. It can be observed in the present set of experiments, scan speed remains constant at a moderately high value. This high scan speed is beneficial not only for understanding the complex phenomenon of pulse frequency on the micro-groove geometry but also to reduce the surface roughness in a considerable amount. Pulse frequency varies inversely with the laser beam energy when the laser power is constant. Therefore, when pulse frequency is increased during the present set of experiments keeping other process parameters are constants, laser beam energy reduces. This phenomenon holds with the moderately high settings of scan speed.

In contrast, this phenomenon reverts with the combination of moderately low settings of scan speed with increased pulse frequency. Low settings of pulse frequency lead to an increase in laser beam energy. This high laser beam energy causes more heat input to the micro-groove surface. Thus melting of more amount of material is observed. Therefore, cut width and depth dimensions are relatively high at low pulse frequency. This phenomenon also holds for producing rough micro-groove surfaces at low pulse frequency.

With the increase of pulse frequency with moderately high settings of the number of passes, a reduction laser beam penetration occurs due to low peak power. The effect of spot overlapping also has a pivotal role in micro-groove topology. Besides, the melted material is not removed entirely due to the absence of assist gas. The remaining melted material is re-solidified at the micro-groove edges at high settings of pulse frequency. Therefore, low peak power at high settings of pulse frequency causes decrement in the dimensions of both cut width and depth.

Along with this, increment in surface roughness is observed at higher values of pulse frequency. The combined effect of lesser removal of material and the lesser amount of re-solidified material due to low peak power causes an increment in surface roughness values. Hence, better finished micro-groove is observed with the decrement of pulse frequency.

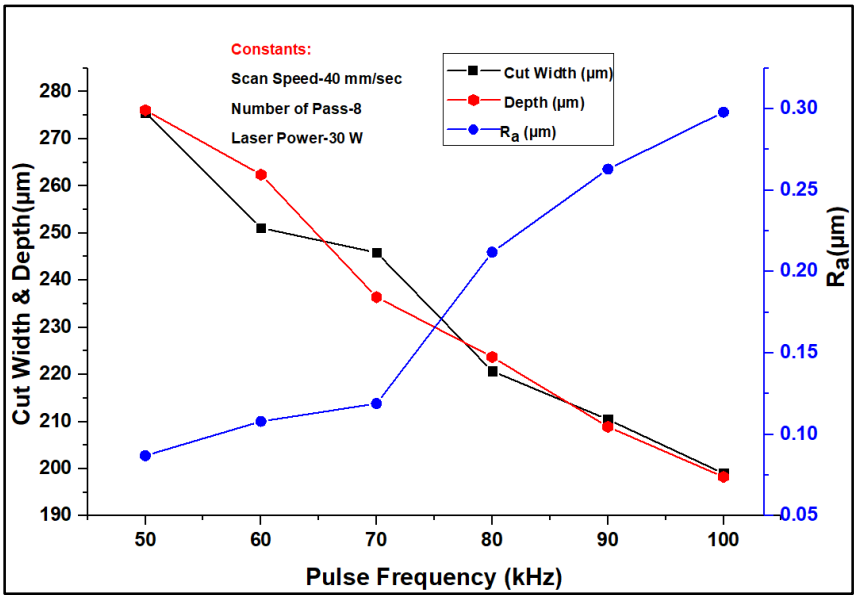

Figure 4.8 Effect of pulse frequency on cut width, depth, and R_a

4.7.3 Influence of Number of Pass on Cut width, Depth, and Surface Roughness on Ti-6Al-4V Micro-Grooves

Figure 4.9 shows the influence of the number of pass on cut width, depth, and surface roughness of fiber laser machined micro-groove surfaces. Scan speed of 40mm/sec, a pulse frequency of 50 kHz and laser power of 30 W are kept as constants. The present parametric combinations of 12 number of experiments reveal that experiments are carried out with at high heat input to the micro-groove surfaces. It can be also observed from figure 4.9 that the cut width, along with depth dimensions increases with the higher number of passes. This phenomenon happens due to the striking of the laser beam on the work-piece surface repetitively during pulse on time. Besides, the length of focus is altered every time as the number of passes goes on increasing. As a result of that spot size of the laser beam is increased significantly. Therefore, when the laser beam is in defocus condition after removal of material, the penetration rate is gradually decreased. Due to the repetitive strike of the laser beam on the work-piece surface and pulsed mode operation of the fiber laser system, the depth and width increase simultaneously.

Along with the increase in depth and cut width dimensions, an excess amount of molten material is removed from the surface. However, some amount of molten material is re-solidified on the side-wall of the micro-grooves because of the absence of inert gaseous systems in existing machining setup. The moderate-high settings of scan speed lead to the phenomenon of spattering

at the edges of the micro-groove surfaces. Therefore, due to the combined effect of spattering and re-solidification, the dimensions of cut width are reduced after a specific increment of the number of passes as seen in figure 4.9.

The higher number of passes also causes re-solidification of molten material along with the periphery of the micro-grooves. The re-solidified materials contribute to the decrement of surface roughness of micro-grooves. Thus, uniform surfaces are produced at a high number of passes and vice versa.

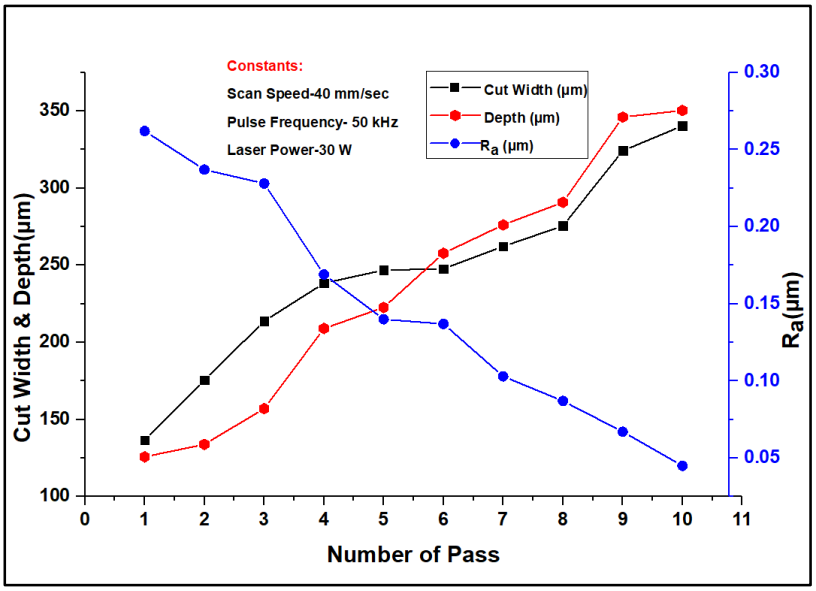

Figure 4.9 Effect of number of pass on cut width, depth, and R_a

4.7.4 Influence of Laser Power on Cut Width, Depth, and Surface Roughness on Ti-6Al-4V Micro-Grooves

Laser power determines the direct energy input to the micro-grooving process. At lower laser power, the energy supplied to the cutting front may be insufficient to cut through the desired depth of the material, whereas at higher laser power, production of clean through cuts necessitates the reduction of scan speed. Laser power also determines the maximum scan speed, which is defined as the minimum speed at which through cut be produced. Both micro-grooving quality and performance are dependent on the laser power.

Figure 4.10 represents the influence of the of laser power on cut width, depth, and surface roughness of fiber laser machined micro-groove surfaces while other process parameters are kept constant at the number of passes of 5, scan speed of 40 mm/sec, pulse frequency of 50 kHz. The

amount of re-solidified material on the micro-grove surface increases with an increase in laser power. Increase in laser power leads to an increase in the dimension of cut width up to a certain extent due to the increase in more power density, power input per unit area.

Also, low settings of pulse frequency produce a higher percentage of spot overlapping, the constant power density at the time of fiber laser micro-machining of Ti-6Al-4V micro-grooves. Hence, better finish surface of micro-groove is observed at low laser power and vice-versa. It is observed that the effect of laser energy in the geometry of the micro-grooves is not having the same functional dependence in both cut width and depth dimensions. The tendency of cut width dimensions is found to be increasing with the combined parametric effects of low laser power, low pulse frequency, and high scan speed. Substantial heat input leads to removal of more amount of molten material from the micro-groove surfaces although the peak power is moderately low due to high settings of the pulse width. Hence dimensions of cut width and depth tend to reduce with the increment of laser power of 20 W. It is also apparent that the focal plane varies each time during pulse off/on time, and the rate of penetration also reduces as the machining time increases.

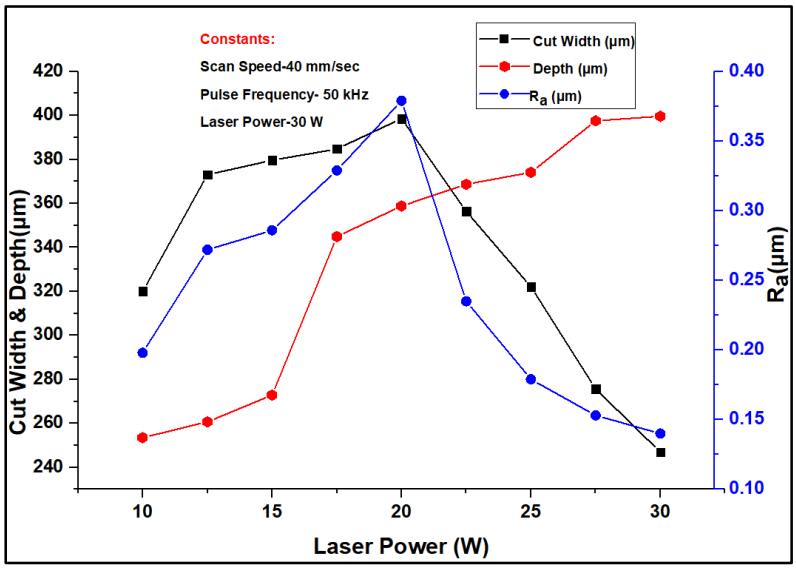

Figure 4.10 Effect of laser power at 100 mm/sec of scan speed on cut width, depth and surface roughness

Figure 4.11 shows the microscopic view of micro-groove profile at the scan speed of 700 mm/sec, the pulse frequency of 80 kHz, laser power of 30 W and number of passes of 8. Figure Figure 4.12 exhibits a microscopic view of the micro-groove profile at scan speed of 40 mm/sec,

pulse frequency of 50 kHz, laser power of 30 W and number of passes of 6. Figure 4.13 shows the microscopic view of micro-groove generated at the scan speed of 30 mm/sec, pulse frequency of 100 kHz, laser power of 30 W and number of passes of 5 respectively. The cut width dimensions are higher for figure 4.12 compared to figure 4.13 due to the higher number of passes. In both the figures, uniform micro-grooves are produced.

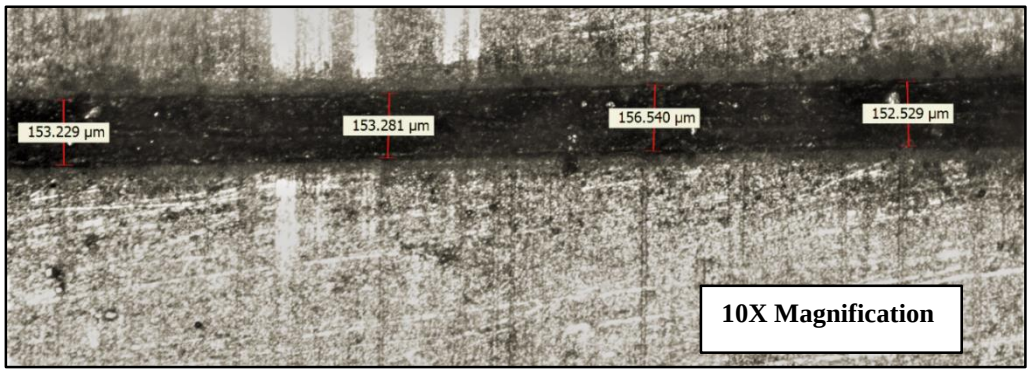

Figure 4.11 Microscopic view of Ti-6Al-4V micro-groove

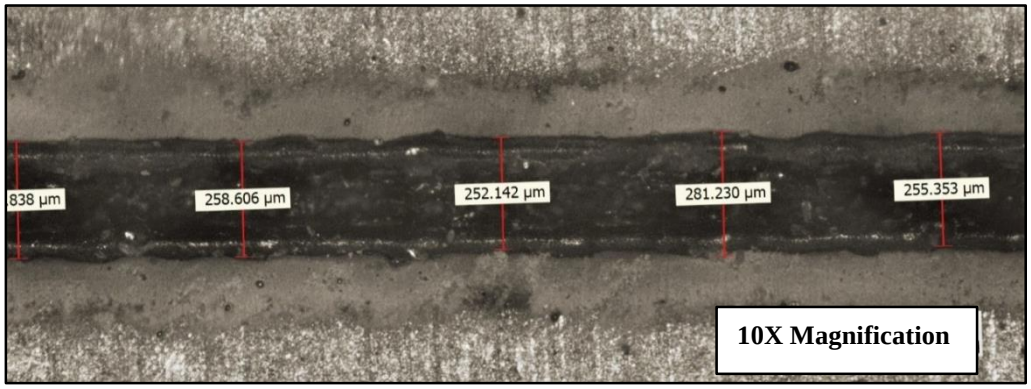

Figure 4.12 Microscopic view of Ti-6Al-4V micro-groove[10]

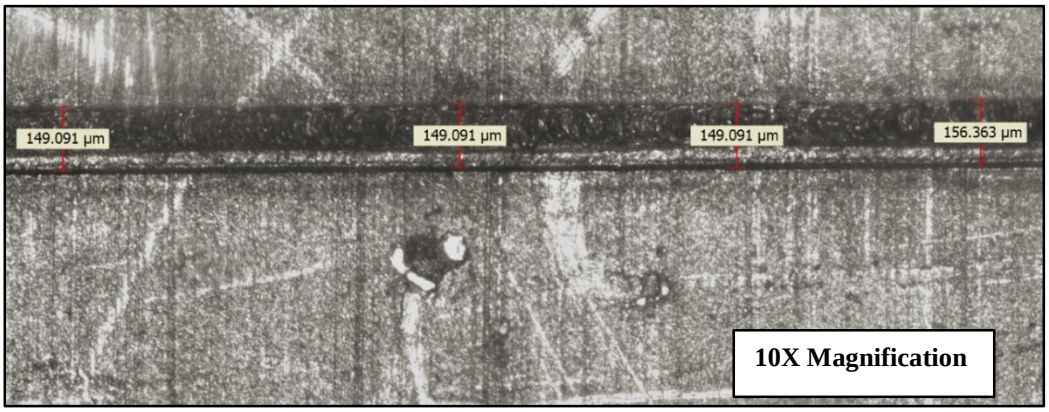

Figure 4.13 Microscopic view of Ti-6Al-4V micro-groove [10]

Figure 4.14 (a) and (b) along with figure 4.15 (a) and (b) represent the 3D views of surface topography of micro-groove surface generated at different parameter settings. At the right side of the 3D view, there is a color scale that shows the measured signal level. Z height data is encoded with that color scale. From figure 4.14 (a), it can be observed that at scan speed of 40 mm/sec at 60 kHz of pulse frequency as compared to scan speed is 700 mm/sec at 80 kHz of pulse frequency, better finished micro-groove surfaces can be obtained. From figure 4.14 (a), it is observed that due to lower laser-material interaction time at a high scan speed of 700mm/sec, comparatively poor surface finish is observed as compared to figure 4.14 (b) for scan speed of 40 mm/sec.

It can also be also observed that from figure 4.15 (a) that at a laser power of 12.5 W when other parameters are constant, better surface topology can be obtained as compared to laser power of 30 W for figure 4.15 (b). The combined effect of the lower scan speed and the higher number of passes produce a higher percentage of spot overlapping in the micro-groove zone due to the formation of re-solidified material. As a result, a better surface finish is observed as shown in figure 4.15 (b).

Thus, selecting a combination of optimum parameters can lead to a better surface quality for potential application in the field of biomedical engineering.

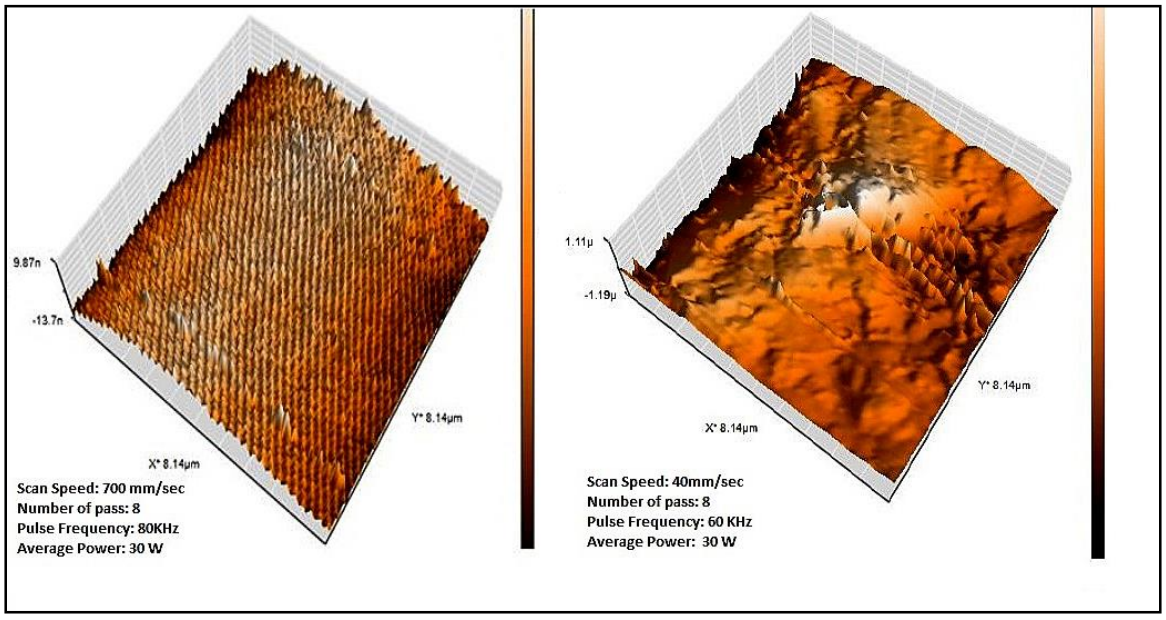

Figure 4.14 (a) and (b) 3D representation of the surface topology of the micro-grooved surface [10]

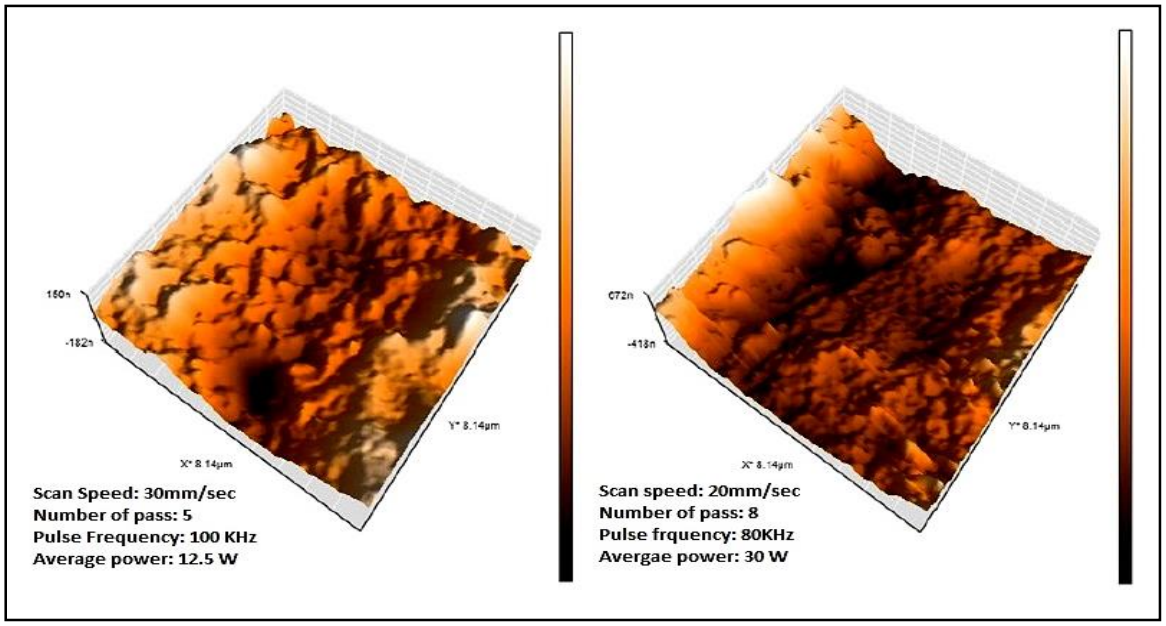

Figure 4.15 (a) and (b) 3D representation of the surface topology of the micro-grooved surface [10]

4.8 Outcomes of the Present Research Work

Fiber laser micro-machining has immense potential for generating micro-grooves on Ti-6Al-4V. The present research work deals with the influence of four process parameters, i.e., laser power of 10 to 30W, the number of passes of 1 to 10; scan speed of 5 to1000 mm/sec; pulse frequency of 50 to 100 kHz during laser micro-grooving on Ti-6Al-4V using 50W diode pumped fiber laser. Different process parametric settings lead to different values of cut width, depth, and surface roughness. From the results of the present experimentation, the following conclusions can be drawn.

(i) Depth and cut/groove width dimensions of micro-groove on Ti-6Al-4V tend to decrease with the higher scan speed with the combination of low pulse frequency, but surface roughness tends to gradually increase owing to low spot overlapping and discontinuous power density at higher scan speed. With the increase of pulse frequency at moderate scan speed, reduction in the dimensions of width and depth of micro-grooves are observed owing to low heat generation.

(ii) At higher values of pulse frequency, rougher micro-groove surfaces are produced. With the increment of number of pass, cut width and depth dimensions both tend to increase. Smooth surface quality is observed due to the increase of number of pass.

(iii) The dimensions of cut width and depth simultaneously increase up to laser power of 20 W, then gradually decrease. Smooth surface quality is observed at low laser power. Thus, the fiber laser system can be successfully implemented for generation of micro-grooves on Ti-6Al-4V with desired surface characteristics and surface profiles.

5. EXPERIMENTAL INVESTIGATIONS INTO FIBER LASER MICRO-GROOVING OF 316L STAINLESS STEEL

5.1. Introduction

Within the domain of austenitic stainless steel, 316L stainless steel is widely used in both bio-medical and automotive industries due to its superior mechanical properties. At present, the utilization of fiber laser micro-machining process on 316L stainless steel (SS) for the manufacturing of stents has increased rapidly. Micro-grooves fabricated from various types of stainless steels are used in different micro-products like micro-thermal devices, micro-heat exchangers, micro-reactors, corrosion resistance, and excellent mechanical properties. Fiber laser micro-machining has a potential application, particularly in micro-grooving operation on 316L stainless steel.

In this present research work, the experiments have been conducted in order to find out the effect of fiber laser process parameters, i.e., scan speed, laser power, and pulse frequency in atmospheric condition as well as in condition of flowing assist air pressure on cut width and surface roughness R_a of micro-groove cut on 316L SS by fiber laser micro-machining process.

Besides, the present research work also deals with a comparative analysis of fiber laser micro-grooving operation of 316L at room temperature along with different elevated temperatures ranging from 100°C to 250°C, with the aid of a developed heating setup. Scan speed and the change in position of a focal point of the laser beam are the two variables considered in the analysis of their effect on the cut width and the HAZ width of the fiber laser generated micro-grooves.

5.2 Selection of Process Parameters and Responses

The process parameters considered for the present research work are laser power, pulse frequency, duty cycle, scan speed, laser peak power, sawing angle, focal point position, and preheating temperatures. The details of the process parameters, i.e., laser power, pulse frequency, duty cycle, scan speed are given in chapter 3. The details of the remaining process parameters are given below:

(i) Laser Peak power: This is pulse energy per pulse duration (J/s = W). Peak power is an essential factor during laser micro-machining operation. During the fabrication of high aspect ratio micro-features, peak power plays an important role.

(ii) **Sawing Angle:** Sawing angle represents the laser beam opening angle and depending on the particular application, the sawing angle is varied. However, for micro-machining operation, higher sawing angle is not preferred due to the wider opening along with the larger dimension of micro-scan profile. Figure 5.1 represents a laser beam sawing angle along with increment in depth achieved through Gyro scan software.

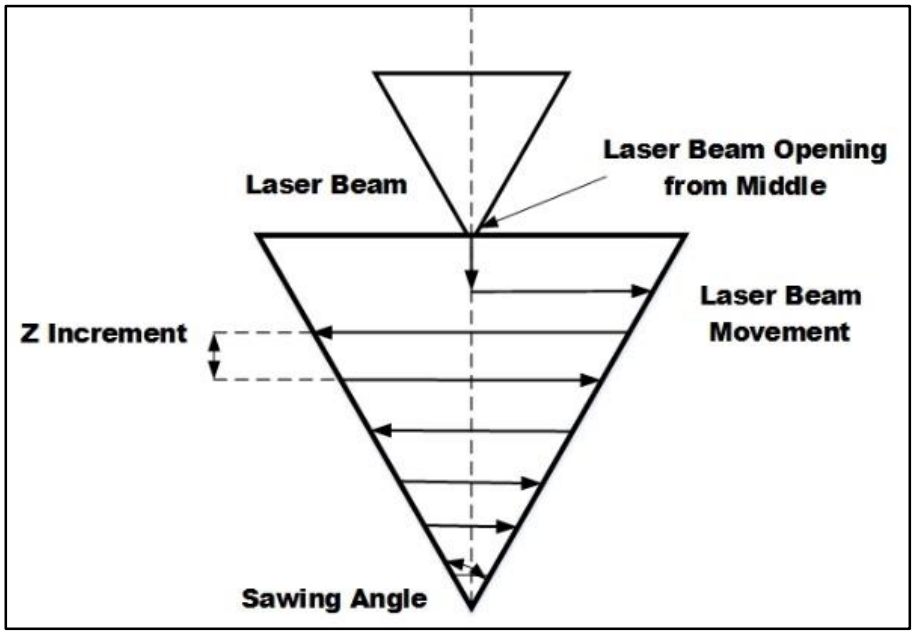

Figure 5.1 Schematic diagram of laser beam movement during the micro-groove formation

(iii) **Temperature:** The experiments are carried out in room temperature and also with elevated temperatures with the aid of developed preheating setup. The preheating set up provides a comparative analysis of the micro-machining characteristics at different temperatures apart from the room temperature.

(iv) **Change in Focal Point Position:** The focal point position has been changed while the numbers of passes are varied as shown in figure 5.2. The changing of focal position, in turn, improves the depth and the uniformity of the fiber laser generated micro-grooves.

(v) **Assist Air Pressure:** High pressure assist air is supplied to remove the molten material from the machining zone as well as to clean the machining zone.

During laser micro-grooving on 316L stainless steel, the machining criteria such as cut width, depth, HAZ width and surface roughness, R_a are measured, and subsequently, parametric analysis has been carried out on micro-grooving characteristics.

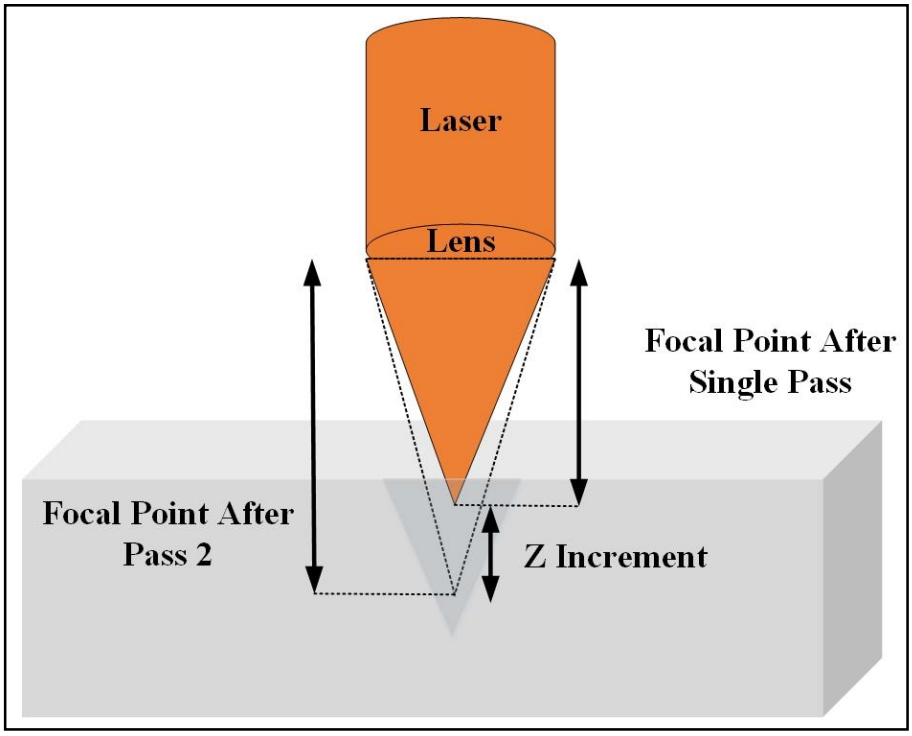

Figure 5.2 Schematic representation of the variation of focal point position of the laser beam at the varying pass

5.3 Properties of 316L

In the present research study, 316L SS is selected with a dimension of 50 mm X 50 mm X 1 mm. The chemical composition of 316L is given in table 5.1. Table 5.2 represents various mechanical and physical properties of 316L.

Table 5.1 Chemical composition of 316L [74]

Grade		C	Mn	Si	P	S	Cr	Mo	Ni	N
316L	Min	-	-	-	-	-	16.0	2.00	10.0	-
	Max	0.03	2.0	0.75	0.045	0.03	18.0	3.00	14.0	0.10

Table 5.2 Properties of 316L [75]

Grade	Tensile Stress (MPa) min	Yield Stress 0.2% Proof (MPa) min	Elongation (% in 50 mm) min	Hardness		Thermal Conductivity (W/m.K)	
				Rockwell B (HR B) max	Brinell (HB) max	At 100 °C	At 500 °C
316L	485	170	40	95	217	16.3	21.5

5.4 Experimental Planning

In the present research study, experiments are carried out on laser micro-grooving of 316L without the supply of assist air, i.e., in atmospheric condition. In addition to this, with a similar set of process parameters, the experiments are repeated with assist air flow at a pressure of 4 kgf/cm^2. The process parameters, considered are laser power of 7.5 W to 20 W, pulse frequency of 55 kHz to 80 kHz and scan speed 0.5 mm/sec to 3 mm/sec. In each set of experiment, one process parameter is kept as a variable while the remaining two other process parameters are kept as constants. Hence, a total of 36 experiments is carried out with multi diodes pumped 50 W nanosecond pulsed fiber laser system in which maximum available peak power is 7.5 kW for the first category of experiments. The experiments are categorized into three sets of experiments in which one set of the process parameter is varied with and without the supply of high pressure assist air. Software designed for micro-scan applications is utilized for the setting of the sawing angle during laser micro-grooving operation. The higher the sawing angle, the higher is the opening of the micro-groove profile. Thus, in order to achieve smaller dimensions of cut width, a low sawing angle is preferred. As a result, in the present research study, the sawing angle is made constant at 0.01°.

In the second category of experiments, a total number of sixty experiments have been carried out at different temperatures, i.e., ambient temperature (24ºC), 200ºC and 250ºC with the variation of the lower range of scan speed ranging from 0.1 mm/sec to 1mm/sec. The other significant parameters such as pulse width, pulse frequency, laser power, number of pass and the assist gas pressure are set at 30 % of the cycle time, 75 kHz, 10 W, 2 and 2.5 kgf/cm^2 respectively from the trial and error. The influence of the scan speed in different temperatures in conjunction with a change in focal position in each number of passes on cut width and the HAZ width of micro-grooves cut on 316L are analyzed and discussed subsequently.

A preheating setup is discussed in chapter 2 has been developed to facilitate high-temperature fiber laser micro-grooving operation on 316L. The workpiece is mounted on the preheating set

up on X-Y table in order to carry out the experiments. Besides, another set of experiments has been carried out by changing the position of the focal point of the laser beam at each number of passes as shown in figure 5.2. The change in focal point, in turn, balances the laser beam penetration rate as compared when the laser beam is kept stationary.

5.5 Measurements

The micro-groove profiles are measured by Leica optical microscope at 1.25X, 20X and 50X optical lenses. The surface roughness (R_a) is measured by a Mitutoyo SJ 410 surface roughness tester with a Gaussian filter. Parameters related to surface roughness measurements are as follows: sampling length (l) of 4 mm and cut off length (λ_c) of 0.8. The measurements of both the cut width and surface roughness are carried out at 5 reference lines, and the result is shown by taking the average of these values. The array of fiber laser fabricated micro-grooves is shown in figure 5.3 utilizing 5X optical lens. For the measurement of depth profile, Talysurf CCI non-contact surface profiler system is also utilized as shown in figure 5.4.

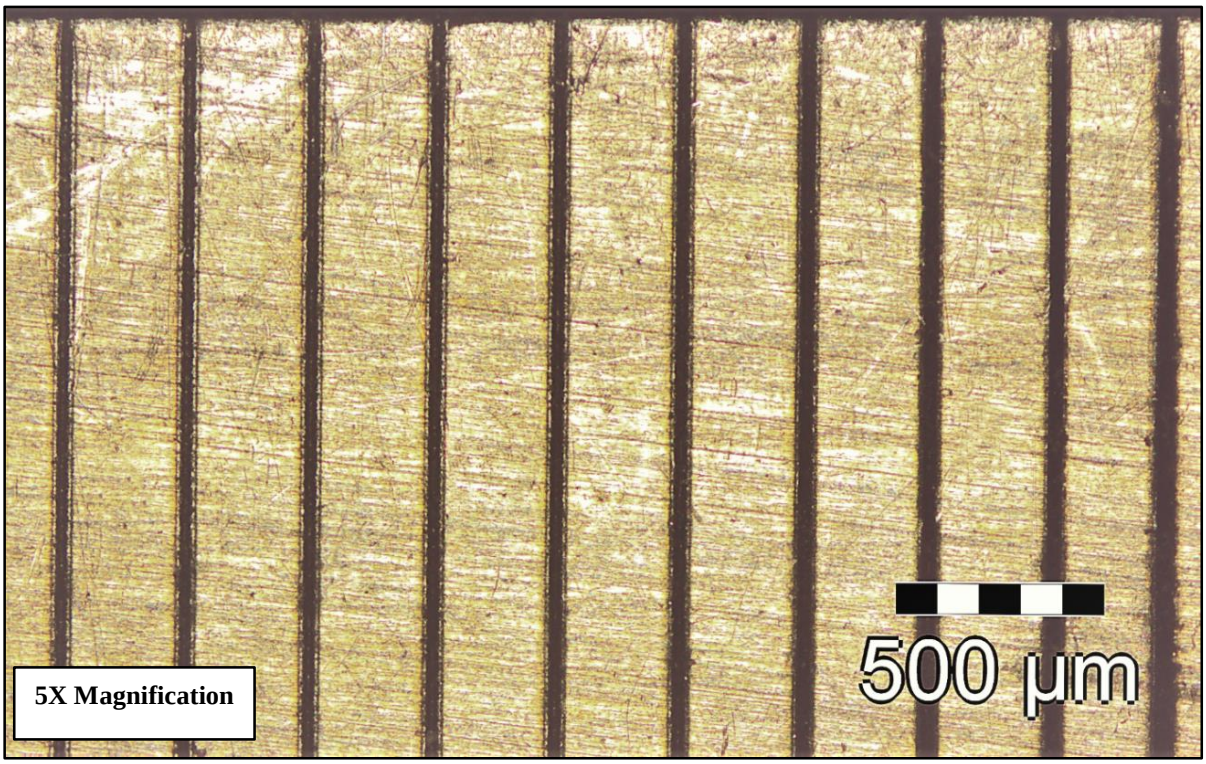

Figure 5.3 Microscopic view of an array of fiber laser fabricated micro-grooves

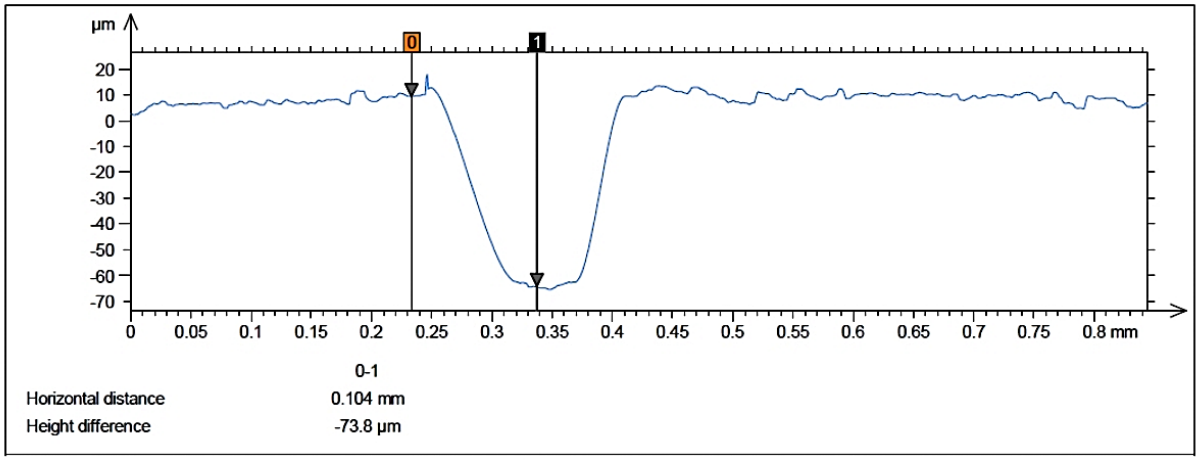

Figure 5.4 Measurement of the depth profile of 316L

5.6 Comparative Study on the Performance of Laser Micro-Grooving on 316L with and without Assist Air

The experiments have been performed with and without assist air supply to study the effect of assist air supply on the performance on laser micro-grooving on 316L SS. The effect of laser power, pulse frequency and scan speed on surface roughness and cut width of fiber laser produced micro-grooves on 316L is shown in table 5.3. The effect of each process parameter on the responses is discussed and analyzed subsequently.

Table 5.3 Values of process parameters and observed responses for micro-groove fabrication on 316L

Exp. No:	Scan Speed (mm/sec)	Laser Power (W)	Pulse Frequency (kHz)	Cut Width without Assist Air (µm)	Cut Width with Assist Air (µm)	Change in Cut Width for Assist Air (%)	R_a without Assist Air (µm)	R_a with Assist Air (µm)	Change In R_a for Assist Air (%)
1	0.05	7.5	55	58.5	46.15	21.11	1.095	1.070	2.28
2	0.05	10	55	47.92	43.28	9.67	1.348	1.654	22.70
3	0.05	12.5	55	63.32	75.39	19.06	1.771	1.820	2.77
4	0.05	15	55	69.82	84.15	20.53	2.786	2.654	4.74
5	0.05	17.5	55	50.96	67.56	32.57	1.787	2.001	11.98
6	0.05	20	55	97.44	74.63	23.41	3.935	3.320	15.63
7	0.05	7.5	55	58.18	62.44	7.32	1.962	1.169	40.42
8	0.05	7.5	60	54.07	70.42	30.24	0.856	1.000	16.82
9	0.05	7.5	65	55.72	56.83	1.99	1.826	0.915	49.89
10	0.05	7.5	70	63.04	55.45	12.04	1.280	0.659	48.52
11	0.05	7.5	75	65.37	37.47	42.68	1.398	0.429	69.31
12	0.05	7.5	80	60.72	32.07	47.18	1.369	1.096	19.94
13	0.5	7.5	80	58.53	49.04	16.21	1.409	1.203	14.62
14	1	7.5	80	57.32	52.22	8.90	2.487	1.216	51.11
15	1.5	7.5	80	55.82	60.62	8.60	1.794	0.618	65.55
16	2	7.5	80	55.02	57.44	4.40	1.752	0.447	74.49
17	2.5	7.5	80	52.34	57.38	9.63	1.587	1.014	36.11
18	3	7.5	80	47.22	54.92	16.31	1.531	0.344	77.53

5.6.1 Effect of Laser Power on Cut Width and Surface Roughness, R_a

In the first set of experiments, the laser power is varied from 7.5 W to 20 W while the other fixed parameters are set at 55 kHz of pulse frequency, 0.5 mm/sec of scan speed and 99 % of the duty cycle. The high value of the duty cycle is considered for all the 36 experiments in order to achieve high laser power. Figure 5.5 corresponds to the effect of laser power on cut width with the supply of assist air and without the assist air supply.

In figure 5.5, it can be observed that in the presence of assist air, the cut width dimensions of the micro-grooves tend to increase more, as compared to the experiments conducted without the supply of assist air. However, the maximum cut width dimension is found to be 97.44 µm in the absence of assist air at 20 W of laser power. An increment in laser power produces a sufficiently high amount of laser peak power in the machining zone. Subsequently, a high amount of energy is further generated by an increase in laser peak power. As a result of this, instantaneous melting and vaporization occur in the machined zone. Therefore, a deeper layer of material is removed and leads to an increment in cut width dimensions. The presence of a high pressure flow of assist air has attributed less formation of re-solidified material at the micro-groove edges, which in turn has increased the cut width dimensions. However, when the laser power reaches at 20 W, sufficient amount of laser pulse energy, as well as laser beam peak power, can remove the re-solidified material from the edges and lead to a steep rise in the cut width dimension.

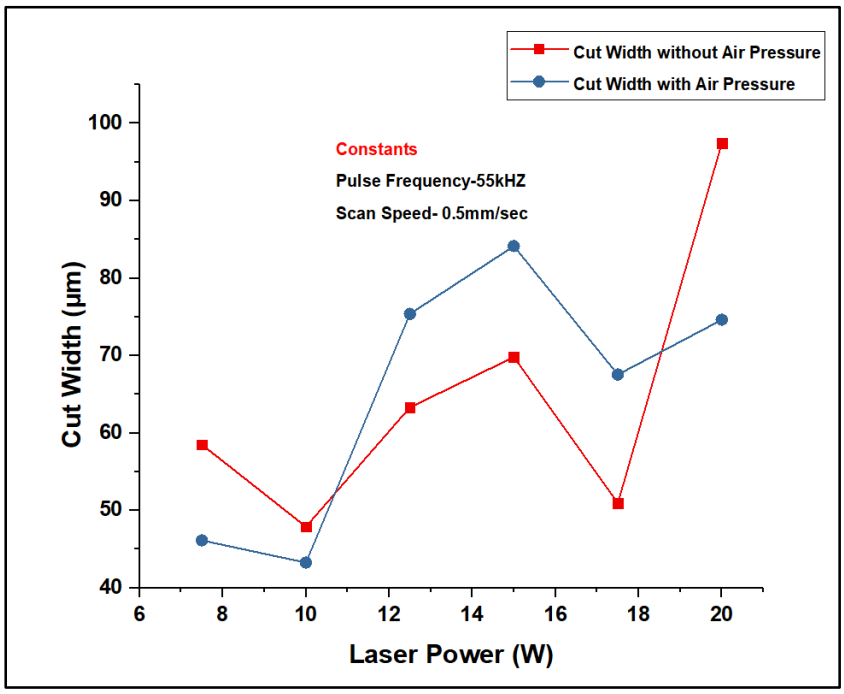

Figure 5.5 Effect of laser power on the cut width

Figure 5.6 represents the effect of laser power on surface roughness R_a with and without the supply of high pressure assist air. The average values of surface roughness, R_a with assist air supply and without assist air are found as 2.13 µm and 2.09 µm respectively. From figure 5.6, it can be observed that with the increment of laser power up to 15 W, R_a tends to increase irrespective of the supply of assist air. A drop in values of R_a can be observed at the laser power of 17.5 W in which the high flow of assist air aids in lowering of R_a value considerably. This phenomenon can be the effect of re-solidified material along the micro-groove zone, which lowers the surface roughness.

Furthermore, with the increment in laser power, there is a rapid increase in R_a value in both the conditions due to the reason that the material from the laser irradiated zone gets the sufficient energy to melt and evaporate instantly. Thus, the laser peak power intensity can penetrate furthermore. However, simultaneous evaporation of the surfaces may occur in the irradiated spot centre, and as a result, the machined surface has a high irregularity. The higher material removal rate is observed during the flow of high pressurized assist air while combining with high laser power.

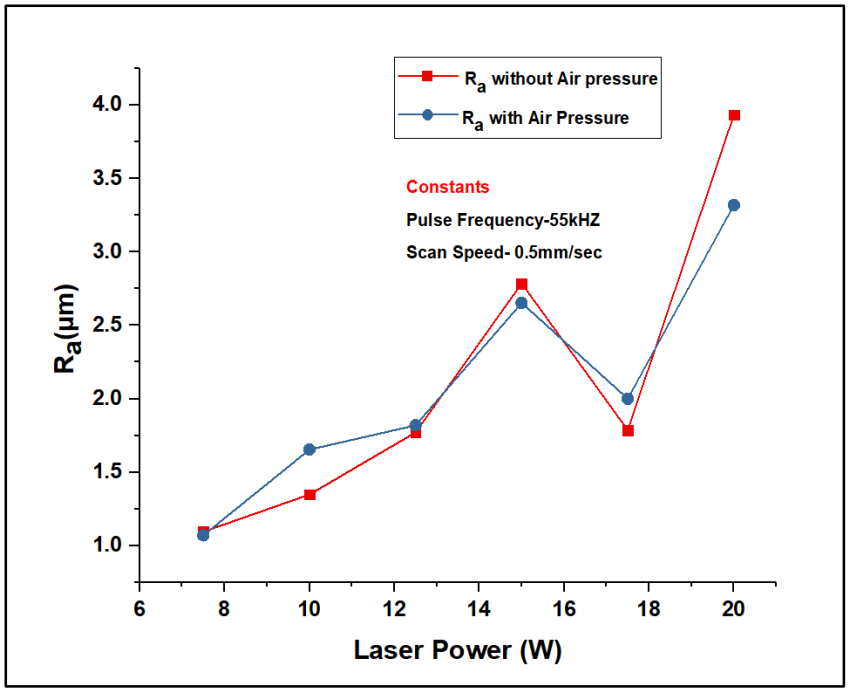

Figure 5.6 Effect of laser power on R_a

5.6.2 Effect of Pulse Frequency on Cut Width and Surface Roughness, R_a

In the second set of experiments, pulse frequency varies from 55 kHz to 80 kHz, whereas the constant parameters are laser power of 7.5 W, scan speed of 0.5 mm/sec with and without the supply of assist air. Figure 5.7 shows the effect of pulse frequency on cut width with and without the supply of assist air. The effect of the supply of high pressure assist air with the increment of pulse frequency is found to be more predominant than the laser power. From figure 5.7, it is observed that in the presence of assist air supply, cut width tends to decrease with the increment in pulse frequency. On the contrary, a reverse phenomenon is observed with the absence of assist air. At 75 and 80 kHz of pulse frequency, a notable decrease in the values of cut width dimensions is observed in the presence of assist air supply. Although, the drop in laser peak power is inevitable at a high pulse frequency setting. A large number of laser pulses induce a more substantial laser material interaction time while keeping the pulse energy constant. Longer laser material interaction time provides a sufficient amount of time for the melting and evaporation of material removal. Although, re-solidification phenomenon along with HAZ are the dominant factors without the supply of assist air. When the high spot overlapping factor in combination with the flow of high pressure assist air, the phenomenon is reversed and leads to the lowering of cut width dimensions. In addition to this, the changes in cut width dimensions without assist air are not as high as compared to the assist air supply. High pressure assist air forces the extra amount of molten material from the machining zone, leading to the reduction in cut width dimension along with the deeper cut width.

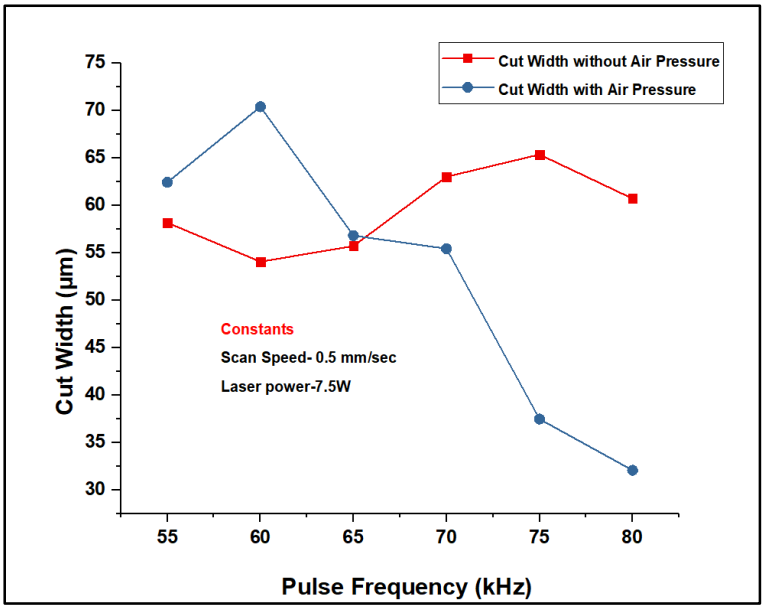

Figure 5.7 Effect of pulse frequency on the cut width

The effect of pulse frequency on surface roughness R_a is shown in figure 5.8. When pulsed laser beam irradiates on 316L SS surface, a thin melted layer is formed on the machined surface. Further, the machined surface is found to be less interrupted by the liquid displacement on the micro-machined zone. This is due to the action of recoil pressure, formed during the fiber laser interaction with 316L surface. As a result, smooth machined surfaces can be observed at a high pulse frequency. The smoother micro-grooves can also be produced when a high jet flow of assist air is applied to remove the molten material from the micro-groove zone. As the material removal rate is low at high pulse frequency (due to low laser beam peak power), the flow of high pressure assist air reduces the attributes of spattering as well as HAZ width from the micro-groove. The absence of assist air supply leads to high values of R_a in comparison to the presence of assist air supply. High peak power, in combination with assist air, significantly reduces R_a in a considerable amount. At 80 kHz of pulse frequency, in the presence of assist air supply, R_a tends to rise as compared to the previous set of values.

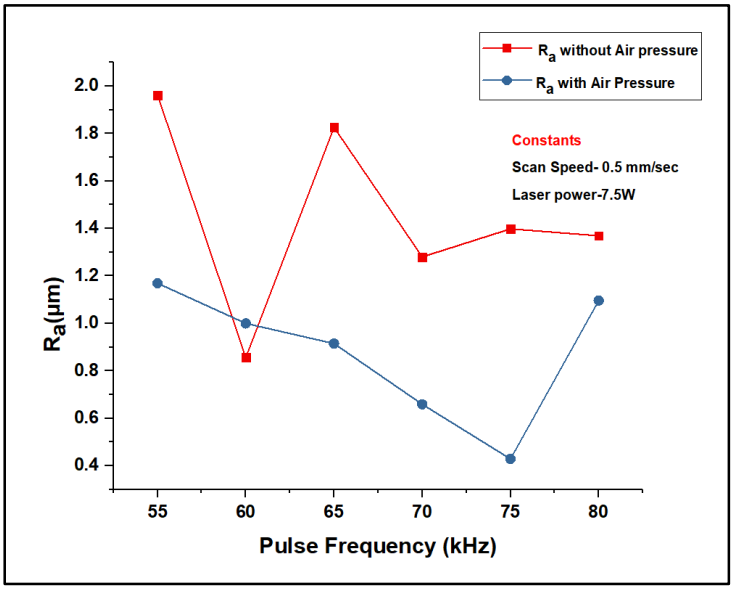

Figure 5.8 Effect of pulse frequency on R_a

At 50 X magnification, the microscopic views of the micro-grooves profiles cut at the variation of pulse frequency in the presence of assist air supply has been shown in figure 5.9 (a) and (b). From figure 5.9 (a) and (b), it is obvious that HAZ is detrimental for non-uniform and profile. A 3D profile of fiber laser fabricated micro-groove on 316L is shown in figure 5.10 at the combination of laser power of 15 W, pulse frequency of 55kHz, scan speed of 0.5 mm/sec and duty cycle of 99%. A surface roughness profile at laser power of 15 W, pulse frequency of 55 kHz, scan speed of 0.5 mm/sec, and duty cycle of 99% is shown in figure 5.11.

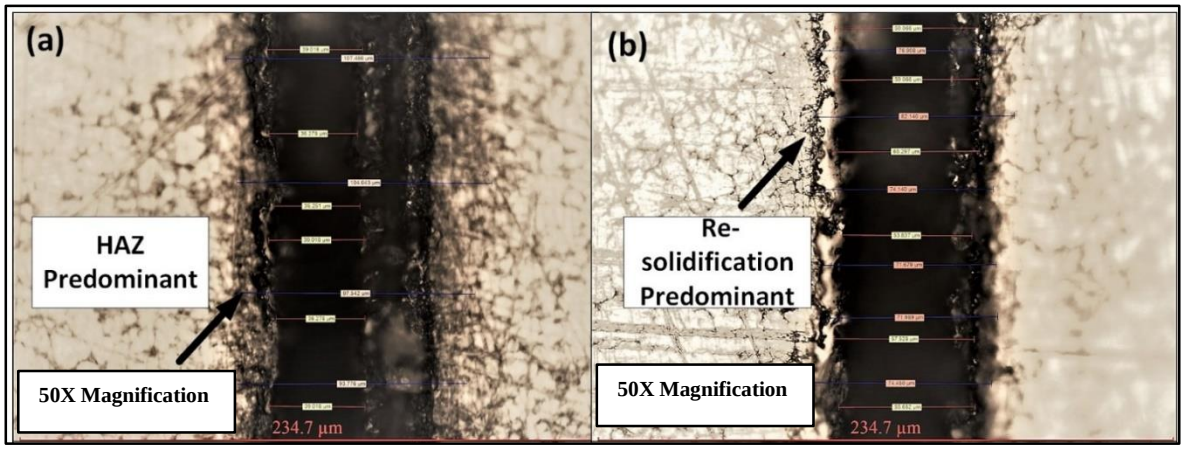

Figure 5.9 Microscopic view of a micro-groove profile at 50X

(a) At 80 kHz of pulse frequency; (b) At 70 kHz of pulse frequency in assist air supply (Constants: laser power of 7.5 W and scan speed of 0.5 mm/sec)

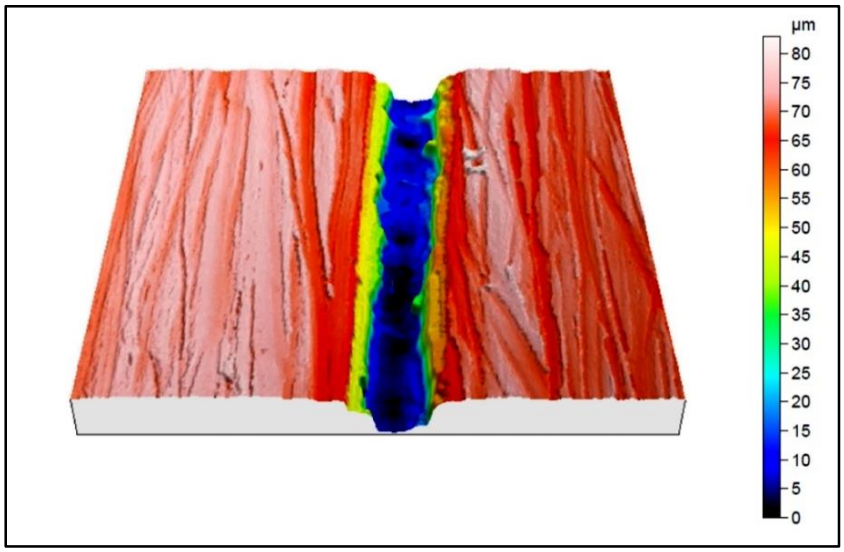

Figure 5.10 3D profile of fiber laser generated micro-groove on 316L

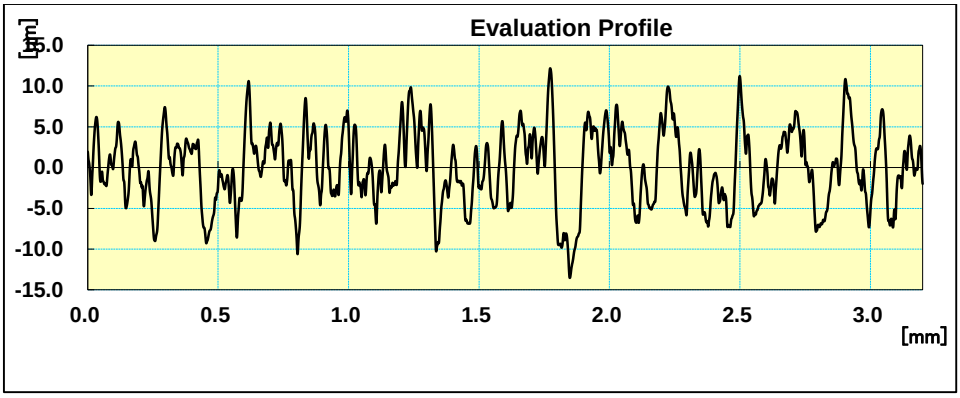

Figure 5.11 Surface roughness profile of fiber laser generated micro-groove with assist air at scan speed of 0.05mm/sec, laser power of 20 W, pulse frequency of 55kHz

5.6.3 Effect of Scan Speed on Cut Width and Surface Roughness, R_a

In the present set of experiments, pulse frequency of 80 kHz and laser power of 7.5 W are kept as constants. The effects of scan speed with and without assist air supply on cut width are shown in figure 5.12. At higher scan speed, cut width without assist air follows a gradual decrease in the cut width dimension as observed from figure 5.12. On the contrary, a cut width dimension in the presence of assist air is more significant at 1.5 mm/sec of scan speed, followed by a gradual decrease in the cut width dimensions. The average dimensions of cut width are comparatively higher when the assist air is supplied at high pressure. This suggests that assist air supply has partially blown away the molten material from the machining zone to facilitate more penetration of the laser beam in the machining zone. Machining time in combination with the assist air determines the homogeneity and uniformity of the micro-groove profiles. When the scan speed increases, it is evident that the machining time will subsequently be reduced, which in turn will lower the cut width dimensions. When the laser beam moves to and fro with the machining zone, some amount of molten material will be accumulated at the machining zone, which will ultimately reduce the laser beam penetration rate. At each pass, the penetration rate will be decreased with or without the supply of assist air. However, a sufficient amount of assist air pressure will lead to the removal of the molten material and subsequently increase the cut width dimensions. This phenomenon holds at higher assist air pressure in combination with a scan speed of 1.5 mm/sec. Nevertheless, low machining time, along with low penetration rate, will ultimately reduce the cut width dimension as observed from figure 5.13.

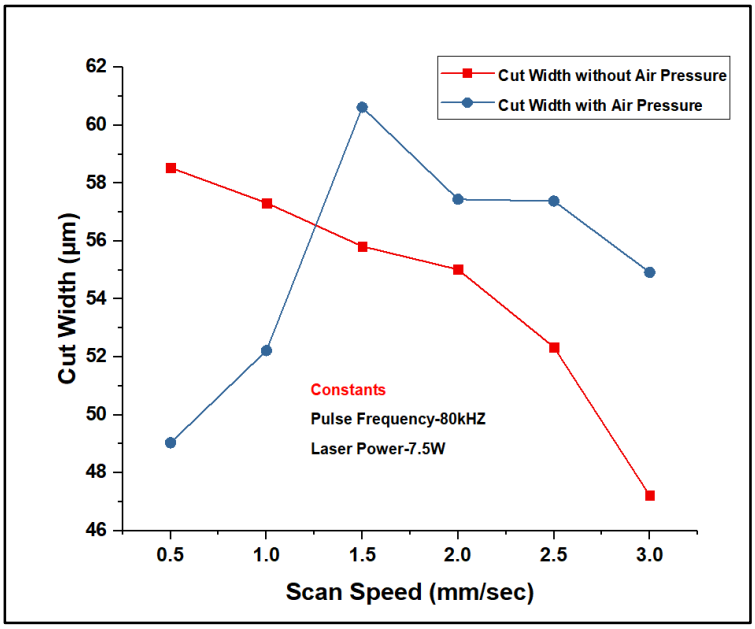

Figure 5.12 Effect of scan speed on the cut width

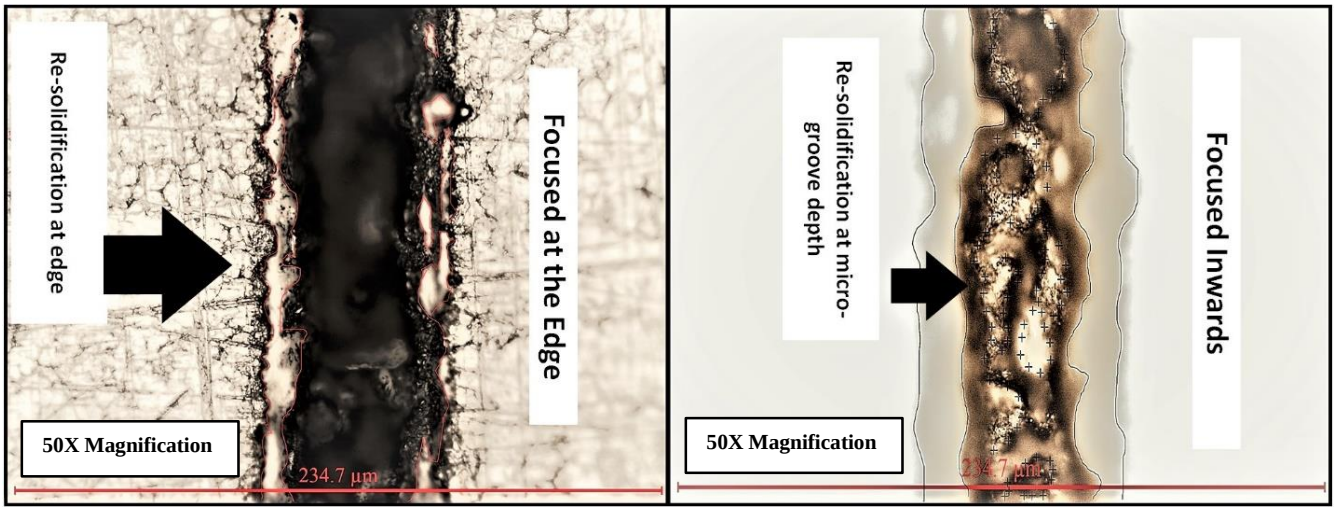

Figure 5.13 Microscopic view of fiber laser fabricated micro-groove profiles at 50X

Figure 5.14 depicts the effects of scan speed on average surface roughness R_a of the cut surface of micro-groove with and without assist air supply. The supply of high pressure assist air has considerably improved micro-groove homogeneity by reducing the surface roughness. Scan speed and pulse frequency are the most critical parameters for determining the laser spot overlapping factor and laser material interaction time. The lower laser material interaction time during high scan speed helps to reduce the surface roughness parameters considerably. When high scan speed (low MRR) in combination with high pressure assist air comes into effect, the excess amount of molten material is blown away. In the presence of assist air, heat dissipation from the molten material also significantly increases. Thus, re-solidification of the molten material on the inner walls of the micro-grooves is observed, as shown in figure 5.14. Without the supply of assist air, it is difficult to remove the extra amount of molten material from the micro-groove periphery. Furthermore, in the absence of assist air, the excess amount cannot be blown away completely, which results in high surface roughness in terms of R_a.

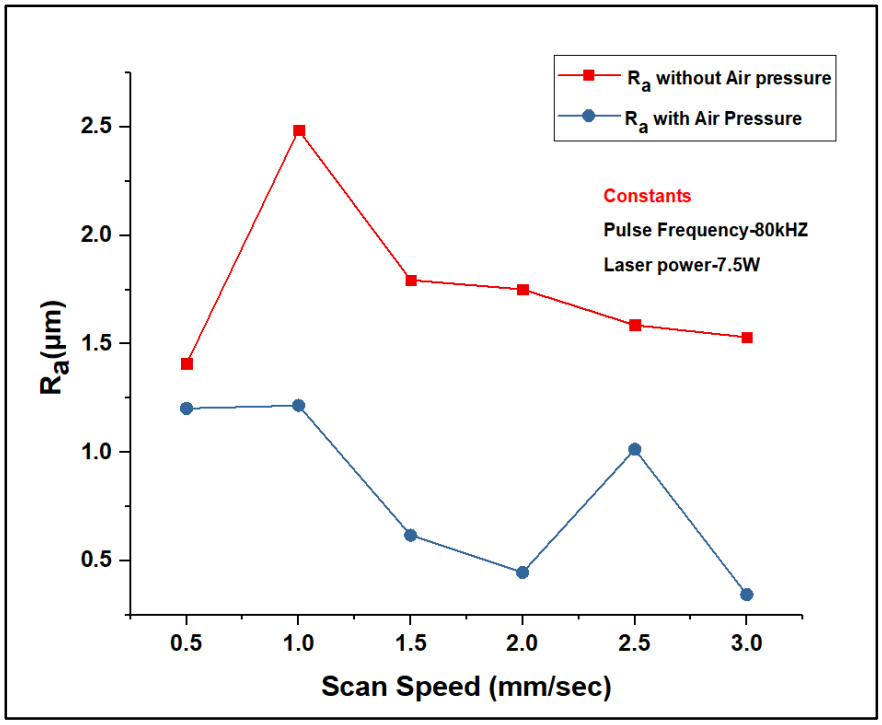

Figure 5.14 Effect of scan speed on R_a

5.7 Comparative Study on the Performance of the Laser Micro-Grooving on 316L with and without Elevated Temperature

In this category of experiments, experiments are classified into two parts. i.e., with and without elevated temperature with the change in the focal point position to the workpiece. Scan speed and focal point position of the laser beam are the two response variables, considered in the analysis of their effect on cut width and the HAZ width of the fiber laser generated micro-grooves. The other significant parameters such as pulse width, pulse frequency, laser power, and the assist gas pressure are set at 30% of the cycle time, 75 kHz, 10 W and 2.5 kgf/cm^2 respectively. Table 5.3 and table 5.4 exhibit the results of the process parameters on the responses.

Table 5.3 Results of cut width at different temperatures with and without change in focal point

Exp. No.	Scan Speed (mm/sec)	Cut Width (µm)			Cut Width (µm) at Change in Focal Position of 0.05 µm			Percentage of change due to change in Focal Position (%)		
		250°C	200°C	24°C	250°C	200°C	24°C	250°C	200°C	24°C
1	0.1	61.00	57.03	79.43	82.92	83.33	87.57	35.93	46.12	10.25
2	0.2	55.72	61.83	80.10	73.55	75.00	91.53	32.00	21.30	14.27
3	0.3	51.97	57.53	73.03	77.83	60.13	84.23	49.76	4.52	15.34
4	0.4	49.26	54.87	71.87	73.56	65.83	85.70	49.33	19.97	19.24
5	0.5	49.17	55.13	76.10	74.75	64.20	81.93	52.02	16.45	7.66
6	0.6	49.86	54.77	74.57	69.72	62.20	79.47	39.83	13.57	6.57
7	0.7	50.17	56.80	73.67	69.13	59.23	84.23	37.79	4.28	14.33
8	0.8	48.50	57.30	74.23	64.66	61.70	82.60	33.32	7.68	11.28
9	0.9	47.13	56.90	69.77	66.80	62.77	79.60	41.74	10.32	14.09
10	1	50.93	57.27	71.90	64.62	60.20	74.30	26.88	5.12	3.34

Table 5.4 Results of HAZ width at different temperatures with and without change in focal point

Exp. No.	Scan Speed (mm/sec)	HAZ Width (µm)			HAZ Width (µm) at Change in Focal Position of 0.05 µm			Percentage of change due to change in Focal Position (%)		
		250°C	200°C	24°C	250°C	200°C	24°C	250°C	200°C	24°C
1	0.1	48.80	25.12	14.73	32.55	24.33	20.11	33.30	3.14	-36.52
2	0.2	44.93	21.20	14.43	20.23	19.53	18.50	54.97	7.88	-28.21
3	0.3	22.87	19.67	10.42	16.66	17.43	14.12	27.15	11.39	-35.51
4	0.4	20.68	19.97	10.60	18.28	16.20	16.40	11.61	18.88	-54.72
5	0.5	18.47	18.68	13.62	17.13	15.07	14.55	7.26	19.33	-6.83
6	0.6	19.50	19.87	12.75	18.27	13.72	14.38	6.31	30.95	-12.78
7	0.7	25.30	15.27	10.58	3.47	13.95	15.36	86.28	8.64	-45.18
8	0.8	19.90	16.37	11.68	20.46	15.38	16.10	-2.81	6.05	-37.84
9	0.9	23.35	16.70	8.78	20.83	14.95	14.61	10.79	10.48	-66.40
10	1	24.35	15.38	9.77	21.10	13.25	12.83	13.35	13.85	-31.32

5.7.1 Effect of Scan Speed and Change in Focal Point Position at Elevated Temperatures on Cut Width of 316L Micro-Grooves

Figure 5.15 deals with the effect of scan speed on cut width at different elevated temperature, whereas figure 5.16 deals with the effect of scan speed on the cut width due to change in focal point position at the elevated temperatures. It can be observed from figure 5.15 that with the increment of scan speed, cut width has an overall tendency to decrease for all the temperatures. At 250°C, the cut width dimensions are the lowest, whereas the cut width dimensions are the largest at the room temperature when there is no change in the focal point position of the laser beam. In comparison, the dimensions of cut width at a downward shifting of focal point position by 50 µm are significantly large compared to cut width dimensions when there is no change in the focal point position. The reason behind is that only a fraction of heat input is conducted into 316L during fiber laser irradiation on 316L. The fraction of conducting energy contributes a considerable amount of HAZ in fiber laser fabricated micro-grooves on 316L. Nakao et al. [76] observed that steels melting is the predominant factor in the material removal and the sign of HAZ is inevitable during laser fabrication of micro-grooves in austenitic stainless.

The density of 316L varies with the temperature, the variation of the pressure inside the micro-grooves may occur, for which re-solidification of the molten material may arise. The re-solidification process starts from the outer lateral boundary of the melt-pool and gradually grows towards the centre of the micro-grooves. During the re-solidification of the molten material may be shrunk, which further leads to the geometrical micro -movement of the molten material. The laser beam penetration increases when the focal point position of the laser beam is varied with each number of passes. As a result, the dimensions of the cut width tend to increase. As in the present set of experiments, 316L is elevated at high temperatures (250°C); the cooling rate of the molten material is increased. As all the experiments are carried out in the presence of compressed air flow instead of inert gas, there is a high possibility of accumulation of the molten material in the micro-groove front along with the formation of oxides.

The re-solidification and distribution of the cooling rate from the micro-grooving area are the critical factors for determining the metallurgical structures of laser fabricated micro-grooves. The prolonged cooling rate of the molten material may produce precipitation of chromium carbide at the grain boundaries [77]. Further, grain refinement may occur due to high cooling rates achieved near the cut profile. The refined grain, in turn, produces uniform micro-grooves with

less waviness at the elevated temperatures compared to the micro-grooves produced in ambient temperature.

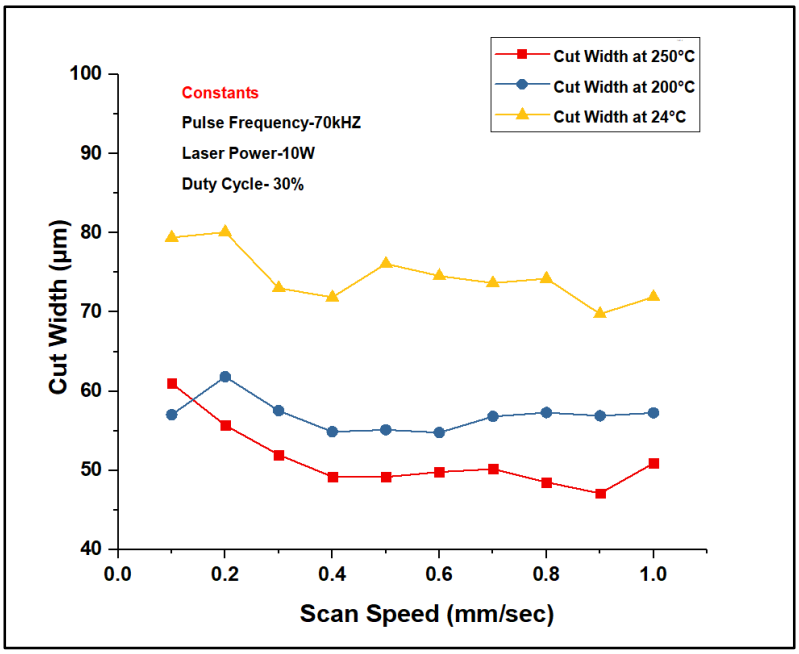

Figure 5.15 Effect of scan speed on cut width at different temperatures

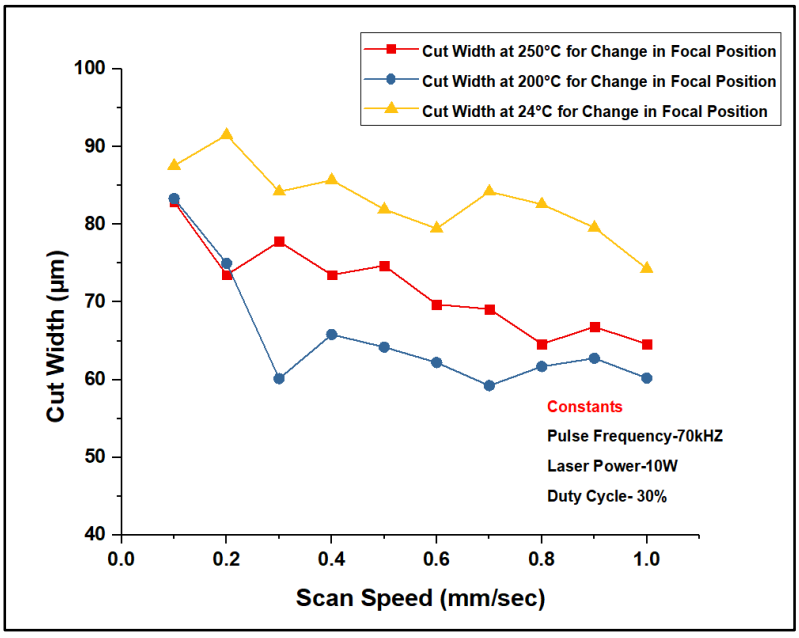

Figure 5.16 Effect of scan speed on cut width at different position of the focal point of the laser beam at different temperatures

5.7.2 Effect of Scan Speed and Change in Focal Point Position at Elevated Temperatures on HAZ Width of 316L Micro-Grooves

Figure 5.17 represents the effect of scan speed on HAZ width at different temperature. The effect of scan speed on HAZ width at a change in the focal position of the laser beam is shown in figure 5.18. From figure 5.17, it is observed that the HAZ width reduces significantly up to the scan speed of 0.7 mm/sec. On the contrary, the dimensions of the HAZ width are significantly lower with the comparison of HAZ width dimensions while any change in the focal point position of the laser beam, as shown in figure 5.18. It can be observed from both the figures (figure 5.17 and 5.18) that with the increment of scan speed, the dimensions of HAZ width are reduced. The dimensions of HAZ width at the downward shifting of focal point position tend to be lower than the dimensions at the constant focal point position. The combined effects of pulse frequency mainly govern the micro-grooving quality and scan speed. When the scan speed is increased, laser-material interaction time is decreased while inducing a significant amount of spattering around the periphery of the micro-grooves. The spattering of the molten material occurs due to the conversion of thermal energy into lattice-vibrational energy before releasing of the atomic particles from the surface. For surface melting and subsequent re-solidification, the solid-liquid interface initially moves away from the micro-grooves and then travels back to the periphery of the micro-grooves with a velocity of v. The relationship between the velocity of the solid-liquid interface with the melting (T_m) and interface temperatures (T_i) is shown in equation 5.1.

$$v \propto (Tm - Ti) \quad \ldots[Eq^n 5.1]$$

Equation 5.1 signifies that the velocity of the molten material is higher when the interface temperature is low. In comparison to this, when the interface temperature increases with the preheating condition, it reduces the velocity of the molten material. In addition to this, temperature gradients also reduce significantly in the irradiated region for the high-temperature of the workpiece during fiber laser micro-grooving operation. As a result of this, low thermal strain and thermally are induced stresses in this region. However, re-solidification in the micro-groove area along with the formation of oxide particles, is inevitable owing to compressed air flow. The spattering phenomenon varies inversely with the homogeneity of the micro-grooves and tends to increase with the increment in the scan speed. The effect of spattering may be

partially eliminated with the downward shifting of focal point position with the different number of passes. The effect of re-solidification, along with spattering, is shown in figure 5.19.

It can be observed from table 5.3 and 5.4 that the cut width and HAZ width dimensions in ambient temperature are relatively low as compared to the elevated temperatures of the workpiece. When the temperature of the surroundings of the fiber laser generated micro-groove of 316L decreases below the melting temperature, local super-cooling of the molten material may occur. As a result of this, the latent heat from the micro-groove surface is released quickly and induces re-solidification. In contrast to the elevated temperature micro-grooving process, high thermal strain and thermally stresses will be induced due to the steep thermal gradient at the micro-grooving zone. The cumulative effect of all the phenomena mentioned above will affect the uniformity of the micro-grooves significantly. Cedelle et al. [78] reported that the preheating of mirror polished stainless steel (304L) substrates at 400°C besides a slight increase in the oxide layer thickness with no composition texturing promotes surface physical texturing at the nanoscale level. The preheating of the substrate over its transition temperature allows cleaning of contaminants present at the surface (molecules of water, grease, dust) and thus improves the solid-liquid contact. Variation in focal point position certainly improves the uniformity of the micro-grooves. Figure 5.20 represents the 3D profile of fiber laser generated micro-groove without a change in focal point position of the laser beam at the combination of scan speed of 0.1 mm/sec, laser power of 10 W, pulse frequency of 70 kHz and duty cycle of 30 %.

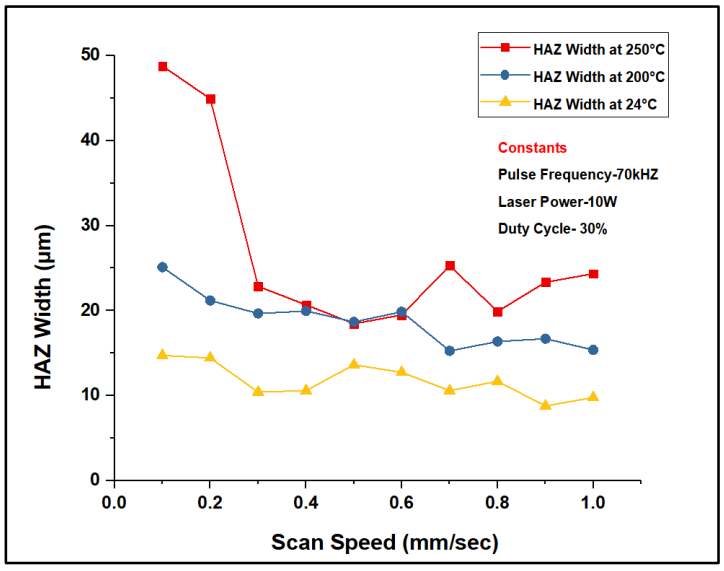

Figure 5.17 Effect of scan speed on HAZ width at different temperatures

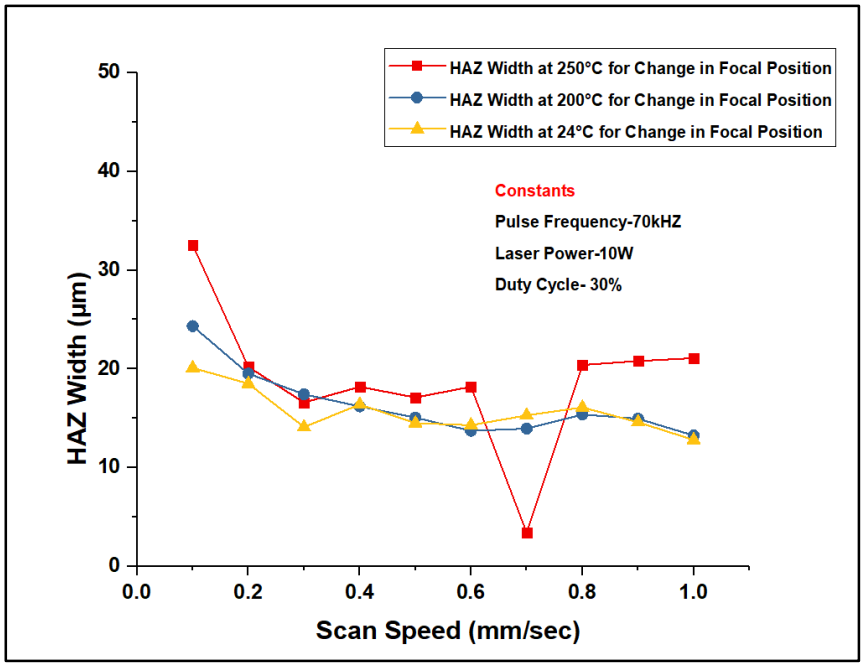

Figure 5.18 Effect of scan speed on HAZ width at different position of the focal point of the laser beam at different temperatures

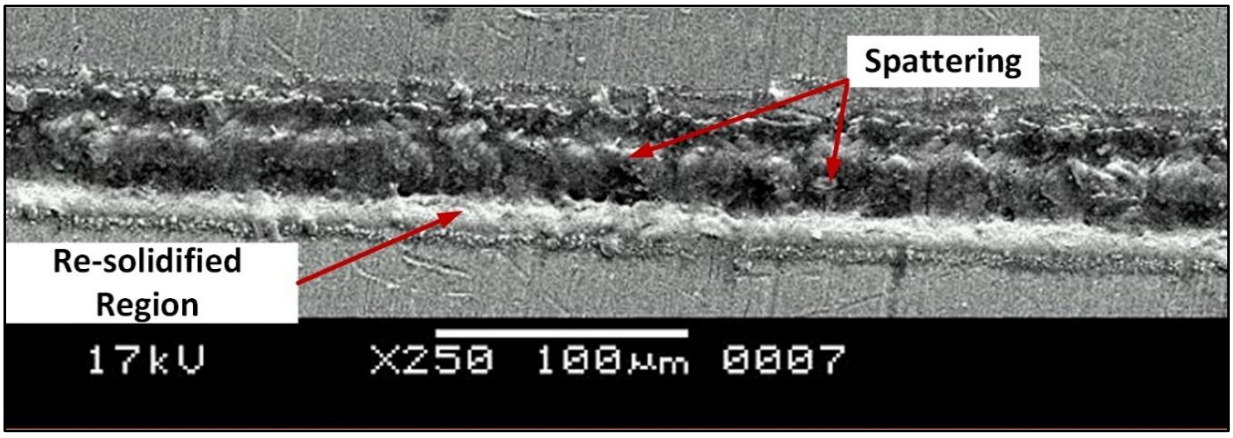

Figure 5.19 Scanning electron microscopic view of a micro-groove (200°c) at 0.4mm/sec and 0.05 mm downward shifting of focal point position

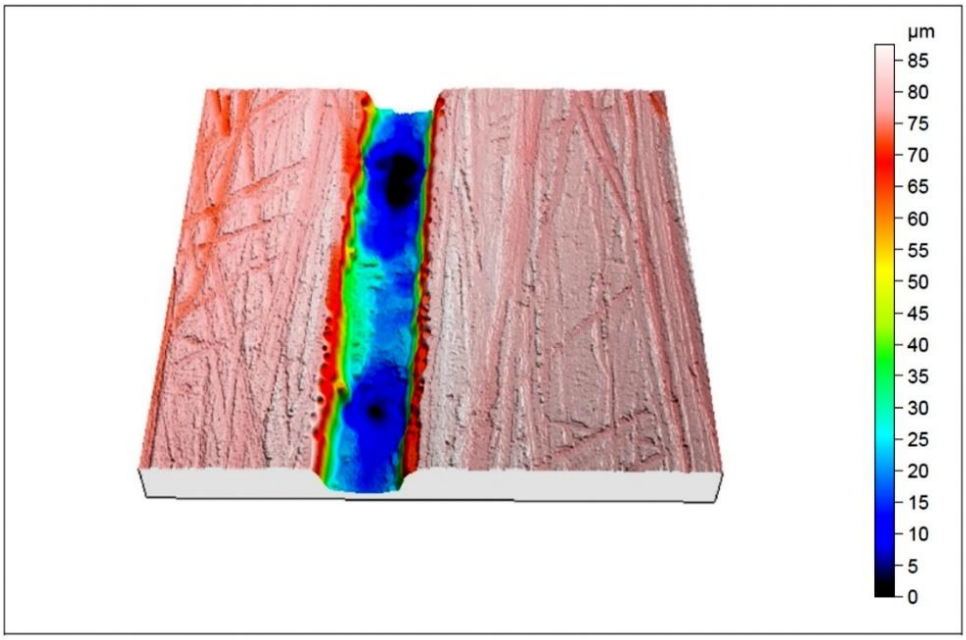

Figure 5.20 3D profile of fiber laser generated micro-groove on 316L

5.8 Outcomes of the Present Research Work

Fiber laser micro-grooving of 316L SS has been studied to analyze the effect of the flow of high pressure assist air, preheated temperatures, and change in the focal position of the laser beam on micro-groove cut width, HAZ width and average surface roughness R_a. From the experimental results, the following conclusions can be drawn:

(i) The effect of assist air supply is found to be more on the cut width dimensions at high values of pulse frequency compared to the values of cut width without the supply of assist air at the same set of process parameters. Without the presence of assist air, the cut width dimensions tend to increase with the increase in pulse frequency, whereas the reverse phenomenon is observed with the aid of assist air.

(ii) The experimental results also indicate that the effect of assist air is prominent in order to achieve a low average surface roughness of the cut profiles on 316L. In the presence of high pressure assist air, the average surface roughness, R_a of the cut profiles increases with the increment of laser power. Due to the supply of high pressure assist air, surface roughness values tend to decrease with the increment in pulse frequency. At higher scan speed in the presence of a jet flow of assist air supply, surface roughness values are

lowered at a considerable amount as compared to the experiments conducted without the supply of assist air.

(iii) The effects of preheating during fiber laser micro-grooving operation are important consideration generating micro-grooves on 316L stainless steel. At 250 °C, cut width tends to decrease, while the HAZ width reduces significantly up to the scan speed of 0.7 mm/sec. On the contrary, the dimensions of the HAZ width are significantly lower in comparison of the HAZ width dimensions during any change in the focal point position of the laser beam. The phenomena described above can be due to the effect of re-solidification, formation of oxide particles along with a spattering of the molten material. The uniformity of the micro-grooves is on the higher side for this set of experiments.

(iv) At 200°C of preheating temperature, with the increment of scan speed, cut width and HAZ width dimensions are reduced. The dimensions of HAZ width at the focus condition on the workpiece to be lower than the dimensions during a change in focal point distance at high scan speed. Low thermal strain and thermally induced stresses along with the high cooling rate of the molten material have attributed in such characteristic features of the cut width and HAZ width of the micro-grooves on 316L.

(v) At the room temperature, the dimensions of the cut width and the HAZ width are the lowest in comparison to the dimensions observed at different elevated temperatures. However, non-uniform micro-groove profiles are also observed during fiber laser micro-grooving on 316L at room temperature. Supercooling of the molten material combined with the high thermal strain at the micro-groove zone are the predominating factors for the non-uniformity of the micro-grooves.

The present research work not only facilitates the use of fiber laser in the domain of micro-machining of 316L but also simplifies the complex phenomena of the micro-grooving on 316L SS.

6. EXPERIMENTAL INVESTIGATION INTO FIBER LASER MICRO-DRILLING ON QUARTZ

6.1 Introduction

Quartz is considered one of the best suitable materials in optoelectronics, micro-optics due to its piezoelectric properties, high mechanical, and frequency stability. Quartz even has improved corrosive resistance and hardness properties compared to various engineering metals. Thus, fabrication of micro-machining features on quartz has observed rapid growth in the domain of micro-electric mechanical systems (MEMS), lab-on-chip devices especially. Past research works have shown that the various non-traditional micro-machining approaches such as ultrasonic machining (USM) [79], electro-discharge machining (EDM) [80], and abrasive water jet machining (AWJM) [81] are rapidly utilized to generate precise micro-machining features on quartz. However, the aforesaid machining approaches suffer from high machining time along with its non-flexibility in compared to the highly flexible and fast machining approach such as laser beam micro-machining process.

The generation of micro-hole on quartz using a fiber laser system is not investigated until now. This research work aims to generate through micro-holes on quartz by fiber laser micro-drilling process and also to conduct successful research analysis to widen the scope of research findings further. The effects of different fiber laser micro-drilling process parameters such as laser power, pulse frequency, duty cycle and assist air pressure on various micro-drilling criteria, i.e. entry diameter, exit diameter, taper angle, heat affected zone (HAZ) thickness and circularity of the fabricated micro-holes on quartz have been discussed hereunder.

6.2 Selection of the Process Parameters and Responses

To carry out, fiber laser percussion drilling on quartz, laser power, duty cycle, pulse frequency, air pressure is selected as the process parameters. The details of each process parameters are discussed in chapter 3.

The micro-drilling response characteristics for fiber laser micro-drilling of quartz are entry diameter, exit diameter, HAZ thickness, circularity. The details of each response are given below.

(i) Entry Hole Diameter: It is the hole diameter at the entrance.

(ii) Exit Hole Diameter: It is the hole diameter at the exit.

(iii) HAZ Thickness: HAZ thickness around the periphery of a micro-hole is given by the following equation 6.1:

$$\text{HAZ thickness} = \frac{\text{Total diameter including HAZ} - \text{Hole diameter}}{2} \quad \ldots[\text{Eq}^{n}\ 6.1]$$

(iv) Taper angle: Taper angle of micro-hole is depicted in the following equation 6.2:

$$\text{Half Taper Angle } \left(\frac{\theta}{2}\right) = \tan^{-1}\left(\frac{\text{Entry Hole Diameter} - \text{Exit Hole Diameter}}{2 \times \text{Material Thickness}}\right) \quad \ldots[\text{Eq}^{n}\ 6.2]$$

(v) Circularity: Circularity of a fabricated micro-hole is given by equation 6.3:

$$C_i = \frac{D_{\min}}{D_{\max}} \quad \ldots[\text{Eq}^{n} 6.3]$$

Where C_i is the average circularity of the individual entrance hole, D_{min} and D_{max} represent the minimum and maximum diameter of the hole (μm) respectively.

Figure 6.1 represents a schematic diagram of the cross-section of a micro-hole to identify entry and exit hole diameter along with the half taper angle of a micro-hole fabricated on quartz.

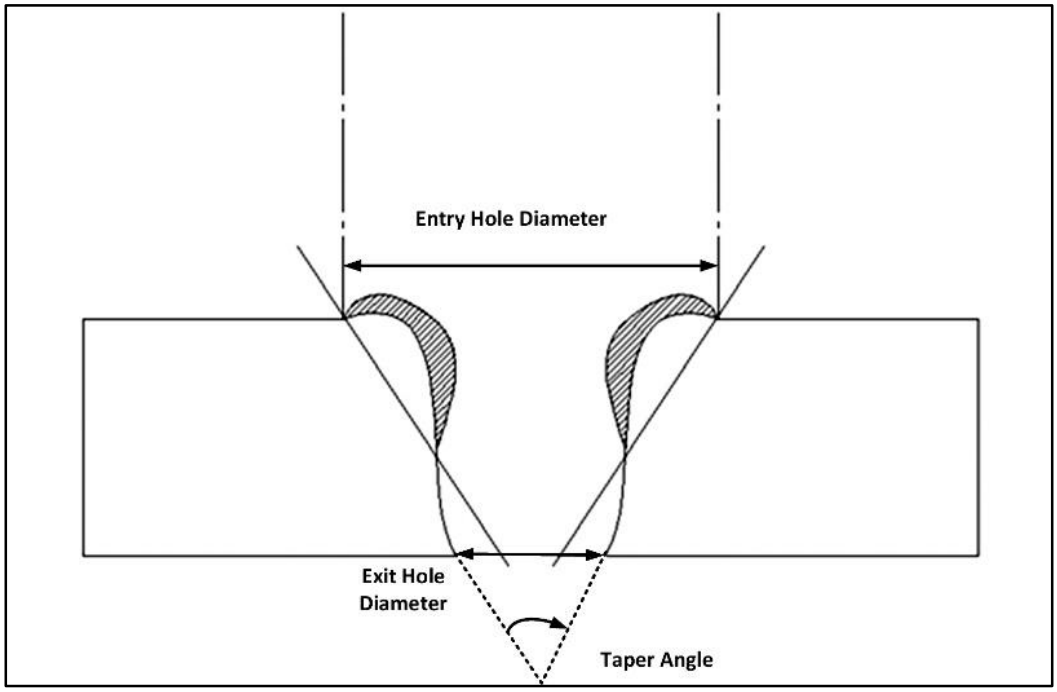

Figure 6.1 Schematic diagram of the cross-section of quartz micro-hole [82]

6.3 Properties of Quartz

A square dimension of transparent quartz having a dimension of 25X25X1 mm of thickness is selected for the experimentation. The properties of quartz are given in table 6.1.

Table 6.1 Properties of quartz [82]

Properties	Value
Coefficient of Expansion	5.54×10^{-7} (K^{-1})
Softening Point	1933 K
Thermal Conductivity	1.37W/m.K
Annealing Point Temperature	1433K
Max Operating Temperature	1423 – 1473 K
Average Specific Heat	771 J/ kg. K
Specific Heat Conductivity	1.48 W/m.K
Density	2.204 g/cm^3
Tensile Strength	49 N/mm^2
Poisson's Ratio	0.17

6.4 Material Removal Mechanism of Quartz by Fiber Laser Percussion Drilling

Laser drilling method is classified under single pulse drilling, percussion drilling, trepanning drilling (commonly employed for the larger diameter of holes) and helical drilling. Laser percussion drilling is attributed as the converging of successive multiple laser pulses at a single point to create a micro-hole which eventually deepens further by multiple reflections of the electrons to increase sudden absorptivity of the laser light. It is difficult to focus the laser beam on the top surface of quartz along with the high conversion of radiated laser energy to thermal energy due to the transparent nature of quartz.

The selection of process parameter should lead to high pulse energy for achieving the ablation threshold energy. The initial value of low pulse energy led to the initiation of ablation of quartz but failed to penetrate through the lower surface of the quartz. Spattering phenomenon, along with the re-solidification of the molten material, plays a crucial role in the low penetration rate of the laser beam on quartz. One way to overcome the problem is to place a low reflective workpiece at the bottom of quartz, which may increase the absorptivity of quartz to some extent.

However, this method is yet to be tested by the researchers. There is also a possibility of high pulse energy may lead to the formation of cracks on quartz. After the ablation threshold is achieved, a thin region of molten material is formed by absorbing the laser light at the target surface. Simultaneously, phase transformation may occur on quartz atomic structure. While the machining time increases, the melt pool is formed, and the surface of this melt pool reaches to the vaporization temperature. Melt expulsion occurs when the pressure gradients on the surface of the molten layer are significantly large to overcome the surface tension forces along with the high flow of gas (may be an inert gas or compressed air). This phenomenon eventually leads to the removal of the molten material from the micro-drilling zone.

Simultaneously, in combination with re-solidification of the molten material at the inner wall and the spattering phenomenon at the periphery of the micro-holes, may lead to the poor circularity of the holes. In addition to this, the viscosity of quartz becomes quite high at higher operating temperature. As a result of this, the flow of molten material is restricted to some extent at high temperatures. At high temperature, most of the positively charged central silicon atoms are pushed down, whereas most of the negatively charged oxygen atoms are pushed upwards. The pushing of oxygen atoms eventually leads to oxidation and the formation of detrimental HAZ. Figure 6.2 represents fiber laser percussion drilling of quartz.

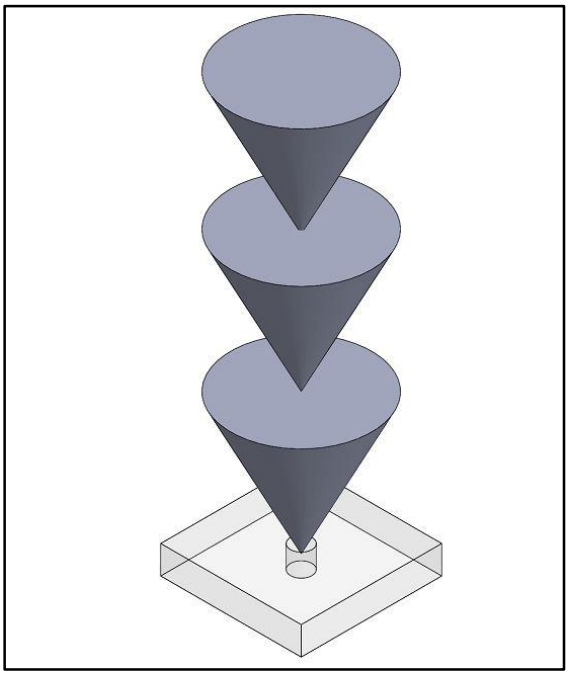

Figure 6.2 Schematic diagram of fiber laser percussion drilling operation [82]

6.5 Preliminary Study of Fiber Laser Micro-Drilling of Quartz

The primary objective of the preliminary experimental work is to understand the effects of fiber laser percussion micro-drilling process parameters, i.e., laser power, pulse frequency, duty cycle along with air pressure on entry and exit hole diameter, half taper angle, entrance hole circularity and HAZ thickness. Selection of the ranges of process parameters is achieved with the aid of pilot experiments at the fixed focal length. Experiments are conducted for the fabrication of an array of micro-holes on quartz has been divided into 4 sets of experiments. Figure 6.3 represents the array of entrance micro-holes with the variation of laser power and pulse frequency. In each set of experiment, a total number of five experiments have been carried out by varying one process parameter at a time, while the other three process parameters are kept as constants. Lowest taper angle among each set of experiments is considered as the primary output criteria for determining the best set of the experiment from each segment. The experiments are performed at zero focal position (i.e., the focal plane on the workpiece surface).

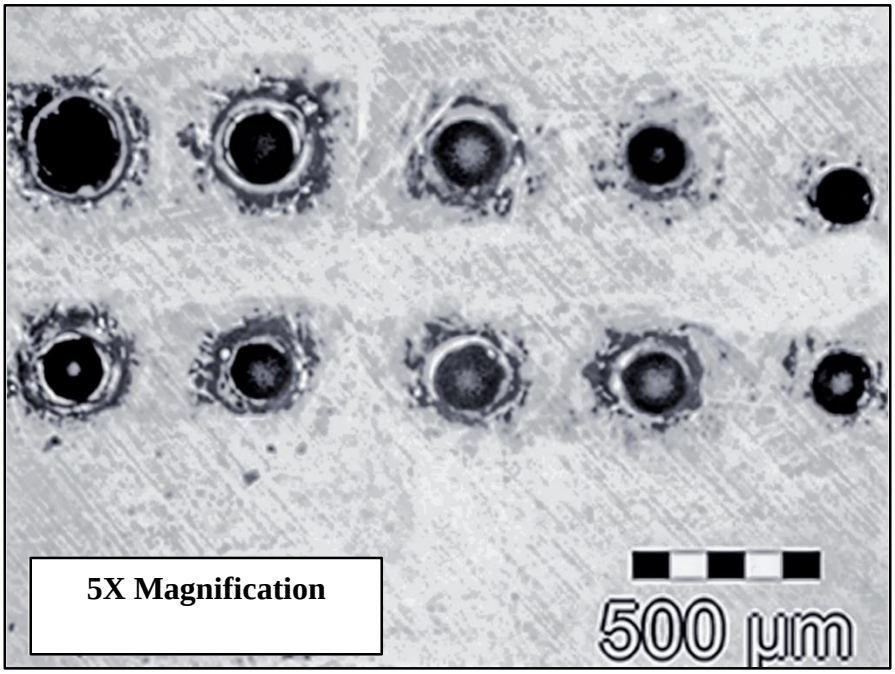

Figure 6.3 Arrays of micro-holes at the entry side at 5X Magnification [82]

The entry and exit hole diameters along with the average HAZ thickness (equation 6.1) are measured using an Olympus STM6-LM optical measuring microscope using 5X, 10X, and 50X lens. Responses described above are measured four times at different locations of the hole geometry, and an average value for each response are considered for the present analysis. From

the entry and exit diameters, the taper angle of the micro-holes of quartz is also measured with the aid of equation 6.2. The circularity of the micro-holes is calculated with the aid of ImageJ software.

6.5.1 Results and Discussion

The effects of the four process parameters such as laser power, pulse frequency, duty cycle and assist gas pressure with respect to the hole diameters (entry and exit), taper angle and hole circularity are discussed and analyzed subsequently. The experimental results are listed in table 6.2.

Table 6.2 The results of the experiments

Exp. No.	Pulse Frequency	Duty Cycle	Laser Power	Assist Air Pressure	Entry Diameter		Exit Diameter		Taper angle	Circularity
					Hole	HAZ thickness	Hole	HAZ thickness	(θ/2)	
	(kHz)	(%)	(W)	(kgf/cm^2)	(µm)		(µm)		°	
1	50	50	27.5	2.5	94.33	45.76	90.91	44.34	0.196	0.845
2	50	50	30	2.5	99.98	56.90	95.33	50.68	0.266	0.867
3	50	50	32.5	2.5	107.05	66.21	99.67	61.97	0.423	0.876
4	50	50	35	2.5	117.53	67.96	108.3	62.08	0.529	0.889
5	50	50	37.5	2.5	124.13	74.74	111.65	65.1	0.715	0.924
6	55	50	27.5	2.5	89.07	44.03	84.6	42.78	0.256	0.915
7	60	50	27.5	2.5	85.75	32.72	81.55	34.76	0.240	0.909
8	65	50	27.5	2.5	76.63	26.08	74.05	31.05	0.148	0.891
9	70	50	27.5	2.5	71.78	29.64	68.93	27.54	0.163	0.879
10	75	50	27.5	2.5	71.53	16.11	68.27	18.44	0.187	0.841
11	65	55	27.5	2.5	74.56	54.74	70.78	47.28	0.216	0.848
12	65	60	27.5	2.5	87.33	56.76	79.90	54.34	0.424	0.895
13	65	65	27.5	2.5	97.05	61.97	85.67	60.2	0.652	0.922
14	65	70	27.5	2.5	98.53	66.98	86.30	63.31	0.700	0.93
15	65	75	27.5	2.5	102.83	67.43	89.51	63.78	0.763	0.938
16	65	55	27.5	1.5	68.17	59.30	58.88	50.08	0.532	0.813
17	65	55	27.5	2	74.35	55.54	62.3	48.10	0.690	0.856
18	65	55	27.5	3	82.56	48.76	73.67	37.84.	0.509	0.876
19	65	55	27.5	3.5	93.78	35. 17	82.91	37.63	0.622	0.907
20	65	55	27.5	4	103.38	29.06	89.86	36.89	0.775	0.913

6.5.1.1 Effects of Laser Power on Taper Angle, Entrance Hole Circularity and HAZ Thickness of Micro-Holes on Quartz

In the present set of experiments, the laser power is varied from 27.5 W to 37.5 W to find out its effect on the micro-hole geometry. Pulse frequency and duty cycle are kept constant at 50 kHz and 50% respectively, along with air pressure of 2.5 kgf/cm^2. Influence of laser power on the

taper angle, and entrance circularity is shown in figure 6.4. Figure 6.5 represents the effect of laser power micro-hole diameters and HAZ thickness.

From figure 6.4, it can be observed that with the increase of laser power, the taper angle has been consistently increasing along with the increment in both entry and exit diameters of the fabricated micro-holes. The entrance circularity tends to increase with the increment in laser power, as shown in figure 6.4. Figure 6.5 shows the increase in HAZ thickness with the increase in laser power. With the increment in laser power at a duty cycle of 50%, laser peak power and pulse energy are increased simultaneously.

When laser power is low, an incomplete expulsion of the ejected material from the micro-drilling zone can be observed, which adheres to the quartz workpiece surface at the periphery of the hole entrance to cause a spattering phenomenon on the periphery of the micro-holes. The spattering of the molten material is one of the inherent defects associated with laser-drilled micro-holes in which the molten and vaporized material formed during the micro-drilling process is not completely ejected. The molten material further re-solidifies and adheres around the periphery of the hole.

When laser power and the subsequent peak power are high enough, the transportation of the molten material increases and the spatter is uniformly distributed around the edges of the entrance micro-holes. In addition to this, thermal stress is generated at the periphery of the micro-holes due to the difference in temperature of the micro-drilling zone and the surrounding surface. The generated thermal stress on the SiO^{4-} unit causes both the silicon and oxygen atoms to displace relative to their equilibrium positions. The positively charged silicon atom displaces from its central position; consequently, it further causes the entire silicon-oxygen tetrahedron molecule to be electrically polarized. As a result, the phenomenon described above combined with the moderate air pressure is subjected to the increment of the entrance hole circularity at high laser power, as shown in figure 6.6. At the initial settings of low laser power, higher spattering phenomenon can be observed along with the non-uniformity of the spatter at the surrounding edges of the periphery of the micro-holes. As a result of this, entrance circularity is affected, and lower circularity is observed at low laser power. Although, the variation of the entrance hole circularity is less with the laser power.

Low absorptivity, combined with high reflectivity of quartz at an infrared wavelength, increase the machining times for the generation of through holes. The irradiated zone is also subjected to prolonged heating when the machining time is elongated. With the increment in time along with the change in focal length of the initial beam breakthrough, the molten material flows downward to the exit holes and further causes the increment in the exit diameters compared to the entry diameter. As a result of this, the diameters of both the entrance and exit holes along with the HAZ thickness tend to increase significantly. The diameters of the entrance and exit holes along with the HAZ thickness in the present set of experiments (set 1) are found to be higher than the remaining set of experiments owing to the generation of high peak power and pulse energy. It can also be observed that the geometry of the entrance hole is significantly dependent on the spattering phenomenon and re-solidification of the molten material.

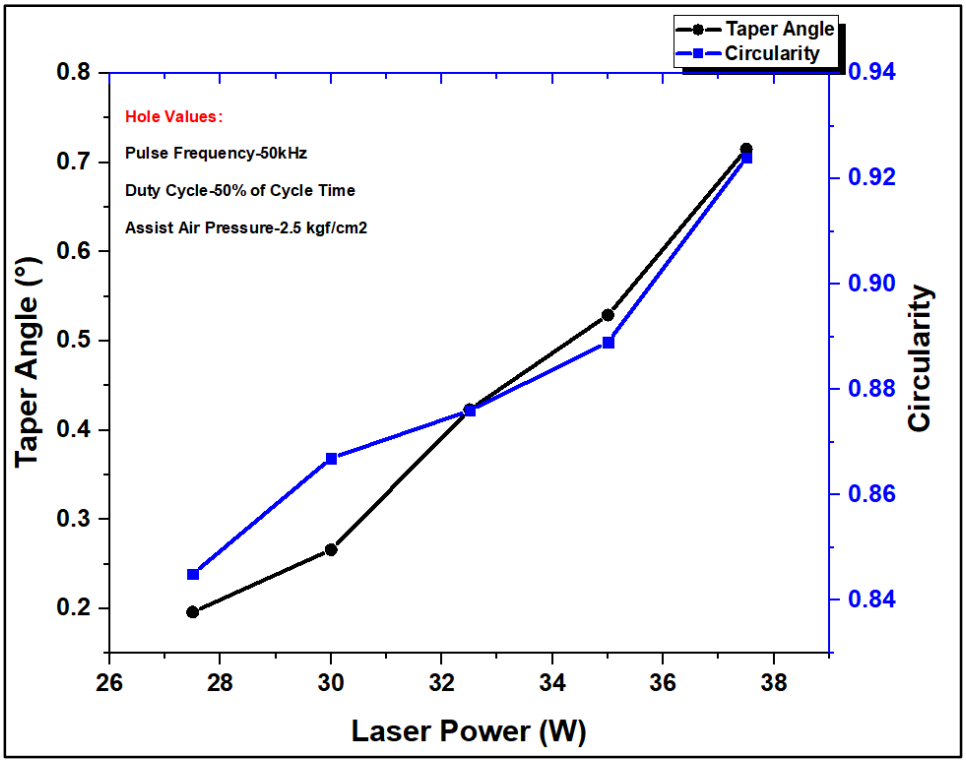

Figure 6.4 Effect of laser power on taper angle and circularity

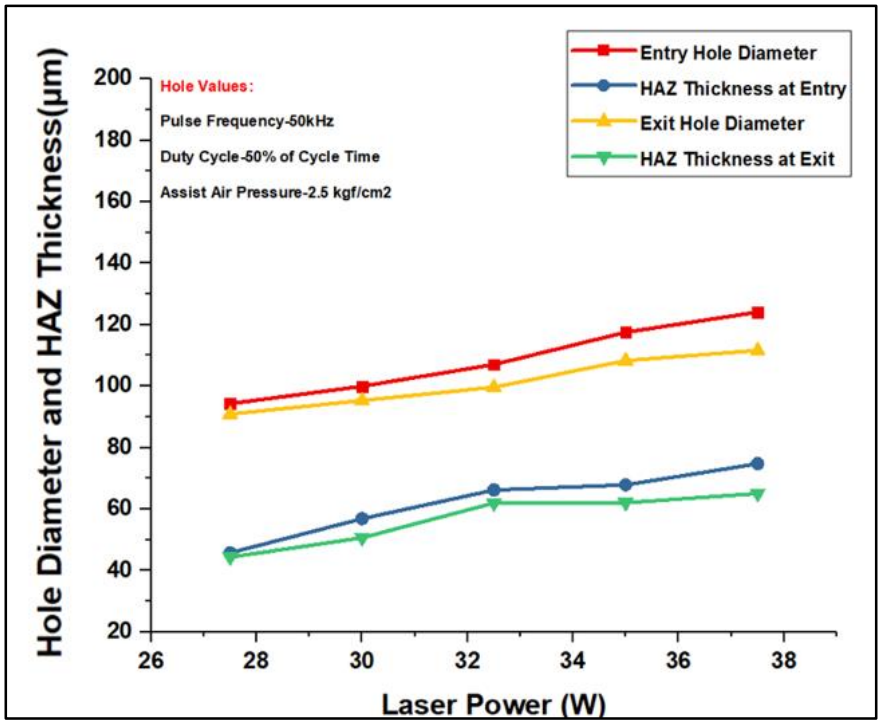

Figure 6.5 Effect of laser power on micro-hole diameters and HAZ thickness

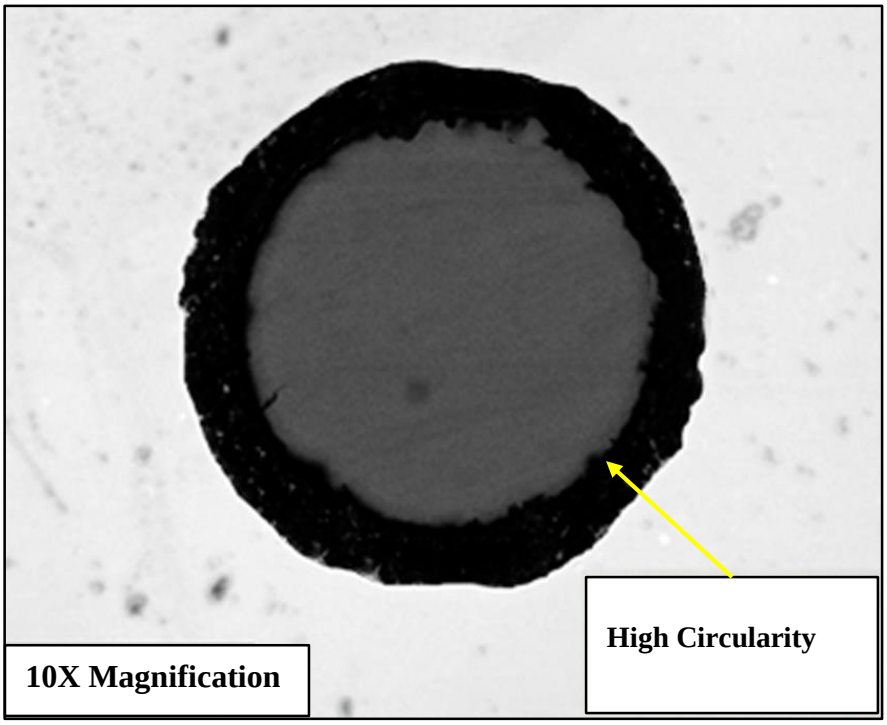

Figure 6.6 Microscopic view of entrance quartz micro-hole in the parametric combination of pulse frequency of 50 kHz, duty cycle of 50%, laser power of 30 W and air pressure of 2.5 kgf/cm^2

6.5.1.2 Effects of Pulse Frequency on Taper Angle, Entrance Hole Circularity and HAZ Thickness of Micro-Holes on Quartz

Pulsed mode operation of the fiber laser system produces a high instantaneous power for a period of a pulse on time and follows by a subsequent period of power off. Pulse frequency is inversely proportional to pulse energy when the laser power and duty cycle are kept constants. Therefore, when pulse frequency is increased during the present set of experiments, keeping the other process parameters as constants, laser beam energy reduces in a significant manner. On the contrary, with the increment of laser pulse frequency, laser pulses will be more, i.e., the number of laser shots will be more during laser irradiation. Simultaneously, with moderate-high laser power of 27.5 W along with nanosecond pulsed fiber laser system, the melt pool around the micro-drilling zone is comparatively large. The Gaussian beam profile also accounts for deep melting and vaporization of quartz along with the formation of mushy zones within the molten pool. Some of the molten material is splashed away from the micro-drilling zone with the aid of air pressure, may take place just below the periphery of the micro-holes. In addition to this, the absorptivity of quartz is mostly dependent on its crystal structure along with the surface characteristics for a given wavelength. When the pulse energy reaches to 75 kHz, a significant reduction of the HAZ thickness for the exit diameters can be observed owing to the low penetration rate of the laser beam.

In this present set of experiments, the effect of pulse frequency (ranges from 55 kHz to 75 kHz) on the hole geometry is analyzed. Figure 6.7 shows the effect of pulse frequency on the taper angle and circularity of the micro-holes, whereas the influence of pulse frequency on the micro-hole diameters and HAZ thickness is shown in figure 6.8. In the present set of experiments, laser power, duty cycle and air pressure are kept constant at 27.5 W, 50% and 2.5 kgf/cm^2 respectively. From figure 6.7, it can be observed that the taper angle tends to decrease with the increment in pulse frequency. The experimental results also reveal that corresponding diameters of both the entry and exit holes tend to decrease with the increment in pulse frequency. The results of the present set of experiments also show that both the entry and exit diameters are relatively smaller compared to the change in laser power. Figure 6.7 also shows the effect of pulse frequency on the entrance micro-hole circularity, which tends to decrease as the pulse frequency goes on increasing. Besides, this, the HAZ thickness for both the entry and exit diameters are significantly lower. However, it is also observed that the HAZ thickness for the

exit diameters tends to decrease with more number of laser pulses, as shown in figure 6.8. The pulse energy and the peak power decrease simultaneously with the increment of pulse frequency.

The effects of pulse frequency on the hole taper are found to be significant. An increment in pulse frequency leads to a large number of pulses, which further leads to the increment of molten material movement exiting from the hole exit. A large number of pulses affects the entry hole and removes the spattering phenomenon from the hole entrance. Hence, the entrance circularity increases. When percussion drilling of quartz is initiated at low pulse energy, spattering phenomenon is significantly higher. This phenomenon reverts at the higher fluences. As a result of this, the taper angle reduces in a more significant manner with the moderately high air pressure of 2.5 kgf/cm^2 combined with a higher number of pulses.

The combination of the duty cycle, pulse frequency, number of pulses, and focal point position are found to be significant on the entrance hole circularity. When pulse frequency increases, the time between two successive incidents of the laser beam time becomes shorter, and the laser energy becomes lower as discussed in the earlier section. As a result of this, the quartz gets melted and solidified with lower agitation and disorder, and thus, higher circularity is formed, as shown in figure 6.9.

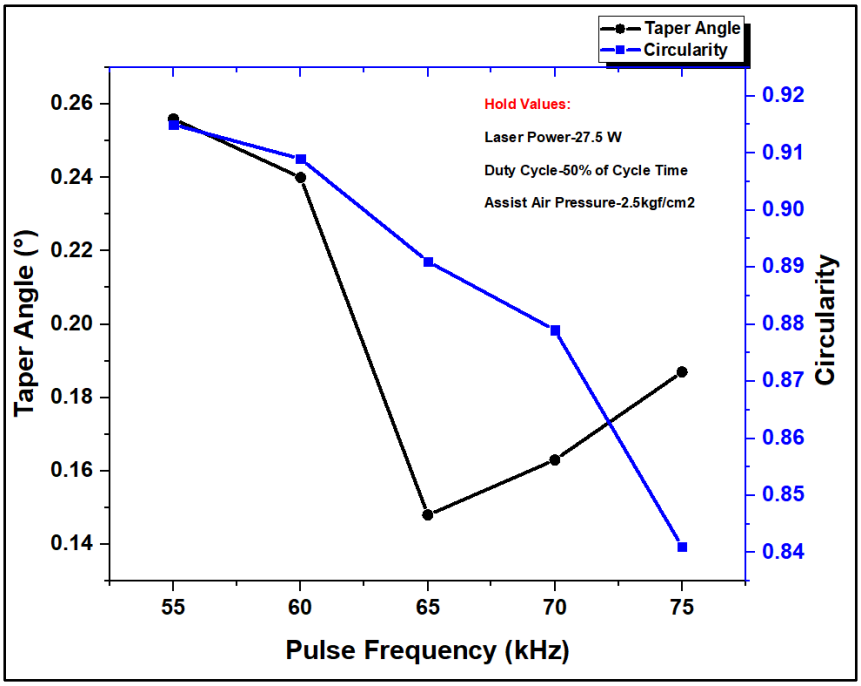

Figure 6.7 Effect of pulse frequency on taper angle and entrance hole circularity

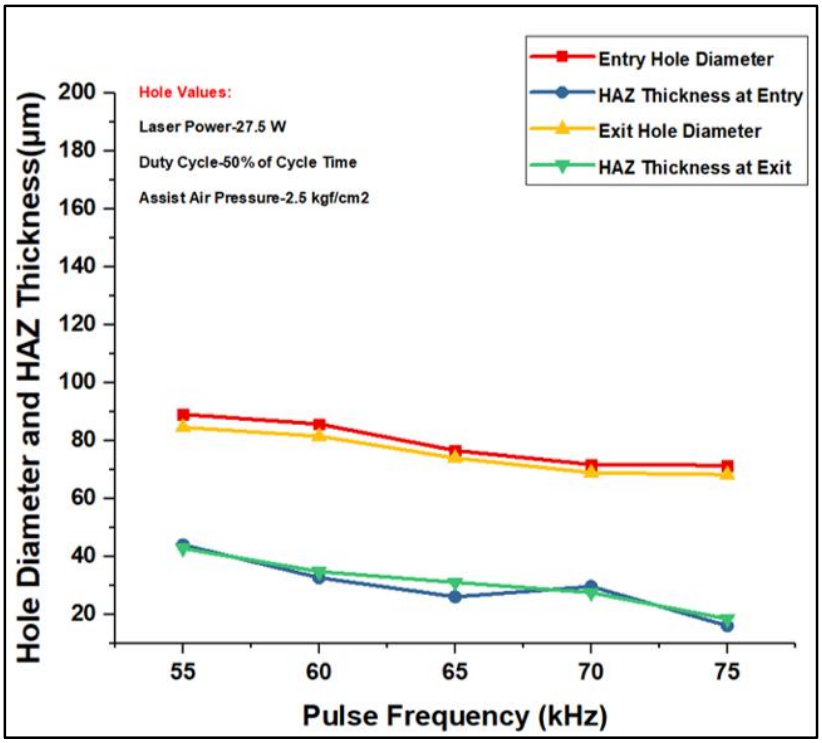

Figure 6.8 Effect of pulse frequency on micro-hole diameters and HAZ thickness

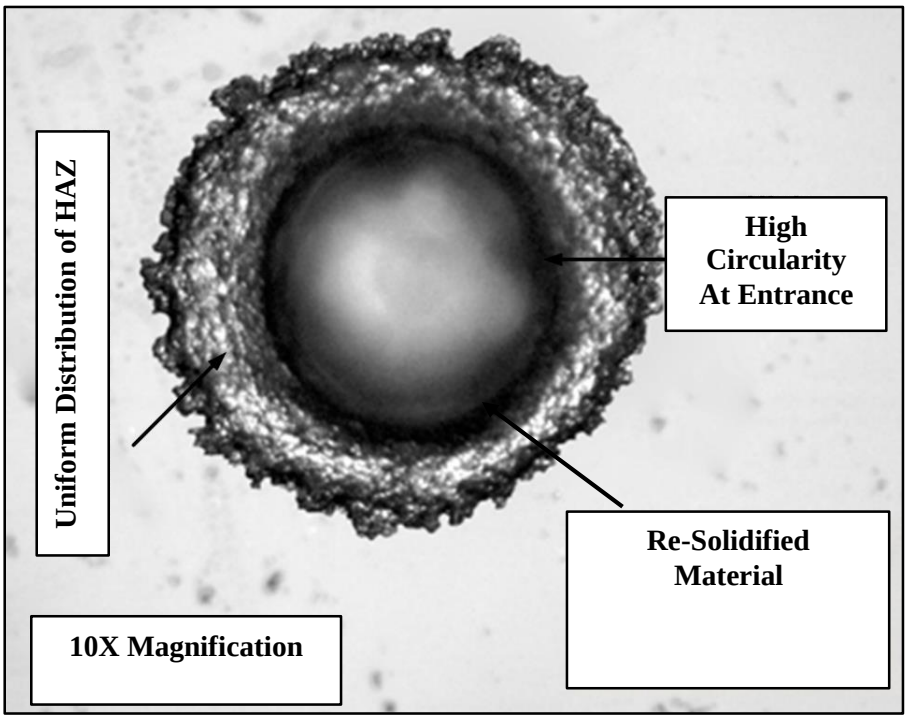

Figure 6.9 Microscopic view of entrance quartz micro-hole in the parametric combination of pulse frequency of 65 kHz, duty cycle of 50%, laser power of 27.5 W and air pressure of 2.5 kgf/cm^2 [82]

6.5.1.3 Effects of Duty Cycle on Taper Angle, Entrance Hole Circularity and HAZ Thickness of Micro-Holes on Quartz

The parametric effects of duty cycle on the entrance hole circularity, taper angle, and HAZ thickness have been analyzed. Influence of duty cycle on the taper angle, and entrance circularity is shown in figure 6.10. Figure 6.11 represents the influence of the duty cycle on the hole diameters and HAZ thickness. In the present set of experiments, pulse frequency and laser power are kept constant at 65 kHz and 27.5 W respectively. From figure 6.10, it can be observed with the increment in the duty cycle; positive taper formation is inevitable. The dimensions of the entry diameter compared to the exit diameter are found to be larger, which result in a larger taper angle. The entrance circularity also increases with the high duty cycle, as observed in figure 6.10. The HAZ thickness on both the sides tends to gradually increase with the increment of the duty cycle, as shown in figure 6.11.

As discussed in the earlier section, if the laser power is more than 37.5 W of laser power in combination with a high duty cycle, then there is a probability of the thermal damage to quartz workpiece. However, the thermal penetration depth varies according to the following equation 6.4:

$$l = 2\sqrt{\kappa \tau_H} \quad \text{…[Eq}^{\text{n}}\text{6.4]}$$

Where, κ , τ_H , l stands for thermal diffusivity, duty cycle, and the depth of thermal diffusion respectively. The equation 6.4 signifies that higher the duty cycle (in the nanosecond), higher the thermal diffusion length. The molten material which flows along the wall of the micro-hole settles around its periphery of the micro-holes. This phenomenon is not only due to surface tension effects but also due to the air pressure in the micro-drilling front. The behavior of the melt ejection plays a significant role in determining the hole geometry and the circularity of the holes. This observation was supported by the previous results of Li L et al. [83]. It is also observed that melt ejection has taken place in the upward direction with the multiple laser pulses. When the duty cycle increases, the laser beam penetration rate decreases gradually due to the decrement of laser peak power. After the initiation of the irradiation of the laser beam on the quartz top surface, the laser beam penetration rate always decreases due to the alternation of the laser beam focal point from the top surface. Although the occurrence of oxidation along with the formation of the re-solidified layer on the walls of the micro-holes, the high set value of laser power along with duty cycle generate high pulse energy. This high pulse energy, in turn,

produces the ablation threshold energy to penetrate throughout the entire thickness of quartz material. As a result of this, diameters of the holes are higher compared to the rest of the experiments. As the penetration rate is lowered with the increment in the duty cycle, the HAZ thickness is more at the entrance as compared to the exit holes. As a result of this, the entrance hole geometry is affected significantly, which further causes an increment in HAZ thickness with the increase in the percentage of the duty cycle.

The experimental results reveal that the taper increases with the increase in the hole diameter due to the accumulation of heat energy at moderate peak power value and high absorptivity at the entrance of the hole. These observations are in agreement with that of Ghorieshi and Nakhjavani [84] and Kacar et al. [85] where it was reported that the taper of the micro-hole increased with the reduction of the laser peak power.

The entrance circularity increases with the increase of the duty cycle. High energy laser combined with lower peak power beam, has a significant role in the entrance hole geometry compared to the exit hole geometry. The material removal rate is decreased significantly, which further increases the machining time. There will be a significant spatter formation and subsequent re-solidification at the entrance at the high duty cycle. However, due to the low penetration rate, the machining time tends to increase. As a result of this, the higher machining time allows the material to be cooled down and distributed evenly around the periphery of the entrance hole.

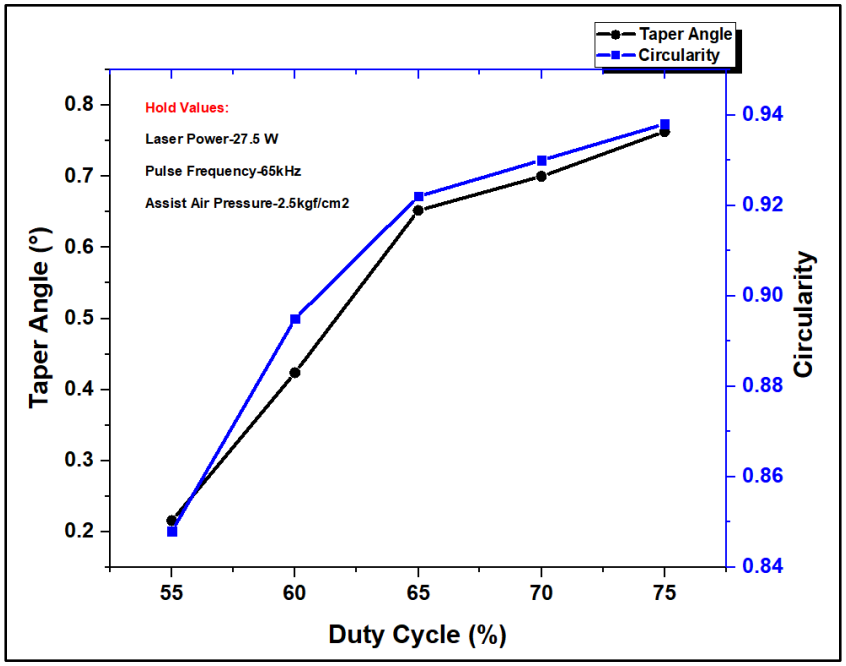

Figure 6.10 Effect of duty cycle on taper angle and entrance hole circularity

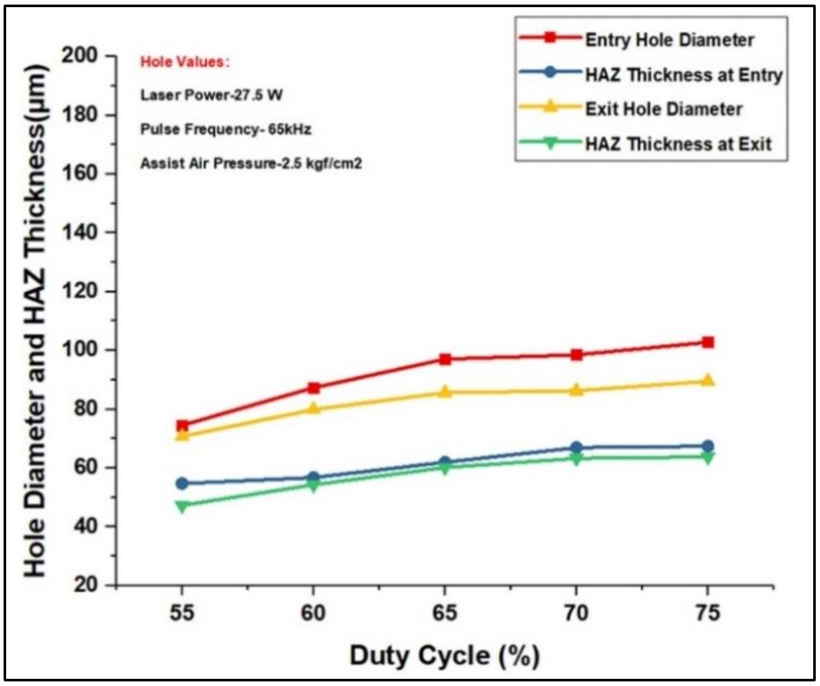

Figure 6.11 Effect of duty cycle on micro-hole diameters and HAZ thickness

6.5.1.4 Effects of Air Pressure on Taper Angle, Entrance Hole Circularity and HAZ Thickness of Micro-Holes on Quartz

Air pressure is crucial for determining hole geometry. The effects of air pressure on the taper angle and entrance circularity are shown in figure 6.12. Figure 6.13 showcases the effect of air pressure of the hole diameters and HAZ thickness. A pulse frequency of 65 kHz, duty cycle of 55% and 27.5 W of laser power are the constant parameters for the present set of experiments. From figure 6.12, it can be observed that both the taper angle and hole circularity have been increased with the increase in air pressure. The entrance hole circularity for the present set of experiments remains on the higher side. Figure 6.13 reveals that there is a decrease in HAZ thickness on both sides of the micro-holes with high air pressure. However, HAZ thickness on the entry side is found to be higher than that of exit side HAZ thickness.

With the increment of air pressure, more amount of material can be removed from the entrance, and a larger diameter can be observed at the entrance holes. At higher air pressure, the effects of air pressure on the hole exit diameter are found to be more significant than that on the hole entrance. The amount of molten material removal is dependent on the flow of assist air. Previously, some of the trial experiments were carried out in an atmospheric condition in order to

compare the effects of air pressure on the hole geometry. At constant pulse energy and peak power, hole geometry in air pressure is more compared to the atmospheric condition.

Higher air pressure combined with moderate pulse energy is subjected to spattering. When pulse energy is moderate combined with low air pressure, removal of the molten material is low. However, as the air pressure increases, heat dissipation from the molten material also significantly increases. The dissipation of heat, in turn, causes re-solidification of the molten material on the inner walls of the micro-holes. Low air pressure, however, fails to remove the heat from the micro-hole periphery along with the removal of molten material. As a result of this, the effect on the hole entry diameter is more than the exit hole diameter with the increment in air pressure. The taper angle increases simultaneously with the increment in air pressure. However, HAZ thickness can be found out to be decreasing in a considerable amount while the air pressure goes on increasing. The cooling effect of high air pressure is more on the entry side. Due to the high ejection of the molten material from the micro-drilling zone, the sensitiveness of HAZ thickness on entry diameters is higher compared to the exit diameters.

The entrance circularity of the hole increases with the increment in air pressure at moderate pulse energy and peak power. Low circularity at the entry of the holes is observed at low assist pressure due to non-uniform distribution of the molten material due to spattering at the edges of the entrance micro-holes.

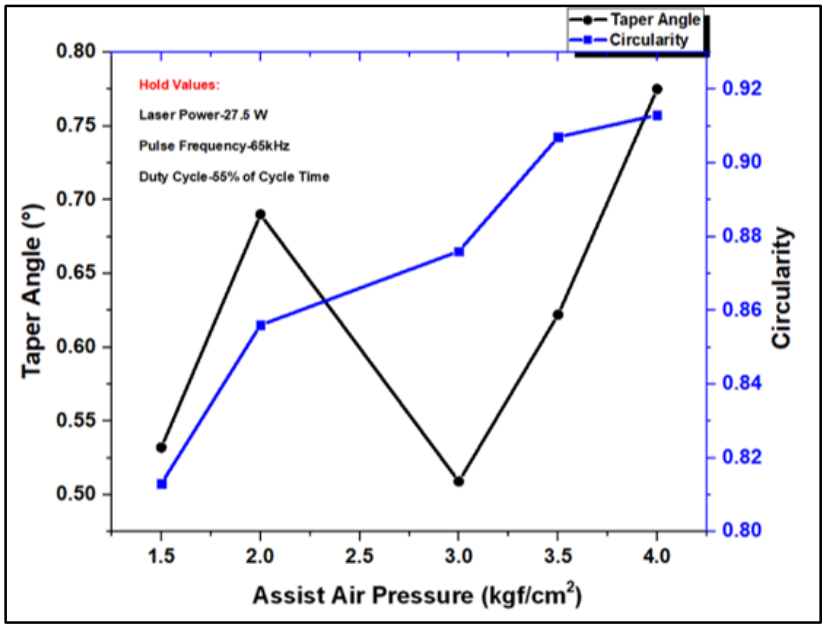

Figure 6.12 Effect of air pressure on taper angle and circularity

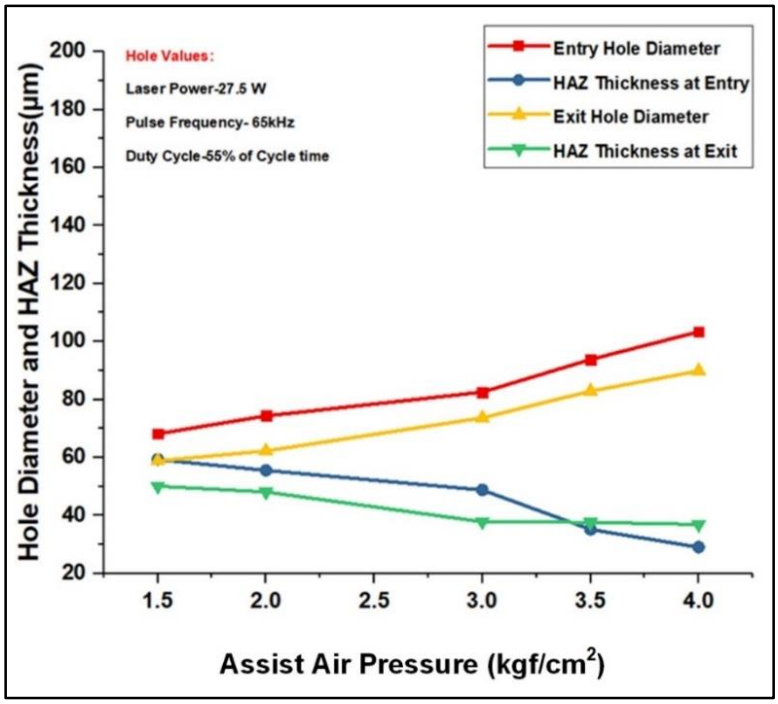

Figure 6.13 Effect of air pressure on micro-hole diameters and HAZ thickness

6.6 Research Findings from Preliminary Study

The preliminary research work facilitates fiber laser system having an infrared region of wavelength and short pulse regime for generating micro-holes on quartz. Laser power of 27.5 to 37.5 W, pulse frequency of 50 to 75 kHz, duty cycle of 50% to 75%, and air pressure of 1.5 kgf/cm^2 to 4 kgf/cm^2 is varied during fiber laser percussion micro-drilling on quartz. Different combinations of parametric values lead to different entry and exit hole diameters along with taper angle, circularity, and HAZ thickness.

From the results of the present experimentation, the following conclusions can be drawn.

(i) The entry and exit hole diameters are increased with the increase in laser power. Higher laser power leads to the high amount of molten material removal and higher entry hole diameter compared to exit hole diameter. The taper angle, HAZ thickness for both the ends of the micro-holes and the entrance hole circularity are also increased with the increment of laser power.

(ii) With the increase in pulse frequency, both the entry and exit hole diameters are decreased sharply. The HAZ thickness for both entry and exit hole becomes lesser at high pulse frequency settings. The micro-holes with high circularities are obtained at

high settings of pulse frequency. The taper angle is low at the moderate value of pulse frequency in combination with low laser power.

(iii) Higher machining time along with high duty cycle, leads to an increment in taper angle and the entrance circularity of the micro-holes. Simultaneously, HAZ thickness is observed to be on the higher side for both the entry and exit sides of the micro-holes on quartz. Significant improvement of the entry hole circularity is observed with high assist air pressure. However, taper angles of the holes are also increased with the increment in air pressure. The variation of entry hole diameter is found to be more sensitive towards the air pressure compared to the exit hole.

The present research work has successfully facilitated the utilization of the fiber laser system for the generation of micro-hole on quartz. The circularity of the entrance holes is found out to be suitable for the present experiments. However, large entry hole diameters to exit hole diameters tend to increase the taper angle in a considerable amount. Further research works can be conducted in order to optimize the parametric combinations for achieving desired micro-hole characteristics.

6.7 Modeling and Analysis of Fiber Laser Micro-Drilling of Quartz

RSM based modeling and subsequent analyses of fiber laser micro-drilling process parameters on fiber laser micro-drilling characteristics of micro-hole generation on quartz have been made. In this experimentation, four factors, along with their five levels have been considered. Table 6.3 represents the actual and corresponding coded values of fiber laser micro-drilling process parameters. Table 6.4 shows the design of experiments matrix of all the process parameters settings.

Table 6.3 Actual and corresponding coded values of fiber laser micro-drilling process parameters

Process Parameters	Unit	Symbol	Levels				
			-2	-1	0	1	2
Laser Power	W	X_1	27.5	30	32.5	35	37.5
Pulse Frequency	kHz	X_2	50	55	60	65	70
Duty Cycle	%	X_3	50	55	60	65	70
Air Pressure	Kgf/cm^2	X_4	1.5	2	2.5	3	3.5

Table 6.4 Design of experiments matrix of values of process parameters and observed responses

Exp. No.	Pulse Frequency (kHz)	Duty Cycle (%)	Laser Power (W)	Air Pressure (Kgf/cm^2)	Entry Hole Diameter (µm)	Exit Hole Diameter (µm)	HAZ Thickness (µm)	Circularity
1	55	55	30	2	91.67	83.62	65.32	0.801
2	65	55	30	2	76.85	71.12	60.35	0.755
3	55	65	30	2	106.5	93.83	68.36	0.825
4	65	65	30	2	88.79	76.86	54.57	0.816
5	55	55	35	2	101.45	91.39	75.56	0.748
6	65	55	35	2	98.74	88.25	73.56	0.780
7	55	65	35	2	95.81	87.93	81.73	0.702
8	65	65	35	2	94.47	84.42	70.65	0.758
9	55	55	30	3	104.26	93.75	62.67	0.795
10	65	55	30	3	93.14	83.92	60.17	0.782
11	55	65	30	3	108.37	95.96	66.89	0.790
12	65	65	30	3	95.67	83.35	55.14	0.834
13	55	55	35	3	113.09	99.97	77.38	0.790
14	65	55	35	3	116.34	100.32	79.85	0.861
15	55	65	35	3	94.74	84.81	90.20	0.719
16	65	65	35	3	103.06	87.91	80.54	0.832
17	50	60	32.5	2.5	93.72	88.75	64.78	0.679
18	70	60	32.5	2.5	85.52	78.85	49.99	0.724
19	60	50	32.5	2.5	112.52	98.63	64.13	0.854
20	60	70	32.5	2.5	107.32	92.08	69.21	0.853
21	60	60	27.5	2.5	94.68	84.15	65.69	0.825
22	60	60	37.5	2.5	103.72	90.99	100.75	0.772
23	60	60	32.5	1.5	87	78.29	68.74	0.785
24	60	60	32.5	3.5	106.33	92.4	72.66	0.831
25	60	60	32.5	2.5	101.21	87.66	69.55	0.820
26	60	60	32.5	2.5	99.55	89.03	71.03	0.808
27	60	60	32.5	2.5	98.23	85.93	68.97	0.815
28	60	60	32.5	2.5	97.84	89.34	70.25	0.805
29	60	60	32.5	2.5	96.98	85.33	68.53	0.812
30	60	60	32.5	2.5	98.98	88.73	69.91	0.811
31	60	60	32.5	2.5	100.18	90.23	69.01	0.825

6.7.1 Development of Empirical Modeling based on RSM

Minitab-17 software has been used for designing the experimental plan. Development of the mathematical models has been carried out utilizing the data obtained during experiments as listed in table 6.4 for fiber laser percussion micro-drilling on quartz. The corresponding empirical equations for the responses, i.e., entry hole diameter (Y_1), exit hole diameter (Y_2), HAZ thickness at entry (Y_3), circularity (Y_4) are obtained as follows:

$$Y_1 = -24 - 1.55 X_1 + 1.17 X_2 + 3.93 X_3 + 48.5 X_4 - 0.0932 X_1 \times X_1 + 0.1098 X_2 \times X_2 + 0.0104 X_3 \times X_3 - 2.28 X_4 \times X_4 + 0.0049 X_1 \times X_2 + 0.3194 X_1 \times X_3 + 0.608 X_1 \times X_4 - 0.3747 X_2 \times X_3 - 1.046 X_2 \times X_4 - 0.043 X_3 \times X_4 \quad ...[Eq^n 6.5]$$

$$Y_2 = -25 - 3.75\,X_1 + 2.42\,X_2 + 4.68\,X_3 + 63.7\,X_4 - 0.0427\,X_1{\times}X_1 - 0.0728\,X_2{\times}X_2 - 0.0201\,X_3{\times}X_3 - 2.73\,X_4{\times}X_4 - 0.0122\,X_1{\times}X_2 + 0.2436\,X_1{\times}X_3 + 0.428\,X_1{\times}X_4 - 0.2622\,X_2{\times}X_3 - 0.865\,X_2{\times}X_4 - 0.526X_3{\times}X_4 \quad ...[Eq^n 6.6]$$

$$Y_3 = -1027.4 + 3.16X_1 + 16.84\,X_2 + 25.51\,X_3 + 99.0\,X_4 + 0.04888\,X_1{\times}X_1 - 0.10437\,X_2{\times}X_2 - 0.2127\,X_3{\times}X_3 - 4.462\,X_4{\times}X_4 - 0.0462\,X_1{\times}X_2 - 0.1819\,X_1{\times}X_3 - 1.157X_1{\times}X_4 - 0.0106\,X_2{\times}X_3 - 0.114\,X_2{\times}X_4 + 0.057\,X_3{\times}X_4 \quad ...[Eq^n 6.7]$$

$$Y_4 = -0.718 + 0.1076X_1 - 0.0337X_2 - 0.0093\,X_3 - 0.350\,X_4 - 0.001501\,X_1{\times}X_1 + 0.000604X_2{\times}X_2 - 0.000743\,X_3{\times}X_3 + 0.00043X_4{\times}X_4 + 0.000210\,X_1{\times}X_2 + 0.001460X_1{\times}X_3 + 0.005750X_1{\times}X_4 - 0.001110X_2{\times}X_3 - 0.006500X_2{\times}X_4 + 0.01300\,X_3{\times}X_4 \quad ...[Eq^n 6.8]$$

6.7.2 ANOVA Test Results of the Developed Models

Analysis of variance (ANOVA) test has been performed using MINITAB software to test the adequacy of the developed models. Table 6.5, 6.6, 6.7 and 6.8 show the results of ANOVA for entry hole diameter, exit hole diameter, HAZ thickness at entry, circularity respectively of fiber laser generated micro-hole on quartz.

Table 6.5 ANOVA table for entry hole diameter

Source	DOF	Adjusted SS	Adjusted MS	F-Value	p-value
Model	14	2109.50	150.678	60.96	0.000
Linear	4	931.38	232.845	94.20	0.000
Pulse Frequency	1	177.29	177.290	71.73	0.001
Duty Cycle	1	14.31	14.307	5.79	0.029
Laser Power	1	207.27	207.270	83.86	0.000
Air Pressure	1	532.51	532.513	215.44	0.000
Square	4	425.31	106.328	43.02	0.000
Pulse Frequency*Pulse Frequency	1	155.25	155.253	62.81	0.002
Duty Cycle*Duty Cycle	1	215.46	215.458	87.17	0.000
Laser Power*Laser Power	1	0.12	0.121	0.05	0.828
Air Pressure *Air Pressure	1	9.25	9.252	3.74	0.071
2-Way Interaction	6	752.81	125.468	50.76	0.000
Pulse Frequency *Duty Cycle	1	0.24	0.243	0.10	0.758
Pulse Frequency *Laser Power	1	254.96	254.961	103.15	0.000
Pulse Frequency *Air Pressure	1	37.00	36.997	14.97	0.001
Duty Cycle*Laser Power	1	351.09	351.094	142.05	0.000
Duty Cycle*Air Pressure	1	109.46	109.464	44.29	0.000
Laser Power*Air Pressure	1	0.05	0.047	0.02	0.892
Error	16	39.55	2.472		
Lack-of-Fit	10	26.95	2.695	1.28	0.395
Pure Error	6	12.60	2.100		
Total	30	2149.04			
			R^2	**R^2 Adjusted**	**R^2 Predicted**
Model Summary			98.16	96.55	91.98

Table 6.6 ANOVA table for exit hole diameter

Source	DOF	Adjusted SS	Adjusted MS	F-Value	p-Value
Model	14	1255.85	89.703	34.25	0.000
Linear	4	676.13	169.033	64.54	0.000
Pulse Frequency	1	233.81	233.813	89.28	0.000
Duty Cycle	1	38.43	38.431	14.67	0.001
Laser Power	1	131.93	131.930	50.38	0.000
Air Pressure	1	271.96	271.959	103.84	0.000
Square	4	157.95	39.488	15.08	0.000
Pulse Frequency *Pulse Frequency	1	32.62	32.616	12.45	0.003
Duty Cycle*Duty Cycle	1	94.80	94.800	36.20	0.000
Laser Power *Laser Power	1	0.45	0.450	0.17	0.684
Air Pressure *Air Pressure	1	13.29	13.290	5.07	0.039
2-Way Interaction	6	421.76	70.293	26.84	0.000
Pulse Frequency*Duty Cycle	1	1.48	1.482	0.57	0.463
Pulse Frequency *Laser Power	1	148.29	148.292	56.62	0.000
Pulse Frequency *Air Pressure	1	18.34	18.340	7.00	0.018
Duty Cycle*Laser Power	1	171.94	171.938	65.65	0.000
Duty Cycle*Air Pressure	1	74.78	74.779	28.55	0.000
Laser Power*Air Pressure	1	6.93	6.930	2.65	0.123
Error	16	41.90	2.619		
Lack-of-Fit	10	22.02	2.202	0.66	0.730
Pure Error	6	19.88	3.314		
Total	30	1297.75			
Model Summary			**R^2**	**R^2 Adjusted**	**R^2 Predicted**
			96.77	93.95	88.14

Table 6.7 ANOVA table for HAZ thickness

Source	DOF	Adjusted SS	Adjusted MS	F-Value	p-Value
Model	14	4996.73	356.91	330.97	0.000
Linear	4	4433.05	1108.26	1027.72	0.000
Pulse Frequency	1	3887.23	3887.23	3604.71	0.000
Duty Cycle	1	502.33	502.33	465.83	0.000
Laser Power	1	11.93	11.93	11.06	0.004
Assist Air Pressure	1	31.56	31.56	29.26	0.000
Square	4	324.12	81.03	75.14	0.000
Pulse Frequency *Pulse Frequency	1	42.7	42.7	39.6	0.000
Duty Cycle *Duty Cycle	1	194.69	194.69	180.54	0.000
Laser Power *Laser Power	1	50.53	50.53	46.86	0.000
Air Pressure*Air Pressure	1	35.59	35.59	33	0.000
2-Way Interaction	6	239.56	39.93	37.02	0.000
Pulse Frequency *Duty Cycle	1	21.3	21.3	19.75	0.000
Pulse Frequency *Laser Power	1	82.72	82.72	76.71	0.000
Pulse Frequency * Air Pressure	1	133.86	133.86	124.14	0.000
Duty Cycle *Laser Power	1	0.28	0.28	0.26	0.617
Duty Cycle * Air Pressure	1	1.31	1.31	1.22	0.287
Laser Power * Air Pressure	1	0.08	0.08	0.08	0.787
Error	16	17.25	1.08		
Lack-of-Fit	10	12.8	1.28	1.72	0.261
Pure Error	6	4.46	0.74		
Total	30	5013.98			
Model Summary			**R^2**	**R^2 Adjusted**	**R^2 Predicted**
			99.66	93.35	98.41

Table 6.8 ANOVA table for circularity

Source	DOF	Adjusted SS	Adjusted MS	F-Value	p-Value
Model	14	0.058882	0.004206	103.91	0.000
Linear	4	0.012933	0.003233	79.88	0.000
Pulse Frequency	1	0.004760	0.004760	117.61	0.000
Duty Cycle	1	0.000060	0.000060	1.49	0.240
Laser Power	1	0.004108	0.004108	101.50	0.000
Assist Air Pressure	1	0.004004	0.004004	98.93	0.000
Square	4	0.028115	0.007029	173.66	0.000
Pulse Frequency*Pulse Frequency	1	0.023485	0.023485	580.23	0.000
Duty Cycle*Duty Cycle	1	0.002496	0.002496	61.66	0.000
Laser Power*Laser Power	1	0.000556	0.000556	13.73	0.002
Assist Air Pressure*Assist Air Pressure	1	0.000118	0.000118	2.92	0.107
2-Way Interaction	6	0.017834	0.002972	73.44	0.000
Pulse Frequency*Duty Cycle	1	0.001600	0.001600	39.53	0.000
Pulse Frequency*Laser Power	1	0.005476	0.005476	135.29	0.000
Pulse Frequency*Assist Air Pressure	1	0.002070	0.002070	51.15	0.000
Duty Cycle*Laser Power	1	0.005625	0.005625	138.98	0.000
Duty Cycle*Assist Air Pressure	1	0.000306	0.000306	7.57	0.014
Laser Power*Assist Air Pressure	1	0.002756	0.002756	68.10	0.000
Error	16	0.000648	0.000040		
Lack-of-Fit	10	0.000360	0.000036	0.75	0.671
Pure Error	6	0.000287	0.000048		
Total	30	0.059529			
Model Summary			**R^2**	**R^2 Adjusted**	**R^2 Predicted**
			98.91	97.96	95.86

(a) ANOVA for Entry Hole Diameter

The results of the analysis of variance (ANOVA) for the model of entry hole diameter is given in table 6.5. The p-value for model, linear, and square terms of entry hole diameter are less than 0.05. The p-value of the lack of fit for entry hole diameter is found as 0.395. The p-value is used to determine the significance of the factors. The analysis is carried out at a 95% confidence level. Thus, a process parameter or their combination are considered significant if the p-value is less than 0.05. As the p-value for lack of fit for entry hole diameter model is higher than 0.05, this indicates that the lack of fit is significant. Hence, the data are well fitted in the model for entry hole diameter. In addition to this, R^2, R^2 (adjusted) and R^2 (predicted) values are close to 1 for this model. Therefore, the developed model for the entry hole diameter is adequate for prediction.

(b) ANOVA for Exit Hole Diameter

ANOVA table 6.6 shows the results of the ANOVA test of the model for exit hole diameter. From the results, it is observed that the model, linear as well as square terms, p-value are less than 0.05. The associated p-value for lack of fit is 0.730. The lack of fit is insignificant that means the fit is significant. The lack of fit value indicates that the developed empirical model on exit hole diameter represented by equation 6.6 is statistically significant and adequate at 95% confidence level. Besides, R^2, R^2 (adjusted) and R^2 (predicted) values are close to 1 for this model. Therefore, the developed model of exit hole diameter is valid.

(c) ANOVA for HAZ Thickness

From ANOVA table 6.7, it is found that p-value of lack of fit for HAZ thickness is 0.261, which is insignificant. The associated p-values for the model, linear, and square term values for HAZ thickness are found to be below of 0.05. Thus, the developed empirical model for HAZ thickness represented by equation 6.7 is highly significant and adequate at a confidence level of 95% to represent the relationship between HAZ thickness on quartz and the fiber laser process parameters. Besides, R^2, R^2 (adjusted) and R^2 (predicted) values are close to 1 for this model.

(d) ANOVA for Circularity

Table 6.8 represents the results of the ANOVA test for entry hole circularity of the micro-holes generated on quartz. From table 6.8, it is observed that the associated p-value for linear effect and four process parameters are less than 0.05 for circularity. The lack of fit value for the model is found as which is insignificant. As a result, the fit value for the developed model is significant. Thus, the developed empirical model on circularity represented by equation 6.8 is highly significant and adequate at a confidence level of 95% to represent the relationship between circularity and the fiber laser process parameters.

6.7.3 Analysis of Fiber Laser Process Parameters based on Response Surface and Contour Plots

The various response surfaces have been plotted between one process criteria and two process parameters at a time, while the other two remaining process parameters are kept at constant values. The results of parametric analyses of entry hole diameter, exit hole diameter, HAZ

thickness and circularity with respect to process variables such as laser power, pulse frequency, duty cycle, and air pressure have been discussed with the aid of surface and contour plots.

6.7.3.1 Parametric Influences on Entry Hole Diameter of Micro-Holes on Quartz

From figure 6.14, it is observed that the entry hole diameter gradually decreases with an increase in pulse frequency, and linearly increases with an increase in laser power. It is also observed from the plot that the entry hole diameter is low at a higher value of laser power in combination with a higher value of pulse frequency. Incomplete expulsion of the ejected material from the micro-drilling zone at a lower value of laser power combined with the moderate value of assist air supply may lead to a lower value of entry hole diameter. Low energy per pulse may also be the reason behind the observed phenomenon.

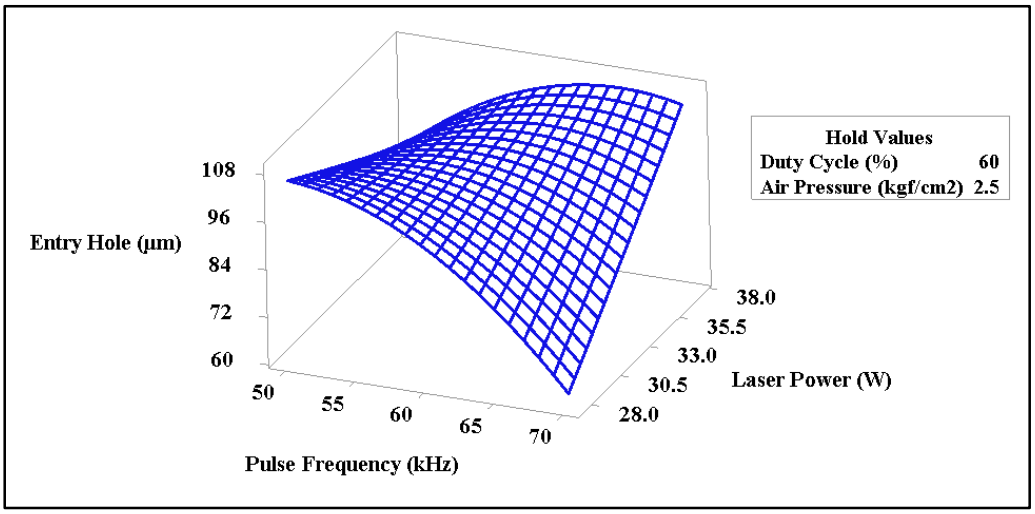

Figure 6.14 Surface plot for influences of pulse frequency and laser power on entry hole diameter

Contour plot, as shown in figure 6.15, indicates the most viable ranges of laser power and pulse frequency to achieve the desired entry hole diameter in the range of 90 µm to 100 µm. Figure 6.15 also justifies the observation of surface plot of entry hole diameter with laser power and pulse frequency when the other two process variables are kept constant at their intermediate values.

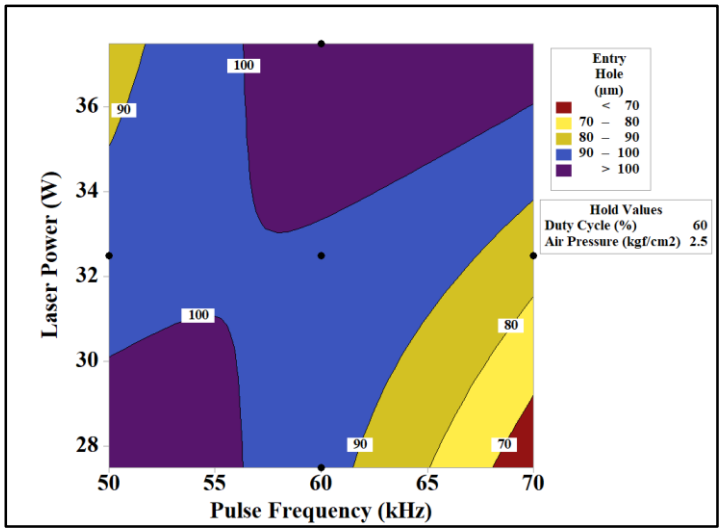

Figure 6.15 Contour plot for influences of pulse frequency and laser power on entry hole diameter

Figure 6.16 reveals the surface plot of the entry hole diameter due to the effect of duty cycle and air pressure. It is observed from figure 6.16 that entry hole diameter increases with an increment in duty cycle at low air pressure. The entry hole diameter linearly increases at a low value of the duty cycle. However, it is also found that the air pressure has a minimal effect on the entry hole diameter at a higher value of duty cycle. Moderate value of laser power and pulse frequency at a higher value of duty cycle may generate lesser peak power, results in a lower volume of molten debris at the top surface of micro-holes of quartz. The debris may adequately be removed by high assist air pressure to achieve higher dimensions of the entry hole.

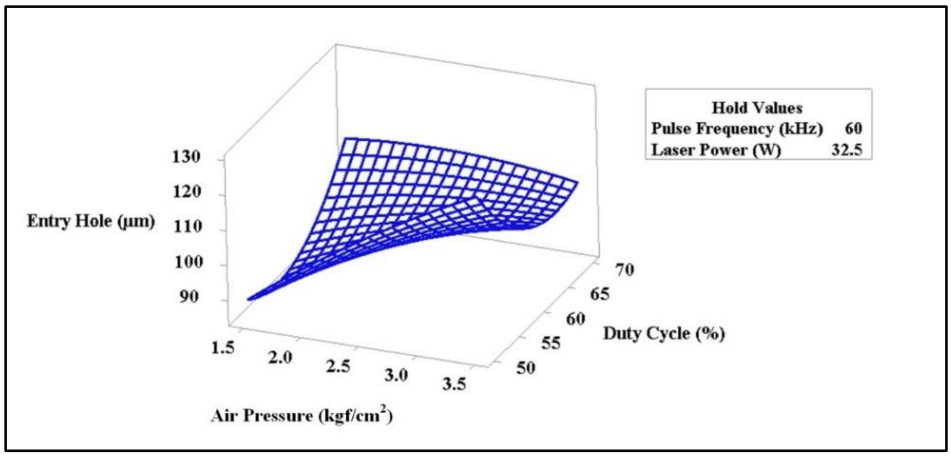

Figure 6.16 Surface plot for influences of air pressure and duty cycle on entry hole diameter

Figure 6.17 exhibits the contour plot between air pressure and duty cycle for the entry hole diameter. From figure 6.17, it is observed that the largest confined region of the contour diagram is the most favored range of entry hole diameter, i.e., 100 µm to be achieved during the present experimental investigation. The second smallest contour area points out at the parametric situation to attain the lowest value of the entry hole, i.e., 90 µm.

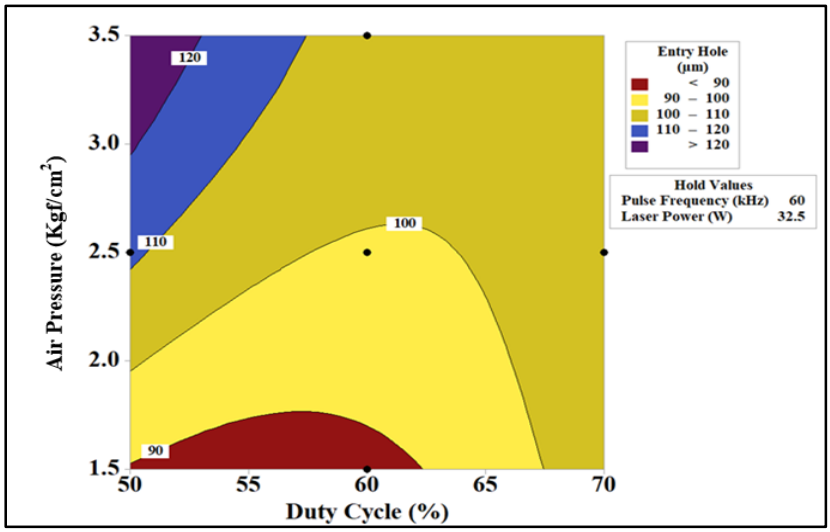

Figure 6.17 Contour plot for influences of air pressure and duty cycle on entry hole diameter

6.7.3.2 Parametric Influences on Exit Hole Diameter of Micro-Holes on Quartz

Figure 6.18 indicates the surface plot for the influences of laser power and pulse frequency on the exit hole diameter. Figure 6.18 reveals that exit hole diameter decreases with an increase in pulse frequency at a lower value of laser power and vice versa. An increment in pulse frequency leads to an increase in number of pulses, results in the splashing of melt pool, which leads to re-solidification of that molten debris in the inner wall of the micro-drilled hole. Thus, the lowest hole diameter is achieved at the lowest value of laser power and a high value of pulse frequency when pulse energy at its lowest value.

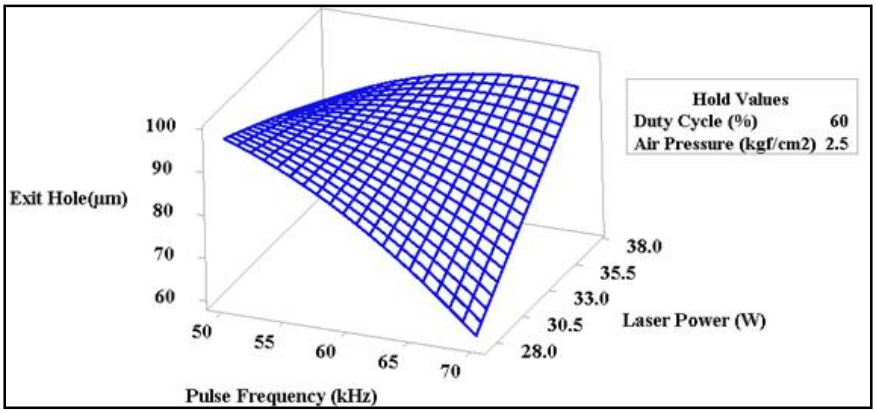

Figure 6.18 Surface plot for influences of laser power and pulse frequency on exit hole diameter

Figure 6.19 exhibits a functional interaction between laser power and pulse frequency. The largest confined surface of the plot indicates at the high value of exit hole diameter when the duty cycle and air pressure are kept constant at 60% and 2.5 kgf/cm^2, respectively.

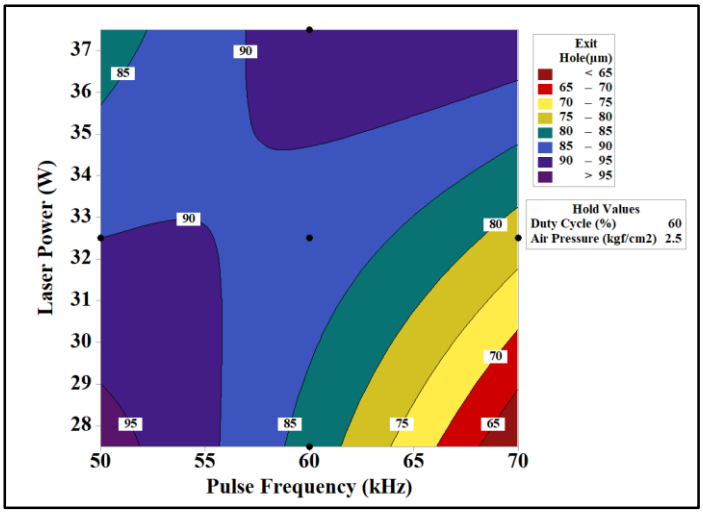

Figure 6.19 Contour plot for influences of laser power and pulse frequency on exit hole diameter

Figure 6.20 shows the surface plot for the interaction of duty cycle and air pressure on the exit hole dimension. It is evident from figure 6.20 that the exit hole diameter increases with an increase in duty cycle; however, is reversed with a decrease in air pressure. Peak power increases at a low duty cycle, which causes an increment in the penetration depth of the irradiated laser beam. A higher value of peak power in conjunction with the laser power of 32.5 W along with pulse frequency 60 kHz, produces a reasonable amount of melt pool in the micro-drilled surface.

The lower value of air pressure cannot remove the entire molten debris from the drilling zone. The phenomenon mentioned above may be the reason behind the generation of higher exit hole diameter at a lower value of the duty cycle.

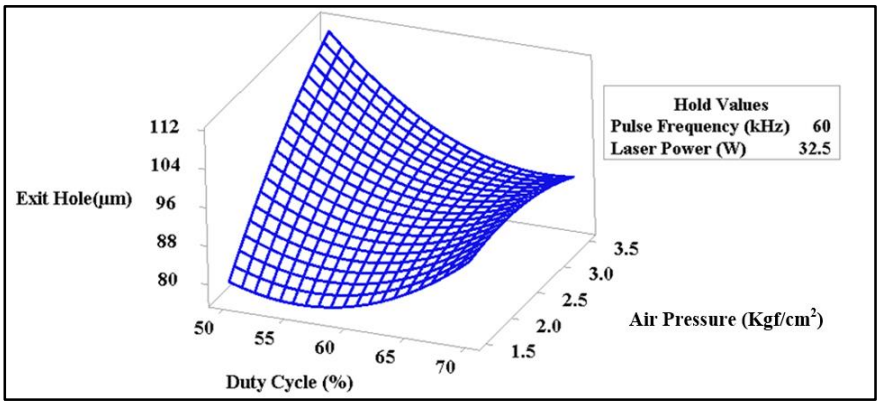

Figure 6.20 Surface plot for influences of duty cycle and air pressure on exit hole diameter

Figure 6.21 represents the contour plot due to the interaction of the duty cycle and air pressure on the exit hole dimensions of quartz. The contour plot indicates at the most viable range of exit hole diameter is achieved due to the interaction of process parameters described above. It is also observed that desirable low value of exit hole diameter (80 µm) is achieved when air pressure kept around at 1.5 kgf/cm^2 along with duty cycle within the range of 50 to 60 % of cycle time. The contour plot findings also justify the surface plot of the exit hole diameter due to the influences of air pressure and duty cycle.

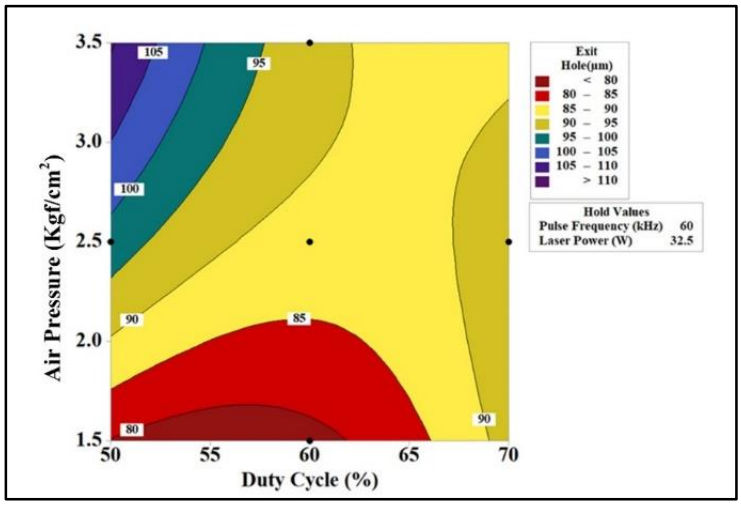

Figure 6.21 Contour plot for influences of duty cycle and air pressure on exit hole diameter

6.7.3.3 Parametric Influences on HAZ Thickness of Micro-Holes on Quartz

Figure 6.22 represents the surface plot for the interaction of pulse frequency and duty cycle for HAZ thickness. From the surface plot for figure 6.22, it is found that both pulse frequency and duty cycle have a considerable effect on the response, i.e., HAZ thickness. HAZ thickness decreases with an increase in pulse frequency. HAZ thickness marginally increases to 60% of duty cycle then decreases with further increase in the duty cycle. Pulse per energy is comparatively high at a lower value of pulse frequency when laser power kept constant at 32.5 W with variation in duty cycle. Increase in duty cycle causes prolonged heating of the workpiece due to the increase in interaction time between the laser beam and the workpiece, which further increases HAZ thickness of fiber laser fabricated micro-holes on quartz.

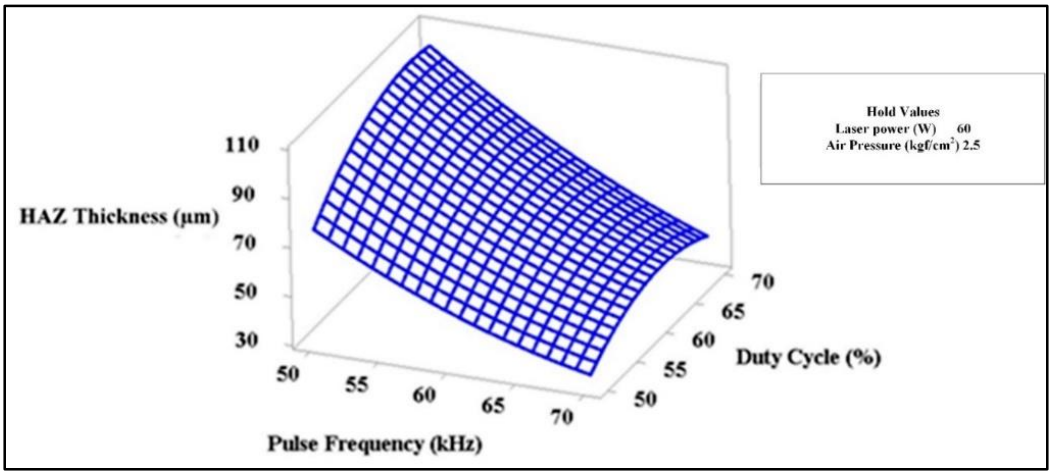

Figure 6.22 Surface plot for influences of pulse frequency and duty cycle on HAZ thickness

The elliptical shape of the contour plot, i.e., figure 6.23, indicates good interaction laser power and air pressure for the HAZ thickness values. The largest confined elliptical region indicates at the most favored dimension of HAZ thickness ranging from 50 to 60 µm within the chosen design space, whereas the smallest one indicates at the lowest value of HAZ thickness (< 40 µm) with the parameter settings of pulse frequency of 65 kHz to 70 kHz along with duty cycle at 50%, laser power at 32.5 W and air pressure at 2.5 kgf/cm^2.

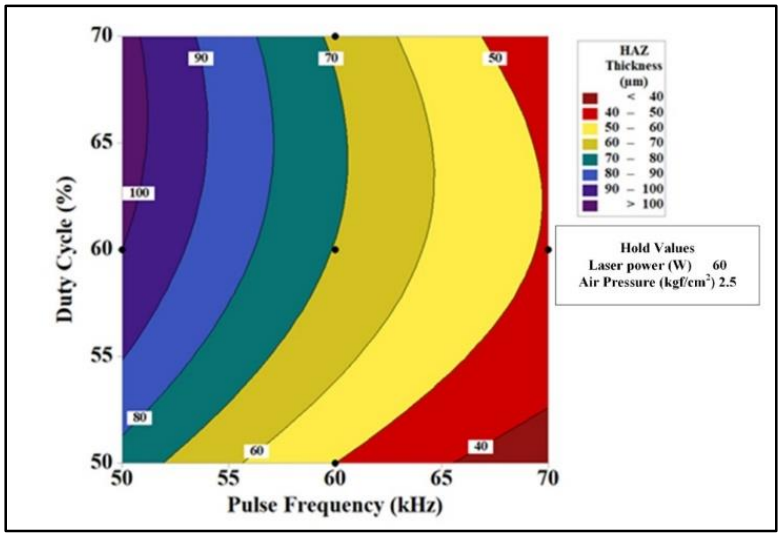

Figure 6.23 Contour plot for influences of pulse frequency and duty cycle on HAZ thickness

Figure 6.24 shows the influences of laser power and pulse frequency on the HAZ thickness of the fiber laser generated micro-holes on quartz. It is observed from the surface plot that HAZ thickness is linearly decreasing with an increase in the value of pulse frequency. HAZ thickness increases with an increase in laser power at a lower value of pulse frequency whereas shows a decreasing tendency with an increase in laser power at a higher value of pulse frequency. Energy density at the point of interaction is more for the lower value of pulse frequency with the moderate or higher value of pulse frequency, and comparatively lower thermal diffusivity of quartz at elevated temperature may be the reason behind the increase in HAZ thickness.

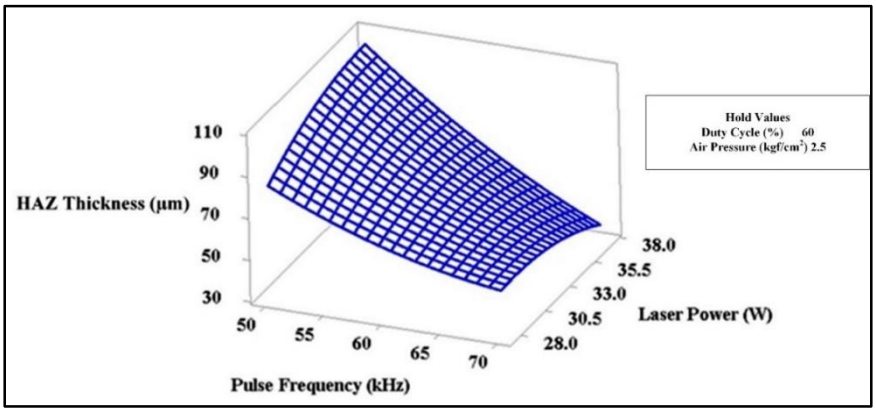

Figure 6.24 Surface plot for influences of pulse frequency and laser power on HAZ thickness

Figure 6.25 shows the contour plot for the interaction of pulse frequency and laser power on HAZ thickness. The contour plot represents a functional interaction between two controllable process variable when the other two process variables at kept constant at their respective middle values. The smallest elliptic region indicates the lowest value of HAZ thickness, which can be attained with proper settings of process variables with the highest value of laser power and pulse frequency.

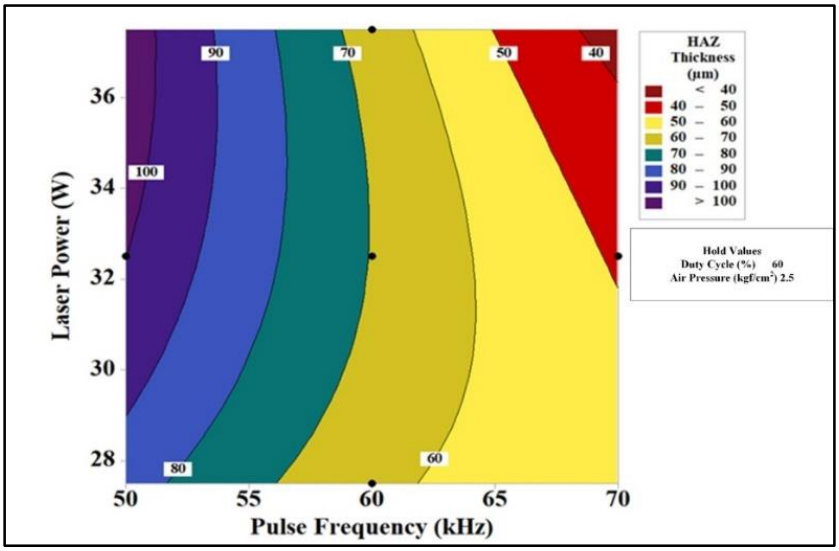

Figure 6.25 Contour plot for influences of pulse frequency and laser power on HAZ thickness

6.7.3.4 Parametric Influences on Entrance Hole Circularity of Micro-Holes on Quartz

Figure 6.26 illustrates the influence of the duty cycle and pulse frequency on the entrance hole circularity. It is observed that the circularity increases with an increase in pulse frequency up to 65 kHz, then decreases with further increase in pulse frequency. It is also found that the hole circularity gradually decreases with an increase in duty cycle at a lower value of pulse frequency, but increases with an increase in duty cycle at a higher value of pulse frequency. High Intensity of pulse energy in conjunction with high peak power at the lower value of pulse frequency and duty cycle may lead to a uniform spattering of molten debris on the edge of the periphery of the drilled hole. As a result, an increment in hole circularity of fiber laser generated micro-holes is observed.

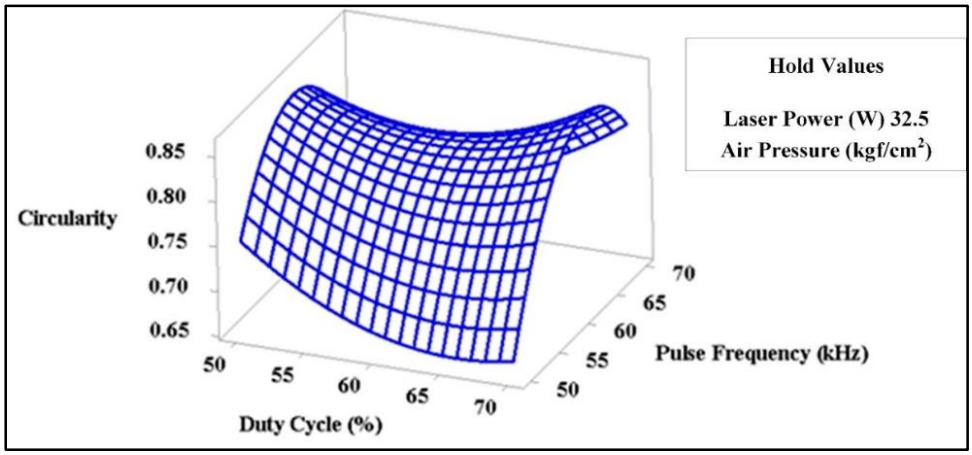

Figure 6.26 Surface plot for influences of duty cycle and pulse frequency on hole circularity

Figure 6.27 shows the contour plot for the hole circularity due to the influences of pulse frequency and duty cycle. The contour plot reveals that a significant interaction between two process variables, i.e., pulse frequency and duty cycle. The largest confined region indicates the most favored outcome from the present experimental range, whereas the second smallest confined zone indicates at the most preferred parametric condition to achieve the highest value of hole circularity.

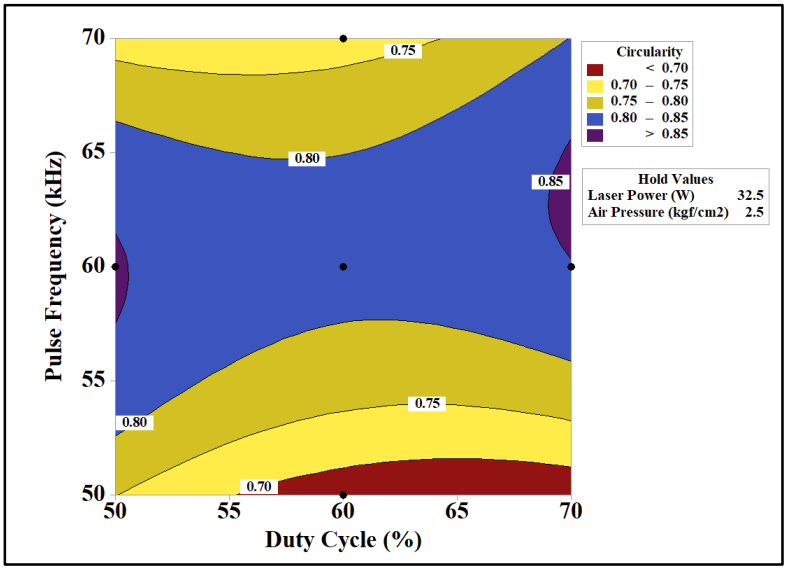

Figure 6.27 Contour plot for influences of duty cycle and pulse frequency on hole circularity

Figure 6.28 reveals a parabolic nature of the surface plot for the hole circularity due to the interaction between pulse frequency and air pressure. The highest value of hole circularity can be

achieved at moderate value pulse frequency, i.e., 55 to 60 kHz. It is also observed from figure 6.40 that at the lower value of pulse frequency, air pressure has a very small or no effect on the hole circularity. On the contrary, the hole circularity linearly increases with the increase in air pressure at a higher value of pulse frequency. A decrease in pulse off time due to an increase in pulse frequency results in a decrease in agitation, forming a melt pool at the top surface of the workpiece. Lesser agitation on the melt pool in terms of surface tension leads to form a smooth edge of the micro-drilled hole. Pulse frequency is inversely proportional to pulse energy when the laser power and duty cycle are kept as constants at their moderate values. The high pulse energy of a Gaussian laser beam produces adequate melt pool and increases the spattering effect. The lower value of air pressure is incapable of sweeping away the spatters or properly removes the melt pool from the micro-drilled zone, leads to the formation of the non- uniform edge of the micro-drilled hole. As a result, low circularity is observed.

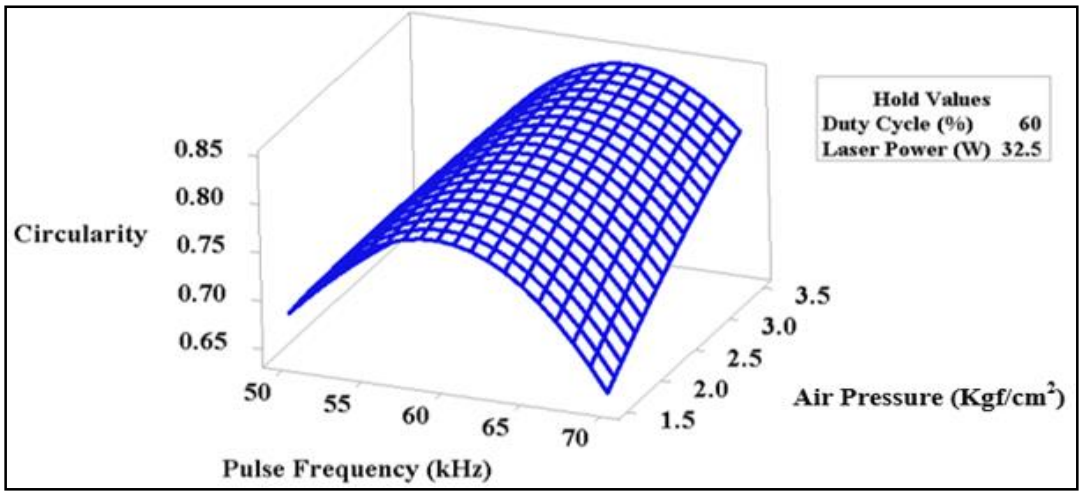

Figure 6.28 Surface plot for influences of pulse frequency and air pressure on hole circularity

Figure 6.29 indicates the interaction between pulse frequency on hole circularity via a contour plot. The elliptic shape of contours shows a functional interaction between air pressure and pulse frequency. The second largest confined zone indicate at the parametric options at which the highest value of hole circularity can be attained.

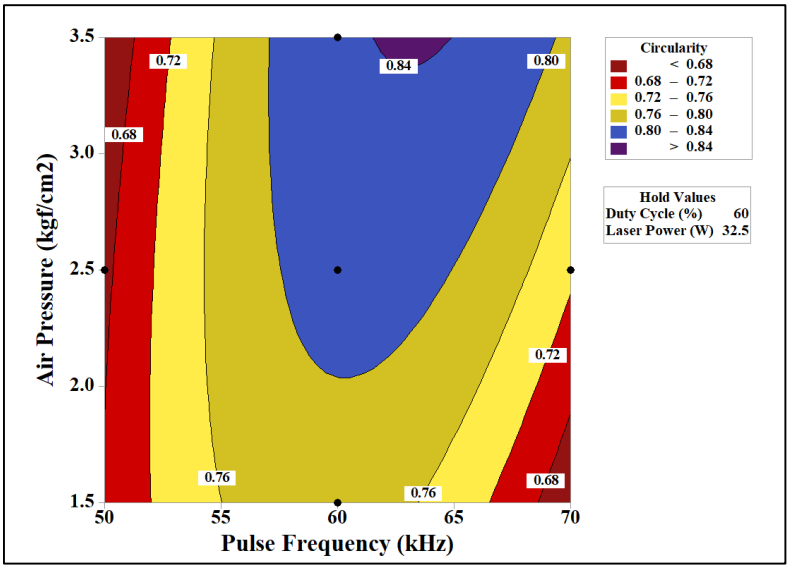

Figure 6.29 Contour plot for influences of pulse frequency and air pressure on hole circularity

6.8 Parametric Optimization of Fiber Laser Micro-Drilling of Quartz

For achieving optimal parametric combination during fiber laser micro-drilling of quartz, single-objective, as well as multi-objective optimization, has been performed using MINITAB software.

6.8.1 Single Objective Optimization of the Responses

The results of single-objective optimization for entry hole, exit hole, HAZ thickness and hole circularity during the generation of micro-holes on quartz by fiber laser micro-drilling, have been shown in figure 6.30, 6.31, 6.32 and 6.33 respectively.

It is found from the figure 6.30, that minimum hole entry diameter of 65.71 µm can be achieved at pulse frequency of 65 kHz in conjunction with duty cycle of 55%, laser power of 30 W and air pressure of 1.50 kgf/cm^2.

Figure 6.31 shows that the minimum hole exit diameter of 63.75 µm can be achieved at pulse frequency of 64 kHz with duty cycle of 55%, laser power of 30 W and air pressure of 1.50 kgf/cm^2.

It is found from the optimization plot of figure 6.32 that the lowest value of HAZ thickness 49.90 µm can be attained at the pulse frequency of 70 kHz, duty cycle of 55%, laser power of 29 W and air pressure of 2 kgf/cm^2.

Figure 6.33 illustrates that the parametric settings required to achieve the maximum hole circularity of 0.88 at entry side are pulse frequency of 65 kHz along with duty cycle of 50 %, the laser power of 37 W and air pressure of 2.50 kgf/cm^2.

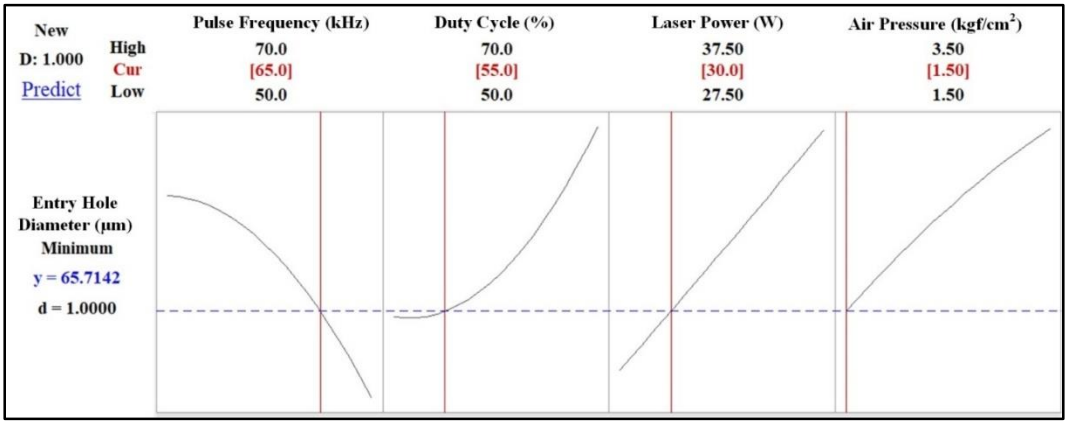

Figure 6.30 Single-objective optimization results for entry hole diameter

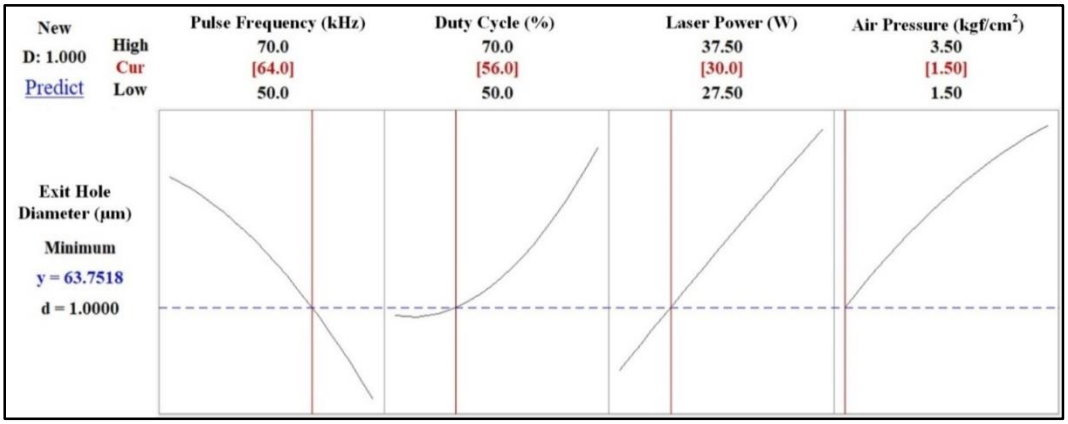

Figure 6.31 Single-objective optimization results for exit hole diameter

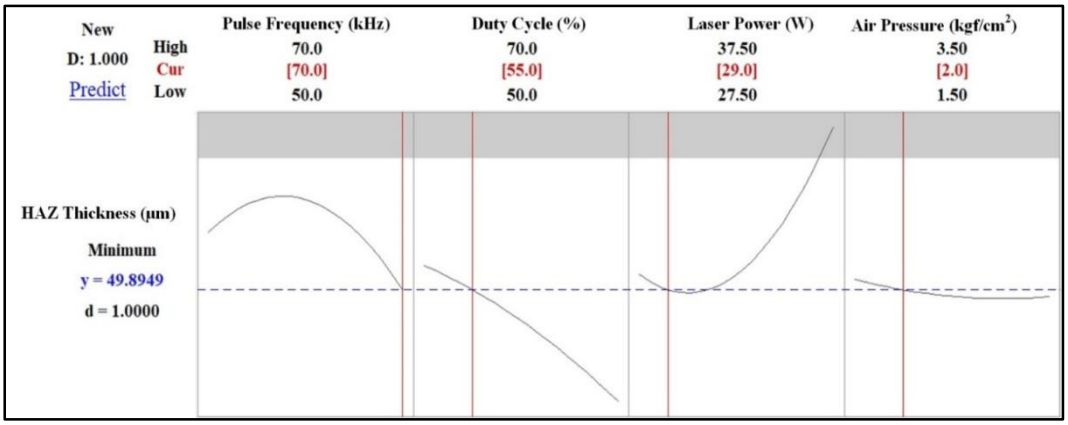

Figure 6.32 Single-objective optimization results for HAZ thickness

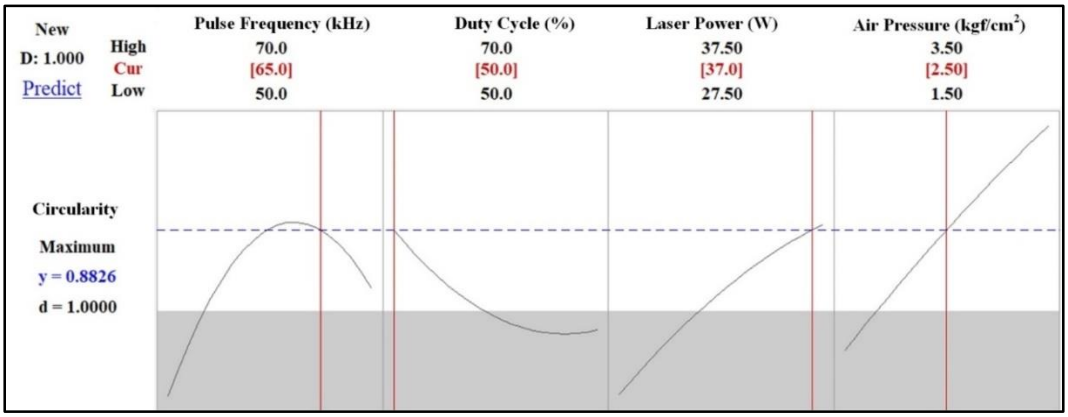

Figure 6.33 Single-objective optimization results for hole circularity

6.8.2 Multi-Objective Optimization of the Responses

Simultaneous optimization in terms of multi-objective optimization is carried out in order to find out the optimal parametric settings for the desired values of the responses, as shown in figure 6.34. From figure 6.34, it is found that all the optimal value of responses is degraded during multi-objective optimization comparatively to single objective optimization, but the value of D of 1, which indicates the optimal condition. The optimal parametric setting of pulse frequency of 64.75 kHz in conjunction with the duty cycle of 62.5 %, laser power of 29 W and air pressure of 1.50 kgf/cm^2 predicts the entry hole diameter of 76.53µm, the exit hole diameter of 67.33 µm, HAZ thickness of 58.06 µm, and hole circularity of 0.79.

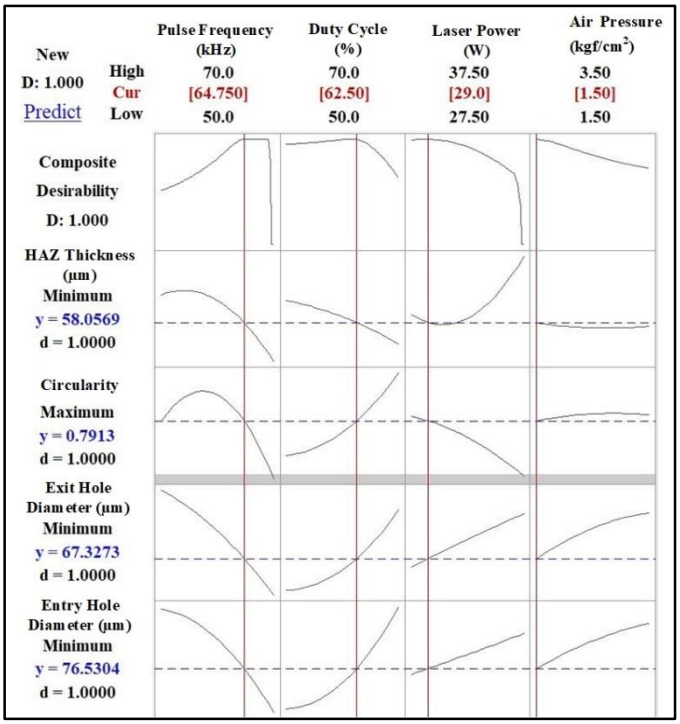

Figure 6.34 Multi-objective optimization results for entry hole, exit hole, HAZ thickness and hole circularity

6.8.3 Confirmation Experiments

Confirmation experiments are conducted to validate the predicted results at the optimized experimental parameter settings. The mean prediction errors of the experimental values are evaluated to compare the experimental values of the four responses with their optimized values. A total of five confirmation experiments are conducted. The experimental values of the entry hole diameter and exit hole diameter are shown in table 6.9, whereas table 6.10 shows the experimental values of HAZ thickness and circularity. The mean prediction errors for entry hole diameter, exit hole diameter, HAZ thickness, and circularity are found out to be 3.39 %, 3.92 %, 4.11 %, and 2.53 % respectively. The calculated error values indicate that the produced results are a close agreement with the predicted results. Figure 6.35 shows the microscopic image at 50X of fiber laser generated micro-hole on quartz at optimized combinations of process parameters.

Table 6.9 Comparison between multi-objective optimization results with actual results for Entry hole and exit hole diameter

Exp. No:	Entry Hole Diameter (µm)			Exit Hole Diameter (µm)		
	Minimum value	Actual value at optimum condition	Percentage of Errors (%)	Minimum value	Actual value at optimum condition	Percentage of Errors
1	76.53	78.56	2.65	67.32	64.56	4.10
2	76.53	79.1	3.36	67.32	63.97	4.98
3	76.53	78.35	2.38	67.32	64.12	4.75
4	76.53	79.98	4.51	67.32	65.65	2.48
5	76.53	79.65	4.08	67.32	64.78	3.77
Mean Percentage of Errors (%)=3.39				**Mean Percentage of Errors (%)=3.92**		

Table 6.10 Comparison between multi-objective optimization results with actual results for HAZ thickness and circularity

Exp. No:	HAZ Thickness (µm)			Circularity		
	Minimum value	Actual value at optimum condition	Percentage of Errors (%)	Minimum value	Actual value at optimum condition	Percentage of Errors
1	58.05	55.19	4.93	0.79	0.82	3.80
2	58.05	55.79	3.89	0.79	0.81	2.53
3	58.05	55.16	4.98	0.79	0.78	1.27
4	58.05	55.98	3.57	0.79	0.82	3.80
5	58.05	56.32	2.98	0.79	0.78	1.27
Mean Percentage of Errors (%)=4.11				**Mean Percentage of Errors (%)=2.53**		

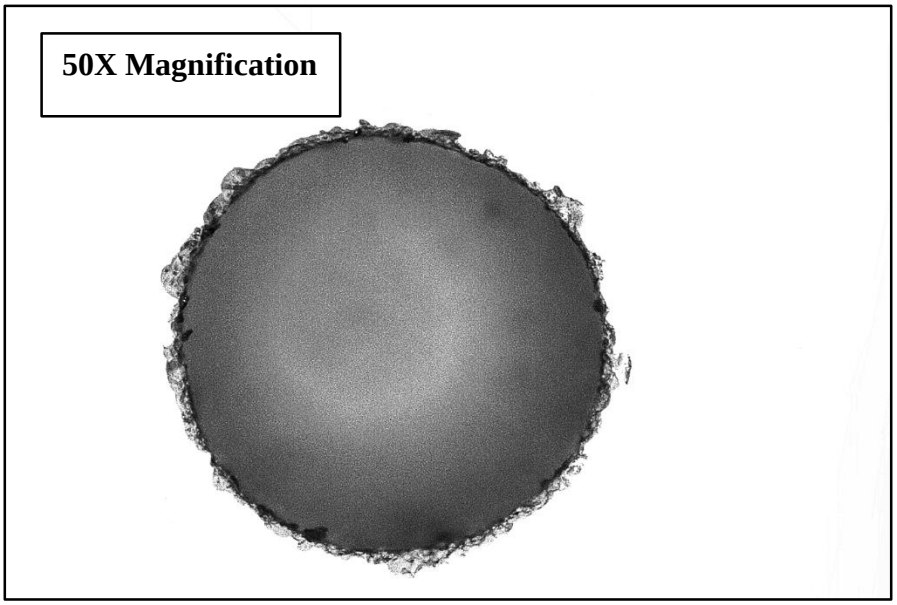

Figure 6.35 Microscopic image of quartz micro-hole at 50X magnification at the optimal condition

6.9 Outcomes of the Present Research Work

In the present research work, a nanosecond pulsed fiber laser system is utilized to generate micro-holes on transparent quartz. An RSM based experimental design is utilized to carry out a total of 31 experiments to analyze the effect of various process parameters on the entry and exit hole diameter, HAZ thickness, and circularity of micro-hole drilled on quartz. From the ANOVA table, the p-value of the lack of fit for entry hole diameter is found as 0.395, whereas the p-value of the lack of fit for exit hole, HAZ thickness and hole circularity are obtained as 0.730, 0.261 and 0.671 respectively. The developed mathematical models on both hole diameters, HAZ thickness, and entry hole circularity are adequate for prediction during fiber laser micro-drilling on quartz.

Single objective optimization results show that for obtaining minimum entry hole diameter 65.71 μm, a combination of pulse frequency of 65 kHz along with duty cycle of 55%, laser power of 30 W and air pressure of 1.50 kgf/cm^2 is required. For achieving minimum exit hole diameter (63.75 μm) along with minimum HAZ thickness (49.89 μm) the combination of the process parameters are pulse frequency of 64 kHz with duty cycle of 55%, laser power of 30 W and air pressure of 1.50 kgf/cm^2; pulse frequency of 70 kHz, duty cycle of 55%, laser power of 29 W and air pressure of 2 kgf/cm^2 respectively. On the contrary, to obtain the maximum hole circularity

(0.88) the combination of the process parameters are pulse frequency of 65 kHz along with duty cycle of 50 %, laser power of 37 W and air pressure of 2.50 kgf/cm^2.

Finally, multi-objective optimization results illustrate that the parametric settings of pulse frequency of 64.75 kHz combined with duty cycle of 62.5 %, laser power of 29 W and air pressure of 1.50 kgf/cm^2 are set to achieve the minimum entry hole diameter of 76.53 μm, minimum exit hole diameter of 67.33 μm, minimum HAZ thickness of 58.06 μm, and maximum hole circularity of 0.79. The conformity tests reveal that the errors for entry hole diameter, exit hole diameter, HAZ thickness and circularity are found out to be 3.39 %, 3.92 %, 4.11 %, and 2.53 % respectively, and the predicted results a very close agreement with the experimental results.

7. EXPERIMENTAL INVESTIGATION INTO FIBER LASER SURFACE TEXTURING ON HASTELLOY C-276

7.1 Introduction

At the present scenario, controlling surface characteristics such as friction, wear rates, fatigue failure of a given material needs special attention in order to utilize the material for various manufacturing applications. Thus, texturing of the surface quality of that workpiece needs to be carried out according to the required field of applications. Over a wide range of surface texturing methods, employment of a laser processing method is preferable due to its flexibility and reduction of time and cost simultaneously. The tribological characteristics of the given material can be reduced or increased according to the manufacturing requirement through laser surface texturing method. Laser surface texturing process can change the surface characteristics of a given workpiece. Cross grooves, linear grooves, and dimple-shaped impressions are the most common procedures in connection with the laser surface texturing process.

At present, nickel alloys are highly desirable in various manufacturing applications where high temperature and corrosion are involved. Among the various nickel alloys, Hastelloy series has gained a rapid boom in various automotive domains, especially in bearing applications. Hastelloy C-276 is also one of the preferred choices of material over other Hastelloy series materials in extreme environmental condition due to its high molybdenum content and other superior properties. The presence of low percentages of carbon in the alloy also restricts against precipitation of carbide during a laser welding process. As a result, corrosion resistant welded structures are maintained throughout the process.

However, the aforesaid superior properties of Hastelloy C-276 have also contributed to the difficulty of attaining an excellent surface finish during machining of the alloy. As a result, several researchers have centralized their research on super alloys dealing with on aerospace industry [86]. The amount of research works on Hastelloy C-276 is primarily limited to the laser welding method. In the past, only a few researchers have tried to analyze the laser processing method on Hastelloy C-276 on the aspect of wear resistance.

In the present work, an effort has been made to analyze the different surface roughness parameters during the fiber laser surface texturing of Hastelloy C-276. However, no previous research studies were conducted on the laser textured surface of Hastelloy C-276 to determine an

average surface roughness, maximum height of the profile, skewness, and kurtosis parameters. The aim of the research work to analyze the effect of laser process parameters on these responses as well as to obtain the desired roughness parameters values for the utilization of textured Hastelloy C-276 surface in various high power applications. Also, a comparative study of the responses, as mentioned above, has also been carried out at different temperatures to find the effect of each process parameter on the responses.

7.2 Selection of the Process Parameters and Responses

The selected process parameters for fiber laser surface texturing of Hastelloy are laser power, pulse frequency, duty cycle, and scan speed. The detail of each process parameters is discussed in chapter 3. The surface characteristics for fiber laser surface texturing of Hastelloy are average surface roughness (R_a), maximum height of the profile (R_z), skewness (R_{sk}) and kurtosis (R_{ku}).

7.3 Properties of Hastelloy C-276

In the present research work, Hastelloy C-276 is having a dimension of 50 mm X 50 mm X 1 mm dimension selected for the analysis of considered process parameters on the responses. The chemical composition of Hastelloy C-276 is given in table 7.1. The microscopic view of the untreated Hastelloy C-276 surface is shown in figure 7.1 at 10 X magnification.

Table 7.1 Chemical composition of Hastelloy C-276 [87]

Ni	Mo	Cr	Fe	W	Co	Mn	C
Remainder	15.0-17.0	14.5-16.5	4.0-7.0	3.0-4.5	2.5 max	1.0 max	.01 max
V	**P**	**S**	**Si**				
.35 max	.04 max	.03 max	.08 max				

Figure 7.1 Microscopic view of an untreated surface of Hastelloy C-276 at 10X magnification

7.4 Experimental Strategy for Fiber Laser Surface Texturing on Hastelloy C-276

The untreated surface of Hastelloy C-276 is treated with multiple overlapped micro-grooves for the texturing of the surface characteristics. Repetition of multiple laser micro-grooves is selected as the fabrication method of textured regions on the workpiece surface. In the present setup, Hastelloy C-276 is placed on a workpiece table to move in X and Y directions with relative motion. The length of a micro-groove is set at 5 mm, and a total number of 250 micro-grooves is repeated with a transverse overlap distance of 7 µm between each other. During the trial runs, it was observed that as the distance between the two micro-grooves (at Y direction) is lowered, the amount of overlaps between two continuous micro-grooves is increased notably. 7 µm is the lowest transverse feed for the present fiber laser system due to the system limitation. Equation 7.1 deals with the correlation between transverse feed and transverse overlap factor. From equation 7.1, the transverse overlap percentage is measured as 66.67 % for the distance between two consecutive grooves of 7 µm. The combination of 250 micro-grooves and transverse feed of 7 µm results into a square area of 5 X 5 cm^2. The number of repetitions of the grooves is kept constant at 1. During the trial runs, the effect of assist air is found useful only at high pressure for which the assist air pressure is kept constant at 4 kgf/cm^2. The schematic representation of the

laser texturing process and the formation of the textured region is shown in figure 7.2 (a) and (b), respectively. A photographic view of multiple fiber laser generated textured surfaces is shown in figure 7.3.

$$\text{Transverse Overlap} = \frac{\text{Laser Spot Diameter at foused condition-Transverse overlap distance}}{\text{Laser Spot Diameter at foused condition}} \times 100\% \quad ...[\text{Eq}^{n}\,7.1]$$

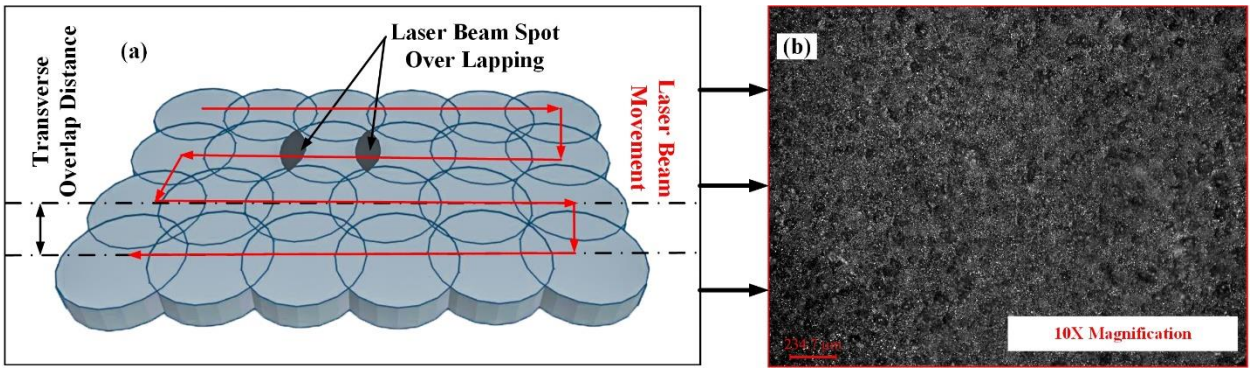

Figure 7.2 (a) Schematic representation of the laser surface texturing process; (b) formation of the textured surface

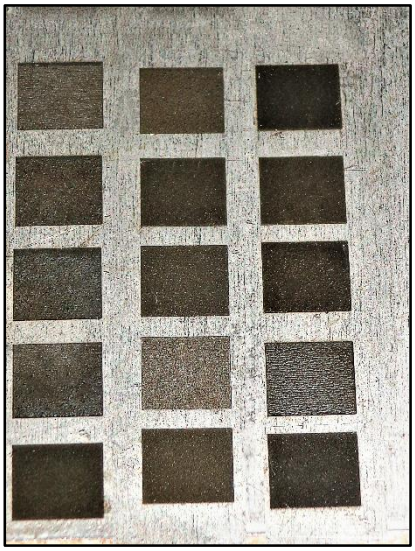

Figure 7.3 Photographic view of the fiber laser textured surfaces on Hastelloy C-276

The surface roughness parameters R_a, R_{sk}, R_{ku}, and R_z have been measured by Mitutoyo SJ 410 surface roughness tester with a Gaussian filter. The responses are calculated following the ISO 1997 standard. Table 7.2 represents the measurement condition using Mitutoyo SJ 410 surface roughness tester. The measurements are repeated at five reference lines, and the result is the

average of these values. Talysurf CCI non-contact surface profiler system is also utilized to show the 3D profiles of the laser textured surfaces as well as their corresponding roughness profiles.

Table 7.2 Mitutoyo SJ 410 Measuring Conditions

Work Name	**Sample**	**Operator**	**Mitutoyo**
Measuring Tool	SurfTest	Abhishek Sen	Ver2.00
Standard	ISO 1997	N	4
Profile	**R**	**Cut-Off**	**0.8mm**
λs	2.5μm	Filter	GAUSS

7.5 Preliminary Study of Fiber Laser Surface Texturing on Hastelloy C-276

During the preliminary experimentation, the effect of laser power, scan speed, and pulse frequency are evaluated at different temperatures, i.e., room temperature and preheating temperatures of 100°C and 200°C for the analysis of R_a, R_{sk}, R_{ku}, and R_z. The range of laser power is varied from 7.5 W to 25 W, whereas the pulse frequency and scan speed are varied from 50 kHz to 90 kHz and 1 mm/sec to 8 mm/sec respectively. The experiments have been carried out by one factor at a time (OFAT), i.e., one process parameter is varied, and others are kept as constants to assess each process parameter on the considered responses at different temperatures. For each process parameter, a total of 8 experiments have been carried out at room temperature. The same set of experiments is repeated at preheating temperatures, i.e., 100°C and 200°C. Therefore, a total of 24 experiments have carried out for the evaluation of each process parameter on the responses. With the developed preheated setup (discussed in chapter 2), the experiments have been carried out at different preheating temperatures. The constant parameters are single pass, assist air pressure of 4kgf/cm^2, and duty cycle of 50%.

7.5.1 Results and Discussion

The effects of the three process parameters such as scan speed, laser power, and pulse frequency for R_a, R_{sk}, R_{ku}, and R_z are shown in table 7.3, 7.4, 7.5 respectively. Effect of each process parameter on the considered responses is discussed and analyzed hereunder.

Table 7.3 Results of scan speed on R_a, R_{sk}, R_{ku}, and R_z

Exp. No.	Scan Speed (mm/sec)	R_a at Room temp. (µm)	R_a at 100° C (µm)	R_a at 200° C (µm)	R_z at Room Temp. (µm)	R_z at 100° C (µm)	R_z at 200° C (µm)	R_{ku} at Room Temp	R_{ku} at 100° C	R_{ku} at 200° C	R_{sk} at Room Temp	R_{sk} at 100° C	R_{sk} at 200° C
1	1	8.57	8.98	8.91	34.71	33.23	31.2	3.58	3.38	3.29	-0.51	-0.83	-0.74
2	2	6.11	5.98	5.11	34.71	28.65	27.82	3.72	3.16	2.95	-0.4	-0.28	-0.20
3	3	4.61	4.89	4.73	30.21	28.32	28.28	2.80	2.76	2.63	0.05	-0.13	-0.07
4	4	4.97	5.03	4.61	29.17	26.89	26.59	2.77	2.56	2.4	0.18	0.09	0.02
5	5	4.50	3.52	3.34	27.88	23.22	22.26	2.69	2.66	2.39	0.36	0.19	0.13
6	6	4.31	1.65	1.71	25.39	14.1	13.48	2.63	2.32	2.26	0.35	0.25	0.19
7	7	3.51	0.78	0.56	20.61	6.2	3.79	2.65	2.66	2.39	0.35	0.39	0.36
8	8	3.50	0.65	0.32	19.21	3.32	3.4	2.63	2.50	2.03	0.31	0.35	0.38

Table 7.4 Results of laser power on R_a, R_{sk}, R_{ku}, and R_z

Exp. No.	Laser Power (W)	R_a at Room temp. (µm)	R_a at 100° C (µm)	R_a at 200° C (µm)	R_z at Room Temp. (µm)	R_z at 100° C (µm)	R_z at 200° C (µm)	R_{ku} at Room Temp	R_{ku} at 100° C	R_{ku} at 200° C	R_{sk} at Room Temp	R_{sk} at 100° C	R_{sk} at 200° C
1	7.5	0.23	0.2	0.46	2.39	1.35	3.56	1.78	2.43	2.21	-1.12	-0.51	0.11
2	10	1.16	1.6	0.84	8.11	10.38	10.56	2.87	2.4	2.45	-0.17	-0.31	0.11
3	12.5	1.18	3.49	2.36	16.07	19.46	19.65	2.66	2.47	2.55	-0.02	-0.26	0.13
4	15	4.61	4.89	4.73	30.21	28.32	28.28	2.8	2.76	2.63	0.053	-0.13	0.08
5	17.5	5.51	5.67	4.42	31.79	30.13	32.62	2.98	2.87	2.63	0.07	0.05	0.04
6	20	7.12	6.06	5.18	39.66	36.36	32.09	3.89	2.9	2.69	0.22	0.07	0.11
7	22.5	7.04	6.93	6.83	42.00	37.59	41.48	5.49	2.92	2.7	0.67	0.14	0.14
8	25	7.84	7.13	8.72	44.73	43.85	42.14	8.94	2.94	2.75	0.71	0.24	0.23

Table 7.5 Results of pulse frequency on R_a, R_{sk}, R_{ku}, and R_z

Exp. No.	Pulse Frequency (kHz)	R_a at Room temp. (µm)	R_a at 100° C (µm)	R_a at 200° C (µm)	R_z at Room Temp. (µm)	R_z at 100° C (µm)	R_z at 200° C (µm)	R_{ku} at Room Temp	R_{ku} at 100° C	R_{ku} at 200° C	R_{sk} at Room Temp	R_{sk} at 100° C	R_{sk} at 200° C
1	50	3.46	11.29	10.58	27.48	44.56	45.15	7.66	4.64	5.23	-0.73	-0.32	-0.33
2	55	3.39	8.19	8.72	24.33	44.13	40.32	6.35	3.22	4.04	-0.66	-0.1	0.01
3	60	3.67	7.58	6.83	22.73	41.27	39.75	5.16	2.98	3.41	-0.42	-0.13	0.08
4	65	4.61	7.50	6.61	21.78	41.01	36.17	3.80	2.76	2.96	0.053	-0.05	0.10
5	70	4.36	6.61	5.46	15.42	36.25	31.97	3.21	2.62	2.73	0.11	0.12	0.22
6	75	1.38	4.81	4.79	9.12	32.63	28.11	2.85	2.49	2.62	0.32	0.12	0.24
7	80	1.02	4.89	4.73	8.21	28.32	25.83	2.80	2.46	2.63	0.49	0.16	0.26
8	85	1.02	4.47	3.92	7.98	15.47	14.93	2.82	2.39	2.53	0.73	0.41	0.40

7.5.1.1 Effect of Scan Speed on R_a, R_{sk}, R_{ku}, and R_z of Textured Surfaces on Hastelloy C-276

In the present set of experiments, the scan speed is varied from 1 mm/sec to 8 mm/sec to find out its effect on the surface characteristics of the textured surface of Hastelloy C-276. The constant

parameters are single pass, laser power of 15 W, pulse frequency of 80 kHz, assist air pressure of 4 kgf/cm^2, and duty cycle of 50%.

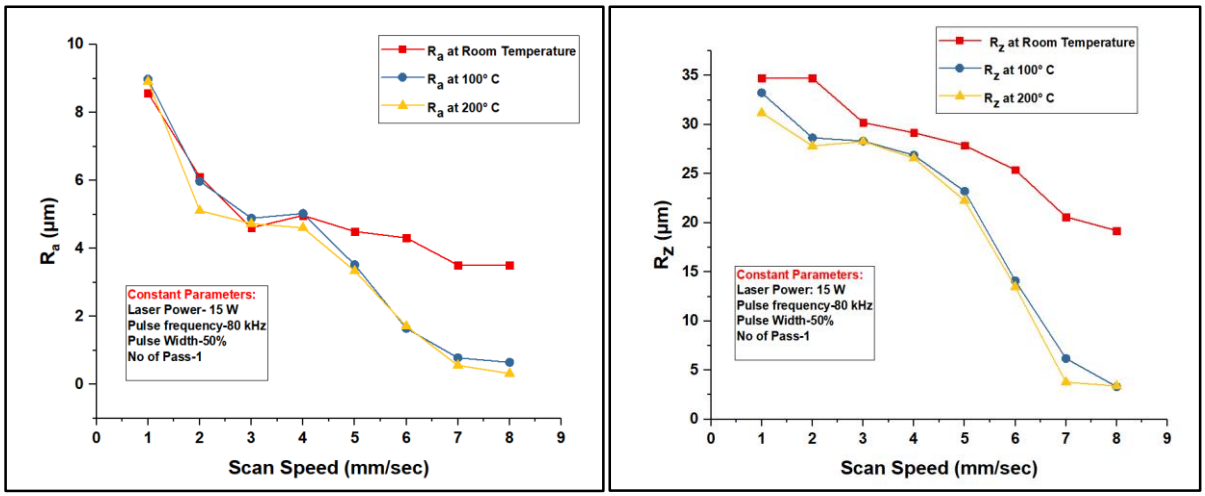

7.4 (a) **7.4 (b)**

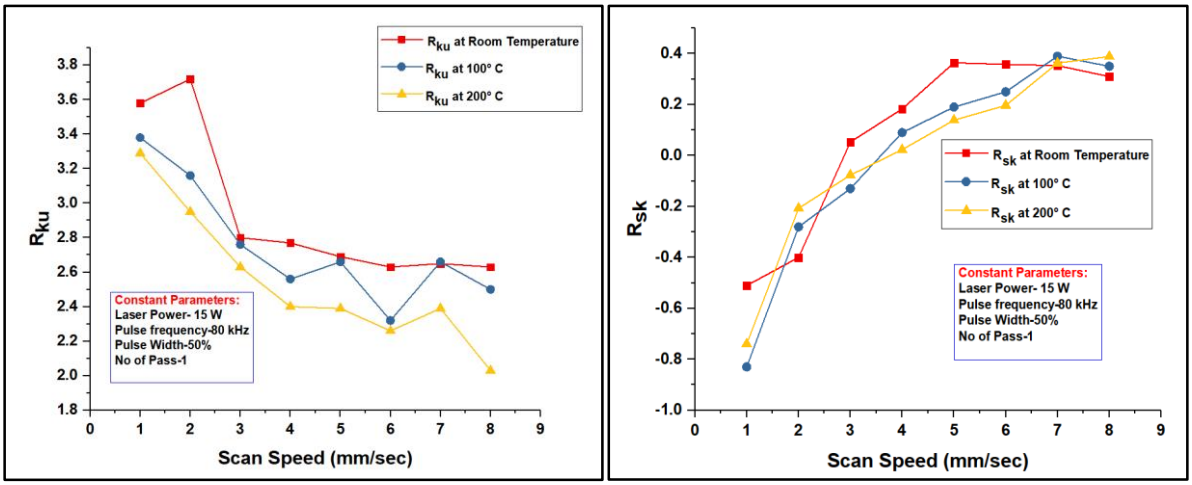

7.4 (c) **7.4 (d)**

Figure 7.4 (a-d) Effect of scan speed on surface profile (R_a, R_z, R_{ku}, R_{sk}) at different temperatures

Figure 7.4 (a) to (d) represent the effect of scan speed on the surface characteristics at different temperatures during fiber laser surface texturing on Hastelloy C-276. It is observed from the figure 7.4 (a) that R_a tends to decrease with an increase in scan speed within the selected range of process parameters. From figure 7.4 (b) and (c), it is found that R_z and R_{ku} both are decreased for the increment of scan speed for any temperature. The reverse phenomenon is observed for R_{sk}.

The preheated condition, combined with varying scan speed shows lower ranges of surface characteristics during fiber laser processing of Hastelloy C-276 compared to fiber laser surface texturing at room temperature. From figure 7.4 (b), it is also observed that the value of picks measured at the texturing zone is much less for the preheated condition. From figure 7.4 (a) and 7.4 (b), the surface profiles are also overlapped at various points for the selected range of process parameters. It is also found from the plot 7.4 (c) and 7.4 (d) that scan speed has a significant effect on the kurtosis and skewness values when other process parameters are kept as constants. A decrement in laser-material interaction time at high scan speed leads to the formation of a lesser amount of melt pool which may be removed from the texturing zone rapidly with the flow of assist air. Besides, the decreased interaction time also attributes in restricting the thermal energy accumulation at the top surface and further provides better surface quality at the texturing zone. The preheated condition also reduces the immediate cooling effect at the texturing zone and generates proper grain alignment, which leads to lower values of surface characteristics. Figure 7.5 shows the surface roughness profile of the textured surface of Hastelloy C-276 for the preheating temperature of 200° C during scan speed of 8 mm/sec, laser power of 15 W, pulse frequency of 80 kHz, assist air pressure of 4kgf/cm^2, and duty cycle of 50%. Figure 7.6 represents a corresponding microscopic view of the textured surface on Hastelloy C-276 at the same combination of process parameters.

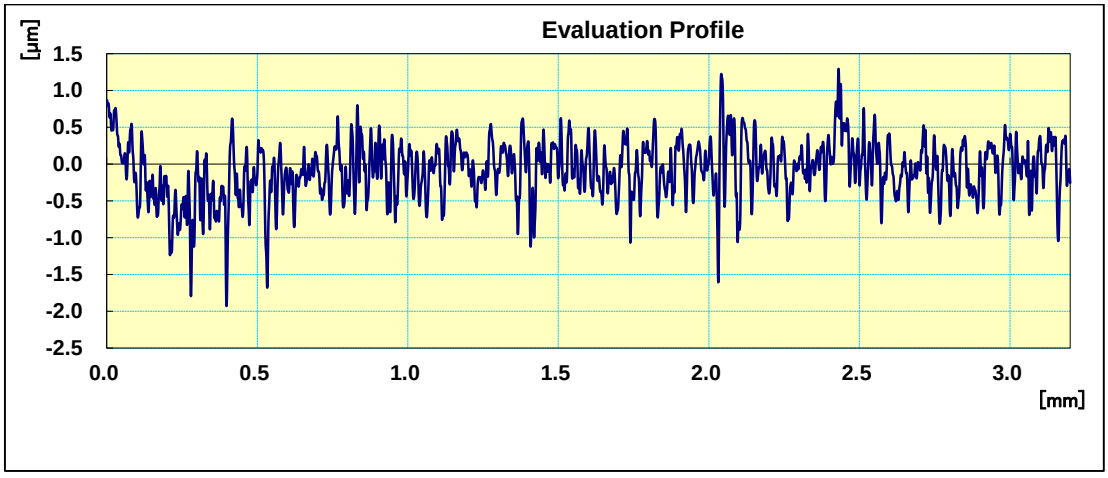

Figure 7.5 Surface roughness profile at the preheating temperature of 200° C

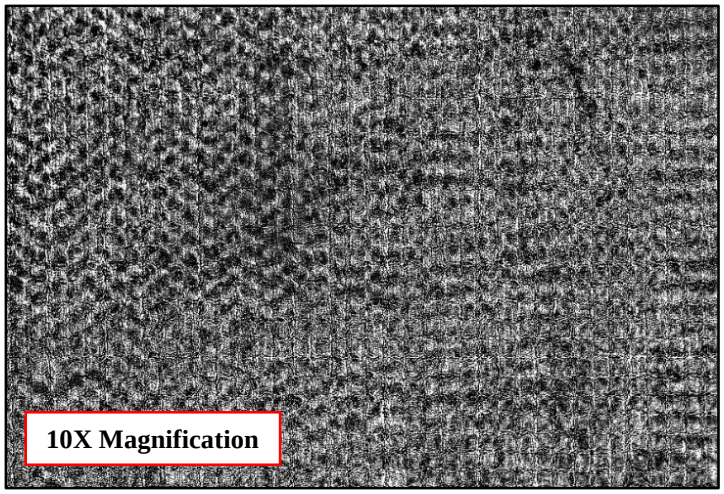

Figure 7.6 Microscopic view of Hastelloy C-276 textured surface at the preheating temperature of 200° C

7.5.1.2 Effect of Laser Power on R_a, R_{sk}, R_{ku}, and R_z of Textured Surfaces on Hastelloy C-276

The effects of laser power on the surface quality are observed from figure 7.7 (a) to (d) during fiber laser surface texturing on Hastelloy C-276. The constant parameters are single pass, scan speed of 3 mm/sec, pulse frequency of 80 kHz, assist air pressure of 4 kgf/cm^2, and duty cycle of 50%.

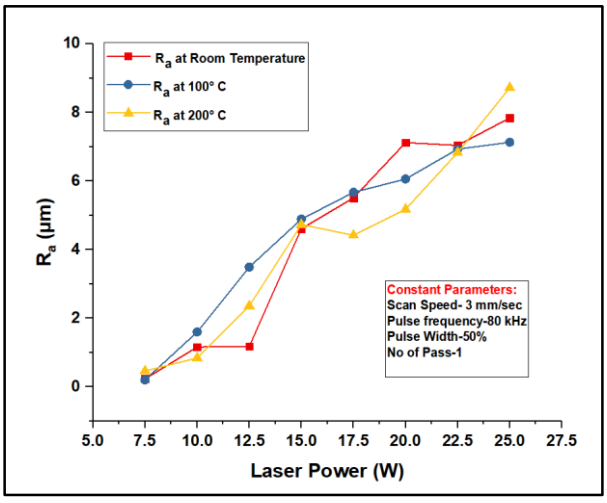

7.7 (a)

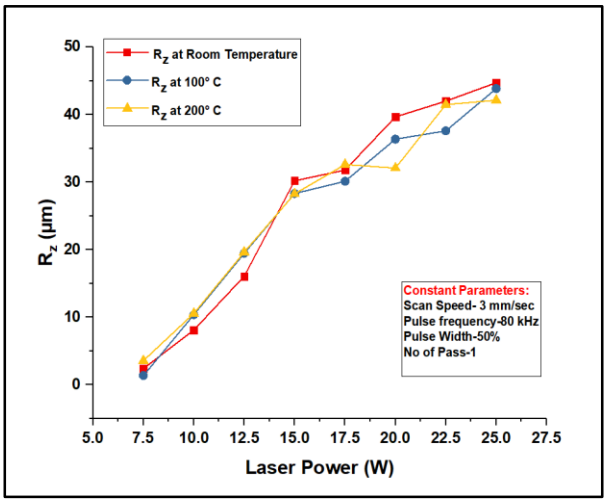

7.7 (b)

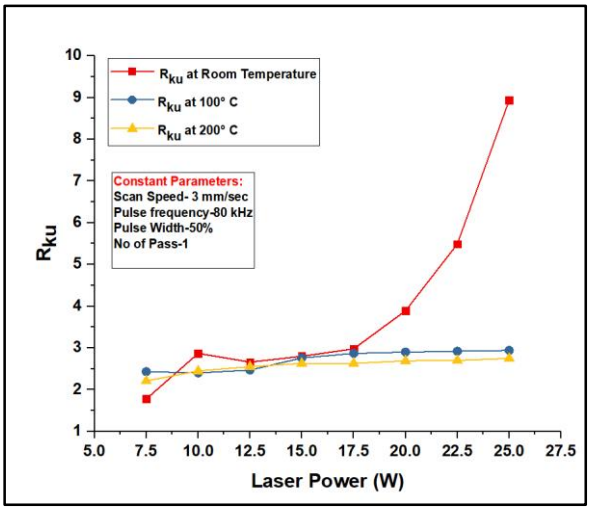

7.7 (c)

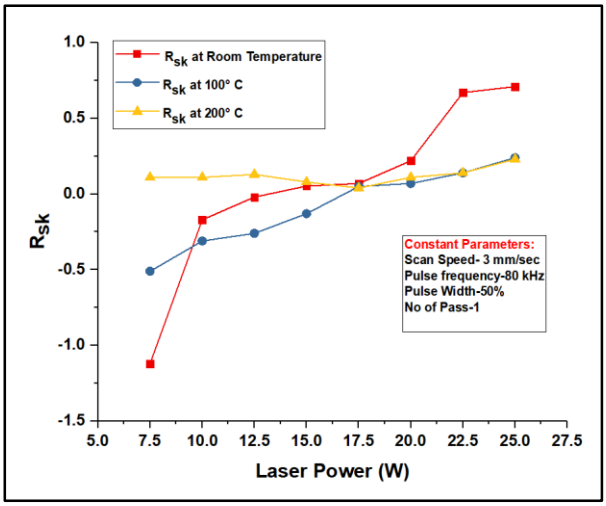

7.7 (d)

Figure 7.7 (a-d) Effect of laser power on surface profile (R_a, R_z, R_{ku}, R_{sk}) at different temperatures

From figure 7.7 (a), it is observed that surface quality has been degraded with an increase in laser power at any temperature. The increment of R_a value with laser power is almost linear with the workpiece temperature at 100°C, whereas a nonlinear increment of R_a is observed with the other two selected thermal condition of workpiece. Figure 7.8 shows the microscopic view of the textured surface of Hastelloy C-276 at high laser power (room temperature). Figure 7.8 shows the re-solidified material at the textured surface, which attributes in higher surface characteristics. It is also found that comparatively lower R_a value can be achieved when the workpiece is preheated at 100°C. On the contrary, higher value of R_a is achieved when the workpiece is preheated at 200°C.

At high laser power, the deviation of surface quality in terms of pick formation is high at low laser power, as shown in figure 7.7 (b). It is found in figure 7.7 (c) that the values of surface kurtosis have not changed with the change in laser power at the preheated condition of the workpiece. However, the value of R_{ku} increases sharply at room temperature, after the value of laser power exceeds 17.5 W. It is also observed from figure 7.7 (d) that preheated condition leads to skewness close to zero. Incorporation of more thermal energy with increased laser power leads to the formation of more melt pool which is not removed from the irradiated zone rapidly and moves further along the path of laser beam movement. Thus, the thermal energy distribution to the neighboring zone of the textured surface is an important consideration. The cooling of the

melt pool may not uniform throughout the region of irradiation, and non-uniform surface tension plays a vital role in the variation of surface characteristics. The adverse effect of sudden cooling with a moderate scan speed of 3 mm/sec can be eliminated by preheating of the workpiece. Figure 7.9 shows the surface roughness profile of the textured surface of Hastelloy C-276 for the preheating temperature of 100° C during laser power of 22.5 W, pulse frequency of 80 kHz, scan speed of 3 mm/sec, assist air pressure of 4kgf/cm^2, and duty cycle of 50%.

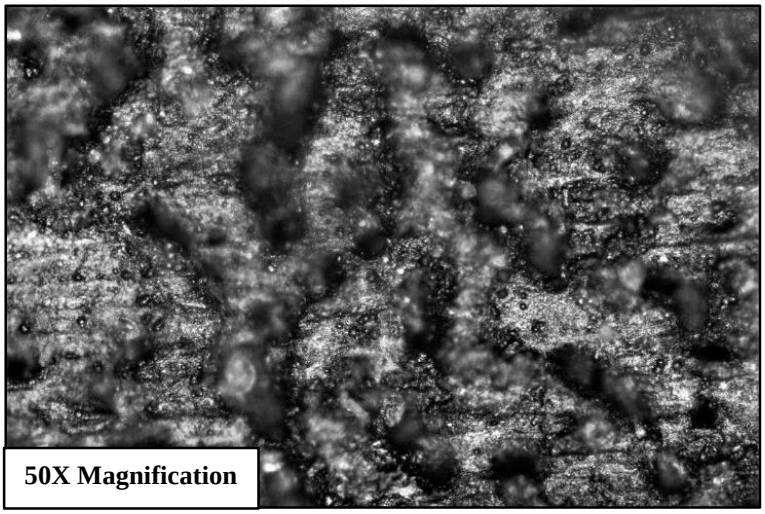

Figure 7.8 Microscopic view of Hastelloy C-276 textured surface at the preheating temperature of room temperature

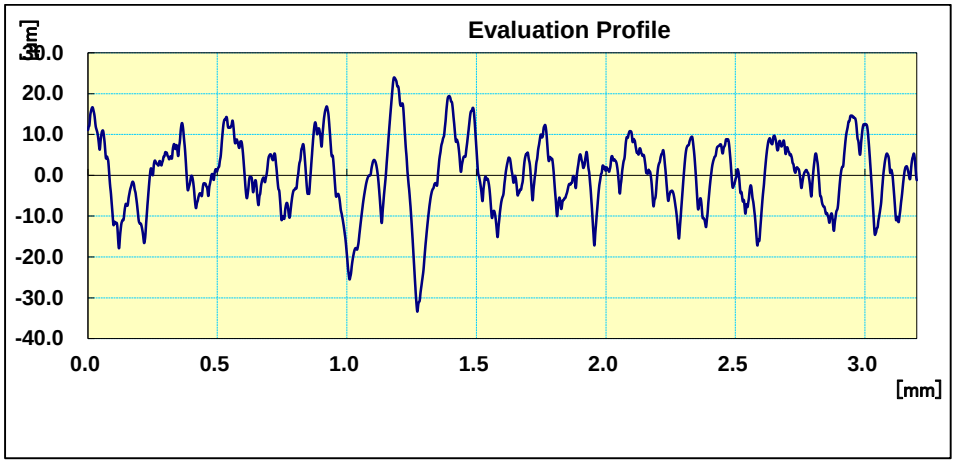

Figure 7.9 Surface roughness profile at the preheating temperature of 100° C

7.5.1.3 Effect of Pulse Frequency on R_a, R_{sk}, R_{ku}, and R_z of Textured Surfaces on Hastelloy C-276

Figure 7.10 (a) to (d) showcase the effect of pulse frequency for R_a, R_{sk}, R_{ku}, and R_z at varying temperature when laser power of 15 W, scan speed of 3 mm/sec, pulse width of 50%, assist air pressure of 4 kgf/cm^2, and single pass are kept as constants.

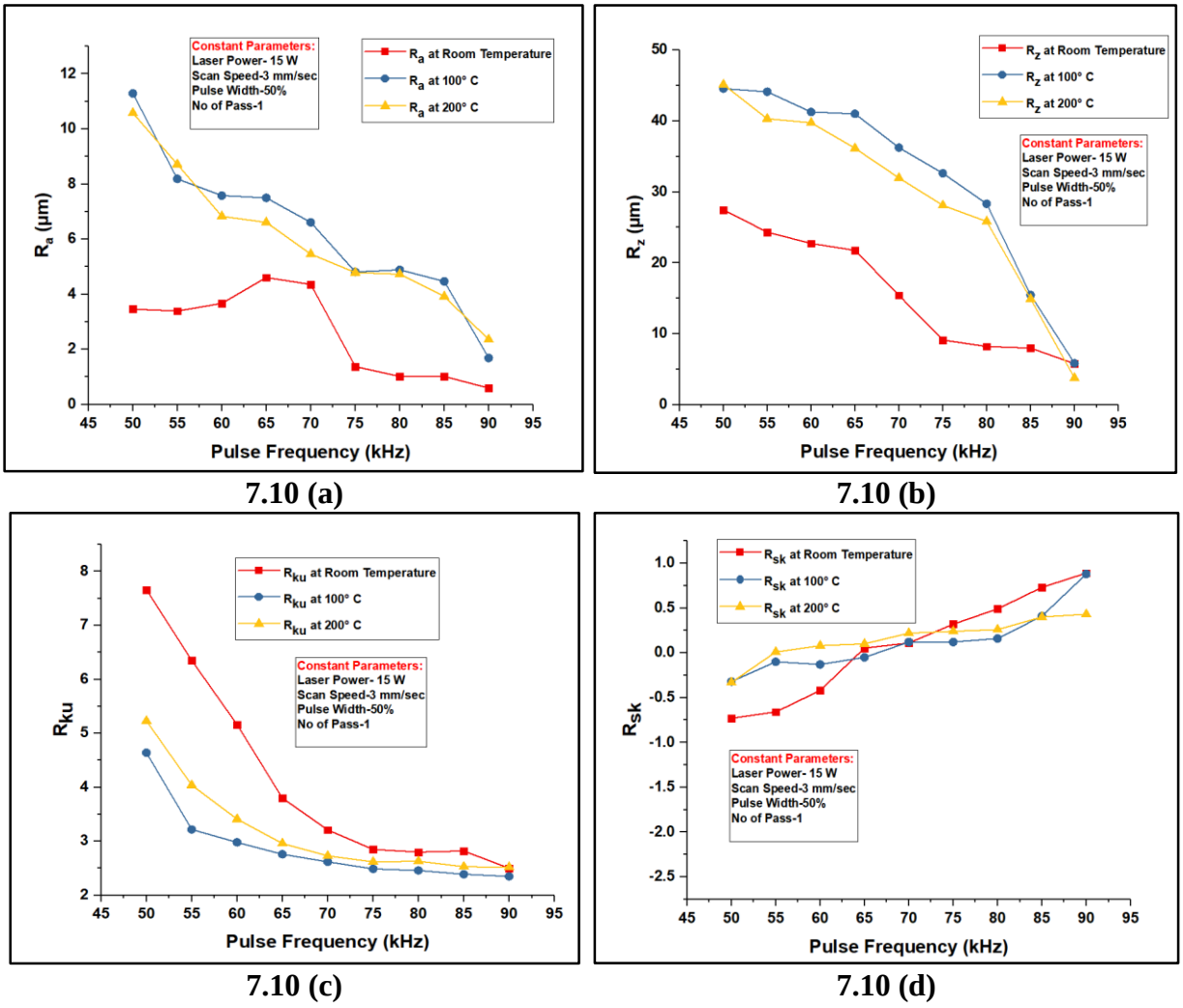

Figure 7.10 (a-d) Effect of pulse frequencies on surface profile (R_a, R_z, R_{ku}, R_{sk}) at different temperatures

It is observed from figures 7.10 (a-d) that the low value of surface characteristics can be achieved when the workpiece is kept at room temperature. It is found from figure 7.10 (a) that R_a value firstly increases with an increase in pulse frequency up to 65 kHz and then decreases at

room temperature when other process variables are kept as constants. R_a value decreases with further increase in pulse frequency.

From figure 7.10 (b), it is found that the value of R_z decreases with an increase in pulse frequency for any temperature, which indicates a lesser deviation on the surface profile. It is found in figure 7.10 (c) that the sharpness of the profile picks is much less for texturing at the preheated condition. It is also observed in figure 7.10 (d) that skewness is nearer to zero at the preheated condition. Increase in pulse frequency causes an increment in spot overlapping and reduction of time between two successive pulses, which results in lesser undulation and rippling effect of melt pool at moderate laser power and scan speed. This phenomenon helps to generate better surface finish in and around the texturing zone. The preheated condition also helps to incorporate an adequate amount of thermal energy at the texturing zone, which may assist a uniform re-solidification of the remaining of molten material at a higher value of pulse frequency. Thus, better surface quality at the preheated condition is produced. Higher energy density at a lower value of pulse frequency produces comparatively a large amount of melt pool, which may not be removed from the texturing zone properly. Thus, it leads to non-uniformity of re-solidified materials. The combination of phenomena described above causes degradation of the quality characteristics in terms of the surface profile. Figure 7.11 shows the surface roughness profile of the textured surface of Hastelloy C-276 at room temperature during pulse frequency of 60 kHz, laser power of 15 W, scan speed of 3 mm/sec, pulse width of 50%, assist air pressure of 4kgf/cm^2, and single pass.

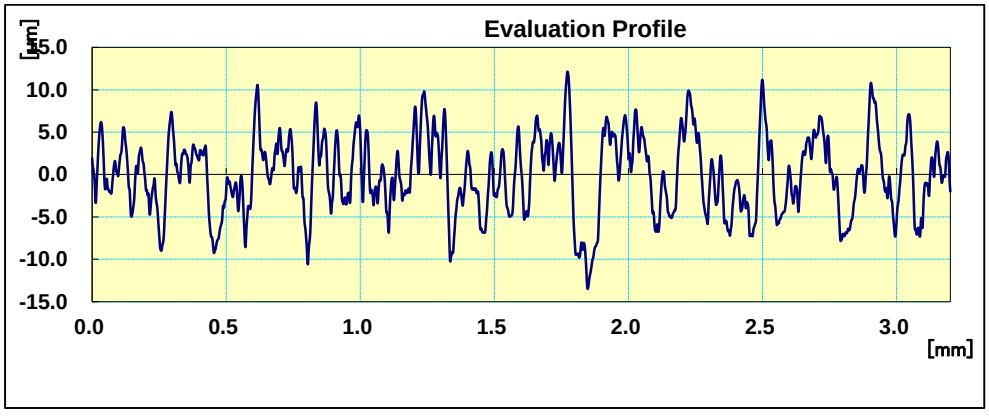

Figure 7.11 Surface roughness profile at the room temperature

7.6 Research Findings from Preliminary Study

The preliminary research work facilitates fiber laser system having an infrared region of wavelength and short pulse regime for surface texturing on Hastelloy C-276. Laser power of 7.5 W to 25 W, pulse frequency of 50 kHz to 90 kHz and scan speed of 1 mm/sec to 8 mm/sec are varied during fiber laser surface texturing on Hastelloy C-276 at varying temperatures. From the results of the present experimentation, the following conclusions can be drawn:

(i) Surface roughness, R_a shows a decreasing tendency with an increase in scan speed. For scan speed of 3 mm/sec to 4 mm/sec, R_a almost remains unchanged for scan speed at preheating temperature of 100°C, while marginally decreasing at 200°C. R_z and R_{ku} are decreased for the increment of scan speed at any temperature of preheating; however, the reverse phenomenon is observed for R_{sk}. The preheated condition provides a better result at varying scan speed on the surface characteristics during fiber laser surface texturing on Hastelloy C-276.

(ii) Surface characteristics in terms of R_a, R_z, R_{ku}, and R_{sk} are increased with an increase in laser power for any temperature of preheating. High thermal energy at high laser power leads to the formation of the melt pool. The adverse effect of sudden cooling with a moderate scan speed of 3 mm/sec is eliminated drastically by preheating of the workpiece.

(iii) R_a value firstly increases with an increase in pulse frequency up to 65 kHz and then decreases at room temperature. For the elevated temperatures, R_a is gradually decreasing for the increment of pulse frequency. R_z decreases with an increase in pulse frequency for any temperature, which indicates a lesser deviation on the surface profile. For this set of experiments, the lower value of R_{ku} is achieved at room temperature compared to the elevated temperatures. The skewness is found nearer to zero at the preheated condition compared to room temperature for low values of pulse frequency. The preheated condition provides a better surface quality in terms of R_{sk} due to the incorporation of an adequate amount of thermal energy at the texturing zone which aids in forming a uniform re-solidification of the remaining of molten material at a higher value of pulse frequency. On the contrary, at the room temperature, lower values of R_a, R_z, and R_{ku} are observed for the selected range of pulse frequency.

7.7 Modeling and Analysis of Fiber Laser Surface Texturing of Hastelloy C-276

In the course of the design of experiments, a response surface methodology (RSM) is chosen, namely, the central composite design (CCD) method. CCD deals with four controllable factors:

laser power, pulse frequency, duty cycle, and scan speed with five different levels. The constant parameters are set as a transverse feed of 7 µm, single pass for the repetition of liner micro-grooves and assist air pressure of 4 kgf/cm^2. The experimental analyses have been performed using Minitab 17 software for a total of 31 experimental runs. In table 7.6, the experimental design, along with observed results, are listed. The analysis of variance (ANOVA) has been performed to analyze as to how the process parameters are affecting the fiber laser texturing process. The confirmations of the derived mathematical models are carried out subsequently. Finally, multi-objective optimization of the process parameters is also carried out to achieve desired surface roughness values.

Table 7.6 Experimental design and observed values of responses

	Process Parameters				Responses		
Exp. No.	**Laser Power (W)**	**Pulse Frequency (kHz)**	**Duty Cycle (%)**	**Scan Speed (mm/sec)**	**R_a (µm)**	**R_{sk}**	**R_{ku}**
1	15.0	70	50	5	6.25	0.28	2.91
2	17.5	65	40	3	9.13	0.42	3.77
3	17.5	75	40	7	6.22	0.3	2.25
4	15.0	70	50	5	6.43	0.21	2.92
5	12.5	75	60	7	5.16	0.1	1.35
6	15.0	70	50	5	6.40	0.28	2.95
7	15.0	70	50	9	5.08	0.11	1.65
8	17.5	75	40	3	7.92	0.23	2.65
9	15.0	70	50	5	5.98	0.23	2.93
10	15.0	70	50	5	5.88	0.28	2.92
11	12.5	75	60	3	4.08	0.16	2.73
12	15.0	70	50	5	6.25	0.27	2.78
13	15.0	70	70	5	5.48	0.53	2.57
14	12.5	65	60	7	2.99	-0.22	1.46
15	15.0	70	50	5	5.99	0.27	2.80
16	17.5	65	60	7	5.69	0.07	2.27
17	12.5	75	40	3	5.01	-0.21	2.38
18	10.0	70	50	5	2.86	-0.33	2.29
19	17.5	65	40	7	4.04	0.18	2.97
20	17.5	65	60	3	9.92	0.28	2.92
21	15.0	60	50	5	5.52	-0.19	2.34
22	12.5	65	60	3	3.99	0.27	2.91
23	15.0	70	50	1	8.66	0.49	3.54
24	15.0	80	50	5	7.01	-0.03	1.16
25	12.5	75	40	7	4.62	-0.14	1.22
27	17.5	75	60	3	8.44	0.31	2.39
28	12.5	65	40	3	5.10	0.11	3.09
29	20.0	70	50	5	8.71	0.17	3.31
30	17.5	75	60	7	7.95	0.43	1.73
31	12.5	65	40	7	2.13	-0.22	1.92

Based on the results of laser surface texturing on Hastelloy C-276, statistical analyses have been conducted to validate the developed mathematical models of responses. Mathematical models are developed to correlate the process parameters and performance criteria. The details of developed mathematical models of responses (Eq^{n}. 7.2, 7.3, and 7.4) are given below.

$$R_a = -5.1 + 2.077X_1 - 0.047X_2 + 0.143X_3 - 5.312X_4 - 0.01952X_1^2 - 0.00004X_2^2 - 0.003708X_3^2 + 0.0374X_4^2 - 0.01447X_1X_2 + 0.01336X_1X_3 - 0.1029X_1X_4 - 0.00042X_2X_3 + 0.07380X_2X_4 + 0.01719X_3X_4 \quad ..[Eq^n 7.2]$$

$$R_{sk} = -13.22 + 0.4060X_1 + 0.3923X_2 - 0.0786X_3 - 0.7840X_4 - 0.01365X_1^2 - 0.003686X_2^2 + 0.000393X_3^2 + 0.00231X_4^2 + 0.001804X_1X_2 - 0.002034X_1X_3 + 0.00698X_1X_4 + 0.001110X_2X_3 + 0.00927X_2X_4 - 0.000618X_3X_4 \quad ..[Eq^n 7.3]$$

$$R_{ku} = -54.18 + 0.834X_1 + 1.604X_2 - 0.0609X_3 - 0.609X_4 - 0.00691X_1^2 - 0.012167X_2^2 - 0.000287X_3^2 - 0.02332X_4^2 - 0.00604X_1X_2 - 0.005421X_1X_3 + 0.03309X_1X_4 + 0.002361X_2X_3 + 0.00288X_2X_4 - 0.00189X_3X_4 \quad ..[Eq^n 7.4]$$

Here, X_1, X_2, X_3, X_4, Y_1, Y_2, Y_3 represent as laser power, pulse frequency, duty cycle, scan speed, arithmetical mean surface roughness, skewness, and kurtosis respectively. Table 7.7 represents the ANOVA test results for R_a, R_{sk}, and R_{ku}. The results consist of degrees of freedom (DOF), F-value, and p-value. The p-value corresponding to lack of fit of the models for responses R_a, R_{sk}, and R_{ku} width are 0.229, 0.133, and 0.112 respectively. The p-value is used to determine the significance of the factors. The analysis is carried out at a 95% confidence level. Thus, a process parameter or their combination is considered significant if the p-value is less than 0.05. As all these values of p are greater than 0.05, this indicates that the lack of fit is significant. Hence, the data are well fitted in the models for all the responses. In addition to this, the goodness of fits for all the models shows that the R^2, R^2 (adjusted) and R^2 (predicted) is close to 1 for all the models. It sums up that the developed models for R_a, R_{sk}, and R_{ku} are statistically adequate for predicting the responses.

Table 7.7 Analysis of variance (ANOVA) for response surface quadratic model of R_a, R_{sk}, and R_{ku}

		R_a		R_{sk}		R_{ku}	
Source	**DOF**	**F-Value**	**p-Value**	**F-Value**	**p-Value**	**F-Value**	**p-Value**
Model	14	104.02	0.000*	58.89	0.000*	97.55	0.000*
Linear	4	288.44	0.001*	96.94	0.002*	243.09	0.000*
Laser Power	1	807.62	0.000*	267.04	0.000*	149.34	0.000*
Pulse Frequency	1	49.60	0.003*	9.28	0.008	207.17	0.001*
Duty Cycle	1	26.11	0.000*	31.84	0.000*	55.89	0.000*
Scan Speed	1	270.42	0.000*	79.62	0.000*	559.96	0.003*
Square	4	17.81	0.000*	72.66	0.000*	70.63	0.000*
2-Way Interaction	6	38.55	0.000*	24.35	0.000*	18.48	0.000*
Lack-of-Fit	10	1.87	0.229**	2.54	0.133**	2.77	0.112**
Model Summary		**R^2-98.91%, R^2 (Adjusted)- 97.96%, R^2 (Predicted)- 94.90%**		**R^2-98.10%, R^2(Adjusted)-96.43%, R^2(Predicted)-90.63%**		**R^2-98.84%, R^2 (Adjusted)- 97.83%, R^2 (Predicted)- 94.24%**	

*Significant at 95% confidence interval; **not significant at 95% confidence interval

Further, the insignificant terms obtained from the ANOVA table for all the three responses are eliminated by a backward elimination method. As the RSM model is based on 95% confidence level, the associated terms whose p-values are higher than 0.05, are eliminated from the previously obtained equations (Eq^n. 7.2, 7.3 and 7.4). The textured equations of R_a, R_{sk}, and R_{ku} are:

$$R_a = -3.42 + 2.077X_1 - 0.0737X_2 + 0.1129X_3 - 5.313X_4 - 0.01950X_1^2 - 0.003707X_3^2 + 0.0374X_4^2 - 0.01447X_1X_2 + 0.01336X_1X_3 - 0.1029X_1X_4 + 0.07380X_2X_4 + 0.01719X_3X_4 \quad ...[Eq^n 7.5]$$

$$R_{sk} = -15.26 + 0.5370X_1 + 0.4248X_2 - 0.0807X_3 - 0.7918X_4 - 0.01380X_1^2 - 0.003725X_2^2 + 0.000383X_3^2 - 0.002034X_1X_3 + 0.00698X_1X_4 + 0.001110X_2X_3 + 0.00927X_2X_4 \quad ...[Eq^n 7.6]$$

$$R_{ku} = -51.12 + 0.627X_1 + 1.579X_2 - 0.0990X_3 - 0.519X_4 - 0.011890X_2^2 - 0.02160X_4^2 - 0.00604X_1X_2 - 0.00542X_1X_3 + 0.03309X_1X_4 + 0.002361X_2X_3 \quad ...[Eq^n 7.7]$$

The following equations are utilized for further analysis of the process variables on the laser textured surface roughness parameters.

7.7.1 Influence of Process Parameters on the Surface Criteria

The various response surfaces have been plotted between one process criteria and two process parameters at a time, while the other two remaining process parameters are kept at constant values. The results of parametric analyses of R_a, R_{sk}, R_{ku} for the process parameters such as laser power, pulse frequency, duty cycle, and scan speed have been discussed with the aid of surface and contour plots.

7.7.1.1 Parametric Effects on the Surface Characteristic, R_a

Figure 7.12 and 7.13 exhibit the surface plot and contour plot, respectively for investigating the influences of pulse frequency and scan speed on the average surface roughness of Hastelloy C-276 textured surfaces. The constant parameters are laser power of 15 W and duty cycle of 50 % of cycle time. The interaction between pulse frequency and scan speed leads to highest fit value for R_a. Figure 7.12 and 7.13 identify the interrelationship between pulse frequency and scan speed is significant. R_a varies significantly with the variation in both scan speed and pulse frequency. The low value of R_a is achieved at high scan speed combined with low pulse frequency.

High scan speed reduces the laser-material interaction time significantly compared to low scan speed. When the laser irradiates on Hastelloy C-276 at high scan speed, a decrement in the material removal rate (MRR) occurs. Therefore, at high scan speed, the amount of molten material is reduced considerably. The low molten material attributes to the lowering of surface roughness, R_a values at high scan speed combined with low pulse frequency. As a result, the homogeneity of the textured surface improves considerably.

At low pulse frequency, the melted layer thickness decreases considerably. The reduction of melted layer thickness in low pulse frequency value increases the surface homogeneity as well as uniformity of the surfaces. As a result of those phenomena described above, low arithmetical mean surface roughness values are obtained at high scan speed in combination with low pulse frequency.

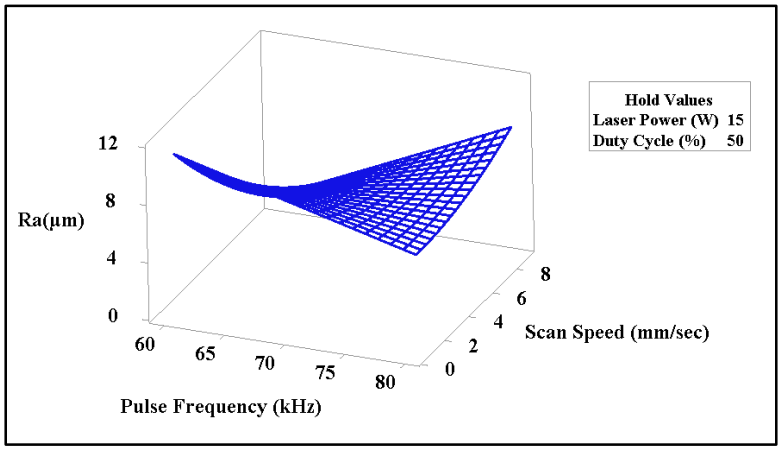

Figure 7.12 Surface plot for influences of pulse frequency and scan speed on R_a

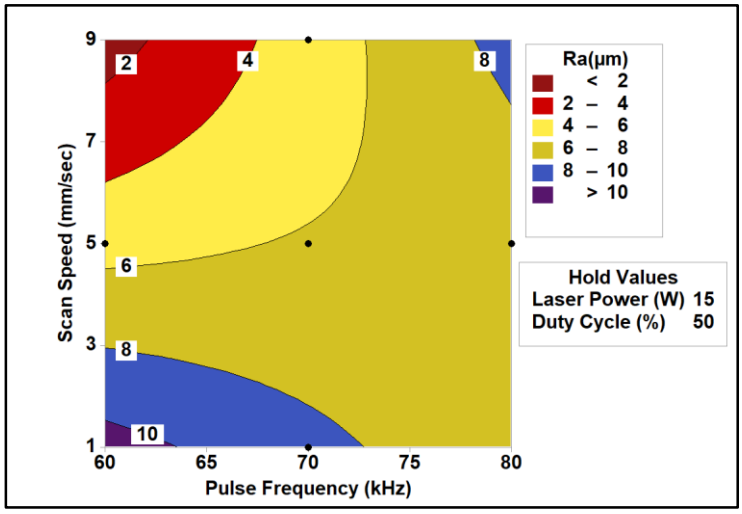

Figure 7.13 Contour plot for influences of pulse frequency and scan speed on R_a

Figure 7.14 and 7.15 identify the surface plot and contour plot respectively due to the influence of laser power and duty cycle on R_a when pulse frequency of 70 kHz and scan speed of 5 mm/sec are kept as constants. The smallest ellipse in figure 7.15 identifies the lowest surface roughness value, i.e., 2 µm at low laser power in combination with the high duty cycle. The effect of laser power on R_a is more prominent as compared to the duty cycle. Thus, at high laser power for any value of duty cycle leads to non-uniformity of the textured surface.

When the laser power is high, the material from the textured surface gains a sufficient amount of energy for rapid melting. The maximum peak power intensity is achieved at the spot center of laser irradiation due to the Gaussian mode of distribution of the fiber laser beam. A gradual decrease at the irradiated spot edges occurs following the phenomenon. As a result, the melting

phenomenon occurs at the spot edges along with the evaporation in the irradiated spot center. These phenomena lead to higher irregularities on the textured surface at high laser power. However, an increment of duty cycle leads to increment in average laser power, but simultaneous decrement in laser peak power. Thus, due to the combined effect of low peak power as well as high average laser power during high duty cycle, surface homogeneity increases.

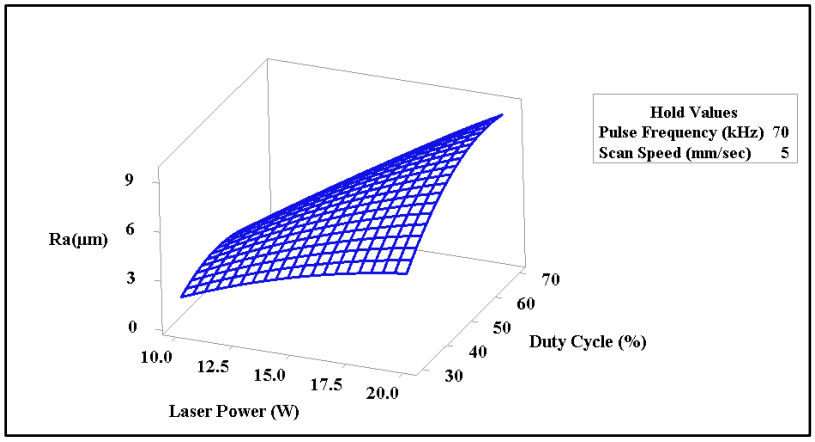

Figure 7.14 Surface plot for influences of laser power and duty cycle on R_a

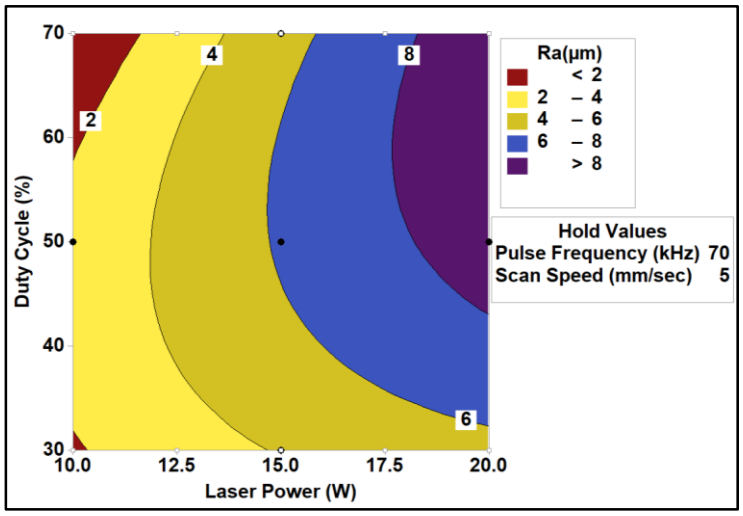

Figure 7.15 Contour plot for influences of laser power and duty cycle on R_a

7.7.1.2 Parametric Effects on the Surface Characteristic, R_{sk}

Figure 7.16 depicts the surface plot for investigating the combined effect of pulse frequency and scan speed on R_{sk} when laser power of 15 W and duty cycle of 50 % of cycle time are kept as constants. Figure 7.17 shows the effect of pulse frequency and scan speed on R_{sk} via contour

plot. The interaction between pulse frequency and scan speed leads to highest fit value for R_{sk}. The average of skewness values is found to be 0.1594. Figure 7.15 and 7.16 show that high scan speed in combination with low pulse frequency leads to negative skewness profile, which suggests that textured profiles imply to vertical profiles. The negatively skewed surface have better fluid retention capability as well as bearing property. Hence, better surface performance for bearing application is achieved when the surfaces have negative skewness values.

At high scan speed, low laser-material interaction time implies vertical profiles of the textured surfaces. Peaks predominate over the valleys on the textured surface at high scan speed in combination with low pulse frequency. At high pulse frequency, the number of laser pulses is increasing on the laser-irradiated surface. Besides, the spot overlapping factor is also increasing simultaneously with high pulse frequency. Thus, the surface is treated with valleys over peaks at high pulse frequency.

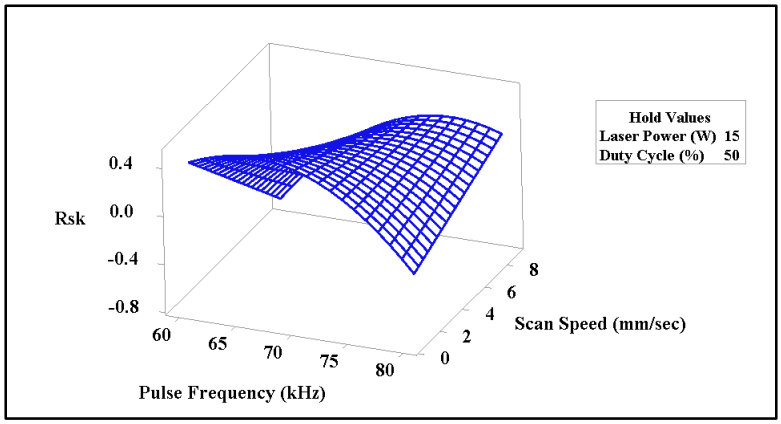

Figure 7.16 Surface plot for influences of pulse frequency and scan speed on R_{sk}

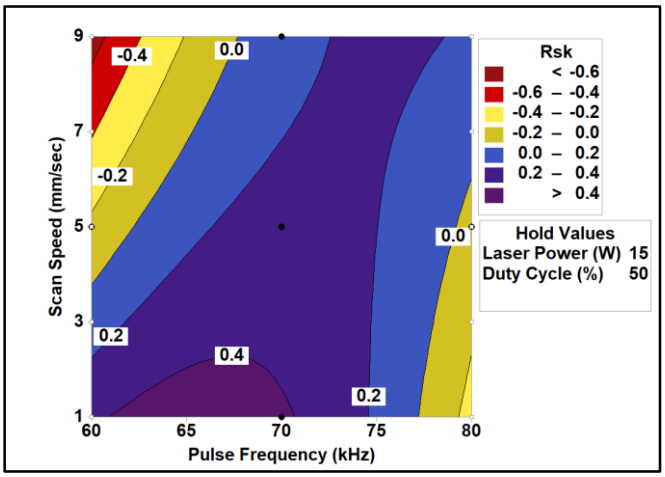

Figure 7.17 Contour plot for influences of pulse frequency and scan speed on R_{sk}

Figure 7.18 and 7.19 identify the surface plot and contour plot respectively, for analyzing the influence of laser power and duty cycle on R_{sk}. The constant parameters are pulse frequency of 70 kHz and scan speed of 5 mm/sec. From figures 7.18 and 7.19, it can be identified that both laser power and duty cycle have a significant effect on skewness profiles of the fiber laser textured surface on Hastelloy C-276. Low laser power combined with 55 % of duty cycle leads to negative skewness profiles. With the increment of laser power, textured surfaces imply positive skewness profiles.

During pulsed fiber laser surface texturing on Hastelloy C-276, the temperature would rapidly oscillate due to the alternation between laser on and off within a whole repetitive pulse cycle. As a result, the thermal gradient in the surface texturing zone is significant. On the other hand, the growth rate is also high due to fiber laser pulsed mode of operation. Thus, more refined grains are obtained in the textured zone when the duty cycle is lowered. Besides, when the surface is treated at high laser power, the asperities undergo yielding a profile. With the more increment in laser power, restructuring of the asperities on the textured surface takes place. The textured surfaces tend to have higher peaks than valleys at high laser power. Thus, favorable skewness profiles are observed at high laser power.

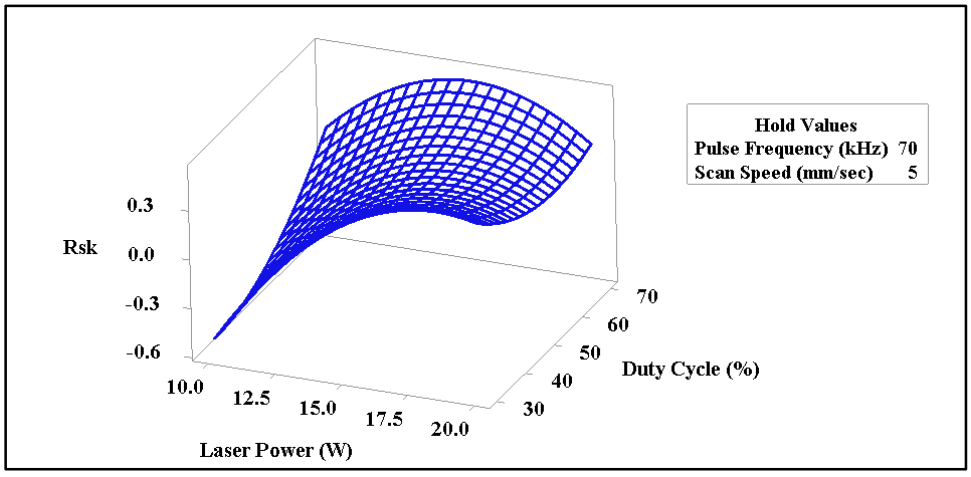

Figure 7.18 Surface plot for influences of laser power and duty cycle on R_{sk}

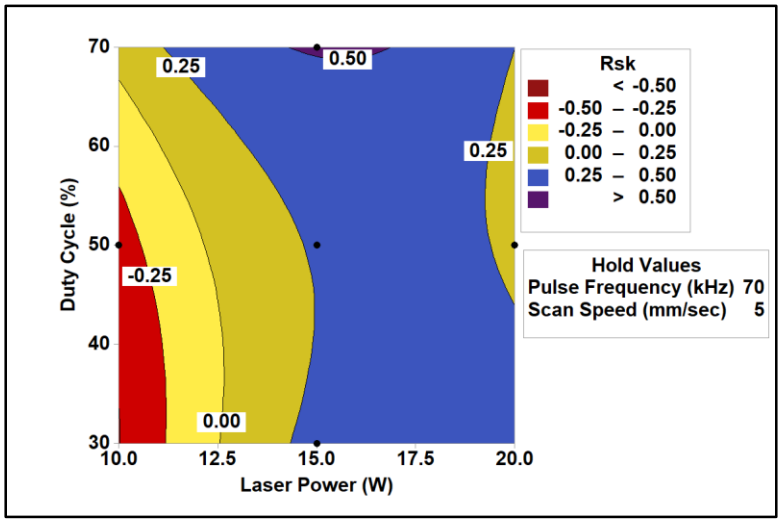

Figure 7.19 Contour plot for influences of laser power and duty cycle on R_{sk}

7.7.1.3 Parametric Effects on the Surface Characteristic, R_{ku}

Figure 7.20 and 7.21 represent the surface plot and contour plot, respectively, for analyzing the effect of laser power and scan speed on R_{ku}. The constant parameters are pulse frequency of 70 kHz and duty cycle of 50%. The combined effect of laser power and duty cycle has produced the highest fit value for R_{ku}. The average kurtosis value is 2.5232, which lies within 0 to 3. This range of the kurtosis value signifies that fiber laser textured square profiles are Gaussian. Laser texturing process fulfills the requirements of the central limit theory of statistics, in which the events are numerous, random, and cumulative. When the kurtosis value of the considered surface is high, then the surface is treated as spiky. The surface is considered as bumpy when kurtosis value is low. Figure 7.20 and 7.21 reveal that the high value of scan speed combined with low laser power lead to low kurtosis value. The zone of different kurtosis values is highly dependent on scan speed rather than that of laser power.

The kurtosis value reduces when the scan speed increases. On the contrary, minor changes in response are observed for the variation of laser power. Yilbas et al. [88] reported that that laser treatment enhanced the surface hydrophobicity of Hastelloy C-276 because of the formation of micro-pillars at the laser treated surface. Low scan speed, in combination with low laser power, significantly increases the kurtosis of the surfaces. At the lowest value of scan speed and laser power, the kurtosis value exceeds the Gaussian range (> 4) as observed in figure 7.21. Suitable bearing surfaces tend to have a high kurtosis and a negative skew since there need to be flat regions to provide low contact stresses and deep valleys to provide lubricant reservoirs.

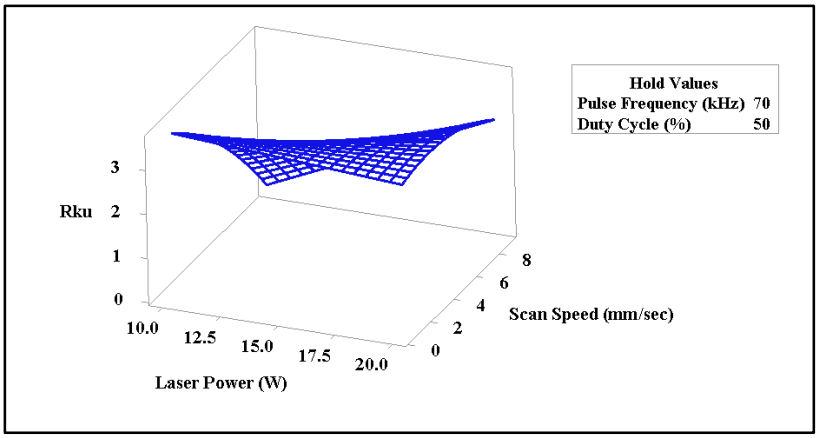

Figure 7.20 Surface plot for influences of laser power and scan speed on R_{ku}

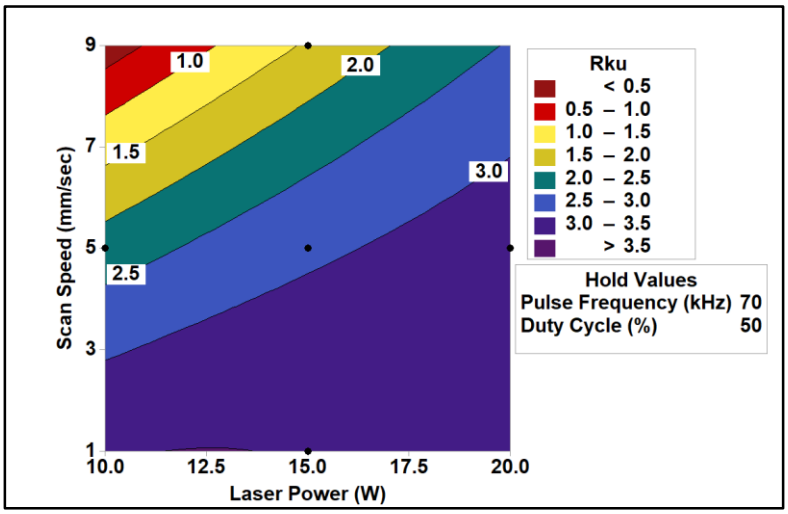

Figure 7.21 Contour plot for influences of laser power and scan speed on R_{ku}

Figure 7.22 and 7.23 reveal the combined effect of pulse frequency and duty cycle on R_{ku} via both surface plot and contour plot, respectively. Laser power of 15 W and scan speed of 5 mm/sec are kept as constants. Figure 7.23 indicates that R_{ku} values from 2.0 to 2.5 are achieved during a wide range of variation of pulse frequency from 60 to 75 kHz for any value of the duty cycle. Figure 7.23 also shows that there is a significant interaction between the process parameters, and the experimental results are accurate. It is also observed that the pulse frequency is a more dominant factor on R_{ku} as compared to the duty cycle.

As observed in both the figures 7.22 and 7.23, kurtosis values tend to increase up to pulse frequency of 75 kHz. Following that, kurtosis values tend to decrease gradually. The low laser beam penetration rate at higher values of pulse frequency causes the phenomenon above. In

addition to this, randomness in the surface profile is more at low pulse frequency with any value of duty cycle. However, higher pulse frequency results in a lower kurtosis value. As the profiles turn out to be in Gaussian range, the surfaces provide better control over wear and friction as compared to the untreated region.

Figure 7.24 to 7.26 reveal surface roughness profiles at different process parameter settings. Figure 7.27 (a) shows the 3D topology of the textured surface at the parametric condition of laser power of 10 W, pulse frequency of 70 kHz, duty cycle of 50% and scan speed of 5 mm/sec. The textured region shows up to 37.5 µm depth from the top face for the length of 0.8mm. In the combination of laser power of 12.5 W, pulse frequency of 65 kHz, duty cycle of 40% and scan speed of 7 mm/sec, fiber laser textured surface of Hastelloy C-276 is shown in figure 7.27 (b). Figure 7.27 (b) indicates homogeneity throughout the textured region as compared to figure 7.27 (a).

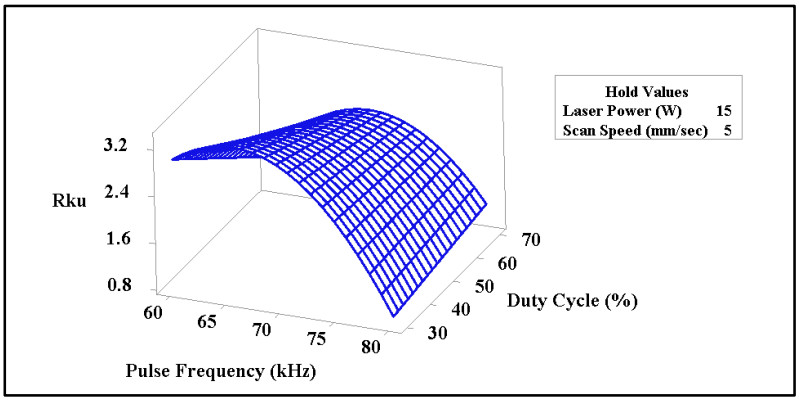

Figure 7.22 Surface plot for influences of pulse frequency and duty cycle on R_{ku}

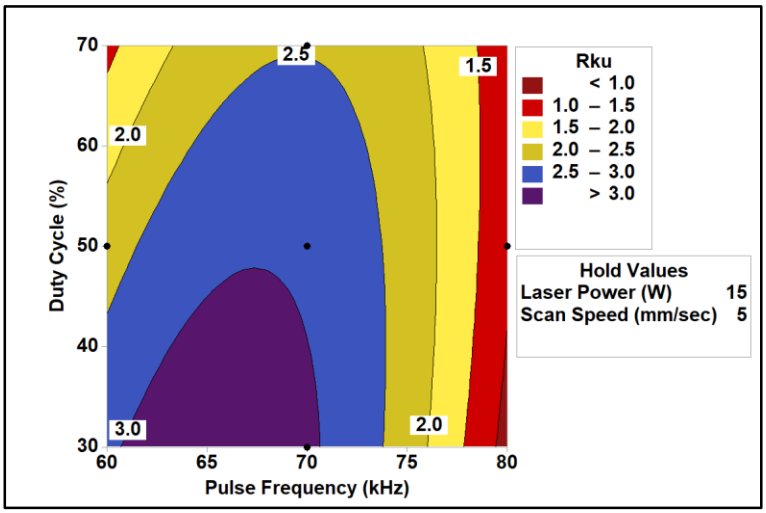

Figure 7.23 Contour plot for influences of pulse frequency and duty cycle on R_{ku}

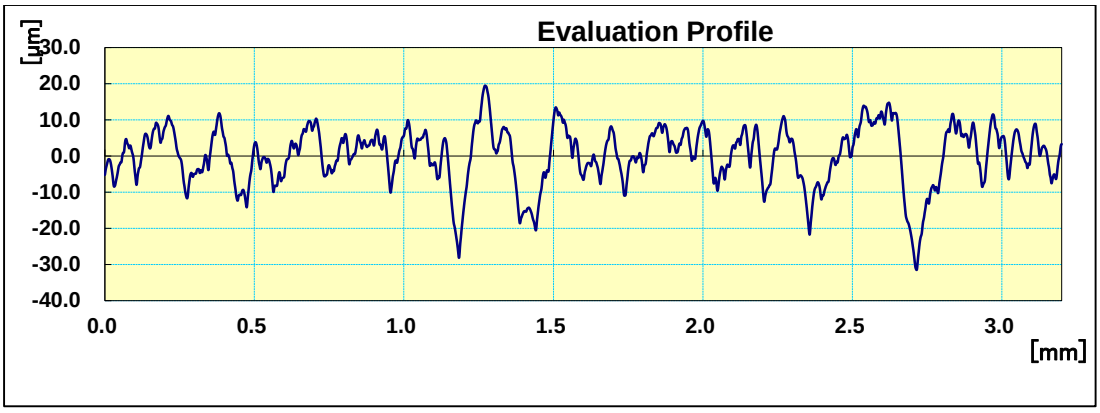

Figure 7.24 Surface roughness profile at laser power of 15 W, pulse frequency of 70 kHz, duty cycle of 50%, and scan speed of 5 mm/sec

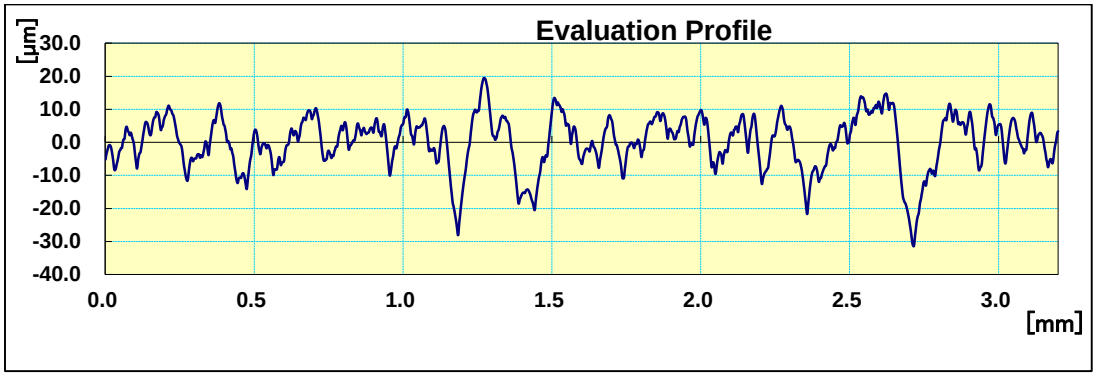

Figure 7.25 Surface roughness profile at laser power of 10 W, pulse frequency of 70 kHz, duty cycle of 50%, and scan speed of 5 mm/sec

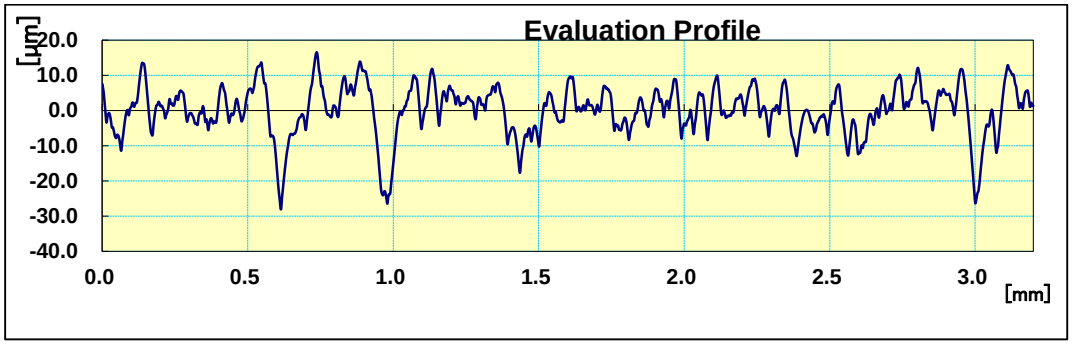

Figure 7.26 Surface roughness profile at laser power of 15 W, pulse frequency of 70 kHz, duty cycle of 70%, and scan speed of 5 mm/sec

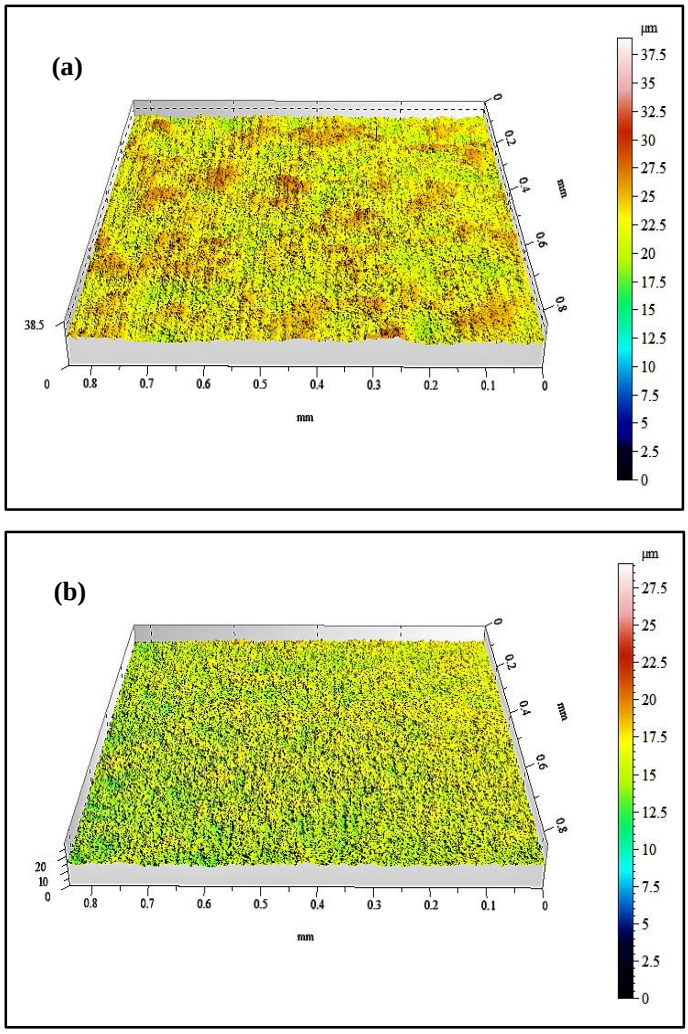

Figure 7.27 (a) and (b) 3D topology of the textured profile of Hastelloy C-276

7.7.2 Multi-Objective Optimization

Multi-objective optimization analysis is performed to achieve the target value of all three responses, i.e., R_a, R_{sk} and R_{ku} of the fiber laser textured surface profile of Hastelloy C-276, based on the developed mathematical equations (7.5), (7.6) and (7.7). The multi-objective optimization aims to achieve the target value arithmetical mean surface roughness of 1.2 µm along with positive kurtosis value of 3. Besides, optimized negative skewness value of -0.3 also aims for the utilization of the textured Hastelloy surface in bearing applications. Negative skewness value of the considered surface suggests that surfaces have excellent fluid retention and lubricating properties. The surface with a positive value of skewness can wear off during high power applications. Multi-objective optimization results for the three responses are shown

in figure 7.28. The current optimized parameter settings for achieving the lowest R_a, R_{sk}, and R_{ku} are laser power of 19.93 W, pulse frequency of 60 kHz, duty cycle of 38.96 % along with scan speed of 8.41 mm/sec. Figure 7.29 shows the microscopic view of the textured surface on Hastelloy C-276 at the optimized machining condition.

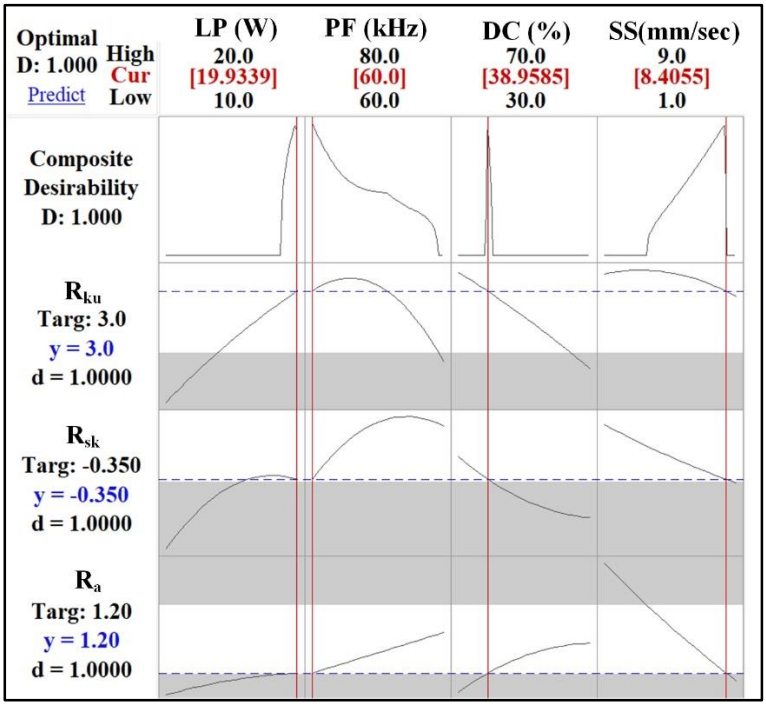

Figure 7.28 Multi-objective optimization results for R_a, R_{sk}, and R_{ku}

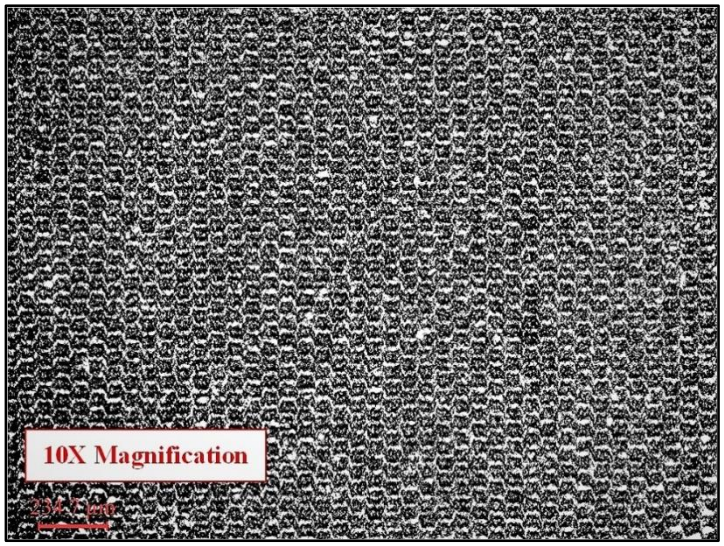

Figure 7.29 Microscopic view of the textured surface on Hastelloy C-276 at optimized condition

7.7.3 Confirmation Experiments

Confirmation experiments are conducted to validate the predicted results at the optimized experimental parameter settings. The mean prediction errors of the experimental values are evaluated to compare the experimental values of the three responses with their optimized values. A total of five confirmation experiments are conducted. The experimental values of R_a, R_{sk}, and R_{ku} at optimized process parameter settings are shown in table 7.8. The mean prediction errors for R_a, R_{sk}, and R_{ku} are found out to be within 3.41%, 4%, and 3.87% respectively. The calculated error values indicate that the produced results are a close agreement with the predicted results.

Table 7.8 Comparison between multi-objective optimization results with actual results

Exp. No:	R_a (µm)			R_{sk}			R_{ku}		
	Target Value	Actual value at optimum condition	Percentage of Errors	Target Value	Actual value at optimum condition	Percentage of Errors	Target Value	Actual value at optimum condition (µm)	Percentage of Errors
1	1.2	1.241	3.30	-0.35	-0.365	4.11	3	3.11	3.54
2	1.2	1.229	2.36	-0.35	-0.364	3.85	3	3.137	4.37
3	1.2	1.262	4.91	-0.35	-0.363	3.58	3	3.148	4.70
4	1.2	1.241	3.30	-0.35	-0.368	4.89	3	3.06	1.96
5	1.2	1.239	3.15	-0.35	-0.363	3.58	3	3.15	4.76
Mean Percentage of Errors (%)=3.41				**Mean Percentage of Errors (%)=4**			**Mean Percentage of Errors (%)=3.87**		

7.8 Outcome of the Present Research Work

Fiber laser surface texturing on Hastelloy C-276 with the aid of response surface methodology based experimental design is also carried out. ANOVA test of each of the model reveals that the experimental values of all the three responses are well fitted in for all the response criteria. The optimized values of process parameters are found as laser power of 19.93 W, pulse frequency of 60 kHz, duty cycle of 38.96 % and scan speed of 8.41 mm/sec. The optimized target values set for R_a, R_{sk}, and R_{ku} are obtained as 1.2 µm, -0.35 and 3 respectively. The textured Hastelloy C-276 surface at optimized settings can be utilized for bearing applications. The conformity tests reveal that the errors for R_a, R_{sk}, and R_{ku} are found out to be within 3.41%, 4%, and 3.87% respectively, and the predicted results are a close agreement with the experimental results.

8. GENERAL CONCLUSIONS

8.1 General Conclusions

Fiber laser micro-machining process has excellent potential for generating different micro-features on a wide range of engineering materials. In the present work, an infrared fiber laser system working in nanosecond pulse regime has been effectively applied for generating micro-channels, micro-grooves, micro-holes and surface textured profiles on PMMA, Ti-6Al-4V and 316L, quartz and Hastelloy C-276 respectively. An in-depth experimental analysis has been conducted to find out the feasibility of fiber laser micro-machining process on those aforesaid materials as well as the effect of different process parameters on the considered responses.

Based on the results of experimental investigation, modeling, analysis, and optimization of fiber laser micro-machining process for generating micro-features on various engineering materials and within the limitation of resources, the following conclusions can be drawn:

(a) Fiber Laser Micro-Channeling on PMMA

(i) In-depth study of the performance characteristics of multi diodes pumped fiber laser reveals that it is one of the most suitable machine tools to process difficult to machine materials in micro-domain. The preliminary experimental study on PMMA to fabricate micro-channels with the aid of the fiber laser deals with the influence of four process parameters such as scan speed from 10 mm/sec to 300 mm/sec, pulse frequency from 50 kHz to 90 kHz, laser power of 5 W to 15W and number of passes of 1 to 5.

(ii) With the increment of scan speed during different settings of average laser power, the cut width of the micro-channels on PMMA tends to reduce due to the effect of spattering and less material interaction time. The depth dimensions are significantly low and tend to decrease at higher scan speed for any value of laser power within the considered range.

(iii) HAZ width and depth of the micro-channels do not vary considerably, although, the cut width of the micro-channels reduces to a considerable extent with the increment of pulse frequency. The effect of the number of passes leads to more uniformity of the micro-channel profiles and significant increment in the depth dimensions of the micro-channels. Cut width dimensions of the micro-channels are also found to be increasing with the higher settings of the number of passes. The higher number of passes have also improved aspect ratios of the micro-channels on PMMA.

(iv) The developed mathematical models are validated by analyzing ANOVA of the considered responses, i.e., cut width, depth, and HAZ width during fiber laser micro-channeling on PMMA.

(v) Further, a multi-objective optimization is carried out to achieve the optimal results of cut width, depth, and HAZ width, which are 115.89 µm, 138.57 µm, and 110.62 µm respectively. The optimal parameter settings are scan speed of 30 mm/sec, pulse frequency of 57.22 kHz, laser power of 5 W, number of pass of 2. The percentage of error obtained from the predicted and actual experimental results at optimal condition is found below 5%, which signifies good acceptability of prediction analysis of fiber laser machining of micro-channels on PMMA.

(b) Fiber Laser Micro-Grooving on Ti-6Al-4V

Fiber laser micro-machining has immense potential for generating micro-grooves on Ti-6Al-4V. The present research work deals with the influences of four process parameters, i.e., laser power of 10 W to 30W, the number of passes of 1 to 10; scan speed of 5 mm/sec to 1000 mm/sec; pulse frequency of 50 kHz to 100 kHz during laser micro-grooving on Ti-6Al-4V using 50W diode pumped fiber laser.

(i) The depth and cut width dimensions of micro-groove on Ti-6Al-4V tend to decrease with the higher scan speed with the combination of low pulse frequency, but surface roughness tends to gradually increase owing to low spot overlapping and discontinuous power density at higher scan speed. With the increase of pulse frequency at moderate scan speed, reduction in the dimensions of cut width and depth of micro-grooves are observed owing to low heat generation.

(ii) At higher values of pulse frequency, rougher micro-groove surfaces are produced. With the increment of the number of passes, cut width and depth dimensions both tend to increase. Smooth surface quality is observed due to the increase in the number of passes.

(iii) The dimensions of cut width and depth simultaneously increase up to laser power of 20 W, then gradually decrease. Smooth surface quality is observed at low laser power. Thus, the fiber laser system can be successfully implemented for generation of micro-grooves on Ti-6Al-4V with desired surface characteristics and surface profiles.

(c) Fiber Laser Micro-Grooving on 316L

Fiber laser micro-grooving of 316L SS has been studied to analyze the effect of the flow of high pressure assist air, preheated temperatures, and change in the focal position of the laser beam on micro-groove cut width, HAZ width and average surface roughness R_a. From the experimental results, the following conclusions can be drawn:

(i) The effect of assist air supply is found to be more on the cut width dimensions at high values of pulse frequency compared to the values of cut width without the supply of assist air at the same set of process parameters. Without the presence of assist air, the cut width dimensions tend to increase with the increase in pulse frequency, whereas the reverse phenomenon is observed with the aid of assist air.

(ii) The experimental results also indicate that the effect of assist air is prominent in order to achieve a low average surface roughness of the cut profiles on 316L. In the presence of high pressure assist air, the average surface roughness, R_a of the cut profiles increases with the increment of laser power. Due to the supply of high pressure assist air, surface roughness values tend to decrease with the increment in pulse frequency. At higher scan speed in the presence of a jet flow of assist air supply, surface roughness values are lowered at a considerable amount as compared to the experiments conducted without the supply of assist air.

(iii) The effects of preheating during fiber laser micro-grooving operation are important consideration generating micro-grooves on 316L stainless steel. At 250 °C, cut width tends to decrease, while the HAZ width reduces significantly up to the scan speed of 0.7 mm/sec. On the contrary, the dimensions of the HAZ width are significantly lower in comparison of the HAZ width dimensions during any change in the focal point position of the laser beam. The phenomena described above can be due to the effect of re-solidification, formation of oxide particles along with a spattering of the molten material. The uniformity of the micro-grooves is on the higher side for this set of experiments.

(iv) At 200°C of preheating temperature, with the increment of scan speed, cut width and HAZ width dimensions are reduced. The dimensions of HAZ width at the focus condition on the workpiece to be lower than the dimensions during a change in focal point distance at high scan speed. Low thermal strain and thermally induced stresses along with the high

cooling rate of the molten material have attributed in such characteristic features of the cut width and HAZ width of the micro-grooves on 316L.

(v) At the room temperature, the dimensions of the cut width and the HAZ width are the lowest in comparison to the dimensions observed at different elevated temperatures. However, non-uniform micro-groove profiles are also observed during fiber laser micro-grooving on 316L at room temperature. Supercooling of the molten material combined with the high thermal strain at the micro-groove zone are the predominating factors for the non-uniformity of the micro-grooves.

(d) Fiber Laser Micro-Drilling on Quartz

The preliminary research work facilitates the fiber laser system for generating micro-holes on quartz. Laser power of 27 W to 37.5 W, pulse frequency of 50 kHz to 75 kHz, duty cycle of 50% to 75% and assist air pressure of 1.5 kgf/cm^2 to 4 kgf/cm^2 are varied during fiber laser percussion micro-drilling on quartz.

(i) The entry and exit hole diameters are increased with the increase in laser power. Higher laser power leads to the high amount of molten material removal and higher entry hole diameter compared to exit hole diameter. The taper angle, HAZ thickness for both the ends of the micro-holes and the entrance hole circularity are also increased with the increment of laser power.

(ii) With the increase in pulse frequency, both the entry and exit hole diameters are decreased sharply. The HAZ thickness for both entry and exit hole becomes lesser at high pulse frequency settings. The micro-holes with high circularities are obtained at high settings of pulse frequency. The taper angle is low at the moderate value of pulse frequency in combination with low laser power.

(iii) Higher machining time, along with high duty cycle leads to an increment in taper angle and the entrance circularity of the micro-holes. Simultaneously, HAZ thickness is observed to be on the higher side for both the entry and exit sides of the micro-holes on quartz. Significant improvement of the entry hole circularity is observed with high assist air pressure. However, taper angles of the holes are also increased with the increment in air pressure. The variation of entry hole diameter is found to be more sensitive towards the air pressure compared to the exit hole.

(iv) An RSM based experimental design is utilized to carry out a total of 31 experiments to analyze the effect of various process parameters on the entry and exit hole diameter, HAZ thickness, and circularity of micro-hole drilled on quartz. From the ANOVA table, the p-value of the lack of fit for entry hole diameter is found as 0.395, whereas the p-value of the lack of fit for exit hole, HAZ thickness and hole circularity are obtained as 0.730, 0.261 and 0.671 respectively. The developed mathematical models on both hole diameters, HAZ thickness, and entry hole circularity are adequate for prediction during fiber laser micro-drilling on quartz.

(v) Single objective optimization results show that for obtaining minimum entry hole diameter 65.71 μm, a combination of pulse frequency of 65 kHz along with duty cycle of 55%, laser power of 30 W and air pressure of 1.50 kgf/cm^2 is required. For achieving minimum exit hole diameter (63.75 μm)along with minimum HAZ thickness(49.89 μm) the combination of the process parameters are pulse frequency of 64 kHz with duty cycle of 55%, laser power of 30 W and air pressure of 1.50 kgf/cm^2; pulse frequency of 70 kHz, duty cycle of 55%, laser power of 29 W and air pressure of 2 kgf/cm^2 respectively. On the contrary, to obtain the maximum hole circularity (0.88), the combination of the process parameters are pulse frequency of 65 kHz along with duty cycle of 50 %, laser power of 37 W and air pressure of 2.50 kgf/cm^2.

(vi) Finally, multi-objective optimization results illustrate that the parametric settings of pulse frequency of 64.75 kHz combined with duty cycle of 62.5 %, laser power of 29 W and air pressure of 1.50 kgf/cm^2 are set to achieve the minimum entry hole diameter of 76.53 μm, minimum exit hole diameter of 67.33 μm, minimum HAZ thickness of 58.06 μm, and maximum hole circularity of 0.79.

(e) Fiber Laser Surface Texturing on Hastelloy C-276

The research work also facilitates fiber laser surface texturing on Hastelloy C-276. From the results of the present experimentation, the following conclusions can be drawn:

(i) Surface roughness, R_a shows a decreasing tendency with an increase in scan speed. For scan speed of 3 mm/sec to 4 mm/sec, R_a almost remains unchanged for scan speed at preheating temperature of 100°C, while marginally decreasing at 200°C. R_z and R_{ku} are decreased for the increment of scan speed at any temperature of preheating, however, the reverse phenomenon is observed for R_{sk}. The preheated condition provides a better result at varying

scan speed on the surface characteristics during fiber laser surface texturing on Hastelloy C-276.

(ii) Surface characteristics in terms of R_a, R_z, R_{ku}, and R_{sk} are increased with an increase in laser power for any temperature of preheating. High thermal energy at high laser power leads to the formation of the melt pool. The adverse effect of sudden cooling with a moderate scan speed of 3 mm/sec is eliminated drastically by preheating of the workpiece.

(iii) R_a value firstly increases with an increase in pulse frequency up to 65 kHz and then decreases at room temperature. For the elevated temperatures, R_a is gradually decreasing for the increment of pulse frequency. R_z decreases with an increase in pulse frequency for any temperature, which indicates a lesser deviation on the surface profile. For this set of experiments, the lower value of R_{ku} is achieved at room temperature compared to the elevated temperatures. The skewness is found nearer to zero at the preheated condition compared to room temperature for low values of pulse frequency. The preheated condition provides a better surface quality in terms of R_{sk} due to the incorporation of an adequate amount of thermal energy at the texturing zone which aids in forming a uniform re-solidification of the remaining of molten material at a higher value of pulse frequency. On the contrary, at the room temperature lower values of R_a, R_z, and R_{ku} are observed for the selected range of pulse frequency.

(iv) Fiber laser surface texturing on Hastelloy C-276 with the aid of response surface methodology based experimental design is also carried out. ANOVA test of each of the model reveals that the experimental values of all the three responses are well fitted in for all the response criteria. The optimized values of process parameters are found as laser power of 19.93 W, pulse frequency of 60 kHz, duty cycle of 38.96 % and scan speed of 8.41 mm/sec. The optimized target values set for R_a, R_{sk}, and R_{ku} are obtained as 1.2 µm, -0.35 and 3, respectively. The textured Hastelloy C-276 surface at optimized settings can be utilized for bearing applications. The conformity tests reveal that the errors for R_a, R_{sk}, and R_{ku} are found out to be within 3.41%, 4%, and 3.87% respectively, and the predicted results are a close agreement with the experimental results.

It is evident that the existing research work on fiber laser micro-machining on different engineering materials ranging from polymer, quartz to difficult to machine materials such as Ti-6Al-4V, Hastelloy C-276 will provide useful information about the optimum process parameter settings to achieve the desired quality micro-machining features, required for the specific field of

applications. It is expected that existing research work for fabrication micro-channel on PMMA has the potential for biomedical applications, especially in orthopaedics and biological applications for the analysis of DNA due to the minimization of cost. It is also expected that the present work on fiber laser micro-grooving on Ti-6Al-4V will open up various aerospace, automotive and biomedical applications. The development of preheating setup and utilizing it for fiber laser micro-grooving on 316L can serve a wide range of biomedical applications, especially for fabricating stents. In addition to this, micro-hole fabrication on quartz utilizing fiber laser will also be expected to open up signal processing and biological sensing interfaces related applications due to cost-effectiveness and flexibility. Finally, surface texturing on Hastelloy C-276 with the aid of fiber laser will lead to serving various high power applications and bearing applications. The developed preheating setup while surface texturing of Hastelloy C-276 is expected to reduce the failures related to high power applications.

8.2 Future Scope of the Present Work

At this stage, the author feels that further research and development work is needed in this area to make the fiber laser micro-machining system highly applicable for generating complex profile or shape on other advanced engineering materials. Hence, the further scope of the research includes:

(i) To carry out an experimental investigation into fiber laser micro-machining of other polymers and glass materials for different biomedical applications.

(ii) To carry out fiber laser turning operation on different advanced materials.

(iii) To carry out experiments and also to analyze the fiber laser process parameters to generate the helical and spiral grooves of different shapes and sizes in the micro-engineering domain.

(iv) To carry out further study on different new and hard to machine advanced composites and super alloys for better understanding and generate technology guidance for fiber laser processing of these kinds of engineering materials.

However, the author believes that the present investigation and subsequent analysis will provide fruitful and technical information to the researchers, scientists, and engineers who are working in the area of fiber laser micro-machining area. It can also provide direction for the advancement of fiber laser micro-machining process on generating different complex shaped profiles of a wide range of engineering materials which are highly demanded in various engineering fields.

BIBLIOGRAPHY

1. El-Hofy, H. (2005). *Advanced Machining Processes: Nontraditional and Hybrid Machining Processes*, Vol. 120. Mcgraw-Hill, New York. ISBN: 0-07-145334-2. DOI: 10.1036/0071466940.
2. Kumar, K., Zindani, D., & Davim, J. P. (2018). Thermal Processes. *Advanced Machining and Manufacturing Processes*, Vol.1. Springer, Cham. ISBN: 978-3-319-76074-2. DOI: 10.1007/978-3-319-76075-9.
3. Majumdar J.D., Manna I. (2013) Introduction to Laser Assisted Fabrication of Materials. *Laser-Assisted Fabrication of Materials*. Springer Series in Materials Science, Vol. 161. Springer, Berlin, Heidelberg. ISBN: 978-3-642-28359-8. DOI: 10.1007/978-3-642-28359-8.
4. Kopfermamm, H., Ladenburg, R. (1928). *International Journal of Research in Physical Chemistry and Chemical Physics*, *139*, 375–385.
5. Tavassoly, M. K. (2010). On the Non-Classicality Features of New Classes of Nonlinear Coherent States. *Optics Communications*, *283(24)*, 5081-5091.
6. Weber, M. J. (1994). *CRC Handbook of Laser Science and Technology Supplement 2: Optical Materials*, Vol. 8. CRC Press, Florida. ISBN: 0-8493-3507-8.
7. Sen, A., Doloi, B., & Bhattacharyya, B. (2017). Fiber Laser Micro-Machining of Engineering Materials. *Non-Traditional Micromachining Processes*, Vol.1. Springer, Cham. ISBN: 978-3-319-52008-7. DOI: 10.1007/978-3-319-52009-4_6.
8. Masuzawa, T., & Tönshoff, H. K. (1997). Three-Dimensional Micromachining by Machine Tools. *CIRP Annals-Manufacturing Technology*, *46(2)*, 621-628. DOI: 10.1016/S0007-8506(07)60882-8.
9. Masuzawa, T. (2000). State of The Art of Micromachining. *CIRP Annals-Manufacturing Technology*, *49(2)*, 473-488. DOI: 10.1016/S0007-8506(07)63451-9.
10. Sen, A., Doloi, B., & Bhattacharyya, B. (2015). Fiber Laser Micro-Machining of Ti-6Al-4V. *Lasers Based Manufacturing*. Vol.1. Springer, New Delhi. ISBN: 978-81-322-2351. DOI: 10.1007/978-81-322-2352-8_15.
11. Tokita, S., Murakami, M., Shimizu, S., Hashida, M., & Sakabe, S. (2009). Liquid-Cooled 24W Mid-Infrared Er: ZBLAN Fiber Laser. *Optics Letters*, *34(20)*, 3062-3064. DOI: 10.1364/OL.34.003062.

12. Olsen, F. O., Hansen, K. S., & Nielsen, J. S. (2009). Multibeam Fiber Laser Cutting. *Journal of Laser Applications*, *21(3),* 133-138. DOI: 10.2351/1.3184436.
13. Kleine, K., Jones, S., Whitney, B., Ku, Y. C., & Fox, J. (2005). U.S. Patent No. 6,927,359. Washington, DC: U.S. Patent and Trademark Office.
14. Meng, H., Liao, J., Zhou, Y., & Zhang, Q. (2009). Laser Micro-Processing of Cardiovascular Stent with Fiber Laser Cutting System. *Optics & Laser Technology*, *41(3),* 300-302. DOI: 10.1016/J.Optlastec.2008.06.001.
15. Jaworski, P., Yu, F., Carter, R. M., Knight, J. C., Shephard, J. D., & Hand, D. P. (2015). High Energy Green Nanosecond and Picosecond Pulse Delivery through a Negative Curvature Fiber for Precision Micro-Machining. *Optics Express*, *23(7),* 8498-8506. DOI: 10.1364/OE.23.008498.
16. Okamoto, Y., Kataoka, N., Tahara, H., Shiwayama, K., & Uno, Y. (2006). Micro Cutting of Thin Copper Plate by Fiber Laser with Laval Nozzle. *Journal Of Laser Micro/Nanoengineering*, *1(3)*, 243-246.
17. García-López, E., Medrano-Tellez, A. G., Ibarra-Medina, J. R., Siller, H. R., & Rodriguez, C. A. (2017). Experimental Study of Back Wall Dross and Surface Roughness in Fiber Laser Microcutting of 316L Miniature Tubes. *Micromachines*, *9(1)*, 4.
18. Niino, H., & Kurosaki, R. (2011). Laser Cutting of Carbon Fiber Reinforced Plastics (CFRP) by UV Pulsed Laser Ablation. *Laser Applications in Microelectronic and Optoelectronic Manufacturing (LAMOM,)* Vol. 7920, 792019. 10.1117/12.876231.
19. Jäschke, P., Wippo, V., Bluemel, S., Staehr, R., & Dittmar, H. (2018). Laser Machining of Carbon Fiber-Reinforced Plastic Composites. *Advances in Laser Materials Processing*, Vol. 2. Woodhead Publishing. ISBN: 9780081012536. DOI: 10.1016/B978-0-08-101252-9.00006-6.
20. Herzog, D., Schmidt-Lehr, M., Oberlander, M., Canisius, M., Radek, M., & Emmelmann, C. (2016). Laser Cutting of Carbon Fibre Reinforced Plastics of High Thickness. *Materials & Design*, *92*, 742-749. DOI: 10.1016/J.Matdes.2015.12.056.
21. Lecourt, J. B., Boivinet, S., Bertrand, A., Lekime, D., & Hernandez, Y. (2015). High-Energy Picosecond Hybrid Fiber/Crystal Laser for Thin Films Solar Cells Micromachining. *High-Power, High-Energy, and High-Intensity Laser Technology II*, Vol. 9513, 951303. DOI: 10.1117/12.2180234.

22. Deladurantaye, P., Cournoyer, A., Drolet, M., Desbiens, L., Lemieux, D., Briand, M., & Taillon, Y. (2011). Material Micromachining using Bursts of High Repetition Rate Picosecond Pulses from a Fiber Laser Source. *Fiber Lasers VIII: Technology, Systems, and Applications*, Vol. 7914, 791404. DOI: 10.1117/12.875265.
23. Mizunami, T., & Ehara, A. (2011). Femtosecond-Pulsed Laser Micromachining and Optical Damage by an Erbium-Doped Fiber-Laser System, *Proceedings of The 36th International Conference On Micro- and Nano-Engineering (MNE), 36th International Conference on Micro- and Nano-Engineering (MNE)*, Microelectronic Engineering, Vol. *88(8)*, 2334–2337. DOI: 10.1016/j.mee.2011.02.102.
24. Qi, H., & Lai, H. (2012). Micromachining of Metals and Thermal Barrier Coatings using a 532nm Nanosecond Fiber Laser. *Physics Procedia, 39*, 603-612. DOI: 10.1016/J.Phpro.2012.10.079.
25. Wu, M., Guo, B., Zhao, Q., Fan, R., Dong, Z., & Yu, X. (2018). The Influence of the Focus Position on Laser Machining and Laser Micro-Structuring Monocrystalline Diamond Surface. *Optics and Lasers in Engineering*, *105*, 60-67. DOI: 10.1016/J.Optlaseng.2018.01.002.
26. Genna, S., Tagliaferri, F., Leone, C., Palumbo, B., & De Chiara, G. (2017). Experimental Study on Fiber Laser Microcutting of Nimonic 263 Superalloy. *Procedia CIRP*, *62*, 281-286. DOI: 10.1016/J.Procir.2016.06.109.
27. Kathuria, Y. P. (2003). Biocompatible Metallic Stent for Medical Therapy. *Laser Florence 2002: A Window On The Laser Medicine World*, Vol. 5287, 52-62. DOI: 10.1117/12.544874.
28. Liu, L., Li, D. B., Tong, Y. F., & Zhu, Y. F. (2016). Fiber Laser Micromachining of Thin NiTi Tubes for Shape Memory Vascular Stents. *Applied Physics A*, *122(7)*, 638. DOI 10.1007/S00339-016-0170-0.
29. Muhammad, N., Whitehead, D., Boor, A., & Li, L. (2010). Comparison of Dry and Wet Fibre Laser Profile Cutting of Thin 316L Stainless Steel Tubes for Medical Device Applications. *Journal Of Materials Processing Technology*, *210(15)*, 2261-2267. DOI: 10.1016/J.Jmatprotec.2010.08.015.
30. Erika, G. L., Alexis, M. T., Juansethi, I. M., Alex, E. Z., & Ciro, A. R. (2016). Fiber Laser Microcutting of AISI 316L Stainless Steel Tubes-Influence of Pulse Energy and

Spot Overlap on Back Wall Dross. *Procedia CIRP, 49,* 222-226. DOI: 10.1016/J.Procir.2015.11.020.

31. Kleine, K. F., Whitney, B., & Watkins, K. G. (2002). Use of Fiber Lasers for Micro Cutting Applications in the Medical Device Industry. *In Proceedings of ICALEO*, 1-10. DOI: 10.2351/1.5065757.
32. Kleine, K. F., & Watkins, K. G. (2003). Fiber Laser for Micro-Cutting of Metals. *Advances in Fiber Lasers*, 4974, 184-193. DOI: 10.1117/12.484171.
33. Liu, L., Li, D., Tong, Y., & Zhu, Y. (2017). The Influences of Assisting Gas Type and Process Parameters on the Fiber Laser Microprofiling of Thin CoCr Tubes for Vascular Stents. *Applied Sciences, 7(6),* 608. DOI: 10.3390/App7060608.
34. Sealy, M. P., Guo, Y. B., Liu, J. F., & Li, C. (2016). Pulsed Laser Cutting of Magnesium-Calcium for Biodegradable Stents. *Procedia CIRP, 42,* 67-72. DOI: 10.1016/J.Procir.2016.02.190.
35. Demir, A. G., & Previtali, B. (2016). Dross-Free Submerged Laser Cutting of AZ31 Mg Alloy for Biodegradable Stents. *Journal of Laser Applications, 28(3),* 032001. DOI: 10.2351/1.4944751.
36. Choi, W. C., & Chryssolouris, G. (1995). Analysis of the Laser Grooving and Cutting Processes. *Journal of Physics D: Applied Physics*, *28(5)*, 873.
37. Biffi, C. A., & Tuissi, A. (2016). Micro-Processing of NiMnGa Shape Memory Alloy by using a Nanosecond Fiber Laser. *Optics & Laser Technology*, *78,* 42-49. DOI: 10.1016/J.Optlastec.2015.10.008.
38. Singh, R., & Melkote, S. N. (2007). Characterization of a Hybrid Laser-Assisted Mechanical Micromachining (LAMM) Process for a Difficult-to-Machine Material. *International Journal of Machine Tools and Manufacture*, *47(7-8),* 1139-1150. DOI: 10.1016/J.Ijmachtools.2006.09.004.
39. Singh, R., Alberts, M. J., & Melkote, S. N. (2008). Characterization and Prediction of the Heat-Affected Zone in a Laser-Assisted Mechanical Micromachining Process. *International Journal of Machine Tools and Manufacture, 48(9),* 994-1004. DOI: 10.1016/J.Ijmachtools.2008.01.004.
40. Biffi, C. A., Lecis, N., Previtali, B., Vedani, M., & Vimercati, G. M. (2011). Fiber Laser Microdrilling of Titanium and Its Effect on Material Microstructure. *The International*

Journal of Advanced Manufacturing Technology, *54(1-4)*, 149-160. DOI: 10.1007/S00170-010-2918-6.

41. Ancona, A., Nodop, D., Limpert, J., Nolte, S., & Tŕnnermann, A. (2009). Microdrilling of Metals with an Inexpensive and Compact Ultra-Short-Pulse Fiber Amplified Microchip Laser. Applied Physics A, *94(1)*, 19-24. DOI: 10.1007/S00339-008-4906-3.
42. Ghosal, A., & Manna, A. (2013). Response Surface Method Based Optimization of Ytterbium Fiber Laser Parameter during Machining of Al/Al_2O_3-MMC. *Optics & Laser Technology*, *46*, 67-76. DOI: 10.1016/J.Optlastec.2012.04.030.
43. Huang, H., Yang, L. M., & Liu, J. (2014). Micro-Hole Drilling and Cutting Using Femtosecond Fiber Laser. *Optical Engineering*, *53(5)*, 051513. DOI: 10.1117/1.OE.53.5.051513.
44. Adelmann, B., & Hellmann, R. (2015). Rapid Micro Hole Laser Drilling in Ceramic Substrates using Single Mode Fiber Laser. *Journal of Materials Processing Technology*, *221*, 80-86. DOI: 10.1016/J.Jmatprotec.2015.02.014.
45. Harp, W. R., Dilwith, J. R., & Tu, J. F. (2008). Laser Ablation using a Long-Pulsed, High-Fluence, CW Single-Mode Fiber Laser. *Journal of Materials Processing Technology*, *198(1-3)*, 22-30. DOI: 10.1016/J.Jmatprotec.2007.06.062.
46. Ancona, A., Röser, F., Rademaker, K., Limpert, J., Nolte, S., & Tünnermann, A. (2008). High Speed Laser Drilling of Metals using a High Repetition Rate, High Average Power Ultrafast Fiber CPA System. *Optics Express*, *16(12)*, 8958-8968.
47. Tu, J., Paleocrassas, A. G., Reeves, N., & Rajule, N. (2014). Experimental Characterization of a Micro-Hole Drilling Process with Short Micro-Second Pulses by a CW Single-Mode Fiber Laser. *Optics and Lasers in Engineering*, *55*, 275-283. DOI: 10.1016/J.Optlaseng.2013.11.002.
48. Stephen, A., Schrauf, G., Mehrafsun, S., & Vollertsen, F. (2014). High Speed Laser Micro Drilling for Aerospace Applications. *Procedia CIRP*, *24*, 130-133. DOI: 10.1016/J.Procir.2014.08.002.
49. Meng, L. N., Wang, A. H., Wu, Y., Wang, X., Xia, H. B., & Wang, Y. N. (2015). Blind Micro-Hole Array Ti6Al4V Templates for Carrying Biomaterials Fabricated by Fiber Laser Drilling. *Journal of Materials Processing Technology*, *222*, 335-343. DOI: 10.1016/J.Jmatprotec.2015.03.016.

50. Pak, A. M., & Moradi, M. (2015). Hole Geometry Features Analysis In Fiber Laser Percussion Drilling Process. *International Journal of Advances in Mechanical & Automobile Engineering, 2(1),* 18-21.
51. Saklakoglu, I. E., & Kasman, S. (2011). Investigation of Micro-Milling Process Parameters for Surface Roughness and Milling Depth. *The International Journal of Advanced Manufacturing Technology*, *54(5-8),* 567-578. DOI: 10.1007/S00170-010-2953-3.
52. Deladurantaye, P., Gay, D., Cournoyer, A., Roy, V., Labranche, B., Levesque, M., & Taillon, Y. (2009). Material Micromachining using a Pulsed Fiber Laser Platform with Fine Temporal Nanosecond Pulse Shaping Capability. *Fiber Lasers VI: Technology, Systems, and Applications*, Vol. 7195, 71951S. DOI: 10.1117/12.809532.
53. Preusch, F., Adelmann, B., & Hellmann, R. (2014). Micromachining of AlN and Al_2O_3 using Fiber Laser. *Special Issue Laser Micro-and Nano- Processing*, *5(4),* 1051-1060. DOI: 10.3390/Mi5041051.
54. Zhou, W., Deng, W., Lu, L., Zhang, J., Qin, L., Ma, S., & Tang, Y. (2014). Laser Micro-Milling of Microchannel on Copper Sheet as Catalyst Support used in Microreactor For Hydrogen Production. *International Journal of Hydrogen Energy*, *39(10),* 4884-4894. DOI: 10.1016/J.Ijhydene.2014.01.041.
55. Genna, S., Leone, C., Lopresto, V., Santo, L., & Trovalusci, F. (2010). Study of Fibre Laser Machining of C45 Steel: Influence of Process Parameters on Material Removal Rate and Roughness. *International Journal of Material Forming*, *3(1),* 1115-1118. DOI: 10.1007/S12289-010-0967-X.
56. F, Tagliaferria., N, Paganob., C, Leoneb., & B, Palumbo. (2012). Statistical Analysis Of Fiber Laser Machining Of Titanium Alloy, *Proceedings Of 6th I*PROMS Virtual International Conference On Intelligent Production Machines And Systems,* 112–117.
57. Biswas, O. F., Sen, A., Kibria, G., Doloi, B., & Bhattacharyya, B. (2016). Experimental Investigation into Spiral Micro-Grooving on Aluminium using Fiber Laser. *Proceedings Of 6th International & 27th All India Manufacturing Technology, Design And Research Conference* (AIMTDR-2016), 16-18.
58. Astarita, A., Genna, S., Leone, C., Minutolo, F. M. C., Squillace, A., & Velotti, C. (2016). Study of the Laser Marking Process of Cold Sprayed Titanium Coatings on

Aluminium Substrates. *Optics & Laser Technology, 83,* 168-176. DOI: 10.1016/J.Optlastec.2016.04.007.

59. Jones, D. R., & Ashby, M. F. (2011). *Engineering Materials 1: An Introduction To Properties, Applications And Design.* 4th Edition, Elsevier. ISBN: 9780080966663.
60. Smallman, R. E., & Ngan, A. H. W. (2007). *Physical Metallurgy and Advanced Materials Engineering,* 7th Edition, Elsevier. ISBN: 978-0-7506-6906-1. DOI: 10.1016/B978-0-7506-6906-1.X5000-8.
61. Sen, A., Doloi, B., & Bhattacharyya, B. (2016). Fibre Laser Microchanneling of Polymethyl Methacrylate (PMMA). *Lasers in Engineering (Old City Publishing), 35,* 123-138.
62. Ali, U., Karim, K. J. B. A., & Buang, N. A. (2015). A Review of the Properties And Applications of Poly (Methyl Methacrylate) (PMMA). *Polymer Reviews, 55(4),* 678-705. DOI: 10.1080/15583724.2015.1031377.
63. Tilley, R. J. (2004). *Understanding Solids: The Science of Materials,* 2nd Edition, John Wiley & Sons. ISBN: 978-1-118-42328-8.
64. Bottom, V. E. (1982). *Introduction to Quartz Crystal Unit Design*, 1st Edition, Van Nostrand Reinhold. ISBN: 978-0442262013.
65. Ji, L., Hu, Y., Li, J., Wang, W., & Jiang, Y. (2015). High-Precision Micro-Through-Hole Array in Quartz Glass Machined by Infrared Picosecond Laser. *Applied Physics A, 121(3),* 1163-1169. DOI: 10.1007/S00339-015-9482-8.
66. Saha, B., Jana, B., Yadav, J. S., Krishna, C. R., Rao, Y. V. H., & Gupta, B. (1996). Development and Certification of Ti-8Al-1Mo-1V Alloy for HP Compressor Blades for Adour Engine Applications. *Bulletin of Materials Science, 19(4),* 661-669.
67. Koyuncu, E., Kahraman, F., & Karadeniz, Ö. (2009). Investigation of Surface Properties of High Temperature Nitrided Titanium Alloys. *Journal of Achievements in Materials and Manufacturing Engineering, 37(2),* 434-441.
68. Henriques, V. A. (2009). Titanium Production for Aerospace Applications. *Journal Of Aerospace Technology and Management, 1(1),* 7-17.
69. Madalena, F. C. A., Alvarães, C. P., Souza, L. F. G., Jorge, J. C. F., & Araújo, L. S. (2015). Mechanical and Microstructural Properties of the Inconel 625 Alloy Weld Overlay Obtained by Electroslag Welding Process. *Proceedings of the 23rd ABCM International Congress of Mechanical Engineering.*

70. Lotsch, H.K.V. (2014). *Springer Series in Optical Sciences,* Vol.182, Springer, Atlanta. ISBN: 978-3-642-45084-6.
71. Jauregui, C., Limpert, J., & Tünnermann, A. (2013). High-Power Fibre Lasers. *Nature Photonics, 7(11),* 861.
72. Yang, P., & Yang, W. (2013). Surface Chemoselective Phototransformation of C–H Bonds on Organic Polymeric Materials and Related High-Tech Applications. *Chemical Reviews, 113(7),* 5547-5594. DOI: 10.1021/Cr300246p.
73. ASM International. Handbook Committee (Ed.). (1990). *Properties and Selection: Nonferrous Alloys and Special-Purpose Materials,* Vol. 2, ASM International. ISBN: 978-0-87170-378-1.
74. Montemor, M. F., Ferreira, M. G. S., Hakiki, N. E., & Belo, M. D. C. (2000). Chemical Composition and Electronic Structure of the Oxide Films Formed on 316L Stainless Steel and Nickel Based Alloys in High Temperature Aqueous Environments. *Corrosion Science, 42(9),* 1635-1650. DOI: 10.1016/S0010-938X (00)00012-3.
75. Cherry, J. A., Davies, H. M., Mehmood, S., Lavery, N. P., Brown, S. G. R., & Sienz, J. (2015). Investigation into the Effect of Process Parameters on Microstructural and Physical Properties of 316L Stainless Steel Parts by Selective Laser Melting. *The International Journal of Advanced Manufacturing Technology, 76(5-8),* 869-879. DOI: 10.1007/S00170-014-6297-2.
76. Nakao, Y., & Nishimoto, K. (1986). Desensitization of Stainless Steels by Laser Surface Heat-Treatment. *Transactions of the Japan Welding Society, 17(1),* 84-92.
77. Sheng, P. S., & Joshi, V. S. (1995). Analysis of Heat-Affected Zone Formation for Laser Cutting of Stainless Steel. *Journal Of Materials Processing Technology, 53(3-4),* 879-892. DOI: 10.1016/0924-0136(94)01761-O.
78. Cedelle, J., Vardelle, M., & Fauchais, P. (2006). Influence of Stainless Steel Substrate Preheating on Surface Topography and on Millimeter-and Micrometer-Sized Splat Formation. *Surface and Coatings Technology, 201(3-4),* 1373-1382. DOI: 10.1016/J.Surfcoat.2006.02.003.
79. Egashira, K., Masuzawa, T., Fujino, M., & Sun, X. Q. (1997). Application of USM to Micromachining by On-The-Machine Tool Fabrication. *International Journal of Electrical Machining, 2,* 31-36.

80. Sarkar, B. R., Doloi, B., & Bhattacharyya, B. (2017). Electrochemical Discharge Micro-Machining of Engineering Materials. *Non-Traditional Micromachining Processes.* Springer, Cham. ISBN: 978-3-319-52008-7. DOI: 10.1007/978-3-319-52009-4_10.
81. Qi, H., Fan, J., & Wang, J. (2015). A Study of the Micro-Machining Process on Quartz Crystals Using an Abrasive Slurry Jet. *Proceedings of The Institution of Mechanical Engineers, Part B: Journal of Engineering Manufacture, 229(3),* 421-434. DOI: 10.1177/0954405414528167.
82. Sen, A., Doloi, B., & Bhattacharyya, B. (2018). An Experimental Investigation into Fibre Laser Micro-Drilling of Quartz. *International Journal of Mechatronics and Manufacturing Systems, 11(2-3),* 182-202. DOI: 10.1504/IJMMS.2018.092874.
83. Li, L., Low, D. K. Y., Ghoreshi, M., & Crookall, J. R. (2002). Hole Taper Characterisation and Control in Laser Percussion Drilling. *CIRP Annals, 51(1),* 153-156. DOI: 10.1016/S0007-8506(07)61488-7.
84. Ghoreishi, M., & Nakhjavani, O. B. (2008). Optimisation Of Effective Factors in Geometrical Specifications of Laser Percussion Drilled Holes. *Journal of Materials Processing Technology, 196(1-3),* 303-310. DOI: 10.1016/J.Jmatprotec.2007.05.057.
85. Kacar, E., Mutlu, M., Akman, E., Demir, A., Candan, L., Canel, T., & Sınmazcelik, T. (2009). Characterization of the Drilling Alumina Ceramic Using Nd: YAG Pulsed Laser. *Journal of Materials Processing Technology, 209(4),* 2008-2014. DOI: 10.1016/J.Jmatprotec.2008.04.049.
86. Al Falahi, M., Fadaeifard, F., Al Falahi, M. D. A., Bin Baharudin, B. T. H. T., & Hong, T. S. (2016). Surface Damages And Tool Wear Mode In End Milling Of Hastelloy-C276 Under Dry And Wet Conditions. *Materials Science and Engineering Technology, 47(12),* 1182-1192. DOI: 10.1002/Mawe.201600534.
87. Hashim, M., Babu, K. S. R., Duraiselvam, M., & Natu, H. (2013). Improvement of Wear Resistance of Hastelloy C-276 through Laser Surface Melting. *Materials & Design, 46,* 546-551. DOI: 10.1016/J.Matdes.2012.10.024.
88. Yilbas, B. S., & Ali, H. (2016). Laser Texturing of Hastelloy C276 Alloy Surface for Improved Hydrophobicity and Friction Coefficient. *Optics and Lasers in Engineering, 78,* 140-147. DOI: 10.1016/J.Optlaseng.2015.10.015.